

# NISSAN TECHNICAL REVIEW

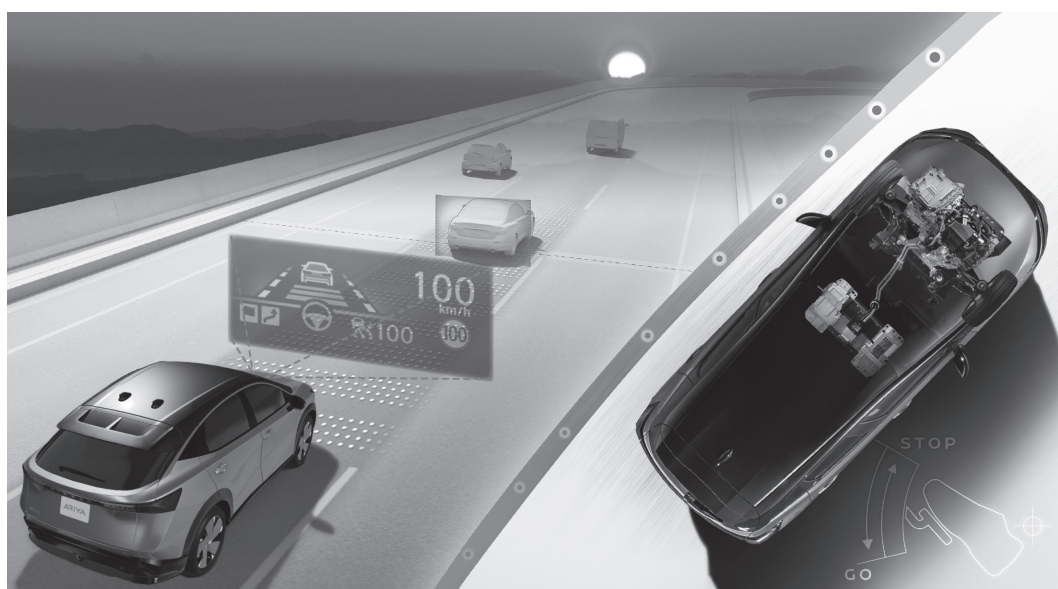
2021  
No.  
**87**



Future-oriented ProPILOT 2.0 / Constantly advancing e-POWER

**NISSAN**  
MOTOR CORPORATION

# NISSAN TECHNICAL REVIEW



2021 No. **87**

# NISSAN TECHNICAL REVIEW 2021 No.87

## Contents

Published in July, 2021

### ◆ Preface

Preface : Efforts of Nissan Toward Advanced Technology Development .....	1
Kunio Nakaguro	

### ◆ Special Feature 1 : Future-oriented ProPILOT 2.0

1. A trustworthy partner .....	5
Kenichi Egawa Akira Higashimata Koichi Onishi	
2. New functions .....	9
Yohei Taniguchi Daigo Atsumura Seiji Tokunaga Katsuhiko Degawa	
3. Supported by vehicle-control technologies .....	13
Yohei Taniguchi Yasuhisa Taira Naoto Sugawara	
4. Intelligent interface .....	19
Nariaki Etori Shohei Nakamura Yasunori Nakazono Kiyoharu Ishigouoka Kenji Maeda	
5. Technologies supporting system reliability .....	25
Takashi Sasayama Kouji Shionome Akira Teranishi	
6. New experimental verification techniques .....	31
Yumi Kubota Koji Sasaki Shimpei Nagae Kenji Ogino	

### ◆ Special Feature 2 : Constantly advancing e-POWER

1. Spreading the appeal of electric drive with e-POWER .....	37
Akihiro Shibuya Toshiyuki Nakajima	
2. Characteristics of e-POWER system and future development .....	43
Naoki Nakada	
3. System technology that provides EV-ness to e-POWER .....	47
Tomoyuki Hanyu Eigo Sakagami Tomohiro Ito Isamu Kazama Yuki Kosaka	
4. Fuel saving technology that satisfies e-POWER' s driving performance .....	53
Hiroschi Kuriki Shuichi Orita Ryuzou Noguchi	
5. Noise and vibration technologies of new Note supporting the EV-ness of e-POWER .....	57
Tetsuya Kawakami Hirotaka Kaneko Yusuke Ienaka Kazuhiko Arai Ryuugo Chiba	
Takanobu Sawada Toru Nakada Masaya Gotou	
6. Electric AWD technology to add value to e-POWER .....	63
Ryoza Hiraku Eigo Sakagami Takeji Katakura	

## ◆ Technical papers

Development of estimation and improvement method for Real World Fuel Economy by using a traffic flow simulation (First & Second Report) .....	67
Yasuki Fukumoto Hiroshi Kuriki Hajime Miura Seishi Shimamura Takahito Nishi	
A Clarification of Relationship Steering Force and Yaw Characteristics to Line Traceability in Small Steering Angle .....	81
Mitsunori Tao	
Development of NV method that combined engine control model and NV model for electrified powertrain .....	89
Masaya Gotou Sho Aizumi Tadashi Nagami Hisayoshi Matsuoka Toshio Enomoto	
Precise Ego-motion Measurement by High Speed Camera.....	95
Hyeoungsung Cho Hidekazu Nishiuchi Hiroshi Satoh Shinichi Nishioka Hiroyuki Sakai Haruo Matsuo	
Environmental Impact Assessment of Battery Electric Vehicles Considering Air Pollutants from Thermal Power Plants .....	101
Gen Saitou Hiromi Asahi	
Development of 0W-8 low viscosity engine oil for fuel efficiency improvement .....	107
Seiichi Nakano Hiroki Saito Yusuke Koike Sachiko Okuda Takumaru Sagawa	
Clarification of Resin Impregnation Mechanism in CFRP C-RTM Forming.....	113
Rieko Yamaguchi Atsushi Mizutani Ryoichi Takatsu Kiyohito Yanagibashi	
Analysis and measurement of PCB heating due to abnormal current and safety conditions .....	119
Tsutomu Horikawa Shingo Inagawa Tsuneaki Yamuchi	

## ◆ Technical Awards

Method of Driving Style Adaptation for Automated Vehicle .....	125
Machiko Hiramatsu Hwaseon Jang Yuki Ito Masaru Yamazaki Takashi Sunda	
A Study of Engine Out PM Emission Mechanism under Low-Temperature Transient Condition and PN Reduction Technology for Direct Injection Gasoline Engines .....	133
Yoshihiro Imaoka Takao Inoue Taisuke Shiraishi	
Evaluation of Equivalent Temperature in Vehicle Cabin by a Mesh-free Simulation (First & Second Report).....	141
Hajime Oi Yasushi Ichikawa Akira Matsumoto	
Development of the First Active Torque Rod in the World .....	157
Masahiko Kondo Koji Tanimura Ryosuke Yamauchi Yuta Oana	
Development of New-generation e-POWER Hybrid Powertrain .....	165
Naoki Nakada Tomoyuki Hanyu Makoto Kimura	
Development of World First Mass Production Variable Compression Ratio Engine .....	171
Shinichi Kiga Shuji Kojima Katsuya Moteki Kazuya Matsuoka Yoshiaki Tanaka	
Analysis of relationship between self-excited oscillation and coulomb friction in spool of electro- magnetic proportional valve and design method for stabilization .....	175
Katsuhiko Sando	



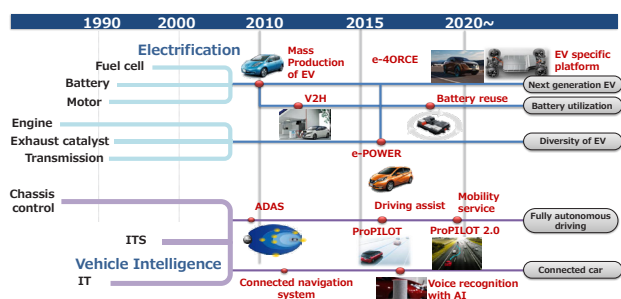
# Efforts of Nissan Toward Advanced Technology Development

Executive Officer, EVP **Kunio Nakaguro**

## 1. Introduction

The competitiveness of Nissan has always originated from advanced technologies. Since the establishment of this company, new technologies that competitors cannot achieve have consistently been developed and commercialized. Over the last two decades, research and development activities based on two pillars of advanced technologies—electrification and vehicle intelligence—have been promoted because these pillars are the key to solving social issues such as resource depletion, environmental problems, traffic accidents, and traffic congestion.

During research and development, the provision of these advanced technologies, which become valuable only when they are widespread as features in vehicles, to as many customers as possible is considered. These efforts have led to the commercialization of electric vehicles (EVs) and e-POWER from the perspective of electrification, and also diverse advanced safety technologies, ProPILOT, and connected technologies with cloud services from the perspective of vehicle intelligence. These advanced technologies have been adopted for different segments and are widely used by customers.



History of advanced technology development by Nissan

However, the decade leading up to 2030 represents an age of uncertainty in which the social environment and technology are changing significantly. In the following sections, recent environmental changes and the technology development strategies utilized by Nissan to cope with them are detailed.

## 2. Challenges surrounding mobility

The social environment has changed significantly over recent years. CO<sub>2</sub> emissions, which are known to be the primary factor causing global warming, have been

increasing annually. Consequently, CO<sub>2</sub> regulations and selling restrictions on gasoline-powered vehicles have become increasingly stringent in major countries.

As the Japanese Government declared in October 2020 that “the Japanese Government aims to reduce greenhouse gas to net-zero by 2050,” leaders in many countries have begun to refer to carbon neutrality. To respond to these social demands, it has become necessary to proliferate electrification and renewable energy on a global scale.

Meanwhile, the mobility efficiency in urban areas has deteriorated owing to the overconcentration of population, while the mobility disadvantage has become more severe in rural areas owing to the reduction in public transportation services and infrastructure, resulting from the decrease in population. In developed countries, the societies of which are aging, the number of traffic accidents caused by elderly people is increasing; thus, driving assist technologies are necessary to help everyone move with more confidence and in a safer manner.

To respond to such environmental changes, technological evolution is promoted by swiftly adopting diverse and advanced technologies, such as new surrounding environment recognition technologies, data science, and artificial intelligence.

## 3. Advanced technology strategy of Nissan

### 3-1. Electrification technologies

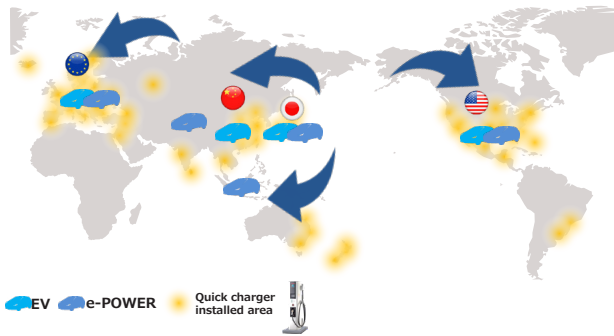
Around the 1990s, Nissan pioneered the research and development of batteries and motors for EVs and launched the industry-first mass-produced EV, Nissan LEAF, in 2010. In addition to vehicles, diverse technologies have been introduced in the market with the objective of making EVs usable with more confidence, such as by considering the usage environment and eco-cycle. For instance, charging infrastructure standards have been established, such infrastructure has been deployed, a vehicle-to-home system has been developed, and the battery reuse business 4R Energy has been established. This abundance of real-world accomplishments and the accumulated data of vehicles and customers at Nissan significantly promote electrification.

Nissan has two major goals regarding the expansion of electrification. One is the realization of its mission to achieve a zero-emission society, and the other is to provide customers with secure, safe, and comfortable means of mobility by utilizing the significant potential of the motor drive.

Owing to its excellent controllability, the motor drive affords ideal acceleration, deceleration, ride comfort, and

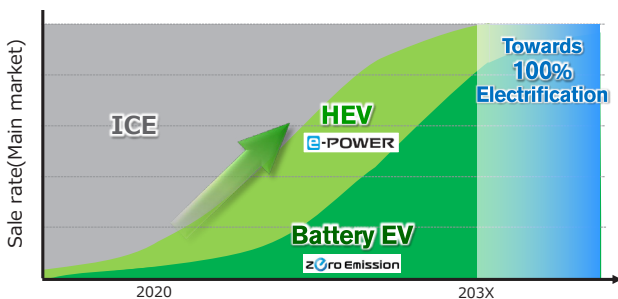
quietness in accordance with the driving environment and the intention of the driver. In addition, motor drives are highly compatible with advanced safety technologies, such as ADAS (Advanced Driver-Assistance Systems) and autonomous driving technologies. Thus, the unique appeal of motor drives will be increased further.

Nissan will continue to offer motor drives to customers worldwide, including regions where the charging infrastructure has not been deployed adequately, by supplying not only EVs but also motor-driven e-POWER, which does not require external battery chargers.



Market deployment of electric powertrain vehicles

According to its business transformation plan, Nissan plans to sell more than 1 million EVs per year by the end of FY 2023, expand the lineup of EV models by more than 8 models, and broaden the segment coverage of e-POWER in the global market.



Future expansion plan for electrification technologies

### 3-1-1. EVs

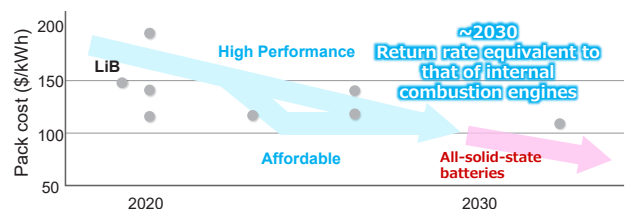
Safety is one of the requirements that Nissan emphasizes when developing and offering EVs. When increasing the battery energy density for higher performance, safety and reliability are ensured by conducting tests under severe conditions, prior to launching the vehicles in the market.

This emphasis on safety is demonstrated by the fact that, as of the end of December 2020, 510,000 units of LEAF have been sold, and thus far, there have been no cases of serious battery-induced accidents. Based on market driving data, severe usage environments continue to be forecasted, and these environments are considered for the high-level reliability designs, test standards, and development.

Furthermore, technology development is promoted to enhance the attractiveness of EVs. One of the essential technologies for this purpose is the unique vibration-damping control technology, realized through the

development of a motor for LEAF. The highly responsive electric powertrain has a higher potential in terms of controllability than an internal combustion engine; however, there are issues such as the jerk experienced by occupants due to a sudden torque increase, and the vibrations caused by torque fluctuations. Vibration-damping control technology plays an important role in precisely controlling these vibrations and generating smooth acceleration. Combining this technology with the knowledge of all-wheel drive and chassis control accumulated over the years has yielded the integrated vehicle control technology e-4ORCE, which will be installed in the Nissan Ariya unveiled this year. Each motor at the front and rear is controlled during both braking and driving and combined with the chassis control in order to achieve a stable and comfortable ride, while also preventing the occupants from recognizing slipping or changes in vehicle posture. Such technologies enable everyone to drive with confidence and comfort.

For the proliferation of electrification, it will be necessary to reduce the cost of electric powertrains and to particularly address the challenge of innovation in battery technology. Specifically, the development of battery materials in cooperation with suppliers to accelerate the research and development of cobalt-free batteries will be promoted, thereby reducing the use of expensive cobalt. For the battery pack, a structure referred to as Cell-to-Pack is also being developed in cooperation with suppliers; in this structure, the cells are directly installed in the pack without modules and the manufacturing process is streamlined. Through these technological innovations, the return rate of these vehicles will be brought to a level equivalent to that of internal combustion engine vehicles before 2030.

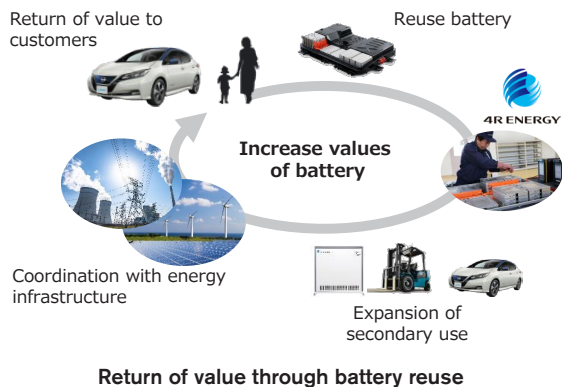


Battery cost reduction

The research and development of all-solid-state batteries that will drastically improve safety and cost competitiveness even further are also being promoted, in cooperation with organizations such as Tokyo Institute of Technology. The most significant challenges associated with this development are the enlargement of batteries applicable to vehicles and their production processes. Material selection and technology development in the manufacturing process will be expedited to achieve early mass production.

Owing to the increased proliferation of EVs, the market for used batteries is expected to expand in the future; therefore, it is necessary to implement measures for their appropriate utilization. Nissan has pioneered the establishment of a company to develop technologies for reused batteries, known as 4R Energy, which was launched in Namie-machi in Fukushima Prefecture. A suitable business model is also being developed; this

model entails sorting the used batteries collected from the market according to their conditions and performances in order to supply them to various secondary users, such that the value of reused batteries can be returned to customers. This model will be expanded as a business to reduce the burden on EV owners, aiming at the further proliferation of EVs.



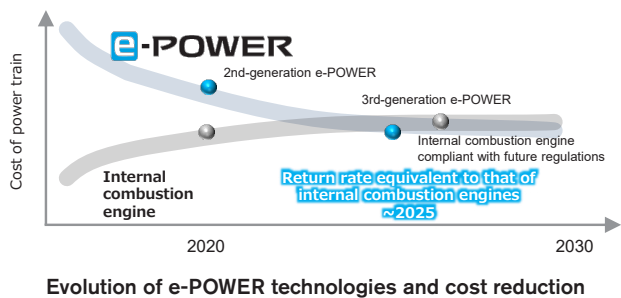
### 3-1-2. e-POWER

The most notable characteristics of e-POWER, which utilizes the same core technology as EVs, are quietness and smooth EV-like driving achieved using a 100% motor drive that yields the maximum torque from the start.

The launch of the new KICKS designed for the Asian market this year represents the first deployment in overseas markets, and local media and journalists have responded positively. For the new NOTE in the Japanese market, a novel powertrain integrated with an inverter and a motor has been implemented in order to further improve the efficiency, acceleration, and quietness.

In addition, a system is being developed for the premium segment by utilizing the characteristics of e-POWER to achieve exceptional quietness by ultimately reducing the vibration transmission from the power-generating engine.

Another challenge in the proliferation of e-POWER is the cost of the powertrain. In addition to developing the battery technology, as in the case of EVs, a simplified system is desired, in which the engine is dedicated to power generation and operation under limited conditions in order to achieve a return rate equivalent to that of internal combustion engines by 2025.



### 3-2. Vehicle intelligence technology

Nissan designs and engineers cars that prioritize a high level of safety. The goal is to reduce the number of deaths due to accidents involving Nissan vehicles to virtually zero. To this end, the safety of Nissan vehicles is

continually being enhanced, partly through the development and adoption of autonomous driving.

Nissan has led the industry by launching various world-first technologies based on its concept of reducing the various risks surrounding vehicles; these technologies include Lane-Keeping Assist, Around-View Monitor, and Emergency Assist for Pedal Misapplication. The competitiveness of Nissan originates from such accomplishments and the high reliability of the systems, similar to the case of electrification technologies.

The objective is to provide all customers with less stressful and more secure, safe, and comfortable driving through autonomous driving technologies, as typified by ProPILOT, as well as connected technologies that deliver diverse information and services to the vehicle occupants. By the end of 2023, it is expected that at least 1.5 million vehicles equipped with autonomous driving technologies will be launched per year.

#### 3-2-1. ProPILOT

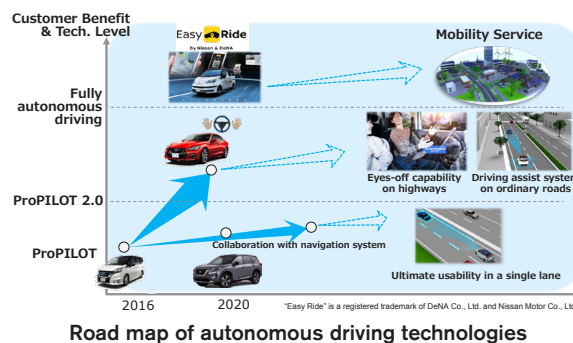
ProPILOT, which was launched in 2016, evolved into ProPILOT 2.0 in 2019. This system offers navigated single-lane highway driving with hands-off capability, the first of its kind in the world. When designing the autonomous driving technologies of ProPILOT, consumer usage on highways was analyzed and examined. This system provides appropriate driving assistance for a wide range of scenarios on highways, from the mainline through the exit, to ensure that customers experience less stress.

This performance and marketability are supplemented by the long-time advantages of Nissan technologies, such as surrounding environmental recognition and control as well as the accumulated technological capabilities for advanced driving, such as redundancy design to ensure safety in the case of a system failure.

#### 3-2-2. Evolution of autonomous driving technologies

For fully autonomous driving in the future, the scenarios under which driving assist is applicable and the level of autonomy must be increased, and systems that everyone can confidently use must also be provided continually.

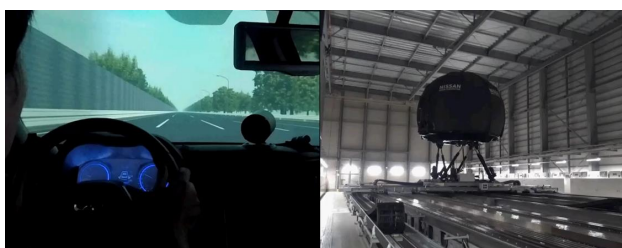
As a part of this technology development, Nissan has been conducting a field test on Easy Ride, in collaboration with DeNA in Yokohama Minato Mirai. In the test, customers are asked to use the vehicle such that the use cases can be determined, the issues associated with practical use can be identified, and continued development for future commercialization can be achieved.



In the real world, fully autonomous driving must

ensure safety in the presence of any obstacles on the road. Consequently, significant efforts are still required to achieve recognition technologies that account for a wide range of customer driving scenes and road environments. Thus, vehicle control technologies as well as the research and development of base components, such as sensors and cameras, will be prioritized.

Commercializing these technologies in the global market requires a greater understanding of the market environment. For this purpose, road environments have been modeled. Development can be streamlined by reproducing different driving scenes worldwide based on the large amounts of data pertaining to market environments and the high-definition map data obtained through the development of ProPILOT. Nissan uses a driving simulator that can reproduce both market environments and actual vehicle behaviors for the development of autonomous driving technologies.



Driving simulator at Nissan Technical Center

### 3-2-3. Connected technologies

For years, Nissan has also been realizing technical innovations in connected technologies that offer various services to the vehicle occupants by connecting the vehicle with cloud services. In 1998, a system known as “Com-Pass Link” was pioneered, which combines vehicles with information technology through services such as a new information service via a car navigation system and mobile phones and also Japan’s first operator service. Subsequently, this system has evolved into Carwings and NissanConnect to commercialize diverse functions and services in the global market, such as the provision of information regarding the deterioration of the vehicle and batteries, location information, optimal route searching, and remote door locking.

In the future, additional services will be provided through exponentially faster communication between cloud services and the servers.

For example, the achievement of the following services is being attempted: remote control and automatic setup of various functions by using smartphone applications to enable the driver to easily perform a series of actions before entering the vehicle and the foresight of driver intentions according to the preferences and behaviors of the driver analyzed using big data in order to incorporate the results with an advanced human-machine interface, such that the driver can intuitively perform different functions during driving.

These functions are supported by alliance cloud services and on-board platforms and will be deployed and promoted globally alongside other carriers and service providers.

The architecture of the system software and hardware

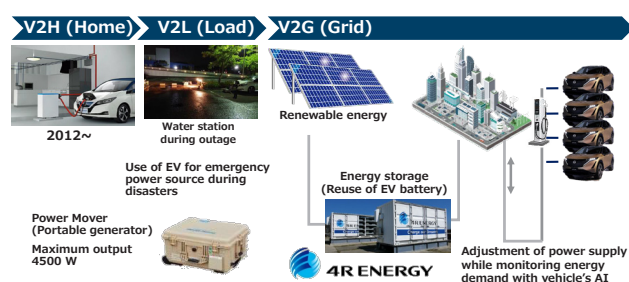
has become increasingly complex with the functional extensions. To address this issue, innovations for development efficiency are being realized by considerably streamlining the system through module design and by adopting automatic function evaluation methods using digital analysis tools.

## 4. Future mobility society

The advanced technologies discussed above help enrich social life, in addition to serving customers who purchase Nissan vehicles.

For example, EVs, also known as energy-stored cars, play an active role in supplying power during disasters. Through the “Blue Switch” project in Japan, Nissan contributes extensively to the society through arrangements with many local municipalities. The vehicle-to-grid system is also being studied for power supply and demand control. This system is enabled by connecting reused battery-based energy storage with existing power grids.

Further, for the mobility-disadvantaged in rural areas, an environment that helps everyone move with confidence and safety is being sought after by fully utilizing the accumulated advanced safety technologies, autonomous driving technologies, electrification technologies, and connected technologies in collaboration with the local municipalities. Simultaneously, the business models generated through these activities are being verified.



Contribution of EV technologies to the energy-based society

## 5. Conclusion

Nissan is working on diverse advanced technologies, in addition to the themes discussed thus far. New ideas are being embedded into different technologies, such as those for further vehicle weight reduction using different types of materials, optimizing interior environments by determining the physical conditions of the occupants based on biosignal recognition, further widening the vision of occupants by developing the Around-View Monitor, evolved autonomous parking, and low-volume multi-part manufacturing using metal 3D printers and die-less forming. The vision of Nissan is to enrich the daily lives of customers worldwide by expanding the appeal of its unique advanced technologies and to enable customers to enjoy these technologies. We are convinced that this vision will shape the future mobility of society. We at the Research and Development Division will work together to continue to embody the “Technology of Nissan.”



## Special Feature 1 : Future-oriented ProPILOT 2.0

## 1. A trustworthy partner

Kenichi Egawa\* Akira Higashimata\*\* Koichi Onishi\*\*\*

## 1. Development of ProPILOT 2.0

After ProPILOT 2.0 (hereinafter referred to as “PP2.0”) was introduced to the market, journalists described it as “safe” and “comfortable” and also used terms such as “buddy” or “partner,” thus suggesting a new person-to-vehicle relationship. With the help of a researcher in psycho-informatics, the reasons for these responses were re-evaluated and three key points were identified:

1. Release from vigilance.
2. Control initiative and understanding others.
3. Skilled driving.

These key aspects indicate that the following development targets (as stated for the development of PP2.0) have been realized:

- The system is capable of automatic driving on highways in a “safe,” “secure,” “convenient,” and “comfortable” manner under certain speed conditions.
- The vehicle motion provides an “in-control” and “relaxed” driving experience to both the driver and the passengers.
- The vehicle exhibits natural traffic behaviors.

Our vision of “autonomous driving” is a “door-to-door” function. The ultimate objective is to transport individuals to nearly any destination that they have set. PP2.0 has now achieved this objective with the current technology.

The function realized by PP2.0 is “point-to-point” (hereinafter, “P2P”), a function that provides diverse assistance to drivers on highways, ranging from route planning to driving operation, when the destination is set in the navigation system. The technical aspects are lane keeping, lane changing, and following distance and vehicle speed control in traffic. In addition to the developments in each of these aspects, navigated route driving has been investigated, which involves route planning at the lane level considering junctions and exits.

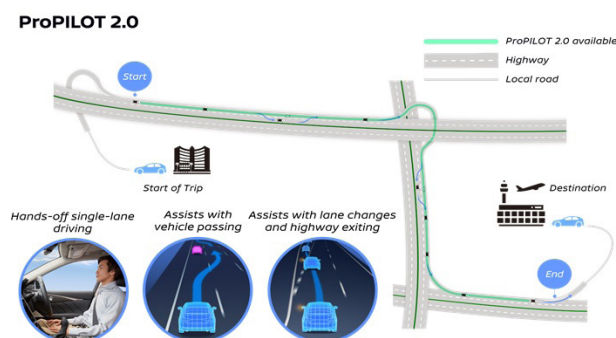


Fig. 1 ProPILOT 2.0 (P2P)

First, the crucial technology for realizing a P2P system is a 3D high-definition map (hereinafter, “3D HD map”), which contains more road surface data (such as the number of lanes, slope angles, and cants) than a standard map. These information data points are used in the driving system, and the P2P function is realized.



Fig. 2 3D HD map

Second, the development factors of PP2.0 include the key terms “reassurance” and “comfort.” Reassurance is fundamentally supported by dynamic performance (hereinafter, “DP”) technology, which is represented as fluent vehicle control, and it has been developed by Nissan Motors over many years. Expressed otherwise, in most road environments, the driver can control the vehicle at any time.

It is also important to clearly inform the driver about the current system conditions. A human-machine interface (HMI) enables the driver to understand how the system is recognizing and judging the surroundings, thus enhancing the trust of the driver. Therefore, a new interactive HMI was developed.

\*Customer Performance and Test Engineering Methodology Innovation Department  
 \*\*\*Customer Performance and Vehicle Test Engineering Department No.1

\*\*Software Engineering Department



Fig. 3 Intelligent interface

The other key term, comfort, is established based on the aforementioned reassurance. Vehicle behaviors that enable the driver to feel ease were identified through extensive DP/human research. Furthermore, comfort was improved by combining the P2P function with a “hands-off” (hereinafter, “H/O”) function to reduce driving operation; consequently, the system reduces fatigue.

## 2. PP2.0 development target

The development concepts of PP2.0 were to “pursue values that customers can use” and to avoid “hard-selling the technology.” The objective was to “provide new value with safe, reassured, convenient, and comfortable driving on the highway.”

Based on DP/human research, which involves fundamental technologies, and the three key technological items of vehicle control, HMI, and safety design, reassurance and comfort were achieved by using the two characteristic functions of PP2.0 (i.e., P2P and H/O) in order to create new objective values. For the measurement of these values, the index of fatigue reduction (fatigue degree) was set, and the corresponding system was developed (Fig. 4).

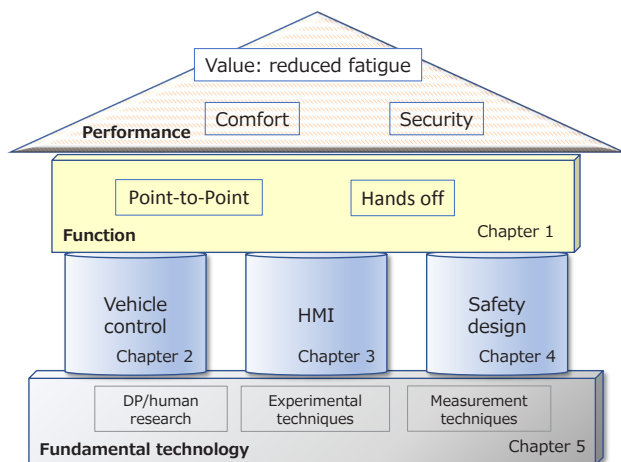


Fig. 4 System target and function hierarchy

To organize the relationships between physiological factors and the vehicle functions, the categories of

physical and nervous fatigue reduction were defined as follows:

- Physical fatigue reduction: reduction of driving operations through the functions of H/O driving and automated lane changing.
- Nervous fatigue reduction: fluent behaviors (vehicle control) and timely provision of information regarding the surrounding conditions (HMI).

Even with the H/O driving and automated lane-change functions, fatigue can occur due to unsmooth vehicle motion or interference with the moving vehicle. Physical fatigue can be decreased by reducing nervous fatigue. By solving these issues, weariless driving can be provided, thereby ensuring reassurance and comfort.

## 3. Psychology of fatigue reduction

PP2.0, which was developed as described above, was assessed by test drivers from Nissan and also journalists. Moreover, as stated initially, to understand the impressions formed by individuals without automobile-related occupations, Prof. Takatsune Kumada (Laboratory of Psycho-informatics, Department of Intelligence Science and Technology, Graduate School of Informatics, Kyoto University) performed two test drives of PP2.0 on a suburban highway in Kyoto City (in November 2019 and October 2020). He provided feedback from the perspective of psycho-informatics. His opinions were as follows:

- ◆ It was a short test drive, and the stress and fatigue induced by driving were low.
- ◆ Little anxiousness and irritation were experienced when following a slower vehicle.
- ◆ A new person-to-vehicle relationship was anticipated.

These opinions and the corresponding hypotheses are discussed below.

### State of vigilance

In a vehicle not equipped with PP2.0, deceleration in accordance with the surrounding traffic induces fatigue. Advanced research\*1) explains this phenomenon as a state of vigilance, in which a continuous anticipatory attitude is retained toward infrequent, uncertain, and low-likelihood phenomena, such as collisions. In a 1956 U.K. symposium, vigilance was defined as “a state in which certain small changes generated at random intervals in an external environment can be detected and handled at all times”\*2). Notable research on vigilance includes the famous studies conducted by Mackworth on radar monitoring. The PP2.0 test-drive response suggests that the partial release from vigilance leads to a more appropriate state for monitoring the surroundings, as compared to that when PP2.0 is not operating, which reduces the fatigue experienced.

### Control initiative and understanding of others

It is generally considered that the loss of control initiative impressions can cause stress; however, PP2.0 achieves a suitable balance between control initiative and role assignment. Control initiative refers to the

perception of driving a car by oneself. In other words, the objective of the driver (i.e., reaching the destination safely) is shared by the car, and the driver assists the car in achieving this objective. During this assignment, the car informs the driver (via the HMI) about what it recognizes and its control operations. In addition, the overall operational control belongs to the human because the car requests control permission from the driver. Consequently, the car acts as a partner to achieve the objective through joint efforts. By releasing the steering wheel when assigning the car to drive, the driver recognizes the role transfer clearly and independently.

This new human-to-car relationship can be interpreted as a development from the stage in which the human and the car recognize the same entities to a stage in which the controls assigned to the car are shared through communication (of shared intentions and targets) to generate a sense of security. A mechanism similar to the psychological concept of “understanding others”<sup>3)</sup> may explain this phenomenon.

#### Skilled driving

Furthermore, after being commissioned to help reach the destination safely, the car also realizes comfortable driving. Car behaviors such as lateral movements and acceleration timing for overtaking are within the expectations of the driver and cause no unnecessary stress. Furthermore, during route-following, which is the lane-keeping driving mode, the driver feels as though the vehicle follows an endless stable line at the center of the lane, which creates a secure feeling and comfort. Such stability increases the trust of the driver in the car and appears to be one of the reasons for fatigue reduction.

It is assumed that these factors invoke moderate levels of trust in the car, creating a secure feeling and comfort during driving and also reducing stress and fatigue. However, the short test drive (~10 min in this case) did not lead to a human-to-car trust relationship. The psychological responses in the market may become apparent only after PP2.0-equipped vehicles are commercially available for use on public roads. Nevertheless, this is an interesting psychological research theme.



**Fig. 5 Prof. Kumada (Kyoto University) and SKYLINE test-drive model**

As described above, the development targets appear to have been achieved from a psychological perspective. In the future, continued research into “new human-to-car relationships” will be performed.

## 4. Summary

The current PP2.0 offers confident and feasible P2P and H/O functions. These have been designed through the multilateral combination of numerous world-first vehicle-control technologies, such as HMIs and safety design technologies. This was achieved through numerous foundational elements, such as DP/human research and experimental/measurement techniques, that required an extensive period for accumulation. We are proud of our ability to deliver the vision and consistent technological developments required for this endeavor.

Consequently, secure, comfortable, and fatigue-reducing performance could be achieved. This new human-to-car relationship has also been suggested from a psychological perspective, albeit further research is required.

This paper describes in detail the technologies required to realize PP2.0.

## References

- 1) T. Sato, J. Kawahara, T. Kumada and M. Aakamatsu : Analysis of Factors Influencing Driver Fatigue Accumulation on Long Trips and Classification of Individual Differences of the Fatigue Accumulation during Long-Term Driving, Transactions of Society of Automotive Engineers of Japan 44(6), p.1451, 2013
- 2) A. Nishioka : Vigilance Taskに関する心理学的諸研究, The Japanese Journal of Psychology 33(3), p.154, 1962
- 3) N. J. Emery, The Eyes Have It: The Neuroethology, Function and Evolution of Social Gaze, Neuroscience & Bio Behavioral Reviews 24(6) p.581, 2000

## Authors



Kenichi Egawa



Akira Higashimata



Koichi Onishi

## Special Feature 1 : Future-oriented ProPILOT 2.0

## 2. New functions

Yohei Taniguchi\*

Daigo Atsumura\*

Seiji Tokunaga\*

Katsuhiko Degawa\*

## 1. Introduction

ProPILOT 2.0 (hereinafter referred to as “PP2.0”) has substantially evolved from the first-generation ProPILOT to create the world’s first driving-assistance system that can guide a vehicle through a multi-lane highway, working in tandem with the navigation-system-planned route. PP2.0 can operate in hands off mode, provided the driver consistently monitors the objects and events and responds immediately to operate the steering wheel in response to the road, traffic and vehicle conditions. This chapter describes the new functions of ProPILOT 2.0.

## 2. New functions of ProPILOT 2.0

## 2.1 ProPILOT 2.0 summary

PP2.0 offers a point-to-point function allowing navigation linked driving such as merging on to a highway when destination is set in the navigation system. When the navigation linked driving is initiated, system supports driving through interchanges and assists overtaking another vehicle until reaching the relevant exit. Provided that the driver always attends to the road ahead and can operate the steering wheel with certainty and immediately in response to the road, traffic, and vehicle conditions, the system operates with hands off with in the same lane and provides wide range driving maneuver support to the driver. In addition, using the navigation data and information of the surroundings from a 360° degrees sensing, the system determines an appropriate lane-change starting point for branching or overtaking whilst following the planned route, and proposes the relevant actions to the driver. Lane-change assistance is initiated by the driver when both hands are placed on the steering wheel and the switch to approve the proposal is operated. Fig.1 illustrates the PP2.0’s operation.

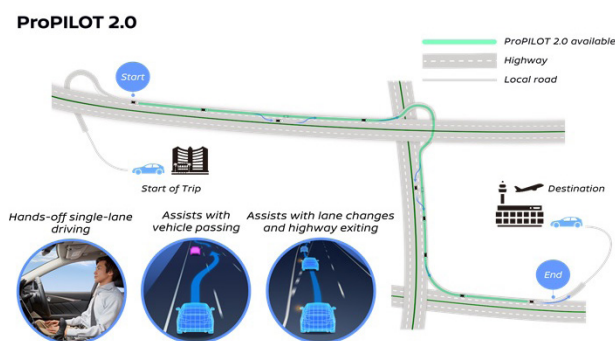


Fig.1 ProPILOT 2.0

PP2.0 integrates and uses seven cameras, five radars, 12 vehicle-mounted sonars, a global navigation satellite system, and 3D High-Definition map (hereinafter, “3D HD map”) data to collect information from the surroundings (i.e., not only from the front but also the right, left, and rear of the vehicle) and determines the correct position on the road. The 3D HD map data include information detailing the road structure, the number of lanes, and the positions of merging points, branching points, and intersections. These information allow system control that foresee the road structure ahead and realize smooth driving as that of an experienced driver. In addition, the vehicle is equipped with a driver-monitoring camera that continuously monitors the driver’s forward gaze.

The PP2.0 sensor-mounting configuration, a 360° sensing image diagram, and a 3D HD map data are illustrated in Fig.2, Fig.3, and Fig.4, respectively.

\*AD/ADAS Advanced Technology Engineering Department

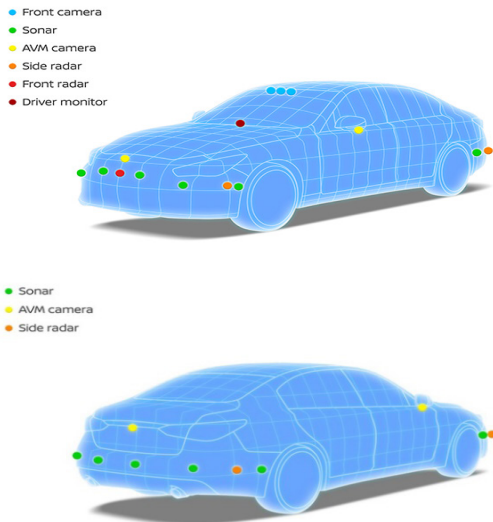


Fig.2 ProPILOT 2.0 sensor configuration

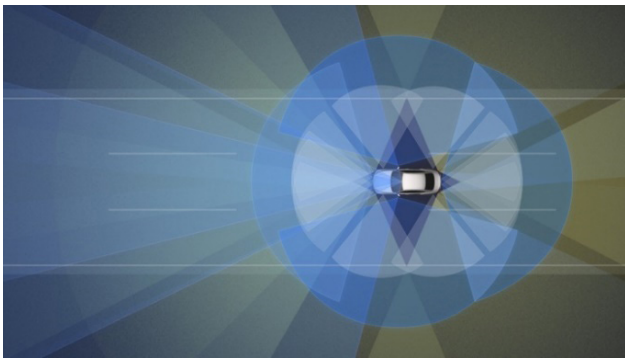


Fig.3 ProPILOT 2.0 360° sensing diagram

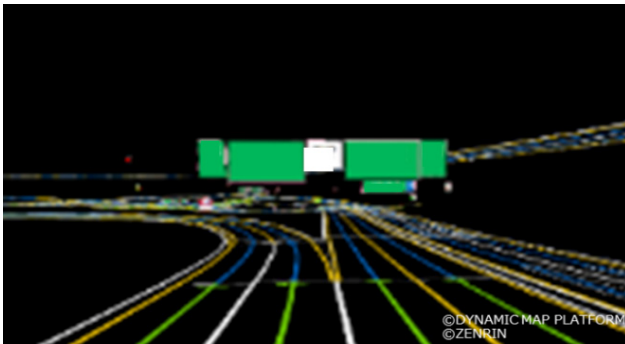


Fig.4 3D High-Definition map

## 2.2 Vehicle-speed/inter-vehicle-distance control functions

The system controls the vehicle speed to maintain the speed preset by the driver. Upon detecting a preceding vehicle, the system controls the headway distance so as to maintain a suitable distance to the vehicle ahead according to the host vehicle speed set by the driver as the upper limit. If the vehicle ahead stops, the PP2.0 vehicle is able to stop as well behind it. After the stop, stop/following driving can resume with respect to the vehicle ahead within 30 s.

If a curve is detected on the road ahead, deceleration control is performed to adjust vehicle's speed according to

the magnitude of the curvature.

If the traffic sign recognition system detects a speed sign, the vehicle's speed is limited to the value detected.

## 2.3 Lane-keeping function

The system assists the driver with steering operations by controlling the steering so that the vehicle travels near the center of its lane. Drivers should remove their hands from the steering wheel as long as they are always attentive to the road ahead and are prepared to operate the steering wheel with certainty and immediately in response to road, traffic, and vehicle conditions.

## 2.4 Route-following assistance function

If a destination has been set in the navigation system, lane changing is proposed to the driver when such maneuvers become necessary to continue to follow the route (e.g., exiting/branching) or when lane-reduction point is reached. When the driver places both hands on to the steering wheel and presses the lane-change assistance switch (located on the steering wheel), the turn signal of the lane change direction begins to flash, and the steering wheel is controlled to assist the lane-change operation. If multiple lane changes are necessary to reach the target lane, sequential lane-change assistance is possible.

### 2.4.1 Lane-change assistance function

When the driver has both hands on the steering wheel and operates the appropriate turn signal device, the system controls the steering to assist the driver in executing the steering wheel operations required for a lane change.

### 2.4.2 Overtaking-assistance function

If a vehicle slower than the driver-set speed is detected ahead, overtaking is proposed to the driver. When the driver has both hands of the steering wheel and presses the lane-change-assistance switch located thereupon, the turn signal towards the overtaking lane is illuminated; then, the steering wheel is controlled to assist the lane-change operation. After passing the vehicle, the system proposes returning to the initial lane to the driver. If the driver presses the lane-change-assistance switch, the turn signal is illuminated towards the initial lane and the system controls the steering to assist the driver in executing the lane-change operation.

The next chapter describes the application of the 3D HD map data required for the lane-change-, overtaking-, and route-following-assistance functions.

## 3. Application of 3D High-Definition map data to lane-change assistance

This chapter explains the judgment process used to determine the feasibility of lane changes and the lane-level driving plan; for this, an example of the 3D HD map data used for the lane-change assistance function is given.

### 3.1 Judgment of lane-change feasibility

Acquiring information pertaining to the lanes ahead is one challenge in realizing lane-change assistance. At the start of the lane change, the camera may not be able to collect comprehensive lane information for the point where the lane change ends. Accordingly, if information is only received from the camera, the appearance of a dividing line forbidding lane changes during the lane change (or other operations) may prevent the lane change. Meanwhile, because the 3D HD map data include lane-level data (e.g., curvatures and dividing lines), the acquisition of road shapes beyond the camera’s detection range allows lane-change opportunities to be judged by considering the section of any lane between the start and end points.

### 3.2 Lane-level driving plan

The lane-change-assistance function proposes lane changes at an appropriate timing (as determined by the system), to allow the vehicle to follow the route recommended by the overtaking-assistance function or navigation system. This judgment is realized through the use of a route plan generated by the system from the lane-level information included in the 3D HD map data. This route plan refers to the indication of the lanes in which the vehicle should remain for certain sections, as well as proposal for guiding the vehicle in to the proper lane.

Fig.5 illustrates the process of generating a lane-level route plan. First, for exit branching on an expressway, the system calculates the number of lane changes required to follow the route recommended by the navigation-system, as well as the distance along the route to the branching point; the results are used to select a lane.

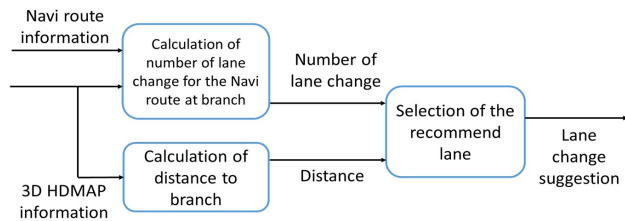


Fig.5 Process of generating lane-level route plan

Next section explains the process of lane-level route planning through an example. Fig.6 schematically shows the road configuration near a highway branching point. Consider that the route recommended by the navigation system extends to the exit (Point P). If the vehicles in the rightmost lane of the through traffic lanes as the exit approaches, the system recommends changing lanes toward the left until the vehicle is in the lane A, The system does not recommend moving to lane B because doing so will increase the number of lane changes needed to exit from point P. If the vehicle is initially traveling in lane B, the system recommends changing lanes to the right and guides the vehicle into lane A. Regardless of the vehicle’s starting lane, system

recommends changing lanes so that the vehicle is ultimately guided in to lane A.

Furthermore, having a lane-level route plan allows proposals such as overtaking another vehicle ahead to be made at an appropriate time. For example, if the route to be followed specifies taking a branch road to the left and also that the distance to the branching point is close. In this case, the system judges that a proposal to pass the preceding vehicle is not given.

As described above, the lane-level route plan (based on 3D HD map data) enables the system to know in which lane the vehicle should travel and lane-changes to be proposed at appropriate timing.

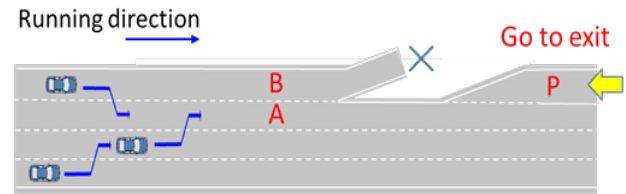


Fig.6 Schematic road layout near expressway branching point

## 4. Off-board linkage function

The PP2.0 system offers an off-board linkage function via a constant telematics communication channel to the server, to perform functions such as 3D HD map-data updating.

The off-board linkage function consists of a vehicle-side storage for the 3D HD map, a 3D HD map electronic control unit (ECU) for outputting the map data, a telematics control unit for communication, and a server for storing and distributing the most recent map data.

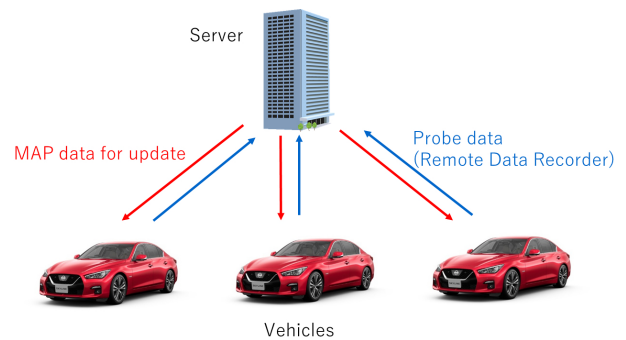


Fig.7 Off-board linkage-system arrangement.

The 3D HD map data are updated several times a year in order to timely capture the latest map data corresponding to the actual road shapes which can alter through the course of the year due to construction or other processes.

The 3D HD map ECU compares the latest server-held map data and the data in the ECU for each operation. If it detects any map data update, the most recent map data is downloaded from the server to update the ECU’s map data, starting with locations nearest to the vehicle as higher priority. This ensures the latest available 3D HD map data to be always used for the driving assistance.

## 5. Summary

The development of this system has led to the commercialization of the world's first driving-assistance system that can guide a vehicle through a multi-lane highway working in tandem with the navigation system-planned route and provided the driver consistently attends to the road ahead and can operate the steering wheel with certainty and immediately in response to the road, traffic and vehicle conditions, the system can operate in hands off mode. As a result, more secure, comfortable, and stress-free driving experiences are available to customers.

In future, we hope to deploy this technology in regions outside Japan, to apply it to greater number of vehicles, and to pursue technological advancements to support driving operations across a wider range of scenarios thereby realizing a safer traffic society and offering new values to automobiles.

## Authors



Yohei Taniguchi



Daigo Atsumura



Seiji Tokunaga



Katsuhiko Degawa



## 3. Supported by vehicle-control technologies

Yohei Taniguchi\* Yasuhisa Taira\* Naoto Sugawara\*\*

### 1. Introduction

Nissan has taken the lead in technological innovations for driver assistance technology as a pioneer in driver assistance technology this field for more than 20 years, developing many world's first technologies<sup>1)-8)</sup>. In 2016, put into practical use the ProPILOT (hereinafter referred to as "PP1.0"), which is an integrated driver-assistance technology in single-lane highway driving.<sup>9)</sup> Then, in 2019, Developed ProPILOT 2.0 (hereinafter, "PP2.0") which was substantially evolved PP1.0 technology.; it operates in tandem with the navigation system and can follow a predefined route (hereinafter, "navigated route-driving") on multiple-lane highways.

The vehicle-control technologies that realize ProPILOT have been based on the control technologies thus far accumulated through the development of various driver assistance systems.

Vehicle speed/vehicle distance control technologies are based on intelligent cruise control (ICC), which was released in 1999. Steering control and lane-keeping control technologies have developed from the lane keep support (LKS) system released in 2001.

This chapter describes the primary controls of vehicle-control technologies, which are essential to realizing the "reassurance" and "comfort" of PP2.0.

#### 1.1 History of control development in driver assistance systems

Nissan's first driver assistance system was the ICC, applied to the CIMA in 1999. Fig.1 shows the driver assistance systems that Nissan has introduced to the market.

The ICC system is based on the vehicle speed control with a traction control, which controls the vehicle speed to a set speed; and constructed the vehicle distance control on top, which is controlled same as driver operation.

These control technologies (traction control/vehicle speed control/vehicle distance control) have also been applied to realize Distance-Control Assist and Forward

Emergency Braking.

Furthermore, LKS has realized the steering controls based on vehicle motion characteristics, and the line trace control to the center of lane which was recognized by camera.

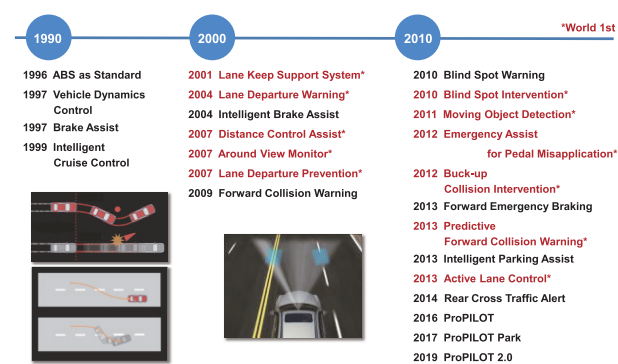


Fig.1 History of driver assistance system development

These control technologies have been evolution with the times and applied as base control technologies in PP1.0 and PP2.0.

### 2. Features of control systems

#### 2.1 Vehicle speed control

In Nissan, the vehicle speed control development has a long history, started from early 1990s', when a control law (which combined robust and model-matching controls) was designed for the cruise control. (Fig.2)

Robust compensator is compensate a control performance to the ever-changing the plant, estimating changes in running conditions (e.g., vehicle characteristics and road gradients) and adjust the control inputs. Model-matching compensator sets the reference model of desired response characteristics, controls the plant which was compensated by the robust compensator. At this time, calculates control inputs as same behavior of reference model. (Model-matching control).

Constructing the control system in this way, realized vehicle-speed controller of high robustness for changes in running conditions (e.g., vehicle weight variations and road gradients).<sup>10)</sup>

\*AD/ADAS Advanced Technology Engineering Department

\*\*Chassis Engineering Department

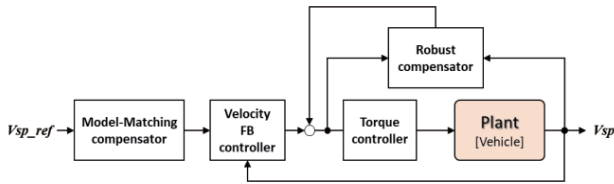


Fig.2 Vehicle speed control block diagram

### 2.2. Vehicle distance control

The vehicle distance controller used in ICC and PP1.0/PP2.0 was designed setting two design indexes, identified from analysis of human driving operations:

- 1) Should be able to set the trajectory after started of vehicle distance control
- 2) Should be stable control performance during vehicle distance control

To meet these requirements, a “two-degrees-of-freedom control based on a reference model” was used; in this, response characteristics and following stabilities can be designed independently. (Fig.3)

The plant should be written by the transfer function for easy to use. Therefore, the vehicle distance controller was built at class structure; using the compensated vehicle speed controller, not control vehicle distance directly. Herewith response characteristic of vehicle distance control is compensated the feed-forward compensator which was designed at the reverse characteristic of the vehicle speed controller. And the tracking performance which is keeping vehicle distance was designed the feed-back control by using pole assignment method. <sup>11)</sup>

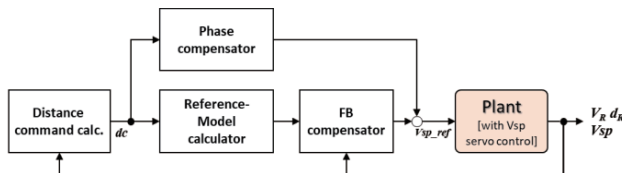


Fig.3 Vehicle distance control block diagram

Farther, natural behaviors not perceived by the driver to be strange, behaviors for controlling traffic congestion were required by the spread of ICC. An important aspect to achieve this is ensuring that the inter-vehicle-distance control characteristics do not cause changes in the speed of the forward vehicle to be amplified and transmitted to the behind vehicles, this prevents traffic-flow disturbances / unevenness and improves road transport efficiency. Expressed otherwise, vehicle group stability should be stabled. In general, to achieve vehicle group stability, the response of vehicle speed must be faster than the change of speed in the forward vehicle; however, it becomes a high gain control, and get worse in the ride quality during follow to the forward vehicle. Therefore, it was improved the vehicle distance controller to balance of vehicle group stability and ride quality in high level, and control response will be felt natural to the driver. <sup>12)</sup> (Fig.4).

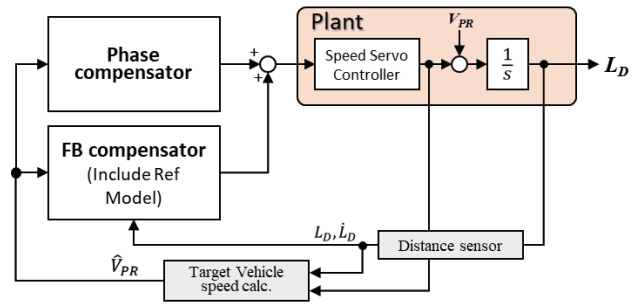


Fig.4 Vehicle distance control block diagram considering vehicle group stability

### 2.3 Lane-keeping control

The lane-keeping controls of PP1.0/PP2.0 are based on the LKS system first commercialized in 2001. The control performances required for LKS is improve and maintain line trace performance and disturbance stability. For control to the vehicle lateral motion, the controller was designed with a state feedback control based on the vehicle model; This controller has the observer which was designed Kalman filter, and using LQ control to meet the required control performance.

In addition, to improve the control performance on curve, controller was added the feedforward compensator which was used a curvature. <sup>13)14)</sup> (Fig.5).

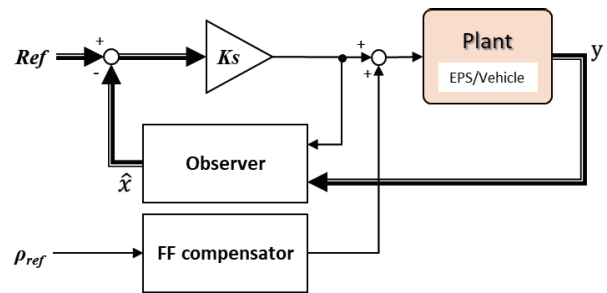


Fig.5 Lane-keeping-control block diagram

## 3. Steering control of ProPILOT 2.0

The steering control of PP2.0 is based on the aforementioned lane-keeping control; using information from camera and 3D High-Definition map (hereinafter, “3D HD map”), calculate a target steering angle for lane-keeping and assistance of lane-change.

### 3.1 Control-system configuration

Fig.6 is a block diagram of the steering control function incorporated in PP2.0. With this control configuration, real-time lane configuration information detected with the cameras is compared with 3D HD map data to enhance the reliability of the information. When it is difficult to secure 3D lane configuration information with the cameras, it is obtained from a 3D HD map to enable accurate calculation of the steering angle needed for the vehicle to travel in the center of its lane.

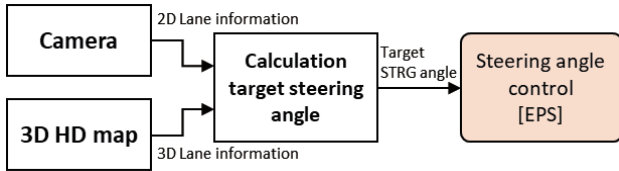


Fig.6 Block diagram of lane-centering control

To verify the steering control capability of PP2.0, tests were conducted on a Nissan proving ground test course to compare the performance of the system with that of a skilled test driver.

### 3.2 Test overview, and test results

Lane centering tests were conducted on a test course with a series of consecutive curves having a radius of 500 to 1000 m (500-1000 R). Data were measured and compared for a case with PP2.0's lane centering control and a case where the skilled test driver drove the vehicle without any lane centering control. The test driver was instructed to drive in the center of the lane as much as possible.

Fig.7 shows the lateral position from the lane center obtained with PP2.0's lane centering control and for the skilled test driver. Fig.8 shows the steering angle results. Fig.7 shows that the results indicate that the lateral position from the lane center was smaller with the control than for the skilled test driver, thereby confirming the high lane centering capability of PP2.0. Fig.8 shows that at the entrance and exit of curves where the steering angle changes, the data show that lane centering control smoothly controlled the steering angle without any overshoot just like the skilled test driver. In addition, on curves where the steering angle was nearly steady for approximately 50-150 s, lane centering control kept the steering angle change smaller than that seen for the

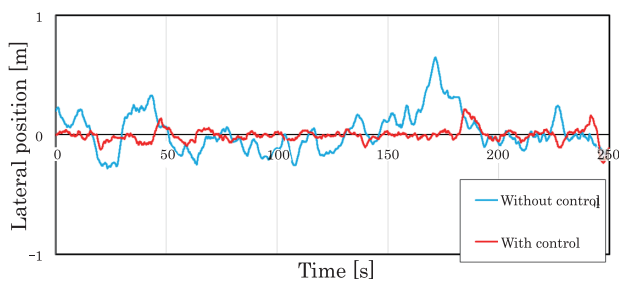


Fig.7 Lane-centering comparison results

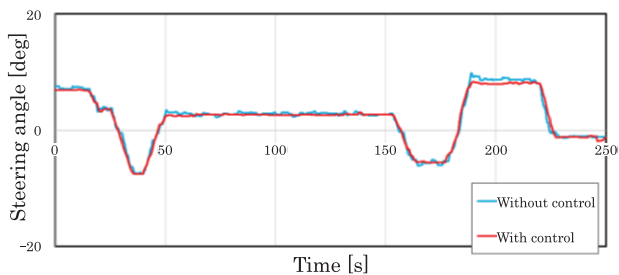


Fig.8 Steering-angle comparison results

skilled test driver.

From the results, it can be confirmed to enable PP2.0 to provide smooth steering angle control equal to or better than that of a skilled test driver.

## 4. Steer-by-wire technology to support steering control

The Nissan SKYLINE is adopt the direct adaptive steering (DAS) as a steering system. DAS is a by-wire system in which the mechanical connections between the steering wheel and tires are replaced with electric signals; both components can thus be independently controlled by disengaging the clutch in the steering shaft. The contribution of DAS to PP2.0 is presented here.

### 4.1 Compatibility of smooth steering-wheel motion and accurate line tracing

The steering control in PP2.0 precisely controls the tire angles, to thereby control the vehicle's lateral motion to a high degree of accuracy. However, the steering wheel motion is also an important factor. Smooth steering-wheel motion increases the system's sense of security. DAS adopts a disconnected steering wheel and tires to execute the control, as described below in terms of the compatibility of these two performance items.

The PP2.0 steering control is summarized in Fig.9. First, a tire-angle command (to perform line tracing) is generated by PP2.0; this command includes a component to determine the vehicle's rough motion and trajectory and a component to fine-tune trajectory shifts generated by road conditions and/or external forces from the road surface. From the PP2.0's tire-angle command, the DAS extracts components that determine the vehicle's rough motion and trajectory, to generate a steering-wheel-angle command for the steering wheel to follow. The steering-wheel motion is converted into a tire-angle command via an operation similar to that used for the driver's steering; this controls the vehicle's motion.

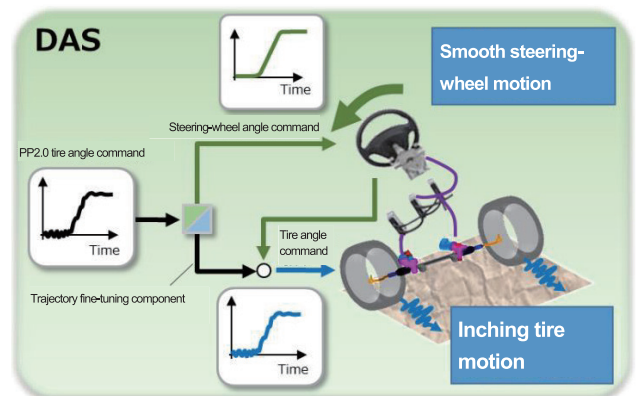


Fig.9 Summary of steering control during ProPILOT 2.0 operation

The structure of the DAS means that the vehicle can move exclusively via tire-angle control, without the steering wheel being turned at all; however, steering-wheel motion is effective in informing the driver of the vehicle's motion. By removing the inching motion that

accompanies fine-tuning and considering only the rough-motion component of the steering-wheel-angle command, the steering wheel can be made to move stably and smoothly; thus, the vehicle's motion can be displayed more clearly to the driver. Several residual components of the tire-angle command are not included in the steering-wheel one; however, these are still directly adopted in the tire-angle control. This allows the tire angle to be controlled according to the full tire-angle command of PP2.0, to achieve accurate line tracing.

Fig.10 depicts an example of the steering-wheel (green) and tire (blue) angles during PP2.0 operation. The steering-wheel angle exhibits a stable, smooth motion, in which only the vehicle's rough motion is expressed. Meanwhile, the tire angles exhibit a continual inching motion, owing to the combination of rough motions and fine-tuning.

Thus, the mutual independence of the steering-wheel and tire controls renders compatible the smooth steering-wheel-angle motions and accurate line-tracing function.

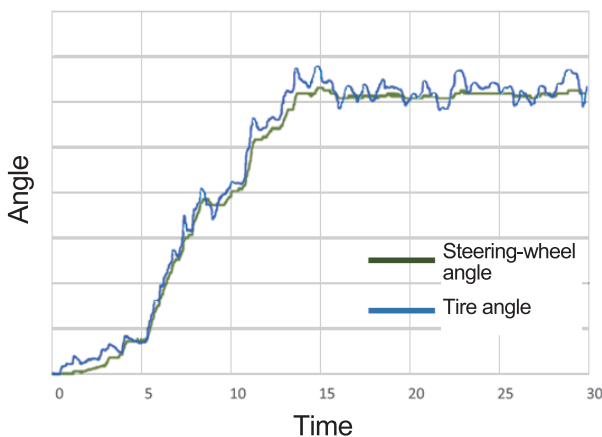


Fig.10 Comparison between steering-wheel and tire angle responses

#### 4.2 Contributions to ease of steering override

Steering override, in which the driver corrects the vehicle's motion, can be executed during PP2.0 operation; for example, the override can be used to avoid fallen objects or to keep distance from vehicles traveling alongside by moving away from the lane center. The line-tracing control force continually acts upon the steering wheel during PP2.0 operation, and the driver must apply steering to override it. Therefore, steering input features allowing the driver to easily override the operating PP2.0 are important.

To this end, existing steering systems generally adopt an electric motor or hydraulic system to generate control forces and overcome external forces from the road surface or system friction. However, in DAS, the steering wheel and tires are disconnected; hence, the external force from the road surface is not transmitted to the steering wheel. Therefore, the flexibility of steering force design and ease of establishing target characteristics represent advantages of PP2.0.

Here, the steering inputs during PP2.0 operation are explained according to the schematic in Fig.12, where we

take right-hand turning as an example. The dotted-blue line and red line indicate the steering input characteristics of a human driver (PP2.0 functions inactive) and PP2.0, respectively. To maintain the turning motion, the steering wheel must follow a steering-wheel-angle command. In DAS, the driver's steering input characteristics are offset, to make the steering force produced by a steering-wheel command as zero. This allows the driver to override the system with their own steering input when steering from a straight-line into a turn; this reduces the driver's burden.

Furthermore, when switching the PP2.0's operations off (i.e., when the driver's steering replaces it completely), the offset for a steering input of zero is gradually decreased, to ensure a smooth transition and a natural steering operation for the driver.

Thus, the DAS system's feature (i.e., the independent controllability of the steering wheel and tires) is utilized to improve PP2.0's performance.

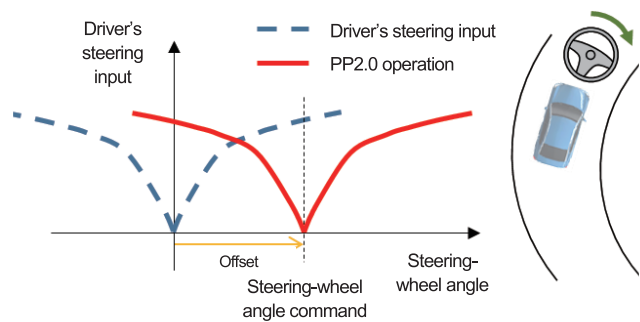


Fig.12 Steering input characteristics during ProPILOT 2.0 operation

## 5. Conclusion

Nissan has taken the lead in technological innovation, retaining its place as a pioneer in driver assistance technology for more than 20 years; in this time, it has developed numerous global technological "firsts."

First, control technology was established to control vehicle speed and vehicle distance at ICC system, and to control lateral motion and steering at LKS system. The combination of these technologies resulted in the development of PP2.0. Furthermore, the advantages of DAS (steer-by-wire systems) has facilitated line-tracing capabilities and smooth steering motions, contributing to driver reassurance.

## 6. References

- 1) O. Sadano et al., Development of the Lane Keep Support System and Brake Assist System with a Preview Function, Nissan Technical Review, No. 48, pp. 13-17 (2001)
- 2) Y. Seto et al., A development of an adaptive cruise control system with low speed following, Nissan Technical Review, No. 58, p. 81 (2006)
- 3) Yasuhisa Hayakawa et al., Development of the LDP (Lane Departure Prevention) System, Nissan Technical

- Review, No. 63, pp. 11-14 (2008)
- 4) Y. Uemura et al., Development of the Intelligent Cruise Control (Navigation-enabled Function) , Nissan Technical Review, No. 63, pp. 15-18 (2008)
  - 5) A. Kanaoka et al., Development of the Around View Monitor, Nissan Technical Review, No. 63, pp. 37-41 (2008)
  - 6) M. Kobayashi et al., Development of the Distance Control Assist System, Nissan Technical Review, No. 63, pp. 7-10 (2008)
  - 7) Y. Hayakawa et al., Blind Spot Intervention System Based on Yaw Moment Control, Nissan Technical Review, No. 72, pp. 6-10 (2013)
  - 8) T. Sugano et al., Development of Back-up Collision Intervention System Nissan Technical Review, No. 72, pp. 10-14 (2013)
  - 9) Nissan News Releases: <https://global.nissannews.com/en/releases/release-c7b1fdaa007748e6f048ff37b018061-160713-02-e> (as of November 7, 2019)
  - 10) Hideo Nakamura, et al.: Effectiveness of a Robust Control Method for Automotive Power train Control, IPC-10 paper 99066 (1999)
  - 11) Akira Higashimata et al., Design of a Headway Distance Control System for ACC, 1999 JSAE Annual Congress Technical paper proceedings, No.114-99, 233
  - 12) Yoshinori Yamamura, et al.: Development of an Adaptive Cruise Control System with Stop-and-Go Capability, SAE Technical Paper, 2001-01-0798 (2001)
  - 13) Hiroshi Mouri et al., Automatic Path Tracking Using Linear Quadratic Control Theory – Control Method for a Straight Path, 1997 JSAE Annual Congress Technical paper proceedings, No.972, 102
  - 14) Hiroyuki Furusho et al., Automatic Path Tracking Using Linear Quadratic Control Theory – Control Method for a Curved Path, 1997 JSAE Annual Congress Technical paper proceedings, No.972, 102

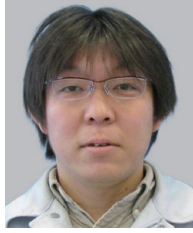
## Authors



Yohei Taniguchi



Yasuhisa Taira



Naoto Sugawara

## 4. Intelligent interface

Nariaki Etori\* Shohei Nakamura\* Yasunori Nakazono\*\*  
Kiyoharu Ishigouka\*\* Kenji Maeda\*\*

### 1. Introduction

This chapter outlines the newly adopted intelligent interface as the human-machine interface (HMI) technology that is key to realizing the “safety” and “comfort” in ProPILOT 2.0 (hereinafter referred to as “PP2.0”). The main functions as interactive HMI, 360° real-time surrounding display, and driver-monitoring system are explained in detail followed by the description on HMI verification methodology.

### 2. ProPILOT 2.0-specific intelligent HMI

The intelligent interface is a HMI uniquely designed to enable the driver to use the advanced driving assistance functions of PP2.0 both easily and appropriately. In other words, it is an intelligent interface for an intelligent driver assistance system, and consists of a HUD (Head up Display), a display on the meter display, operations on the steering wheel switches, and warnings by the driver monitoring system. (Fig.1)

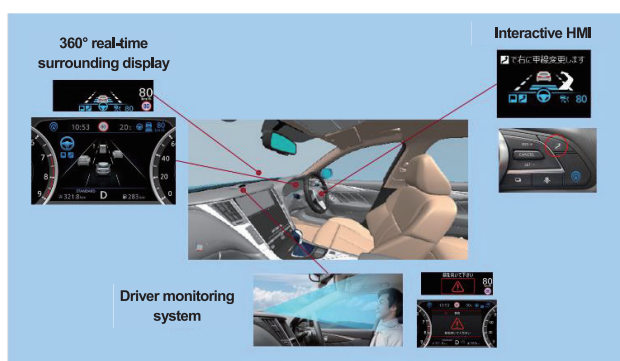


Fig.1 Intelligent interface

PP2.0 is a driving-assistance system in which the vehicle speed, inter-vehicle-distance, and steering control functions of the first-generation ProPILOT (hereinafter, “PP1.0”) have been enhanced by the addition of a hands-off function (for driving within a single lane) and a navigated route driving function that supports lane change at branches and exits and for overtaking.

PP2.0 has three activation states, up from two in PP1.0, due to the addition of hands-off function in the same lane. These modes are as follows: the Intelligent Cruise Control mode (hereinafter referred to as “ICC mode”), in which only the vehicle speed/vehicle to vehicle distance control are activated; the hands-on mode, in which both the vehicle speed/vehicle to vehicle distance control and steering control are activated, but the driver must be able to keep the steering control at all times; and the hands-off mode, in which both the vehicle speed/vehicle to vehicle distance control and steering control are activated and allows the driver to take his hands off the steering wheel under certain situations, assuming that the driver’s attention is on the road ahead and the driver is ready to take over when required. The challenge for an HMI is to design a display system that allows the driver to identify these three states. When two modes are to be identified, an ON/OFF display element can generally be used; however, it is difficult for three or more conditions to be identified with this method. We have widely applied color-coding scheme, which encourages identification by differences in color, to both the functional (e.g., icons, indicators, etc.) and formative (e.g., dividing lines, backgrounds, etc.) display elements on the HUD and meter displays, and to render the three driving modes readily identifiable, we assign them the following colors: white for the ICC mode, green for the hands-on mode, and blue for the hands-off mode (Fig.2). Because color vision differs between individuals, the color-coding system here adopted uses colors selected through color-vision simulations, to incorporate such differences between individuals.

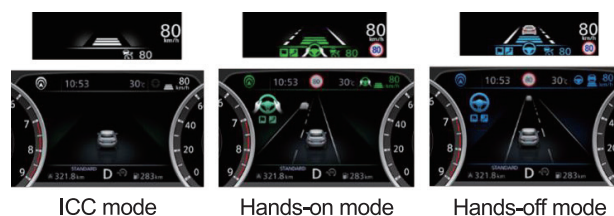


Fig.2 Color-coding for operating condition display

The navigated route driving function (a further function of PP2.0) assists in lane-changing maneuvers

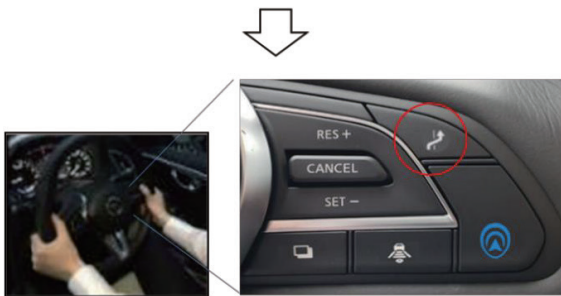
\*AD/ADAS Advanced Technology Engineering Department

\*\*TCustomer Performance and Vehicle Test Engineering Department No.2

when branching is required by the route or overtaking a slower vehicle ahead. The system assesses the conditions and proposes lane-change assistance at an appropriate time; the lane-change assistance starts after the driver confirms the safety and approves the proposal. Here, one issue in HMI is that of constructing display systems that allow the driver to clearly and quickly understand the system’s proposal and operation systems that allow the driver to enter their approval easily and without mis-operation. When solving this issue, it is extremely important to ensure that the proposal and approval processes do not prevent the driver from monitoring the surrounding traffic conditions, because PP2.0 is only a driving-assistance system and the driver remains obliged to monitor the surrounding traffic conditions and drive appropriately at all times. Therefore, the system’s proposal is displayed in simple text and graphics on the HUD, and the driver approved input were assigned to the switch with the best visibility and operability among the steering switches. (Fig.3)



System’s lane-change assistance proposal (HUD)



Driver’s steering switch for approval

Fig.3 System’s proposal and driver’s approval of lane-change assistance operation

Thus, the driver is able to grasp the system’s proposal without deviating their gaze too far from the surrounding traffic conditions, to continually check the vehicle’s safety, and to approve the proposal while holding the steering wheel. If the system proposal and driver approval are completed in a short time and without stress, the driver’s impressions of the HMI naturally change, from the current display/operation impression (i.e., as the driver’s input (operation) vs. the system’s output (display)) to a sense of enhanced interaction with the system. Thus, the HMI items used during lane-change assistance are referred to as “interactive HMI” and mediate communications with the user.

Driving with an interactive HMI is an unprecedented new driving experience, and we believe that it is a revolutionary HMI not only usability improvement but also in perspective of UX (User Experience).

Technological advances allow PP2.0 to a refined

control performance (e.g., smooth acceleration/ deceleration and lane-keeping stability), resulting in a highly advanced driving-assistance system. For the HMI of such systems, the driver’s excessive trust, distrust, and-in particular-excessive trust prevention must be considered to the greatest possible extent. One method for achieving this is to ensure that the driver accurately understands the system’s abilities and can use the system appropriately within the range of these abilities. Accordingly, the surrounding traffic conditions are detected by the system and displayed in 360° and real time on the meter display, to help the driver to understand the system’s detection range and identification abilities at a glance. (Fig.4)



Fig.4 360° real-time surrounding display

Furthermore, a driver-monitoring system is installed to detect whether the driver is monitoring the road ahead; if they are not, the system warns them to attend more closely. This help prevents the driver from neglecting to monitor the surrounding traffic conditions when driving in the hands-off mode. (Fig.5)



Fig.5 Driver-monitoring system and its warning for the driver to attend to the road ahead



### 3. HMI Details

The details of the interactive HMI, 360° real-time surrounding-conditions display, and driver-monitoring device are here described.

#### 3.1 Interactive HMI

To provide lane-change assistance during the branching or overtaking stages of the navigated route driving operation, the system considers the planned route, the speed of the vehicle ahead, and the surrounding traffic conditions; from these data, it proposes lane-change assistance via the HUD and meter display at appropriate timing. (Fig.6)



Fig.6 System's proposal for lane-change assistance

In the HUD, the arrow-shaped graphics indicate the proposal for lane change assistance and the text at the top prompts the driver for approval. The number of display elements is minimized, and these elements are arranged such that the driver's forward vision is not obstructed, to allow the driver to recognize the system's proposal safely. The reason for the lane change is simultaneously displayed on the meter display, to allow the driver can check it if necessary.

Once the driver checks the safety of the surroundings and presses the steering switch (Fig.3), lane-change assistance is started. Because this switch is often operated relatively quickly after the driver receives the system's proposal, it is placed in the upper region of the display, near the periphery of the steering wheel, in consideration of both visibility and operability. Once the driver is familiar with the switch operation, it can be pressed without looking.

During lane-change assistance, driver must place both hands on the steering wheel in preparation for overriding.

Therefore, after lane-change assistance is started, the HUD and meter display switch from the hands-off mode (blue) to the hands-on one (green), to prompt the driver to grasp the steering wheel. It is here that color coding is most effective.

The animated display (i.e., the HUD's graphic arrow pointing from the near to far sides) is displayed from the moment of approval until the lane change commences, and text prompting the driver to check the safety of surrounding is displayed. When the system initiates the vehicle's turn signals to start the lane change, the HUD's graphical arrow becomes green and flashes at the same frequency as the turn signals, to inform the driver that the lane change is in progress. (Fig.7)

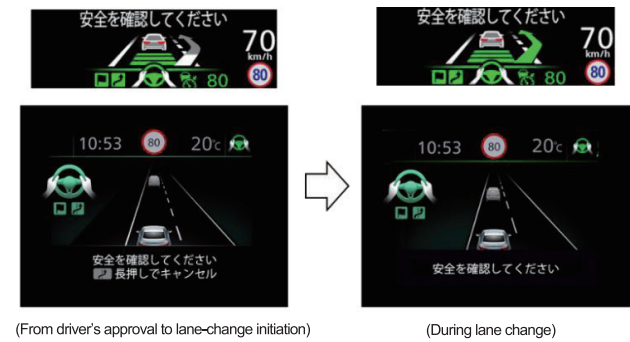


Fig.7 Lane-change assistance display scenes

#### 3.2 360° real-time surrounding display

To help drivers properly grasp the capabilities of the system, the system displays the road environment and traffic conditions that the system is detecting in 360° real time.

As the road environment, the traveling lane, the adjacent lanes and the type of road boundary lines (e.g., solid white, broken white, solid-yellow, and double lines can also be displayed) (Fig.8). In this way, the ability of the 3D High-Definition map data and front camera to detect the surrounding road environment can be expressed in the display.



Fig.8 360° real-time display

As traffic conditions, other vehicles detected in traveling lane and the adjacent lanes are displayed for each vehicle type (e.g., passenger cars, large-sized vehicles, motorcycles, and unknown) (Fig.4); In addition,

the distance of other vehicles in the display was repeatedly tuned to match the actual scenery, resulting in a non-linear scaling of the display position. This allows detected vehicles to be displayed by fusion-processing the outputs from the front camera, front radar, side radars, and other sensors. The driver can grasp the system's detection range and identification capability by comparing the actual space with the displayed one.

Through experiencing various scenes, the driver gradually learns the system's capability via the 360° real-time display, and will be able to use the system appropriately within its capabilities. At the same time, the driver's trust in the system is also enhanced.

### 3.3 Driver-monitoring system

The driver-monitoring system checks the driver for any failure to monitor the road ahead, using the driver's face direction and eye-opening/-closing conditions. It can prompt the driver to attend more closely to the road ahead, to help prevent them from neglecting to monitor surrounding traffic conditions when driving in the hands-off mode. (Fig.5)

The driver-monitoring device is located at the center of the dashboard with its imaging field directed toward the driver's side. It features the following integrated components: a camera lens, infrared light source (LED), optical filter, infrared-light imaging device, image-processing circuit, universal operation circuit, and more. (Fig.9) (Fig.10)

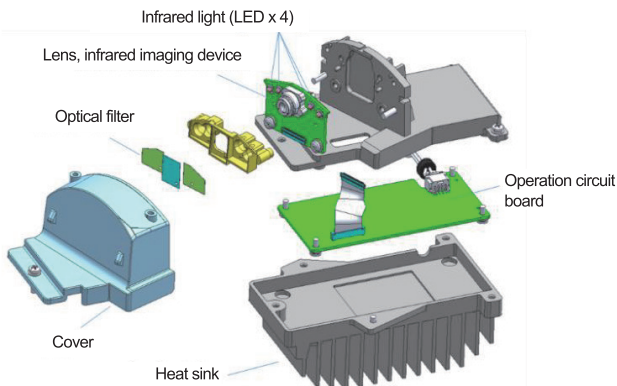


Fig.9 Composition of driver-monitoring device



Fig.10 Driver-monitoring device position

The infrared LED periodically emits infrared light with a wavelength of 940 nm (i.e., the invisible range), and the infrared-light-imaging device synchronizes therewith to capture an image; thus, a clear depiction of the driver's face can be obtained in all light conditions.

The facial organs (i.e., the eyes, nose, and mouth) are extracted from the driver's facial image via pattern-matching processing, and the driver's face direction is calculated from the size and positional relationships of these organs. In addition, the eye-opening/-closing condition is assessed by detailed analysis of the regions surrounding the eyes. When the calculated face direction is oriented beyond a certain angle from the vehicle's direction of motion for a specified period, a monitoring failure is registered and a warning given (Note: when the turn signals are active, this warning is blocked). When the eyes remain closed for a specified time period or face direction or eye-opening/-closing conditions remain likewise unchanged, a failure to monitor the road ahead is registered, and a warning is given.

## 4. Verification of HMI

The verification process for the driving-assistance HMI is here introduced.

### 4.1 Examination of verification items

Using the verification items specified for each system-judgment-generated (i.e., automatically provided by the system, regardless of the driver's operation) and driver-operation-generated (i.e., provided by the driver's operation) information presentation (Table 1), we determined detailed verification items for each evaluation task.

Table 1. Verification items (major items)

Source of information presentation	Feature	Verification item (major items)
System's judgement	Difficult to notice because information automatically presented by system, regardless of driver's operations	<ul style="list-style-type: none"> <li>Time of information presentation is noticeable</li> <li>Presented information is understandable</li> <li>Correct actions can be taken</li> </ul>
Driver's operation	System's response to an operation must be communicated	<ul style="list-style-type: none"> <li>Operation method is known</li> <li>Correct operation is possible</li> <li>Operation completion and control-condition changes are noticeable</li> </ul>

### 4.2 Verification method

For each verification items, scene which lead to workload during recognition / judgement / operation processes were extracted. Examples of the evaluation scenes used to identify tasks in the three operation conditions (ICC, hands-on, and hands-off modes) are shown in Fig.11.

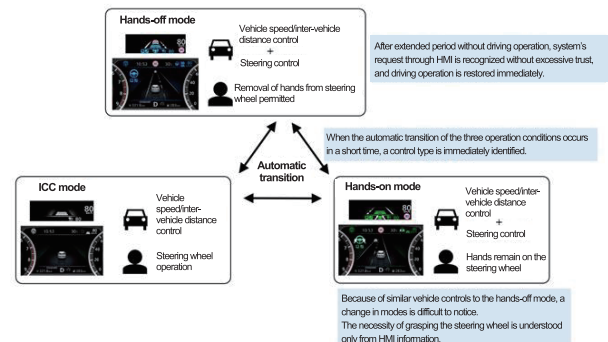


Fig.11 Evaluation scene extraction: identifying the three operating conditions

Simulators were constructed in which the recognition/judgment/operation processes of an extracted evaluation scene could be assessed; then, these were evaluated by experts and experimental participants (representing general customers).

For the simulators, the following two scenarios were prepared: a use case scenario, representing the control and HMI logic in writing; and a driving simulator (hereinafter, "DS"), reproducing the cockpit and vehicle's motion.

First, the use case scenario was used by the experts to verify the compatibility between the combined control and HMI logic and the recognition model for expected users. (Fig.12)

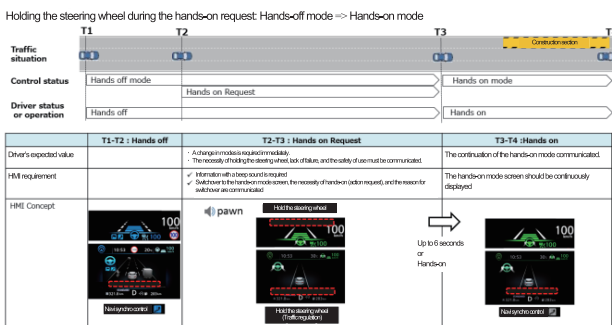


Fig.12 Example of desktop scenario

Next, the HMI specifications of the aforementioned use case scenario were reproduced as an actual driving experience in the DS, to allow the experts and experiment participants to conduct evaluations.

The DS reproduced the traffic flow around the vehicle as well as the surrounding environment (e.g., road structures); thus, the users were naturally motivated to attend closely to the road ahead. An actual road simulation was applied to convey the experience of driving-load reduction, security, excessive trust, and distrust under PP2.0. Specifically, after driving for tens of minutes, the vehicle's behavior and meter/HUD information provisions (according to the PP2.0's control conditions) were reproduced. (Fig.13)

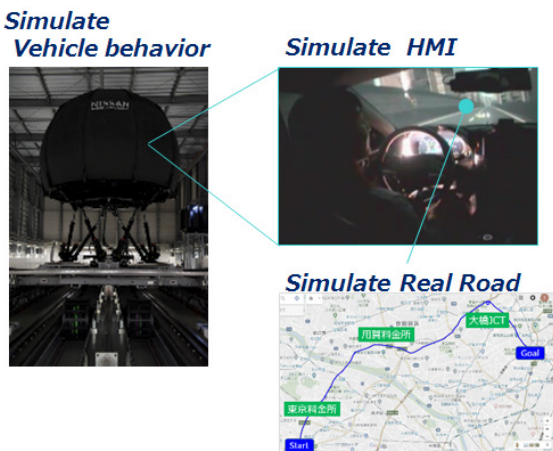


Fig.13 Driving simulator elements

The applied DS consisted a motion system which provided the vehicle's acceleration, an image-projection system which provided visual information, a cockpit system which provided sonic/reactive responses to

controls, and a driver's seat. The dome and the projector system rested on the six-axis oscillation unit (referred to as a hexa-pot) which was mounted on the x-y translation unit allowing movement in the longitudinal and lateral directions, Built in the dome was a turntable that rotated independently of the translation unit and a mock vehicle-cockpit.. Screen surface covered the dome interior with seven projectors combined to project a 360° image. Fig.14 and Fig.15 depict the DS structure and control-system composition, respectively.

The various control signals (e.g., from the steering wheel, brake, and accelerator) and road-surface conditions were inputted to a vehicle-motion analysis model. The steering/braking responses to the controls were calculated and delivered to the driver. By minimizing the deviation to actual driving experience, the DS allowed long enduring tests without the subjects having motion sickness, and reproduced at high consistency driving experience which affect capabilities of driver recognition such as workload, sense of security, excessive trust, and distrust. To this end, the following design aspects were realized: <sup>1)</sup>

- (1) The translation unit moved and responded rapidly whilst generating wide strokes in the x- and y-directions; thus, the drivers felt acceleration as high as that of an actual vehicle, with no delay.
- (2) The large-scale dome displayed a 360° surrounding image with a high response rate, to enhance the realism and to reduce the unnaturalness caused by delayed imagery.

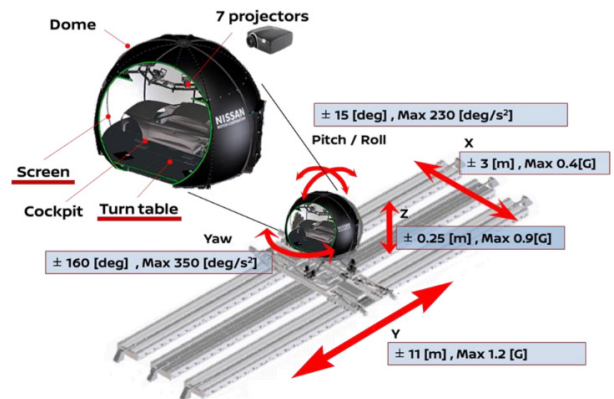


Fig.14 Driving simulator structure

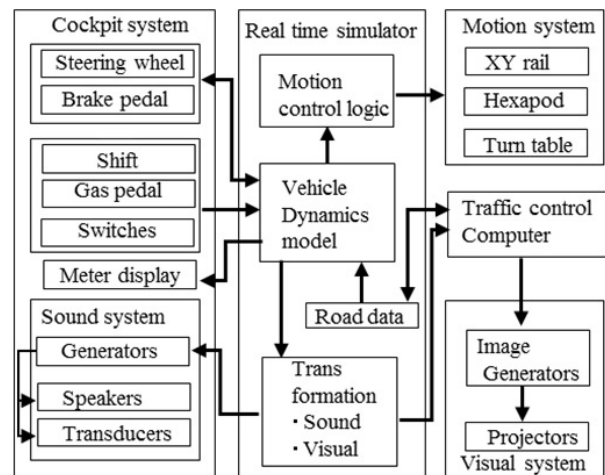


Fig.15 Driving simulator control-system composition

An example evaluation using the DS is here described.

For the scene in which repeated lane changes (to reach the exit of an expressway) were assisted, the following items were evaluated: batch approval, in which the driver approved all of the system’s lane-change proposals at once and immediately; and separate approval, in which an approval operation was performed for each lane change. Driver experiences were used to evaluate these two approval types and their problem areas (Fig.16), and the scenarios were reproduced in the DS (Fig.17) to

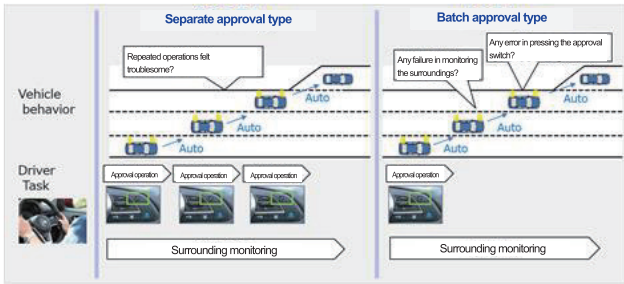


Fig.16 Driving simulator evaluation example: approval task for lane-change assistance to exit

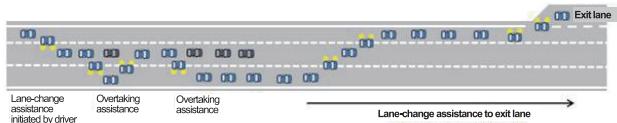


Fig.17 Driving simulator evaluation example: reproduced scene

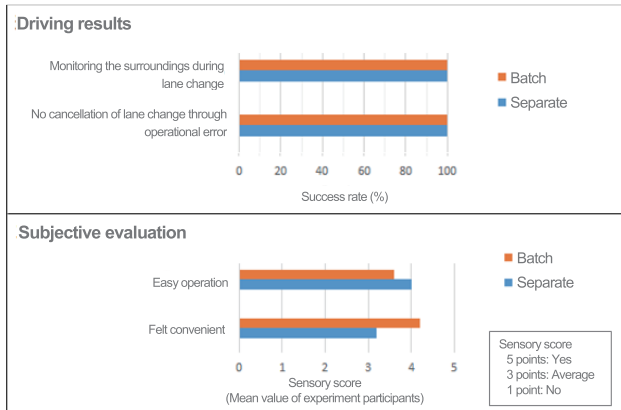


Fig.18 Driving simulator evaluation example: evaluation results

observe driving results and perform subjective evaluations. For both approval types, correct operations and satisfactory operability/convenience were confirmed. (Fig.18)

These evaluation experiments were repeated with several hundreds of participants before finalizing the HMI specifications.

### 4.3 Verification stages

Through the desktop-scenario and DS evaluations, the HMI specifications were verified in the design phase, to enhance the accuracy of the design. In the evaluation phase, prototype vehicles were used to optimize the specification details (e.g., display timing). (Fig.19)

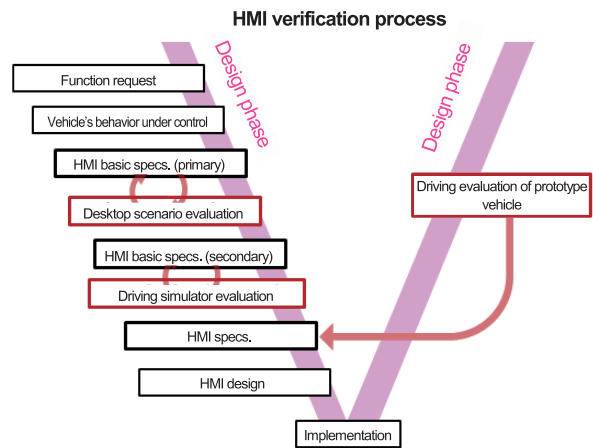


Fig.19 HMI verification process

## 5. Conclusion

The intelligent interface described in this chapter provided comprehensive means for the driver to readily understand the system’s condition/abilities bthrough interaction and helped realize PP2.0, an advanced driving-assistance function , to be easily and appropriately used by the customers.

## 6. References

M. Imamura, M. Tsushima, H. Saito, S. Isa, N. Machida, M. Ishikawa, T. Inoue : Development of Driving Simulator Reducing the Difference from Actual Vehicle Driving Sensation, Proceedings. 2018 JSAE Annual Congress (Spring) ISSN 2189-4558

## Authors



Nariaki Etori



Shohei Nakamura



Yasunori Nakazono



Kiyoharu Ishigouoka



Kenji Maeda

# 5. Technologies supporting system reliability

Takashi Sasayama\* Kouji Shionome\* Akira Teranishi\*

## 1. Introduction

The evolution of autonomous driving technologies has extended the range of driving-assistance functions they offer and increased the scope and importance of their functional safety designs. (Fig.1)

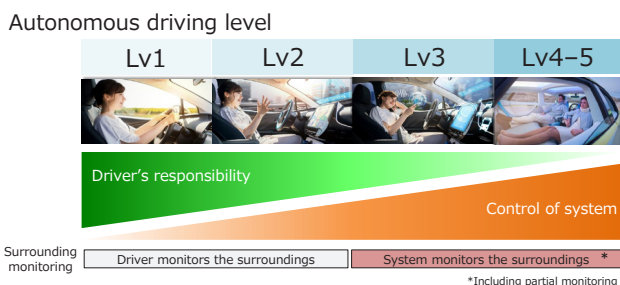


Fig.1 Relationship between autonomous driving level and driver's responsibilities

The ProPILOT 2.0 (hereinafter referred to as “PP2.0”) system allows users to drive without holding the steering wheel in certain road environments, though they still monitor the road. The designs required to help support the safety of this operation differ from those of existing driving-assistance systems. For example, in the event of system technical issue, the first-generation ProPILOT (hereinafter, “PP1.0”) requires the driver to keep their hands on the steering wheel, to immediately override the automatic driving operation. In contrast, PP2.0 allows the driver to continue with “hands off” driving under the specific condition; thus, until the driver overrides the driving operation, the system shall handle the technical issue safely.

This chapter describes the safety/reliability designs essential to realizing “security” and “comfort” in PP2.0.

## 2. Concept of functional safety design

In existing driving-assistance systems (in which the driver always drives with their hands on the steering wheel), the functional safety design addresses safety by working to detect technical issues before they result in critically hazardous events, informing the driver, and

terminating the mis-operating function (Fail silent).

Meanwhile, the functional safety design of PP2.0 not only works to detect technical issues and inform the driver; furthermore, it is designed to maintain operations until the driver takes over (Fail operational). (Fig.2)

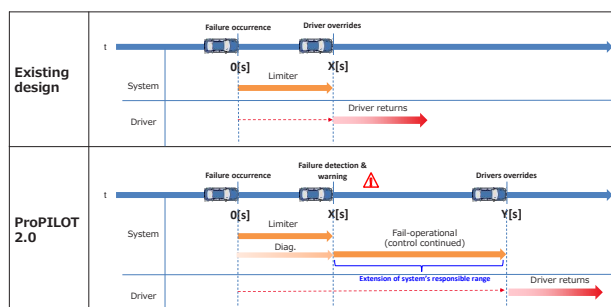


Fig.2 Difference between existing safety designs and ProPILOT 2.0

To maintain safety after a technical issue, the steering and braking functions (which are continuously controlled by the system) and the “informing function” (i.e., that informs the driver of a technical issue) shall be retained; hence, safety is addressed by making each function redundant. If any of these functions fail, a switchover to an unaffected backup system is applied as a safety measure.

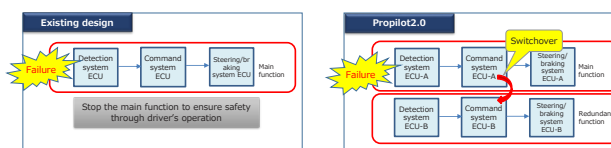


Fig.3 Existing design and ProPILOT 2.0's safeguards against technical issues

To make a function redundant, its components (e.g., its electronic control unit (ECU) and actuators) and electric/electronic infrastructures (e.g., its power sources and communication networks) must also be made redundant.

Furthermore, an important design requirement for maintaining functions with redundant composition is “independence” for the main and backup function systems. Accordingly, this feature is designed to meet the following functional safety requirements:

\*System Integration and EE Architecture Engineering Department

- 1) A single technical issue must not cause both systems to fail simultaneously.
- 2) A technical issue that incapacitates one system must not produce a technical issue in another system.

### 3. Communication network architecture

For the ECU (as described above), if a technical issue occurs, the steering and braking functions are addressed through a redundancy system comprising multiple ECUs. To support the vehicle's safe behavior, its communication network must also be redundant. Expressed otherwise, the communication network is constructed such that the series of signal flows is uninterrupted in the event of abnormalities occurring in the body, harnesses, or other parts of the ECU. The requirements for achieving this can be roughly classified into two items:

- 1) Multiple communication routes (groups) must be ensured for "obstacle/white-line detection" → "command-value operation" → "actuator control."
- 2) These communication routes must be mutually independent.

In communication-network designs, these two requirements can be more precisely broken down into the following four items:

- a) Each group must contain detection-, command-, and steering/braking-system ECUs.
- b) Each group must be composed of mutually independent ECUs (Fig.4).
- c) Communication within each group must be conducted through mutually independent buses (Fig.5).
- d) The ECUs contained in each group must be connected to mutually independent upstream power sources (Fig.6).

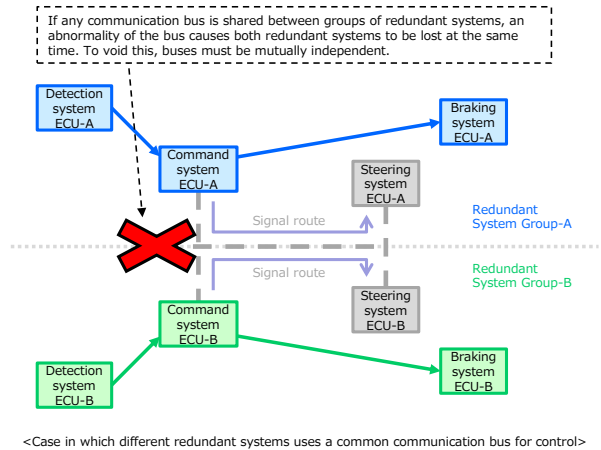


Fig.5 Requirements for buses composing each group

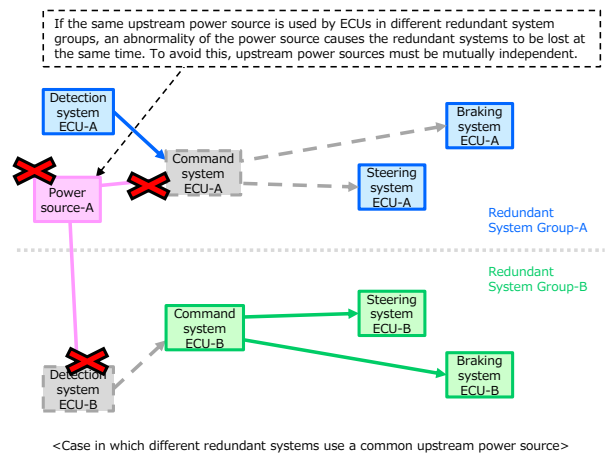


Fig.6 Requirements for upstream power sources composing each group

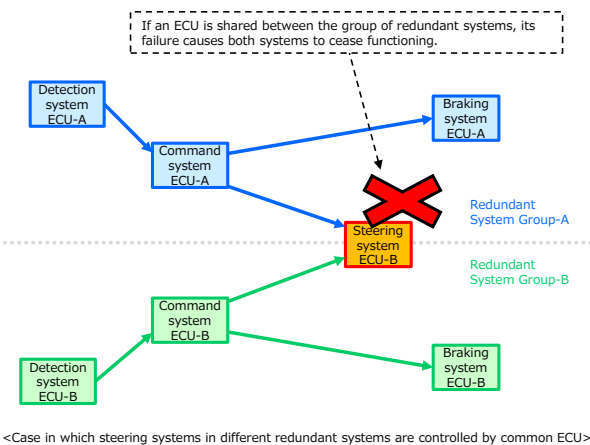


Fig.4 Requirements for ECUs composing each group

A summary of the network topology satisfying these requirements is shown in Fig.7. Under normal conditions, driving assistance is performed by all ECUs depicted in the figure. The communication network is organized such that Group B and/or Group A continues to operate when an abnormality occurs in Group A and/or Group B. Moreover, a communication bus between the groups is provided, to allow each group to monitor and immediately detect abnormalities in its counterpart.

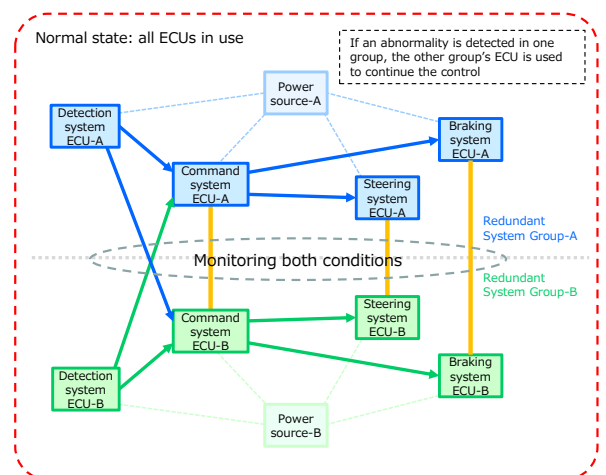


Fig.7 Communication network composition for ProPILOT 2.0

## 4. Power-source system for ProPILOT 2.0

### 4.1 New requirements for power-source systems

Because the all systems are operated by the vehicle's 12 V power source, power-source maintenance is crucial in helping prevent the system from losing functionality.

If driving operations are controlled by vehicle, the following requirements are placed on the power-source system: (1) abnormally high/low voltages must not be allowed, even over short periods, because the ECU continuously maintains the necessary operation processes for driving assistance; (2) because the driver's input is absent, the actuator consumes more power than existing assistance functions and 12V power-source is required higher voltage than the motor's electromotive force.

### 4.2 Summary of power-source system

The power-source system is composed of a main battery; a DC-DC converter, along with its relay and current sensor; a backup battery, along with its relay and sensor; and connecting harnesses. (Fig.8)

During driving operations, the backup battery is connected to the vehicle's 12 V power system, and the vehicle's electrical components are operated by using power from three power sources: the DC-DC converter, main battery, and backup battery. Even if the DC-DC converter fails with a deterioration of the main battery, the backup battery can maintain the voltage and support the driving-assistance which of system's continued operation.

Lead-acid batteries have achieved sufficient performance results on the market (as adopted in the SERENA S-HYBRID and other vehicles); hence, it was selected as the backup battery.

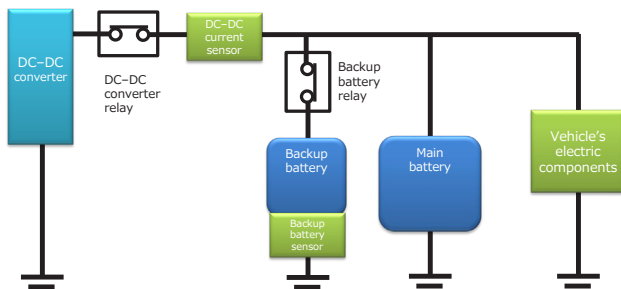


Fig.8 Composition of power-source redundancy circuit

### 4.3 Power-source system problems

The backup battery, an important component in managing power-source redundancy, must continue to operate when the main power source fails; however, an increase in customer burdens (e.g., frequent parts replacement and checks) must be avoided. Therefore, the system itself must maintain its performance over a long period. As described above, actuators require a high power-source voltage, which cannot be maintained under deteriorated backup-battery; thus, to measures to

safeguard against backup-battery deterioration and to ensure accurate battery status diagnoses are essential.

Meanwhile, the DC-DC converter have failure modes of high-voltage and internal short circuiting. These failure modes make it impossible to maintain the power-source voltage by using the backup battery, Therefore some safeguard were also examined against DC-DC converter technical issues.

The technical issues for power-source-system redundancy are as follows:

1. Suppressing deterioration for backup-battery.
2. Correctly diagnosing backup-battery conditions.
3. Handling DC-DC converter short-circuiting/high-voltage technical issues.

### 4.4 Measures for controlling backup-battery deterioration

To apply same size/type lead-acid battery for the main and backup will result in a similar deterioration process in both. Thus, when the main battery reaches its life-span, the sub-battery will do likewise, and its backup function will be lost. Therefore, the backup battery must have a longer life-span than the main one.

The stress applied to a lead-acid battery cannot often be eliminated, because of the battery's functions. However, the backup battery is different from the main battery; for example, no dark-current supply is required during parking, which reduces the battery stress. As described above, the backup battery's long life-span was addressed by thoroughly investigating the deterioration factors of lead-acid batteries and implementing measures to reduce stress. Here, we describe the process of eliminating the main factor: stress-induced capacity reduction of the lead-acid battery.

First, the backup-battery relay was placed upstream of the backup-battery circuit, to disengage the circuit during parking and prevent its discharge through the vehicle's standby current. (Fig.9)

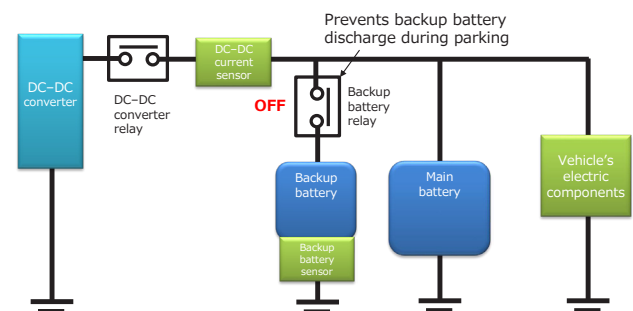


Fig.9 Backup battery relay circuit

Moreover, because excessively high or low charging voltages shorten lead-acid-battery life-spans, the backup battery was placed in parallel with the main battery, such that the applied voltage from the DC-DC converter (including the voltage drop due to the harness) was equalized between both batteries.

These measures ensure that the backup battery can

retain a high charging capacity, to control deteriorations produced by a low-capacity state. In consideration of the vehicle’s quietness, a semiconductor relay (which makes no operation noise) was adopted as the backup battery relay.

#### 4.5 Backup-battery condition diagnosis

Lead-acid batteries are prone to multiple deterioration/failure modes, owing to their chemical/structural characteristics. As described above, the backup battery is managed such that most deterioration modes are controlled, which makes condition diagnosis relatively easy. Meanwhile, the externally observable parameters are limited to voltage, charging/discharging current, and temperature. To diagnose backup-battery conditions with high precision, a circuit configuration designed for more accurate measurement was adopted.

In particular, the battery voltage suffered from larger measurement errors, attributable to the effects of the generator/other-battery voltage, voltage drops through discharge from the measured battery, and other factors. These factors arise because the battery must be connected to a 12 V power grid during measurement.

As a countermeasure, the error factors were eliminated by switching off the backup relay and measuring the voltage with the battery disconnected from the vehicle’s circuit.

#### 4.6 Handling DC–DC converter short-circuiting/high-voltage technical issues

In the event of a short-circuiting/high-voltage technical issue in the DC–DC converter, the battery must be disconnected from the vehicle’s 12 V power grid; to this

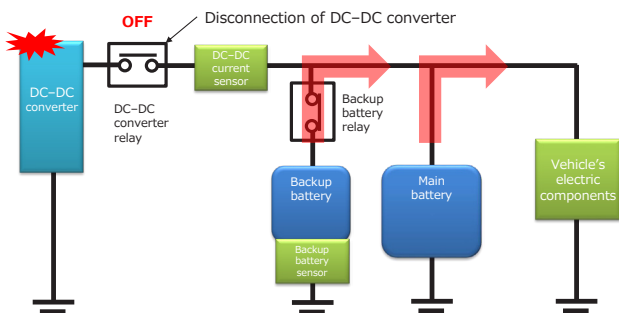


Fig.10 DC-DC converter disconnection during technical issue

end, a DC–DC converter relay was placed between the DC–DC converter and battery. (Fig.10)

This circuit configuration was designed such that its fundamental power-source function was unobstructed. To minimize the relay induced voltage drop, we chose a semiconductor relay, because it can realize a lower ON resistance, large current-carrying capacity, superior durability, and lack of operation noise.

In addition, the backup-battery and DC–DC converter relays are controlled by mutually independent ECUs; this enhances system reliability, because the ECUs cannot be simultaneously switched off by microcomputer runaway during PP2.0 operation.

## 5. Human-error-secure safety design

As the driving-control functions of systems have become more advanced, the potential for increased risk associated with driver errors, such as overreliance on the system and misunderstanding of system function, has increased. A system such as PP2.0, which allows for switching between the driver’s driving mode and system-assisted modes, requires measures to address errors in recognizing the system’s operational status (mode confusion) or conflicts between the driver’s and system’s intentions.

Here, methods of analyzing predictable human errors are explained. Previously, when human-error-derived hazardous event scenarios were analyzed, experts applied brainstorming methods. However, demonstrating the results of such methods is difficult in terms of logicity or comprehensiveness.

In this research, a new analysis method was developed for PP2.0, to objectively and comprehensively deduce hazardous scenarios produced by human errors. The risk analysis was conducted via four steps:

1. Specify an object person (who).
2. Specify a phenomenon (how).
3. Specify an object (what).
4. Specify an environment (where).

This concept was visualized with a description method that imitated goal-structuring notation (GSN), to increase the objectivity of the demonstration. (Fig.11)

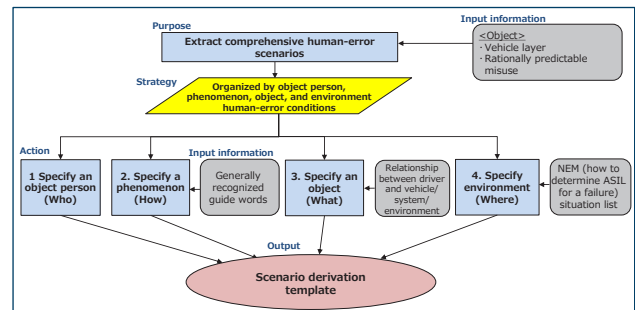


Fig.11 Concept of human-error analysis (GSN)

### 5.1 Specify an object person (who)

First, we specified the object causing the human error; this could include the driver, a passenger in the passenger seat, or passengers in the rear seats.

### 5.2 Specify a phenomenon (how)

Next, we specified a phenomenon for the object person’s human error. Human activities were categorized into “recognition,” “judgment,” and “action.” Possible human errors were comprehensively defined. Among them, highly probably phenomena were specified. (Fig.12)



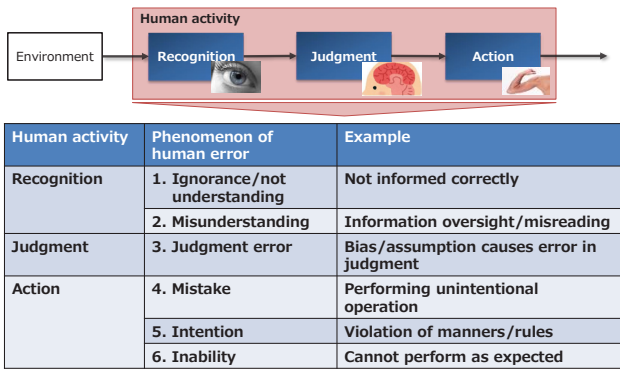


Fig.12 Human-error analysis

### 5.3 Specify an object (what)

Next, we specified the object of the human error; this represented the relationship between the driver and environment/system/vehicle in the systems-theoretic process-analysis control structure. As a result, objects exerting identical effects on the driver were comprehensively extracted; through this, we restricted the number of objects. (Fig.13)

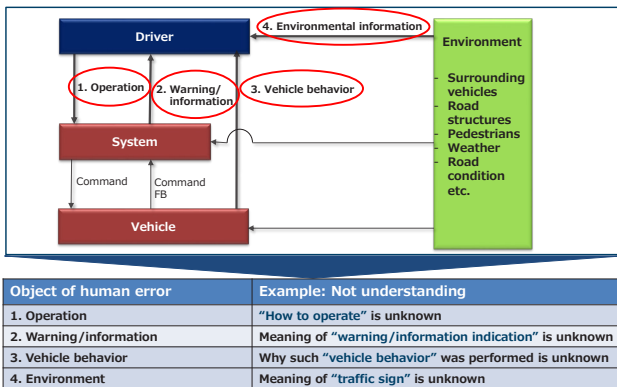


Fig.13 Relationship between driver/system/vehicle/environment

### 5.4 Specify environment (where)

Lastly, we specified the environment that produced the human error, to derive the final hazardous scenario. (Fig.14)

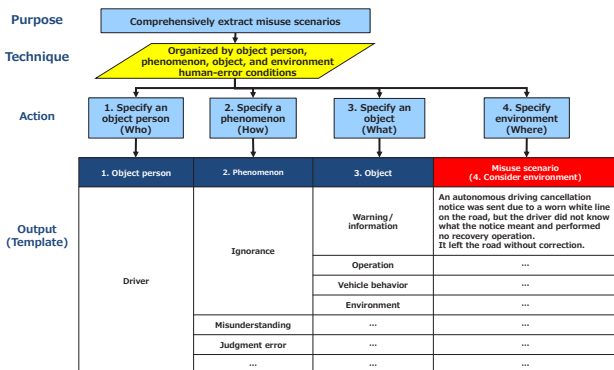


Fig.14 Derivation of human-error scenario

This analysis method was applied to the PP2.0 system, to extract human-error-related scenarios and break down safety measures into functional requirements.

Moreover, this method was proposed to ISO TC22 SC32 WG8 and adopted in ISO PAS 21448 "Road vehicles – Safety of the Intended Functionality," issued in January 2019.

## 6. Summary

The method described in this chapter allows PP2.0 to be designed with advanced safety standards. From the developed safety-design method, PP2.0-specific requirements were derived, and the functional safety design was realized by adding new features. This allowed complicated designs to be avoided and high reliability to be achieved.

## 7. References

- 1) ISO26262-1~10 Road vehicles -Functional safety-

## Authors



Takashi Sasayama



Kouji Shionome



Akira Teranishi

## 6. New experimental verification techniques

Yumi Kubota\* Koji Sasaki\* Shimpei Nagae\*\* Kenji Ogino\*\*\*

### 1. Customer values and their verification

Compared to the first-generation ProPILOT (hereinafter referred to as “PP1.0”), ProPILOT 2.0 (hereinafter, “PP2.0”) adds two new intelligent items: Navigation-route-following function, including lane-change assistance (point-to-point); and a hands-off function when remaining in the same lane.

To realize the navigation-route-following and lane-change-assistance functions, more complicated controls are required to handle multiple lanes instead of single ones. Because lane-change and overtaking scenarios are more complicated, simulation techniques have been used to verify that the relevant systems function appropriately under numerous traffic-flow conditions.

Meanwhile, a crucial aspect of the lane-maintaining hands-off function is the feeling of safety of the vehicle’s motion. For a long time, Nissan Motor has developed technologies to provide customers with a dynamic driving performance over all road conditions and at all times; the results have received customer approval. Numerous research results regarding customer’s perceptions of vehicle behavior and the human mechanism which explains their intention for these behaviors have been incorporated into PP2.0. Here, we discuss this in detail.

This development has been undertaken to facilitate cooperative human-vehicle driving relationships that provide not only convenience but also a sense of mutual interaction towards a destination. The development paths were as follows: knowledge of “how to move a vehicle,” obtained through dynamic performance research, was maximized and utilized; simulation techniques were actively applied; and techniques accumulated through the development of numerous driver-assistance/safety systems, the evolution of intelligent technologies, and human research were combined. The following items represent the PP2.0’s performance-target settings considered in realizing the above, as well as their verification:

- Verification of lane-change actions in complicated traffic environments.
- Vehicle-behavior target settings for controlling discrepancies perceived by the passenger, as well as their verification.

### 2. Verification of lane-change action in complicated traffic environments

To evaluate a lane-change-assistance function (including its relationship to adjacent vehicles), comprehensive verification procedures are required. Accordingly, a coupled simulation environment combining multiple tools was constructed to reproduce traffic flows, the PP2.0 system (sensors and control logic), and vehicle behavior interactions (Fig.1). To ensure the reproducibility of the yaw response to steering (an important feature of lane-changing motions), a highly accurate vehicle model (also used for stability performance evaluations) was adopted, to accurately reproduce the mutual relationships between sensors, control logic, and vehicle behavior (Fig.2).

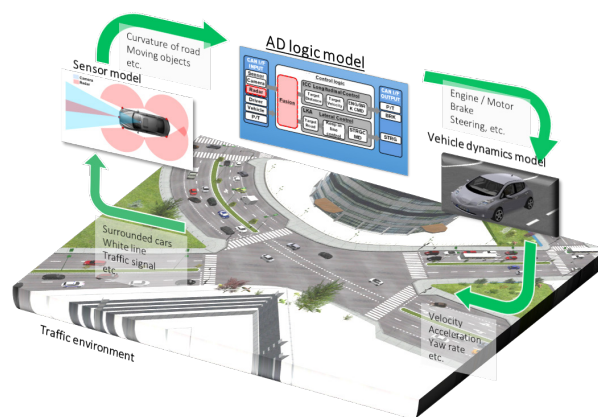


Fig.1 Autonomous driving (AD) simulation platform

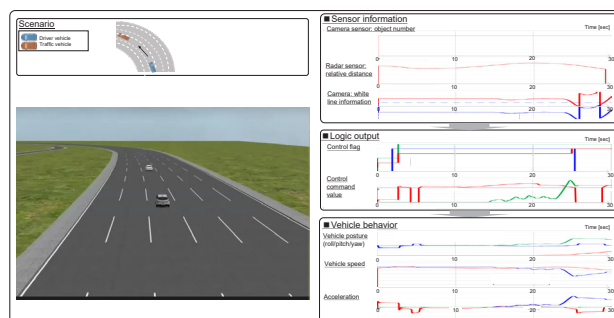


Fig.2 Results of sensor/AD-logic/vehicle-behavior simulations

\*Customer Performance and Test Engineering Methodology Innovation Department  
Department No.2

\*\*Customer Performance and Vehicle Test Engineering  
Department No.1

Next, a simulated branching scene was considered, to examine lane-change motions for a complicated traffic environment. Here, to reproduce multi-vehicle traffic flows (for which practical reproductions are difficult), the PP2.0 vehicle's surroundings were divided into nine blocks. Large-sized vehicles (e.g., buses and trucks) were placed at random in the adjacent divisions, using one vehicle per division (Items 2, 3, 6, 7, and 8 in Fig.3); furthermore, standard-sized passenger cars were placed at random in the forward/backward positions, with one vehicle per division (Items 1, 4, 5, and 9 in Fig.3). Here, the standard-sized passenger cars were described by dynamic traffic parameters (e.g., vehicle speed and acceleration/deceleration), and the lane-change times were set to different levels.

For the simulation evaluations, 1376 test-case patterns were automatically generated using the aforementioned preconditions. Numerous scenes (for which the handling appeared challenging for PP2.0) were included amongst these cases (e.g., a standard-sized passenger car suddenly cutting in from the blind spot of a large-sized vehicle when performing a lane change).

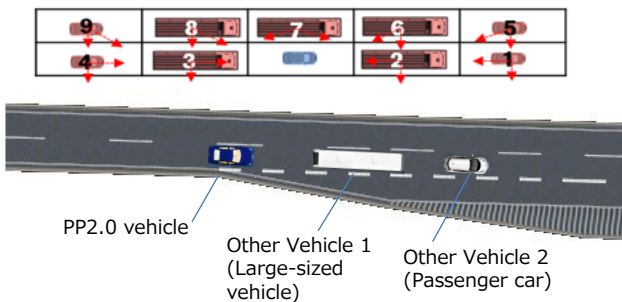


Fig.3 Layout of PP2.0 and other vehicles in branch scene

Furthermore, to process the simulation results, the following list of fully determined results were outputted for several minutes: the relative positions of the PP2.0 and other vehicles; the time-to-collision considering relative speeds; and the successful operation of the control logic (Fig.4).

The table is a dense grid with many columns and rows, representing simulation data. The columns likely represent different parameters such as vehicle positions, speeds, and control logic status. The rows represent time intervals. The data is presented in a structured, tabular format.

Fig.4 List of simulation results for branching scenes

As described above, performing verification with not only actual vehicle but also simulation environments, which reproduce vehicle behaviors when the lane-change-function is activated under any road-shape/traffic-flow conditions, enables more accurate analyses and measures for whether the PP2.0 system exhibit any problems, and if so, what caused them.

### 3. Vehicle-behavior target settings for controlling passenger-perceived discrepancies, and their verification

PP2.0 features a hands-off function for driving within the same lane. Because the driver does not perform driving operations in this mode, conditions of involuntary (passive) motion can be assumed. As shown in the lower part of Fig.5, under involuntary motion conditions, motion compensation (based on motion-estimation results from the brain model (internal) model) is not performed. Therefore, a discrepancy often arises between the amount of perceptions a person receives from the sensory system (i.e., actual perceptions) and the amount subconsciously estimated (i.e., not perceived), which may cause sensory confusion. For the driver to maintain safety during the hands-off mode, generating vehicle behaviors that do not cause sensory discrepancies seems necessary.

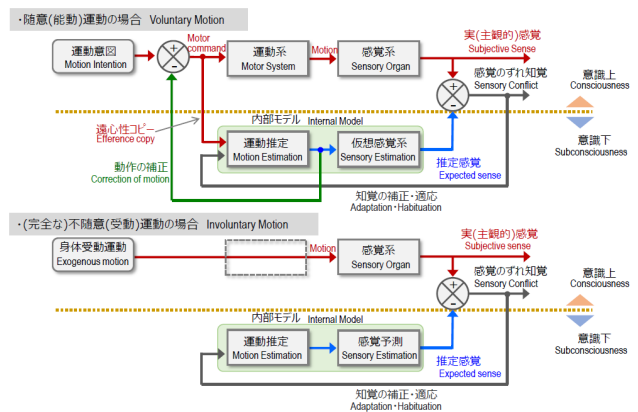


Fig.5 Passenger perception model for voluntary motion/involuntary motion

Nissan Motor has been accumulating research regarding vehicle-motion controls for enhancing passenger comfort. By treating the amount of vehicle operations and the passenger's visual and bodily behavior-related movement perceptions as parameters, optimal vehicle-behavior identifying methods have been constructed. Comfort-enhancing parameters include the in-lane lateral traveling speed (perceived visually), steering speed, bodily received acceleration, and time change thereof (jerk). Next, the vehicle-behavior performance targets were set by assuming that minimizing these perceptions reduces the prevalence of human-perceived discrepancies, leading to feelings of safety.

For example, Fig.6 depicts the time change in the vehicle's lateral acceleration and the angular acceleration of the passenger's body under changes in vehicle-motion parameters<sup>[1]</sup>. V0 specifies the extent to which steering operation was minimized, assuming an improvement in the comfort of a driver performing driving operations (voluntary motion). R1 specifies the direction in which the body roll angular acceleration (a type of movement perception) is minimized, assuming an improvement in

passenger comfort (involuntary motion). This vehicle behavior can be reproduced with a steering robot (as shown in Fig.7) or with a driving simulator. From the results of the subjective vehicle-behavior evaluations performed with in-house participants, the following results were obtained: V0 provided a smooth motion, but a larger perceived posture change, and R1 provided a smaller posture change and a greater perception of parallel motion.

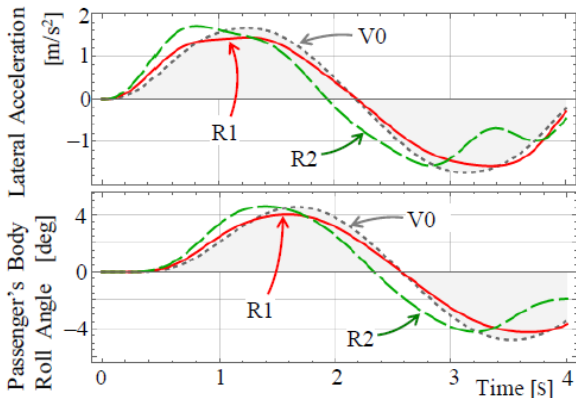


Fig.6 Passenger body angular acceleration vs. time and lateral G vs. time in vehicle, assuming comfort improvement in voluntary motion/involuntary motion

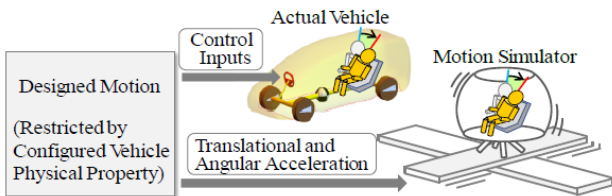


Fig.7 Vehicle behavior evaluation with steering robot/driving simulator

Here, we explain our evaluation of the perceptions received from the sensory system by passengers. The developed vehicle's success in achieving the desired vehicle behavior was evaluated via driving experiments on a proving ground. In these experiments, to check whether the new performance targets were met, we considered the results of two evaluations: subjective (performed by evaluators who actually drove the vehicle) and quantitative (from the measurement data for the actual perceptions). These were regarded as passenger inputs in the passenger perception model (Fig.5). Nissan Motor owns the Rikubetsu Proving Ground (Fig.8), which facilitates evaluations in expressway type environment; the ground includes various road conditions, such as multiple lanes, large-radius turning, complex turning,



Fig.8 Nissan Motor's Rikubetsu Proving Ground

and undulating road surfaces. Moreover, a high-definition map (essential for realizing PP2.0 functions) of the grounds is available. These evaluations were performed by comparing PP2.0's driving with that of an experienced driver familiar with the proving ground.

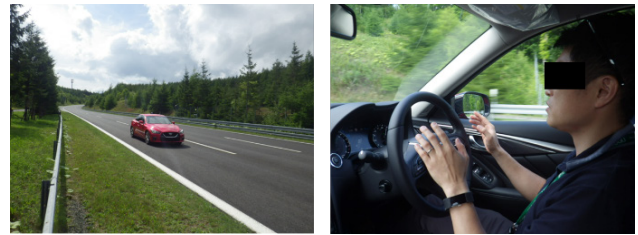


Fig.9 ProPILOT 2.0 evaluation conditions on proving ground

First, a subjective evaluation of PP2.0's hands-off operation (within the same lane) was performed. The following evaluation results were obtained. When driving through a curve, the steering function was initiated early and the amount of corrective steering was small; this realizes a very high level of stability and maximizes the duration of smooth driving operations.

Measurement data to quantitatively support the subjective evaluation results included the in-lane traveling speed (related to the degree of visual perception), steering speed, and distance from the lane center. The comparison results are shown in Fig.10 to Fig.12.

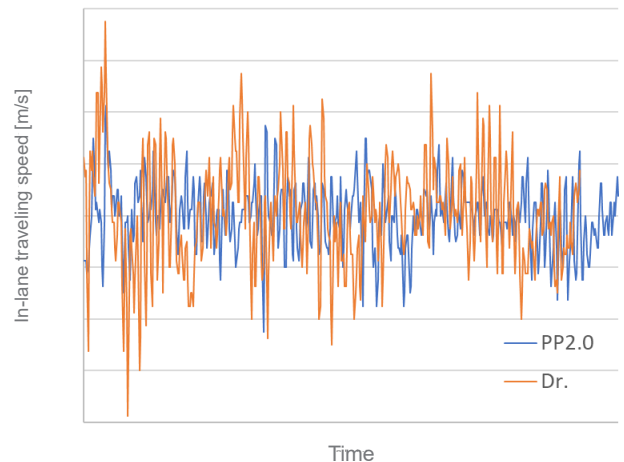


Fig.10 In-lane lateral traveling speed

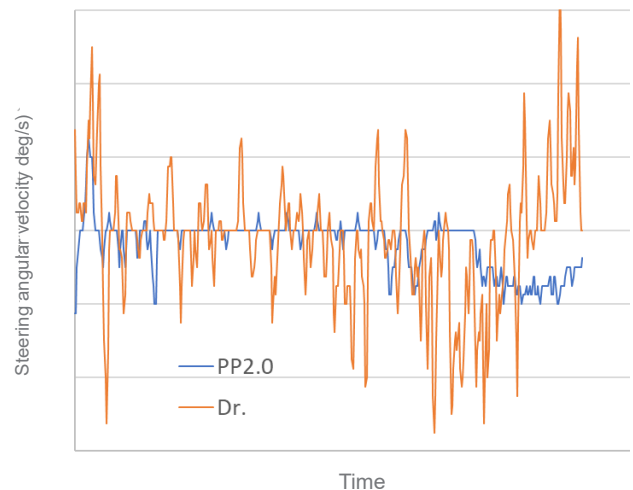


Fig.11 Steering angular velocity

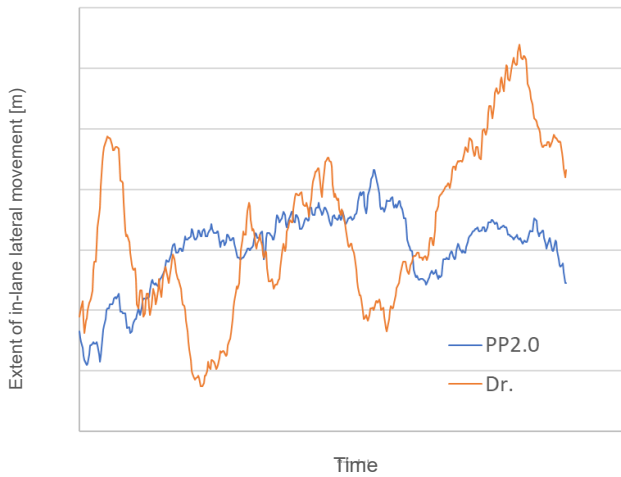


Fig.12 Extent of in-lane lateral movement

Compared to the experienced driver, PP2.0 maintained smaller variability in these values. Therefore, PP2.0 remained at the lane center, controlled the corrective steering, and realized stable behavior.

Meanwhile, as physical quantities related to movement perceptions, longitudinal/lateral accelerations during driving on the S-shaped section were measured. The results are shown in Fig.13, where the vertical and horizontal axes represent the longitudinal acceleration (acceleration G/deceleration G) and lateral acceleration (lateral G), respectively. The two types of G-G diagrams (one for PP1.0 (hands-on) and one for PP2.0 (hands-off)) are shown in different colors. The comparison revealed that the PP2.0 hands-off function maintained the lateral G value for longer, regardless of variation in longitudinal G; furthermore, the right/left lateral G levels were similar, resulting in gentle driving through the S-shaped section. This shows that PP2.0 processes the shapes of upcoming corners beforehand, using the high-definition map; hence, it gently decelerates before entering a corner, requiring only a slight lateral vehicle control when passing through.

As described above, it was confirmed that PP2.0 generated vehicle behaviors that controlled and reduced

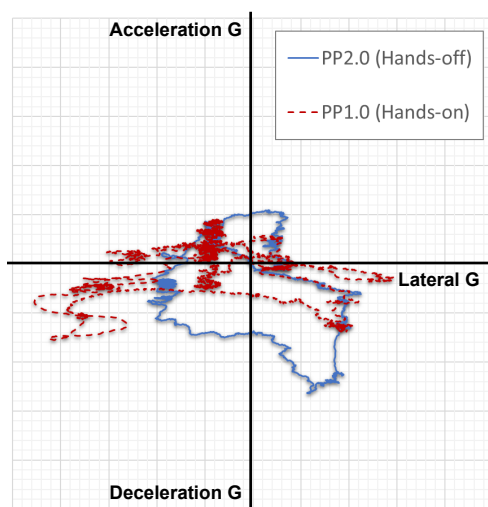


Fig.13 Acceleration/deceleration G and lateral G whilst driving through S-shaped section (G-G diagram)

the amount of visual and movement perceptions, thereby reducing the risk of sensory confusion.

#### 4. Verification of ProPILOT 2.0 fatigue-reduction effect

Finally, to verify whether the target output was achieved in the passenger-perception model (Fig.5) (i.e., whether the passenger experiencing no discrepancies felt safety), the fatigue-reduction effect of PP2.0 over long-distance operations was evaluated in a practical environment (public road), in which customers use the car. User impressions of “ease” were confirmed from the data.

The large quantities of active oxygen generated through excessive physical/mental activities can damage cells; this can produce fatigue factors (FF) [2]. FFs cause fatigue in the brain, resulting in symptoms such as abnormal autonomic nerve functions[2]. The condition of the autonomic nerves can be evaluated using the low-frequency-to-high-frequency ratio (LF/HF) (which indicates the balance between the sympathetic and parasympathetic nerves) and the coefficient of component variance total power (ccvTP) (which indicates the amplitude of activity for the entire autonomic nervous system)[3]. Therefore, we evaluated the fatigue-reduction effects of PP2.0 by measuring heartbeat fluctuations, from which the aforementioned parameters can be derived.

##### Measurement of heartbeat fluctuation

In the experiments, a portable heart-rate meter (MF100, Murata Manufacturing Co., Ltd./Fatigue Science Laboratory Inc.; Fig.14) was used to measure heartbeat fluctuation; the data were converted into the R-R interval with a sampling rate of 100 Hz, and a power spectral density function was found. Then, the LF component (0.04–0.15 Hz), which reflects the acceleration of the sympathetic nervous system, and the HF component (0.15–0.4 Hz), which reflects the acceleration of the sympathetic and parasympathetic nervous systems, were calculated; next, the LF/HF was found by dividing the former by the latter. In addition, the square root of the sum of the LF and HF components was divided by the mean value of the R-R interval, to calculate the ccvTP. To remove the influence of age/sex[4], the ccvTP was converted into a deviation value using the ccvTP data for 10000 people or more (grouped according to generation/sex) and the population ratios of each group[5].



Fig.14 MF100 device

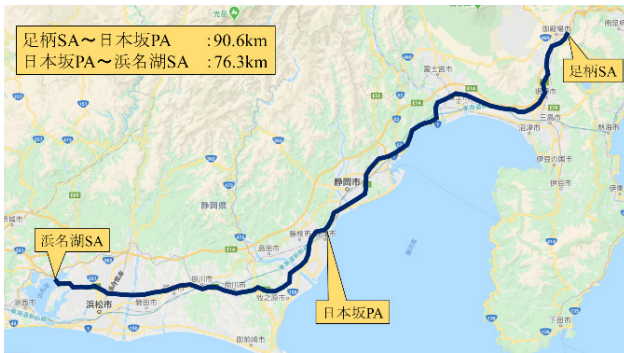


Fig.15 Driving route

### Driving conditions

The experiments were performed on the 167-km road section shown in Fig.15. Experimental participants were grouped into down- and up-route drivers prior to the experiment. Both driver groups were stopped at Nihonzaka PA. The experiment participants drove unassisted on one day and used PP2.0 on the other. The driving modes on the first day were counterbalanced between the experiment participants. Under PP2.0 ON, the PP2.0 mode was applied for as long as possible (except for emergencies). Instructions were left that if the mode temporarily switched to OFF (e.g., due to traffic congestion or construction work), it should be returned to ON immediately after passing the section. The upper limit of the vehicle's speed was set to 100 km/h. Changing the vehicle's speed setting and overtaking were allowed within a safe range. For driving with PP2.0 OFF, participants were instructed to drive as usual at a guideline speed of 100 km/h.

### Experiment participants

The experiments were inspected and approved beforehand by the Experimental Ethics Committee of Nissan Motor Corporation. The experiment participants consisted of 13 people ranging from their thirties to sixties (11 males and two females). Two of them had routinely used autonomous driving functions of Level 1 or higher, as defined by the Society of Automotive Engineers (SAE).

Moreover, the experiment participants were instructed to refrain from the following: drinking alcohol or staying up late on the day before driving, skipping breakfast on the day, and smoking, drinking anything besides water, or eating in the hour before driving.

### Procedure

Once the experiments were prepared, the down-route drivers drove to Ashigara SA (the starting point of the down-route experiments); for this, no driving modes (PP2.0 ON/OFF) were applied. Upon arrival, they took a 15-minute rest before the experiment. First, their heartbeat fluctuations (at rest with eyes closed) were recorded for 2 min. The participants were instructed to mute any audio and to refrain from speech, excessive movement, deep breathing, and so on whilst heartbeat fluctuation was measured. Next, they drove to Nihonzaka PA according to the driving conditions of the day.

Immediately after arrival, they measured their heartbeat fluctuation again. After completion, they drove to Hamanako SA. After arrival at Hamanako SA, they measured their heartbeat fluctuation in the same way, to complete the down-route driver experiments. After a 30-minute lunch break, they took a 1-hour rest in Hamanako SA. The up-route drivers were instructed to refrain from smoking, drinking anything besides water, or eating during the rest. Next, a similar procedure to that applied for the down-route drivers was performed, using Hamanako SA as a starting point. We decided to divide the data into first-half and second-half sections (with Nihonzaka PA as the mid-point) for analysis.

### Results

The LF/HF and ccvTP results are shown in Figs. 16 and 17, respectively. The LF/HF was converted into common-logarithm decibel units. We conducted repeated measurement variance analyses for each of the two factors (i.e., PP2.0 ON and PP2.0 OFF × the driving section (first, second, and entire sections)). The interaction ( $F = 8.96$ ,  $p < 0.01$ ) was found significant for LF/HF, and the main effect of the driving condition ( $F = 9.21$ ,  $p < 0.05$ ) was found significant for ccvTP.

In the sub-effect test results for LF/HF interaction, the driving condition was identified as having a simple main effect in the first-half section ( $F = 7.84$ ,  $p < 0.01$ ), and the driving section was likewise found to have a simple main effect for both PP2.0 ON ( $F = 4.02$ ,  $p < 0.05$ ) and PP2.0 OFF ( $F = 3.55$ ,  $p < 0.05$ ). Meanwhile, in the ccvTP results, a simple main effect of the driving condition was only found to be significant across the entire route ( $F = 7.05$ ,  $p < 0.05$ ). Based on the above results, it was shown that, compared to PP2.0 OFF, PP2.0 ON had a significant calming influence on the autonomic nerve balance in the first section, whereas the ccvTP only indicated a significant difference in autonomic nerve activity over the entire route.

In the ccvTP results (Fig.17), the use of PP2.0 functions can be seen to reduce fatigue. In addition, the ccvTP results for PP2.0 ON tended to be high in both sections and similarly high over the entire route; thus, it can be assumed that fatigue was continuously accumulated from the first section, such that a significant difference appeared only after driving the entire route. Meanwhile, in terms of LF/HF, PP2.0 OFF and PP2.0 ON produced

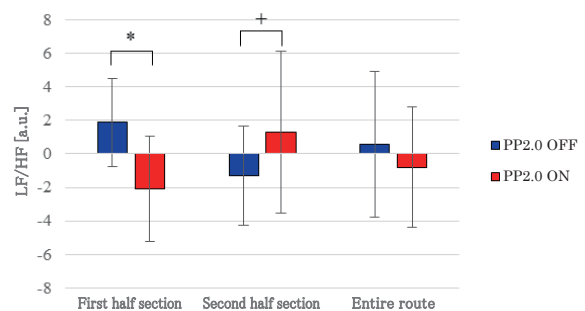


Fig.16 LF/HF comparison

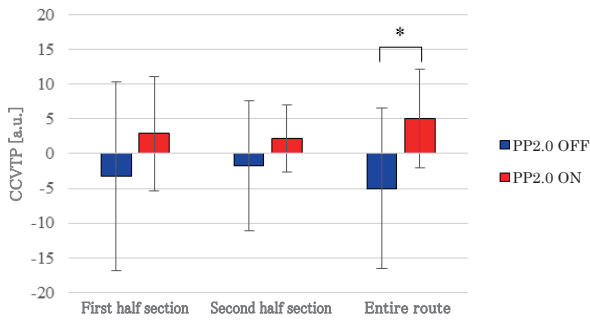


Fig.17 ccvTP comparison

high excitation trends in the first and second sections, respectively (Fig.16). It is thought that LF/HF increases according to the acceleration of the sympathetic nervous system or the control of the parasympathetic one, and the long continuous acceleration of the sympathetic nervous system produces fatigue<sup>[3]</sup>. Thus, it seems that with PP2.0 OFF, the sympathetic nervous system was accelerated in the first section, leading to fatigue accumulation, and the parasympathetic nervous system was accelerated in the second section, which controlled the degree of fatigue accumulation. Meanwhile, with PP2.0 ON, the fatigue accumulation in the first section was small, so that the LF/HF for the second section showed a relative increase.

From these results, we confirmed that in long-distance driving using PP2.0 functions, fatigue accumulation was controlled to be smaller than that measured under normal driving. This suggest that under all traffic environments, PP2.0 can perform lane-change maneuvers with a feeling of safety and produce comforting vehicle behaviors, presenting no discrepancies to passengers.

## 5. Summary

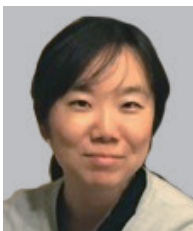
As described above, Nissan Motor's experimental techniques were applied to set targets and evaluate the success of PP2.0 from the perspectives of dynamic performance, control technology, and human science. As a result, PP2.0 has been described by many customers and journalists as not only a convenient function but also as a "buddy"<sup>[6] [7] [8]</sup>.

These results are primarily possible because of Nissan Motor's long-term accumulation of experimental techniques, which could not have been achieved in a short time. Finally, we would like to add that these results were achieved through considerable effort, involving the construction of the world's largest driving simulator (introduced above), a bench-test system of model-/hardware-in-loop simulations, integrated driving-vehicle measurement techniques, and large-scale data-analysis procedures.

## References

- [1] M. Makita, A. Matsushita, Y. Kusayanagi and M. Miura : An Approach to Exploring Vehicle Motion to Enhance Ride Quality of Passenger, Transactions of Society of Automotive Engineers of Japan 50(5), p.1349, 2019
- [2] Y. Watanabe : Fatigue Science & Fatigue Brain Science : Development of Anti-Fatigue Products, Japanese Journal of Biological Psychiatry 24(4), p.200, 2013
- [3] H.Kuratsune : The Prevalence of Fatigue in Japan and Objective Methods for Evaluating Fatigue States, The Japanese journal of stress sciences 32(4), p.271, 2018
- [4] H. Kuratsune : Fatigue level judgment processing system, JP5455071B2 (2011)
- [5] J. Koizumi : Autonomic nervous function age determination system and determination method, JP5455071B2 (2011)
- [6] A. Nakatani : WEB CARTOP (30 Aug. 2019) <https://www.webcartop.jp/2019/08/419804/>
- [7] N. Aoyama : DIME (31 Oct. 2019) <https://dime.jp/genre/797355/>
- [8] H. Aida : Response (22 Nov. 2019) <https://response.jp/article/2019/11/22/329031.html>

## Authors



Yumi Kubota



Koji Sasaki



Shimpei Nagae



Kenji Ogino



# 1. Spreading the appeal of electric drive with e-POWER

Akihiro Shibuya\* Toshiyuki Nakajima\*\*

## 1. Introduction

In 2016, Nissan introduced the NOTE, which features an electric power system called e-POWER, to the Japanese market. e-POWER is 100% motor-driven, with all the power being generated by the engine. Since then, Nissan has continued to increase the number of e-POWER vehicle models. As part of the electrification strategy of Nissan, e-POWER has become an integral component of its electric vehicles as a sustainable technology that achieves sufficient environmental and driving performance simultaneously. This paper covers the history and values of e-POWER, including the technical challenges and future developments.

## 2. Belief in the proliferation of electric drive

### Electrification and intelligence strategy of Nissan ahead of CASE

Nissan commenced its electrification and intelligence study as a technical development strategy in approximately 2005. The strategy was publicized outside the company prior to launching the Nissan LEAF in 2010. Although CASE is a common technology that is currently used by all automotive companies, in 2005, the strategy of Nissan was challenging because it involved the battery electric vehicle (hereinafter referred to as BEV<sup>2)</sup>) and autonomous driving as the core technologies of electrification and intelligence, as shown in Fig. 1. For electrification, Nissan intended to achieve a 100% electric

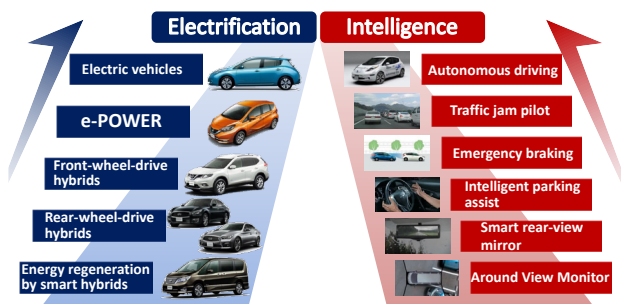


Fig. 1 Electrification and intelligence strategy

drive in the long run, while gradually increasing the ratio of electric drive vehicles.

### Shared motor drive regardless of energy source

The birth of e-POWER was supported by the research and development of power-generating electric vehicles (hereafter referred to as EVs<sup>1)</sup>, which have been promoted as catalysts for the proliferation of BEVs. To achieve an ultimate low-carbon society through electrification, Nissan has researched and developed technologies based on various energy sources, as shown in Fig. 2. These include direct hydrogen fuel cell technology (H<sub>2</sub> FCEV), which uses hydrogen as the fuel; reforming fuel cell technology (e-Bio Fuel-Cell) using reformed biofuel for power generation; and internal combustion engine-based power-generating systems with gasoline as the fuel. All these technologies have been intended to expand the options for energy sources based on technologies for improving BEVs and have aimed at achieving a 100% motor drive.

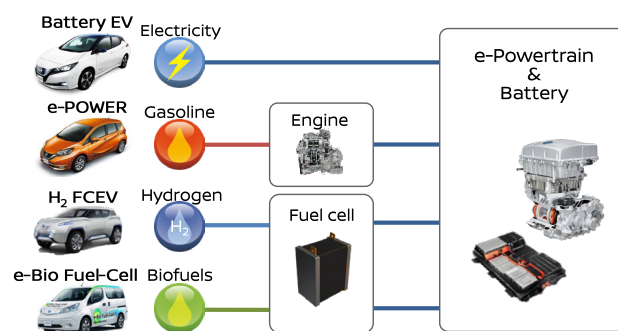


Fig. 2 Energy options for 100% motor-driven systems

Among these options, H<sub>2</sub> FCEV and e-Bio Fuel-Cell show significant potential for the future. However, enhancing their proliferation requires further cost reduction and improvements in convenience, including infrastructure.

By contrast, engine-based power-generating systems can extend the driving ranges of range-extender EVs. These use high-capacity EV-dedicated batteries and

\*Powertrain and EV Project Management Department

\*\*Advanced Vehicle Engineering Department

engines as supplementary power-generating systems. Indeed, Nissan initiated the advanced development of range-extender EVs alongside the product development of the LEAF launched in 2010, as shown in Fig. 3.

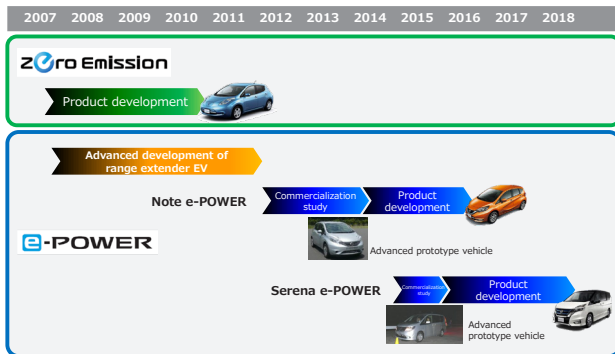


Fig. 3 Development histories of BEVs and e-POWER

For the practical use of e-POWER, Nissan employed the control technology developed for LEAF and the energy management and noise and vibration technologies developed for the range-extender EV. In addition, Nissan needed new breakthroughs such as high-power-density batteries, which will be discussed later in this article.

### Improved response and smoothness of Nissan EVs through the development of LEAF

Essential factors for the proliferation of BEVs include a sufficient driving range, charging convenience, and realistic retail prices. In addition, our predecessors at Nissan strived to provide drivers of motor-driven vehicles with a powerful response and comfortable, smooth driving at the highest level, to ensure that the drivers were enthralled once they drove the vehicles. They were capable of satisfying drivers by expressing the excellence of the systems and control in the form of vehicles.

LEAF was launched globally in 2010 and gained an excellent reputation owing to its driving comfort and high level of quietness, which distinguished it from other motor-driven vehicles. The general BEV models vibrated noisily during acceleration, similar to carts; by contrast, LEAF provided a smooth driving experience even during rapid acceleration and deceleration. Thus, the superiority of LEAF was evident. Furthermore, after a trial ride, all the drivers were smiling; internally, this smile was called the “LEAF smile.”

## 3. Practical use of e-POWER with the main model in Japan

### Start of development aiming at EV-ness<sup>3</sup>

When Nissan decided to launch the NOTE e-POWER in 2014, the hybrid vehicle of a competitor had a significant market share in the compact vehicle segment in Japan. To launch electrification technology as a follower, Nissan needed to improve the fuel economy and also express the uniqueness of this vehicle. Thus, e-POWER, the main driver behind the electrification strategy of Nissan, was developed to define the

characteristic of “EV-ness,” which represents the good driving performance of the Nissan LEAF.

### Challenges different from those of range-extenders

Fig. 4 depicts the e-POWER system. The system is simple and consists of a BEV with an additional engine for power generation. The system configuration is similar to that of the range-extender EV described above; however, some parts are significantly different. Range-extender EVs supply power to the motor from the battery, similar to BEVs. Likewise, e-POWER vehicles also supply power from the battery under normal usage conditions; however, under high-load usage cases in which a high motor output is required, they supplement power by generating it from the engine. Because a smaller battery capacity, as compared to that in a range-extender, is required, the batteries can be downsized, which is advantageous for vehicle installation.

Conversely, achieving a BEV-equivalent “response” necessitated supplying the necessary power as quickly as possible; therefore, the battery output was increased by reducing its internal resistance. Hence, Nissan needed to devise a breakthrough solution to achieve a higher battery power density and create batteries that leveraged the characteristics of e-POWER.

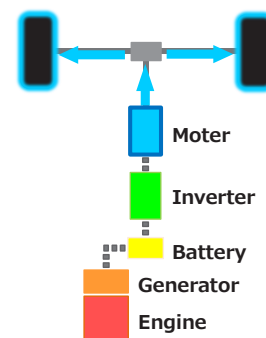


Fig. 4 e-POWER system

Because the system required 100% power generation, the efficiency of the power-generating engine was crucial, and Nissan improved it exclusively for e-POWER. It was also a new challenge to establish noise, vibration, and emission performances under the unique fixed-point operation at the maximum efficiency point, which will be detailed in a later article.

In the system configuration of e-POWER, the motor that drives and the engine that generates power are mechanically separated from each other. Accordingly, Nissan assumed that LEAF-equivalent EV-ness could be achieved easily. However, as the system supplies the maximum power when combining the two types of power from the battery and engine, as discussed earlier, if the power generation of the engine is delayed, the response of the motor is also delayed. By contrast, if the engine is continuously operated to be ready for the power output, the EV-ness will be impaired, leading to poor fuel economy. Solving such trade-offs proved to be a considerable challenge for Nissan, which the

range-extender EVs had not posed. The pertinent details will be discussed in a later article.

### Driving SERENA with a 1.2L engine

The next challenge was to achieve EV-ness with SERENA, which was a larger vehicle than the NOTE. Hence, higher torque and output are required. The motor output and torque were optimized according to the vehicle model, as per the basic specifications shown in Table 1. To optimize the specifications using an engine and motor of the same type, Nissan implemented a modular design by varying the number of cells combined in the battery and the current capacity of the inverter.




				
		NOTE	SERENA	KICKS
Motor (EM57)	Maximum output	80 kW	100 kW	95 kW
	Maximum torque	254 Nm	320 Nm	260 Nm
Engine (HR12)	Maximum output	58 kW	62 kW	60 kW
Battery capacity		1.5 kWh	1.8 kWh	1.5 kWh

Table 1 Basic specifications of 1st-generation e-POWER

The battery ratio of the SERENA is higher than that of the NOTE. However, the challenge was to achieve EV-ness by managing energy and power, as discussed above. Therefore, it was essential to conduct a simulation and also perform a feeling evaluation using an actual vehicle, in order to confirm practicality. As Nissan could not evaluate the SERENA under development on a public road, the vehicle was tested late at night at the reserved Hakone Turnpike several times to evaluate feelings and practicality. Although the concept of driving a SERENA with a 1.2L engine, as described in the presentation materials, was difficult to understand, Nissan improved the EV-ness of the mini-van to the optimal level through repeated driving tests. Nissan performed the final evaluation after the relevant executives experienced the ride comfort during the late-night trial rides at the Hakone Turnpike.

### Ride comfort of e-POWER that stimulates purchase intention once experienced

During the development of clear EV-ness while working on the breakthroughs mentioned above, the key for the successful launch of e-POWER was its simplicity. This characteristic enabled the engineers involved in the development and the concerned internal parties to quickly discover the superiority and difference of e-POWER, as compared to competitors' HEV systems, during the trial rides. They were satisfied with the technology, as evidenced by the LEAF smile described above, and showed the intention to purchase. Although fuel economy is an important factor when purchasing a vehicle, Nissan shifted the point of the discussion to a more important factor, that is, how the ride comfort of

the vehicle could be conveyed to the customers to stimulate their intention to purchase. Nissan needed to convey the following three benefits to customers:

- Linear and smooth acceleration, with the feel of an EV.
- High level of quietness
- Top-level fuel economy in the class

In fact, Nissan held almost 20 test ride events with the concerned internal parties before finalizing the launch of the NOTE and SERENA. Thus, they developed confidence in the vehicles as intended through exceptional performance during the physical demonstrations.

As discussed above, the promotion of EV-ness and the provision of appropriate energy and power management were challenging but exciting aspects of the development of e-POWER. During its development, every step was challenging, including the study of the trade-offs and the judgment criteria that were completely new to Nissan. The details of these challenges will be discussed in future reports.

## 4. Contribution to building of the Nissan brand

### Brand strategy of Nissan evolved from electrification and intelligence

The brand strategy of Nissan, "innovation for excitement," is not only the value that is intended to be offered to customers but also the brand promise.

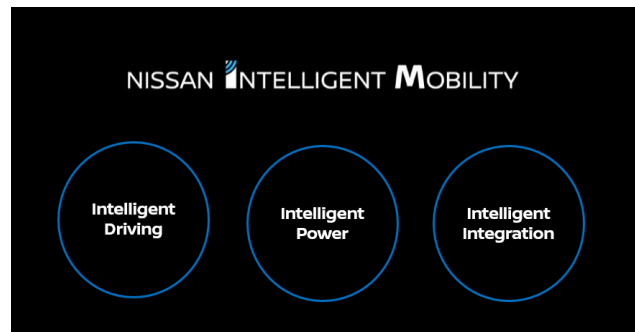


Fig. 5 Nissan Intelligent Mobility

To deploy this strategy in a more competitive manner, Nissan adopted a differentiator, Nissan Intelligent Mobility (NIM), as a slogan. NIM is a generic name for innovations conveying futuristic visions and is composed of the three elements shown in Fig. 5. The three elements are shown in parallel; however, the concept is that the electrification (intelligent power) and intelligence (intelligent driving) described earlier evolved first to create an integrated value (intelligent integration). To summarize, NIM is built on the developed electrification and intelligence strategies.

### Strengthening of the Nissan brand using technology

With the intelligent power of NIM, the objective is to accelerate the enjoyment of clean, quiet, and powerful driving that is unique to Nissan by offering dynamic driving experiences through electrification technology.

As shown in Fig. 6, Nissan embodied clean, quiet, and powerful driving in e-POWER technology to offer customers. In addition, e-4ORCE, which offers a new driving experience by driving with motors on both the front and rear wheels, and e-POWER Drive and e-Pedal, which enable deceleration with the accelerator pedal, are particularly compatible with the electrification technology of 100% motor drive. In this way, they deliver a unique driving experience together with the EV and e-POWER.



Fig. 6 Core technologies of intelligent power

As discussed above, e-POWER has been a key technology for supporting the brand building of Nissan. This is expected to contribute to the strengthening of the brand in the future and to offering new value to customers through technical innovations.

## 5. Delivering to customers worldwide

### Achieving the No. 1 sales position in the segment with first-generation e-POWER

The first-generation e-POWER vehicles, as shown in Fig. 7, quickly impressed customers with the same driving feeling as BEVs, which stimulated their purchase intention and ensured their satisfaction after purchase. The following four points were highly evaluated, which exceeded the expectations of Nissan during development:

- Linear and smooth acceleration, providing the feel of an EV
- High level of quietness
- Top-level fuel economy in the class
- New driving feeling created by the acceleration and deceleration using accelerator pedals

Regarding the sales results, the NOTE achieved the No. 1 sales position in Japan in November 2016 for the first time in 30 years, after which the NOTE and SERENA achieved the highest sales volumes in their respective market segments. As of January 2021, the cumulative sales volumes of the NOTE and e-POWER are 440,000 units, and the sales volume of a subsequent model, KICKS, also shows a favorable trend.

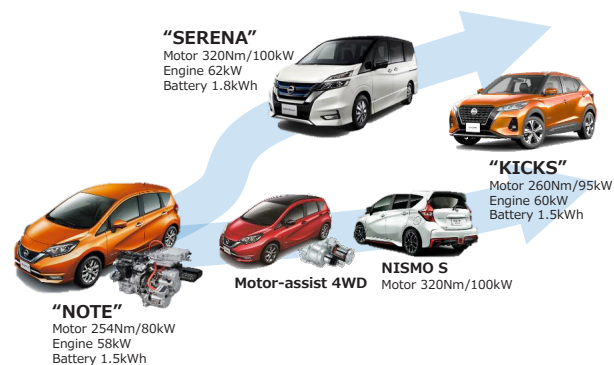


Fig. 7 Lineup of first-generation e-POWER vehicles

### Pursuing further EV-ness in second-generation e-POWER vehicles

The new NOTE, to be fully remodeled in 2021, is an e-POWER-dedicated model equipped with an improved second-generation e-POWER system. With this model, e-POWER has evolved in an ideal direction by providing improved power performance, smoothness, and quietness and creating a more EV-like feeling. To achieve these features, Nissan has improved the motor, inverter, battery, and engine constituting the system to enhance not only the output and torque but also the fuel economy. Quietness has been further improved by reducing the engine operation frequency, optimizing the engine operation timing, and adopting a new control that operates the engine according to road noise. An electric AWD model has also been added to harness the benefits afforded by precise control.

### Power train strategy based on inseparable technologies BEV and e-POWER

As discussed above, e-POWER is inseparable from BEV in the power train strategy of Nissan. These technologies show potential for further improvement and are promising in terms of covering wide segments and regions. This promise is attributed to their practicality, which enables the sharing of parts and control technologies, and also their flexibility, which allows for a modular configuration. Nissan will continue to focus on the driving feeling, quietness, and excellent environmental performance provided by these 100% motor-driven systems.

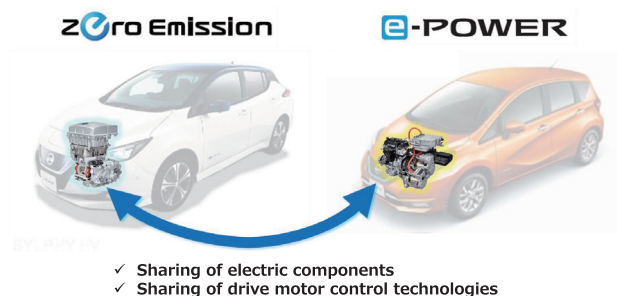


Fig. 8 Inseparable technologies in power train electrification strategy

## 6. Conclusion

Amid the growing global interest in environmental issues, it is said that the automotive industry faces a major once-in-a-century change. Even under these circumstances, Nissan will continuously strive to deliver the pleasure and comfort of a seamless driving experience to customers, while also achieving environmentally friendly fuel economy and emission performance. To attain these goals, Nissan has been expanding the range of e-POWER-equipped vehicle models from the NOTE to the SERENA, the KICKS, and the new NOTE that was launched recently. Nissan will continue to spread the appeal of the electric drive to ensure that customers worldwide can experience the LEAF smile.

### Explanation of terms

- \*1 EV: Vehicle driven by an electric motor alone.
- \*2 BEV: EV driven by battery power alone.
- \*3 EV-ness: The quiet, powerful, and smooth driving feeling unique to electric motor drives
- \*4 EV driving: Driving with e-POWER operated by the battery power alone, with the engine stopped.

## Authors



Akihiro Shibuya



Toshiyuki Nakajima



## 2. Characteristics of e-POWER system and future development

Naoki Nakada\*

### 1. Introduction

This article introduces the electric powertrain, e-POWER, which has been newly developed to enable good driving performance of the Nissan LEAF. e-POWER is 100% motor-driven with 100% power generated by the engine. The following topics are covered in this article: Overview of the system, characteristics unique to BEV<sup>\*1</sup>-like and new features that have been developed by solving various trade-offs at a high level, system design to achieve them, and future expansion.

### 2. 100% motor-driven e-POWER system

The BEV system comprises a drive motor, inverter, lithium-ion battery, and battery charger. For the e-POWER system, while the drivetrain is the same as the BEV, the following alterations have been made: significant reduction of the battery capacity as a power source, elimination of the energy charging function, and the addition of a power-generating gasoline engine and a generator as an alternative power source. It is a simple system that is 100% motor-driven with 100% power generated by the engine. As a 100% motor-driven vehicle, e-POWER can be defined as an EV<sup>\*2</sup> similar to the BEV. The good driving performance of the BEV is inherited, and the fuel economy can be improved by intensively using the optimum fuel consumption range because the power-generating engine is separated from the tires.

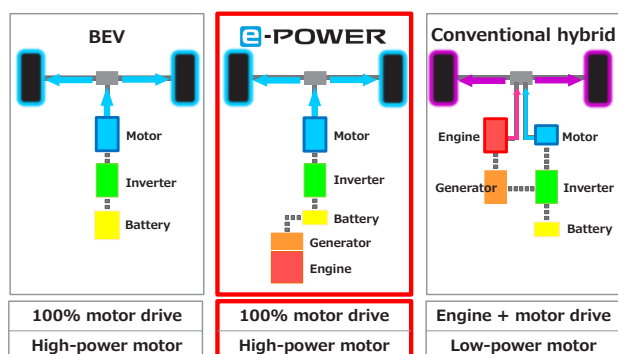


Fig.1 e-POWER system

Thus, e-POWER is an electric powertrain with great flexibility and various possibilities.



Fig.2 Appearance of e-POWER

Fig.2 shows the appearance of the NOTE e-POWER powertrain. As the engine is used for power generation only, it does not need to be positioned near the drive motor. However, we have integrated all the parts as much as possible to fit them compactly in the existing engine compartment.

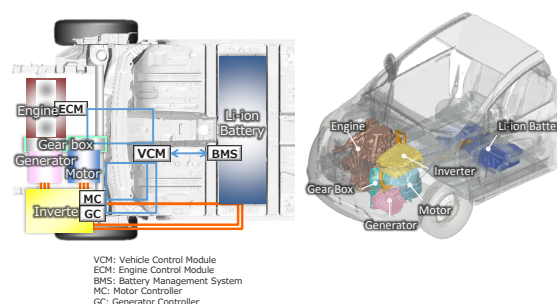


Fig.3 System configuration and layout

The engine is coupled to the generator via the speed increaser and the drive motor to the drive shaft via the speed reducer. Nissan put these two gear sets in a gear box to integrate the drivetrain- and generator-related components. The inverters for the drive motor and generator were placed in a single casing and installed inside the vehicle. A compact battery was installed under the front seat. By adopting this layout, Nissan not only fitted the e-POWER system in the platform of the compact

\*Powertrain and EV Project Management Department

vehicle, NOTE, but also achieved the comfort and ease of loading equivalent to those of gasoline-powered vehicles.

The e-POWER system is controlled by the main controller, the vehicle control module (VCM). The VCM works in conjunction with the MC (Motor Controller), GC (Generator Controller), BMS (Battery Management System), and ECM (Engine Control Module) to perform energy management and traction control by optimum power generation at all times.

### 3. Achievement of BEV-ness and pursuing new values

**EV-ness<sup>\*3</sup> - Smooth, High Response, Quiet**  
**Fuel economy satisfying driving performance**  
**- Top level fuel economy**  
**e-POWER Drive - Easy driving**

#### Challenge of achieving responsive BEV driving

e-POWER achieves responsive, powerful, linear, and smooth acceleration when the accelerator pedal is depressed. By utilizing the characteristics unique to 100% motor drive, a maximum torque can be generated at low revolutions and no transmission mechanism is necessary. This is based on Nissan's motor controlling technology (motor damping control corresponding to the torsional resonance of the drivetrain) achieved through the development of the LEAF. This is a tremendous benefit that conventional hybrid vehicles have never had and is the primary feature of e-POWER.

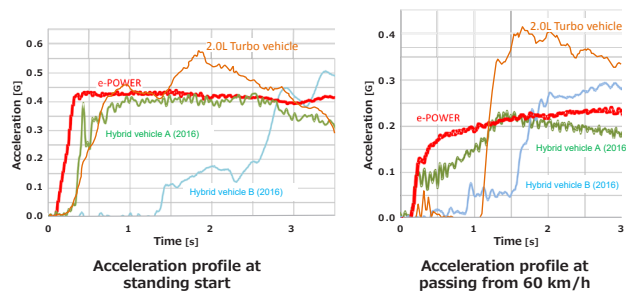


Fig.4 Smooth acceleration of 100% motor drive

The keys to achieving such an excellent performance are the sharing of the power output from the energy-supplying battery and engine and the control of power generation. We have achieved them by optimizing the use of battery energy, engine start timing, and traction characteristics for various acceleration scenes. The details are described in Article 2.

#### Achievement of BEV-like quietness and fixed-point operation

The power generation by the engine that supplies and stores energy can be controlled separately from the drivetrain. Using this mechanism, we achieved BEV-like quietness. In practice, we have achieved it by adopting the following main concepts: active stopping of the engine in the low vehicle speed range and power generation with engine speed at which the driving noise masks the engine noise in the relatively high vehicle speed range. If a

vehicle is driven at a low vehicle speed constantly, the battery energy decreases and the engine must be started to generate power. To address this, power is also instantly generated at an optimum fuel consumption rate with a relatively higher power of 2400 rpm × 76 Nm, 19 kW, which is equivalent to a NOTE's driving load at 120 km/h and is the operation point with a constant engine speed and load (fixed-point operation). In this way, the engine operation time is reduced to extend its stop time. Thus, we were able to stop the engine by approximately 90% at a vehicle speed of 25 km/h or less. However, in this fixed-point operation, we found two issues. One was the discomfort when vehicle speed and engine speed were not synchronized, which did not occur in conventional gasoline-powered vehicles. The other was the gap between EV driving<sup>\*4</sup> and driving during the engine's fixed-point operation at a relatively high engine speed. The former is a characteristic of e-POWER, accepted in the market. We have evolved and improved the latter to apply it to the SERENA and KICKS based on the data and knowledge obtained from the NOTE. This is also described in Article 3. Other technologies for quietness are introduced in Article 5.

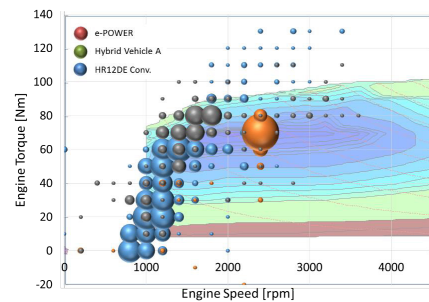


Fig.5 Incidence of engine operation points

#### Enhancement of fuel economy by fixed-point operation

With the power generation control based on fixed-point operation, Nissan has achieved the top-level fuel economy in its class by generating power for the energy required for driving at the point of best fuel consumption ratio, as much as possible. We have designed power generation control in such a way that the most fuel-efficient operation point is selected within the permissible ranges of various requirements. These include power, drivability, noise and vibration, exhaust emission, cooling, air heating, brake booster negative pressure, component protection, and diagnosis. Fuel economy-related information is detailed in Article 4.

#### Pursuing deceleration energy regeneration performance with e-POWER Drive

A new feature offered by e-POWER includes e-POWER Drive, which provides a new driving feeling. Because the driver can control the vehicle by operating only the accelerator pedal, driving will become easier and enjoyable. During the development of the 1st-generation LEAF, Nissan studied the recovery of deceleration energy based on cooperative regeneration with the brake. To



improve the efficiency of energy recovery, Nissan also studied the one-pedal system that performed strong regeneration using only the motor. The main points observed from the development of this strong regeneration system are as follows: discomfort in drivability with respect to accelerator pedal operation, uselessness of strong regeneration mode that cannot be used even though the energy regeneration is large, and the setting of margins for safety and braking force limit on slippery road surfaces. For the 1st-generation LEAF, we set 0.08 G as the upper limit of the deceleration force by the motor regeneration in the ECO-B mode. Then, we further evolved the control of deceleration energy regeneration to generate a deceleration approximately three times that of gasoline-powered vehicles by optimally controlling the regenerative power according to vehicle speed, accelerator pedal operation, and slip ratio between the road surface and tire. Thus, we achieved drivability that allowed the driver to control acceleration and deceleration as intended by depressing and releasing the accelerator pedal. Accordingly, the NOTE e-POWER system did not use the cooperative regenerative system that has been a standard for electric vehicles. Through these efforts, Nissan has developed e-POWER Drive that about 70% of the deceleration of daily driving can be covered by only accelerator pedal operation. This significantly reduces the frequency of accelerator-brake pedal transfer, increases the energy regeneration amount, and offers driving pleasure and fuel economy at the same time.

#### 4. System design for achieving BEV-ness

e-POWER delivers high reliability because of its simple system configuration and ensures a high-quality level due to being equipped with the same system components as those of the LEAF and the conventional NOTE composed of an engine and CVT.

The components shared with the BEV include the drive motor, inverter, 12 V DC/DC converter, and speed reducer. Technologies are also shared for high-voltage safety, sequence control of system start/stop, and traction control. This indicates that e-POWER, like BEV, is also highly advantageous in terms of compatibility with intelligent technologies such as autonomous driving.

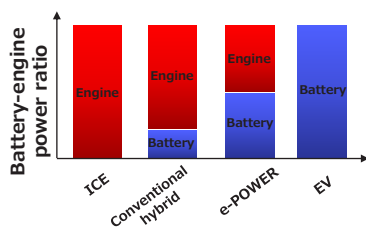


Fig.6 Sharing of battery power and engine power

However, compared with BEV, whose performance is highly dependent on the performance of the battery as an energy source, the performance of e-POWER is highly dependent not only on the battery's performance, such as output and capacity, but also on the power generation performance of the engine as another source of energy.

Fig.6 shows an image of driving power sharing. The battery power of e-POWER accounts for approximately half of that of BEV, and the rest is covered by the engine. The battery capacity required for recovering regenerative energy and extending the EV driving time is 1.5 to 1.8 kWh, which is about a thirtieth of BEVs, although it is larger than that of other hybrid models. When designing the e-POWER system, it was important to properly select the specifications of the drive motor, the battery and engine powers, and the ratio between them to match the vehicle's concept.

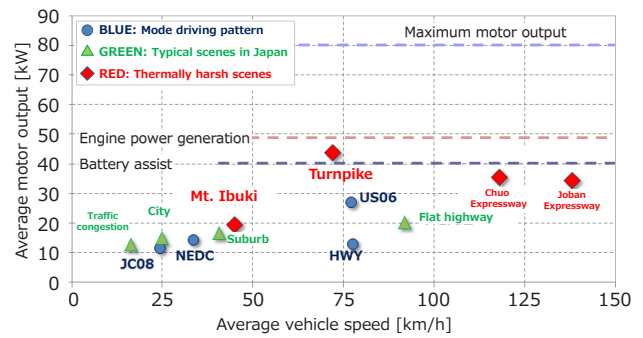


Fig.7 Balance between energy consumption and supply

A vehicle with e-POWER can only run on battery power in the typical driving scenes shown in Fig.7. In a scenario scenes that require a large driving force, powerful acceleration is achieved by adding the power from the generator. Fig.7 shows that the system has been designed to ensure sufficient driving performance even when the energy of the battery depletes and only the power generated by the engine is available. Nissan has optimally designed the power balance between the battery and power-generating engine for the driving power required for the vehicle. This has enabled Nissan to carry over the motor of the LEAF and the gasoline engine of the conventional NOTE.

The performance gets closer to that of the BEV by adopting a larger motor than that of conventional engine-dependent hybrid models and increasing battery power and capacity. However, doing so would increase the system cost and mass and threaten the feasibility of the layout. For this reason, Nissan must not only work on the cost/weight reduction, integration of electric components but also actively solve issues such as improving the efficiency of the integrated layout with the vehicle. In addition, it is important to select appropriate combinations of component specifications according to individual vehicle concepts factoring in the advantages and disadvantages discussed above.

#### 5. Future expansion of e-POWER

The compact car, NOTE, and the mini-van, SERENA, both equipped with the EM57 motor and HR12 engine, satisfy their performance requirements by a change in battery capacities. As this example shows, the components of e-POWER are versatile, and the configuration allows system deployment in a modular manner. The components

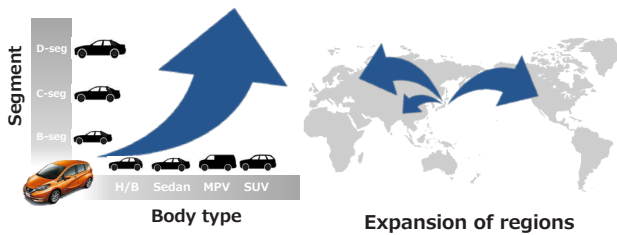


Fig.8 Future expansion of e-POWER

can be used for models in various segments and body types according to the combination of drive performance, power generation capacity, and battery capacity. The combination of the above motor and engine is also adopted in the compact SUV, KICKS.

The good driving performance of e-POWER's 100% motor drive is highly valued in the Japanese market. Due to congestion, the average vehicle speed is low and e-POWER enjoys a good reputation because it is quiet and fuel-efficient enabled by the combination of power generation at the point of best fuel efficiency and motor driving. To increase sales in the global market, Nissan must further improve fuel economy, adapt exhaust regulations and provide solutions for high-speed and high-load driving considering overseas environments. The flexibility of e-POWER has huge potential, allowing system selection and calibration tailored to region-specific usage and customer needs. For future expansion, it is essential to develop electric AWDs that utilize 100% motor-driven e-POWER and add value to e-POWER. The technical direction of the electric AWD system is introduced in Article 5.

## 6. Conclusion

e-POWER is a series hybrid that shares its drive system with the LEAF and uses the existing gasoline engine as its power-generating engine. Accordingly, it can be continuously enhanced along with the evolution of both BEV technology and engine technology.

In the future, expansion of the high-efficiency ranges of electric components and improvement in their efficiency during high-speed driving as well as in the thermal efficiency of the engines is expected. In addition, because e-POWER uses the engine for power generation only and the operation area can be reduced, the engine

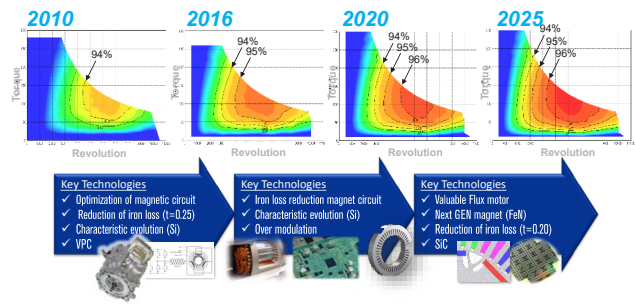


Fig.9 Technological evolution of electric components

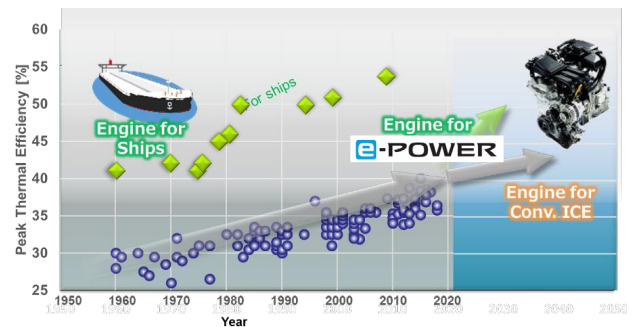


Fig.10 Technological evolution of e-POWER-dedicated engines

has greater potential than conventional engines in terms of efficiency improvement and can be simplified by focusing on the efficiency of fixed-point operation. Nissan will keep striving to develop solutions that only e-POWER can provide thanks to its configuration.

### Explanation of terms

- \*1 BEV: An EV driven by battery power only
- \*2 EV: vehicle driven by electric motor only
- \*3 EV-ness: Quiet, powerful, and smooth driving feeling unique to electric motor drive
- \*4 EV driving: Driving with e-POWER, operated by battery power only with the engine stopped

### References

- 1) 渋谷彰弘ほか: "Development of a brand new hybrid powertrain for compact car market", 25th Aachen Colloquium Automobile and Engine Technology (2016)
- 2) 木村誠ほか: 新型ハイブリッドパワートレイン「e-POWER」、自技会、Vol.72、No.9(2018)

## Author



Naoki Nakada

Special Feature 2 : Constantly advancing e-POWER

### 3. System technology that provides EV-ness to e-POWER

Tomoyuki Hanyu\* Eigo Sakagami\*\* Tomohiro Ito\*\*  
 Isamu Kazama\*\*\* Yuki Kosaka\*\*\*\*

#### 1. Introduction: EV-ness as the goal of e-POWER

Nissan has been developing e-POWER with the basic concept of providing customers comfortable driving utilizing the high-power motor of EV<sup>\*1</sup>. This article discusses the technologies for embodying EV-ness<sup>\*3</sup> in e-POWER equipped with a power-generating engine.

In Nissan, there are three key elements for EV-ness.

- Quietness: Exceptional quietness that conventional engine vehicles cannot offer
- Smoothness: No-shock, smooth feeling at acceleration and deceleration
- High response: Torque characteristic that allows for quick response to driver's operation and accurate link with driver's operation amount

To achieve these performance elements, Nissan developed the following two system control methods for e-POWER: energy management for controlling the power supply from the battery and engine, and power management to achieve torque characteristics unique to the motor drive.

For quietness, energy management is essential to reduce the discomfort the engine start-stop operations performed with operation noise in response to the request for power generation. For smoothness and high response, power management and energy management are essential for calculating the motor torque command in accordance with the driver's request and optimally supplying the power for the calculated torque command from the engine and battery. This article discusses energy management and power management that are the basic control functions of the e-POWER system.

#### 2. Outline of e-POWER's system control

Fig.1 outlines the system control of e-POWER.

This system has been designed based the BEV<sup>\*2</sup> which is also a motor-driven vehicle. Also, the power management for calculating traction is controlled in the same control logic as that for BEV. As for the energy management, the BEV's method has been adopted for the battery. For the combination of the engine and generator, e-POWER's

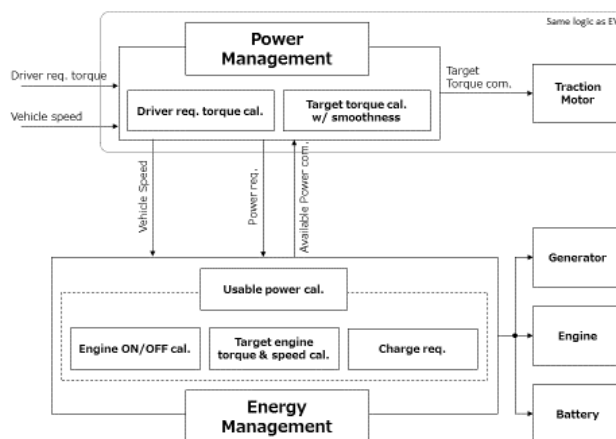


Fig.1 Conceptual diagram of e-POWER's system

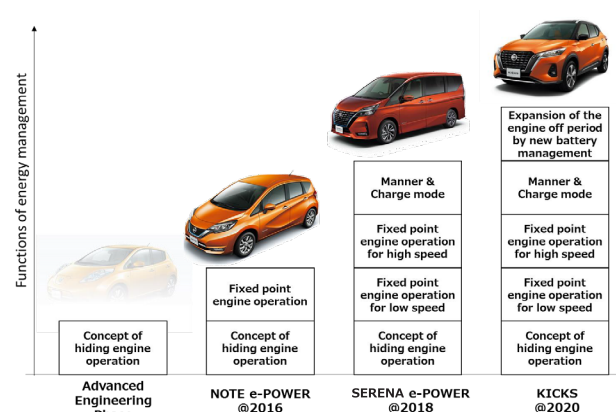


Fig.2 Evolution of energy management

own control block has been added. A charging system is provided for the BEV in place of the engine and generator above.

Because the power management of BEV is used in the traction calculation, the smooth and highly responsive traction characteristics accumulated through the development of the Nissan LEAF are achieved in e-POWER.

\*Powertrain and EV Project Management Department  
 \*\*\*Powertrain and EV Control Technology Department

\*\*Powertrain and EV Performance Engineering Department  
 \*\*\*\*Advanced Vehicle Engineering Department

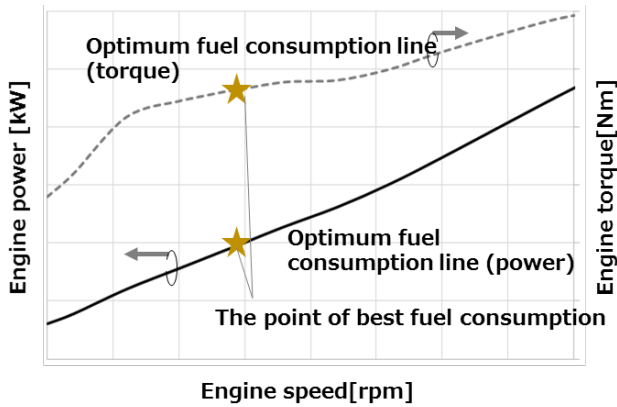


Fig.3 Optimum fuel consumption line and operation

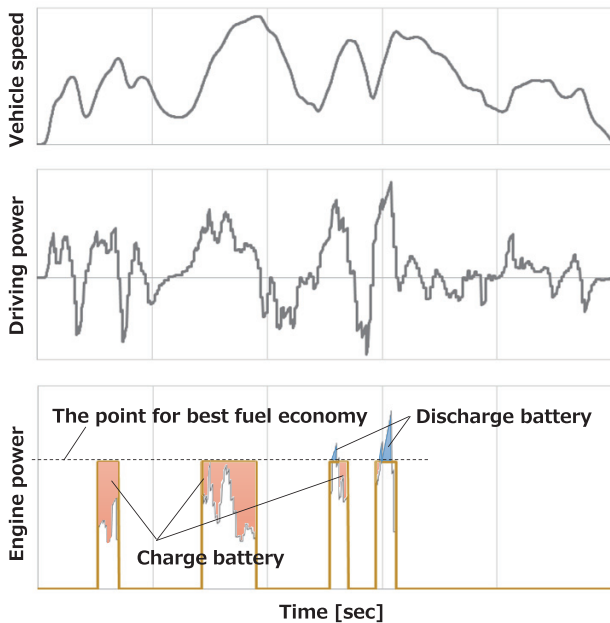


Fig.4 Determination of engine operation points

### 3. Development of energy management: Trade-offs between quietness and power

In e-POWER, the operation of controlling the engine and battery affects various functions and performances, such as fuel economy, acceleration performance, and the heating/cooling function. These functions for controlling engine operation and battery charging/discharging amounts are called energy management. The evolution of e-POWER technology is strongly linked to the improvement of this energy management. Fig.2 shows the evolution.

#### Energy management of NOTE e-POWER

When Nissan started the NOTE e-POWER project, which was scheduled to be launched in 2016, we aimed to develop a system with a greatly reduced battery power and capacity so that the system would satisfy the assembly and cost requirements of a compact car. Two new concepts were developed for achieving high fuel economy based on the concept of masking the engine's

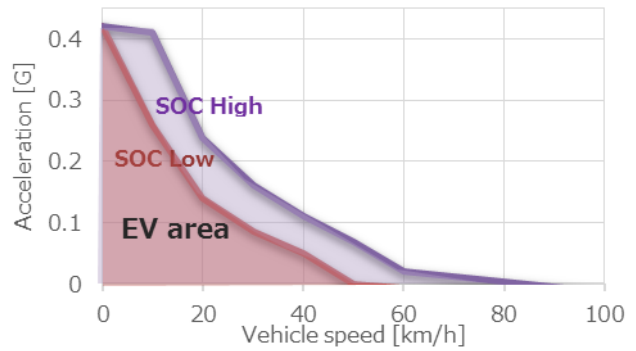


Fig.5 EV range responding to vehicle speed and battery's SOC

operation noise by the vehicle's ambient noise, which had been developed for advanced vehicles.

Concept 1: Improvement of fuel economy

⇒ Increase in the use of the point of best fuel consumption by fixed-point power generation and reduction of the frequency of engine starts

Concept 2: Achievement of EV-ness

⇒ Satisfaction of both response and smooth engine starts

The following describes the above two concepts.

#### Concept 1: Improvement of fuel economy

The basic concept of energy management is to ensure that the power required for driving by generating power is achieved at optimum efficiency. Fig.3 and Fig.4 outline the operation. Fig.3 shows the relationship between the fuel consumption rate characteristics and the power of the engine. The optimum fuel consumption line is a line connecting the operation points per engine power where fuel consumption is the lowest, and the point of best fuel consumption is an operation point where the combustion efficiency is the highest. Because, in case of e-POWER, engine operation points can be flexibly selected regardless of vehicle speed, power can be generated at the operation points on the optimum fuel consumption line according to the required vehicle power. In addition, by compensating for the difference between the required vehicle power and the power generated at the point of best fuel consumption using the battery's charge/discharge power, the use of the point of best fuel consumption is increased to improve fuel economy.

In the low-speed range, the engine's power generation is stopped and EV driving\*4 is performed by battery power only. Thus, when a battery's state of charge (SOC) is high, EV driving can be performed in the higher speed range as well. As the engine operation conditions are not constrained by vehicle speed, e-POWER enables EV driving at higher vehicle speeds.

By adopting this control, e-POWER allows for driving at the point of best fuel consumption more frequently than other systems, as per the distribution of engine operation points shown in Fig.5 in the previous article.

#### Concept 2: Achievement of EV-ness

The battery power of e-POWER is higher than that of conventional hybrid models, which is intended to provide

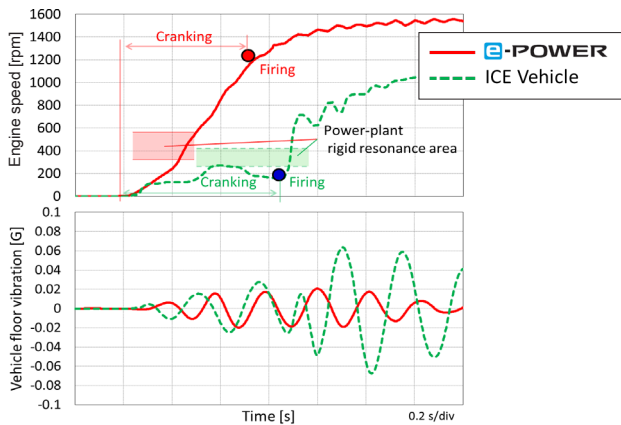


Fig.6 Relationship between engine ignition timing and floor vibration

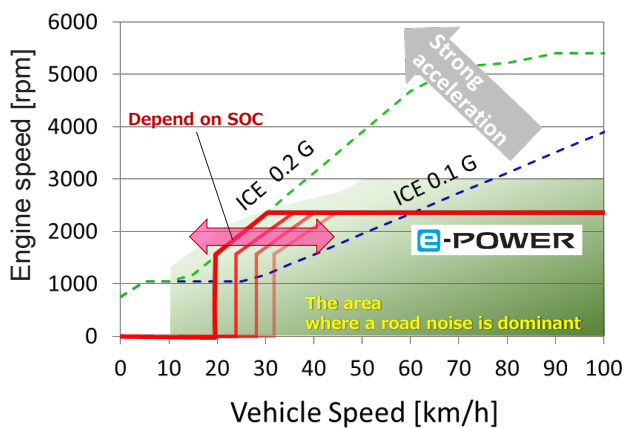


Fig.7 Conceptual diagram of road noise in NOTE e-POWER with respect to engine revolution

customers with the EV's responsive acceleration and quietness as if the engine is not operating. As shown in Fig.5, EV driving is performed during low-speed driving and continues up to high vehicle speeds with the engine stopped.

Because a high-power generator is used as an engine starter, the resonance vibration of the power train is quickly dissipated, as shown in Fig.6., which suppresses the vibration at the start of the engine.

Fig.7 shows the conceptual diagram of the engine revolution control of the NOTE e-POWER. Nissan achieved quietness by disabling the engine in the low-speed range to mask the noise by the ambient noise as far as possible. When rapid acceleration is required, Nissan achieved smoothness by increasing the engine revolutions to securely generate the power required for driving. Through these measures, Nissan achieved EV-ness with e-POWER.

### Energy management of SERENA

For the SERENA, Nissan aimed for a control that satisfies both the quietness in the low-speed range and guarantees energy supply in the high-speed range. This aimed to enhance the image of the large mini-van, wherein family members and friends can enjoy traveling time.

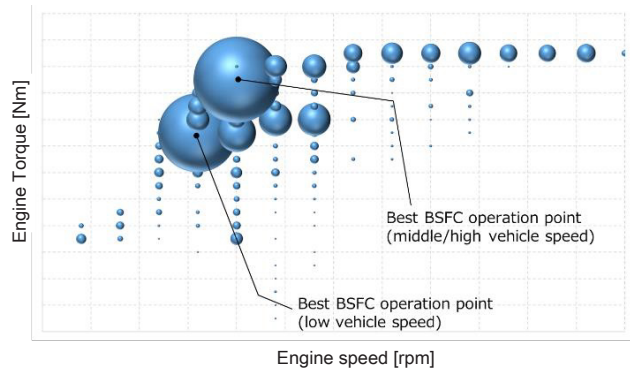


Fig.8 Operation ratios of SERENA's engine operation points

Nissan improved the engine, expanded the optimum fuel consumption range, and provided a point of optimum fuel consumption rate for low vehicle speeds and middle-to-high vehicle speeds. When driving in cities at low vehicle speeds and low loads, quietness was prioritized and power was generated at the point of best fuel consumption on the low revolution side. Because the revolution is low, the output at the point of best fuel consumption decreases, and the power generation for recovering the battery SOC takes longer. However, Nissan has provided measures against vehicle noise and suppressed engine operation noise to a comfortable level. When driving on suburban arterial roads, higher power is generated at the point of best fuel consumption on the high revolution side to expedite SOC recovery so as to quickly respond to a request for high acceleration.

In addition, the SERENA is equipped with a battery with a capacity higher than that of the NOTE and by charging and discharging the battery more actively, engine operation points are controlled at the point of best fuel consumption, although the overall mass of the SERENA is greater.

Fig.8 shows the distribution of engine operation points used when a vehicle is driven in fuel economy mode in Japan. Nissan has precisely controlled the engine operation points by improving the energy management control derived from the development of the NOTE to satisfy both quietness and fuel economy of the mini-van.

Nissan provided the SERENA e-POWER with new functions namely, charge mode and manner mode. Because the engine and drivetrain are not mechanically connected with each other in e-POWER, power can be flexibly generated regardless of the vehicle speed. Utilizing this characteristic, Nissan has developed a function that allows for forcible battery charging regardless of timing and driving mode (charge mode) and a function that allows for quiet, battery-powered driving with the engine stopped (manner mode).

The charge mode can maintain the battery's SOC at a high level, so that it is useful on mountain roads where acceleration force is continuously required. When the driver requires less acceleration, surplus power is actively charged to the battery to maintain the SOC at a high level to provide for an acceleration request in the future. In addition, by using this mode until just before selecting the manner mode, EV-like quietness can also be enjoyed

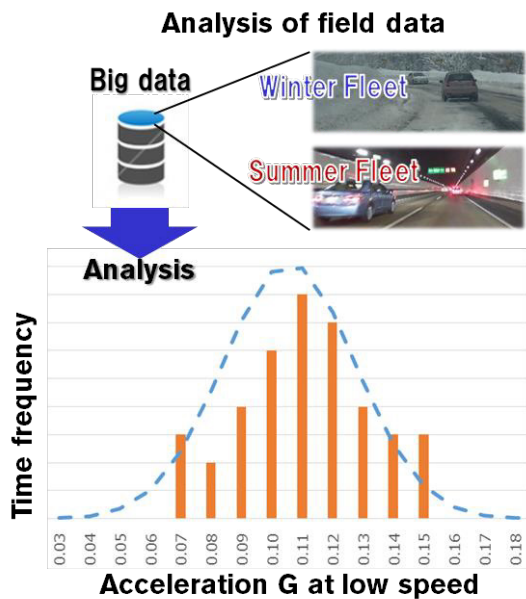


Fig.9 Distribution of accelerations in the Japanese market

for a longer time.

The manner mode is mainly intended to actively stop the engine. Other HEV models also have this type of engine stopping mode, but because e-POWER uses a high-capacity battery, the effect of this mode is large. Combined with the charge mode above, an unparalleled driving experience is provided with the engine stopped.

#### Energy management of KICKS

The energy management of the NOTE and SERENA is based on the intention for acceleration and focuses on the relationship between acceleration and engine start. To enhance EV-ness, Nissan has modified this concept for the KICKS and developed a control that performs SOC management while expanding the range when the engine is stopped.

Analyzing from actual driving data, Nissan assumed that the amount of power that the engine needed to generate to recover SOC was small because only small amounts of energy were required in scenarios where relatively brief acceleration would do. These included turning right at intersections and standing start when a traffic light changes. Accordingly, Nissan has maintained EV mode up to the lowest possible SOC to offer the quietness of EV driving to the driver and has set this control as the concept of energy management.

The criteria for the above control are the upper-limit of acceleration for maintaining EV driving and the setting method of permissible SOC. Unless these criteria are optimally balanced, adverse effects would occur, such as lowering of battery assist power during acceleration and continued power generation when the engine has to be stopped.

To optimize the permissible EV range, Nissan collected actual driving data for the NOTE and SERENA over hundreds of thousands of kilometers. The data was analyzed to investigate the distribution of driver acceleration patterns within the Japanese market. Fig.9

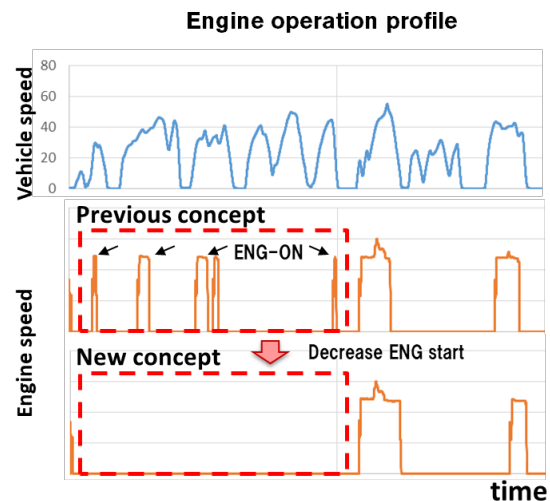


Fig.10 Comparison between new and previous engine operation concepts

shows the distribution of accelerations in the low speed range of approximately 30 km/h or less in the Japanese market. Fig.9 shows that generally, engine start can be avoided during normal driving by maintaining EV driving with an acceleration of approximately 0.15 G. Nissan also obtained data such as the consumption energy per acceleration-deceleration for each required vehicle speed range, which enabled us to optimize the engine start point.

By adopting the energy management of a new concept based on market data analyses, Nissan shifted the supply timing of the energy generated by the engine to a higher-vehicle speed.

Shifting the energy supply timing to a higher vehicle speed has the following two effects. The first is the reduction in the frequency of starts at low vehicle speed where ambient noise is low (reduction of the frequency of engine “start and stop within a short time period”). The second is the reduction of the frequency of engine start/stop by generating power all at once at a high vehicle speed to make effective use of the power generation system.

Fig.10 shows the engine operation modes of the new and old energy management concepts. Nissan has reduced the frequency of engine starts in the low-speed range, particularly the frequency of engine start and stop within a short time period. In the range of 30 km/h or less, Nissan reduced the engine starts to about 70% of that of the old energy management. This control has significantly contributed to the improvement of quietness, which is one of the major features of e-POWER.

#### 4. Development of power management: Satisfaction of both smoothness and response

The traction control derived through the development of the Nissan LEAF is well accepted in the market, and the power management of e-POWER has been derived from that control. However, because e-POWER receives power from the battery and engine unlike an EV, where

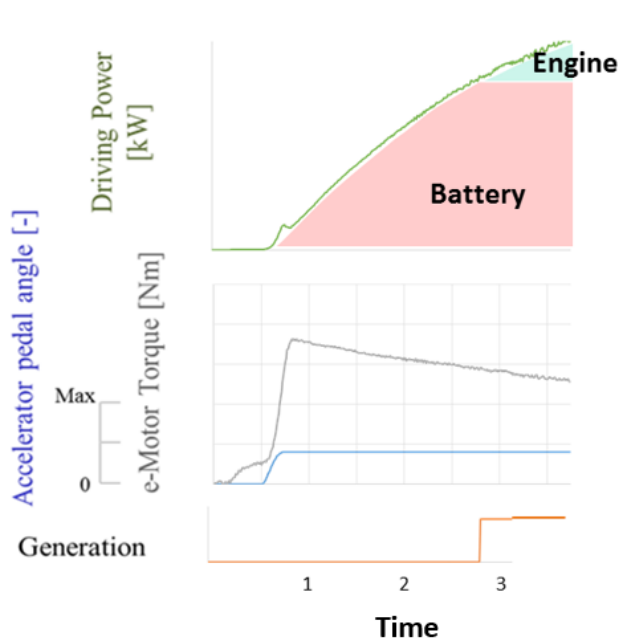


Fig.11 Power distribution when SOC is high

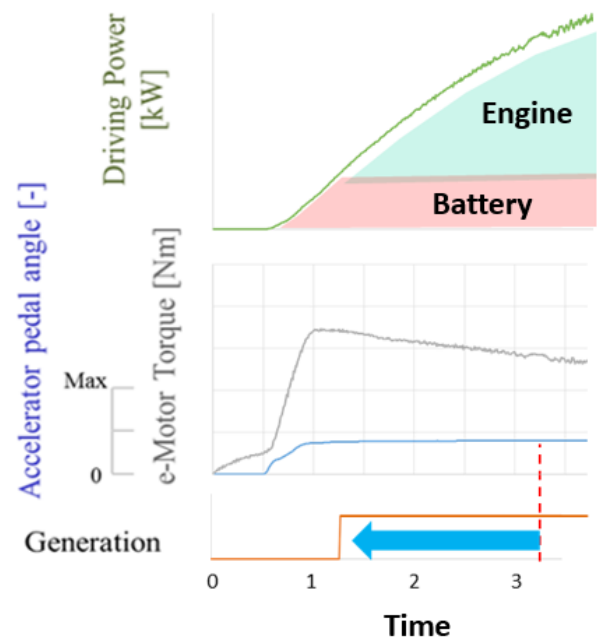


Fig.12 Power distribution when SOC is low

power is supplied from the battery only, the delay of power from the engine affects the acceleration performance.

In this section, we discuss the measures against such issues and the high response and smoothness that provides EV-ness to e-POWER.

#### 4.1 Achievement of acceleration performance independent from SOC

The point of improvement for the power management of e-POWER, which is driven by the power from the engine, unlike the BEV, is the control that does not create the feeling of acceleration drop even when battery power is lowered.

Fig.11 shows the condition at the engine start during acceleration when the battery has sufficient power with a high SOC. EV driving is maintained while suppressing the engine's power generation as long as possible. In contrast, Fig.12 shows the condition when the SOC is low and sufficient power cannot be secured just from the battery. The power generation of the engine is started early so as not to create a feeling of acceleration drop. Through such control, the same acceleration feel is achieved regardless of the system condition.

#### 4.2 Satisfaction of both acceleration feel and fuel economy

As discussed above, e-POWER satisfies the power required by the vehicle by jointly using the engine when the need for acceleration is high.

e-POWER can flexibly control engine revolution, although the increase in the engine's operation noise goes against the quietness of EV-ness. For e-POWER, we have varied engine revolutions so that acceleration feel can be created according to the driver's intended acceleration level suggested by the accelerator opening.

Fig 13 shows the engine revolution behavior at each accelerator opening position. Because fuel economy is also important, the opening position, if small, is controlled to maintain the point of best fuel consumption so as to satisfy both the required fuel economy and quietness. The increased rate of revolution and target revolution enhances the acceleration feel according to the level of the intended acceleration, and the acceleration feel is brought about by engine sound while securing the power required for driving.

### 5. Pursuing further EV-ness

The energy management and power management discussed above have been adopted in the new NOTE after further improvement.

Further evolution of e-POWER deepens the EV-ness.

To improve the quietness, Nissan has been exploring the possibility of extending the engine stop time. In the future, Nissan may be able to combine it with other systems, such as ANC (Active Noise Canceller) that actively deadens the noise. Because the e-POWER's unique power generation control at the point of best fuel consumption can be easily used as the target of the quiet zone of ANC, Nissan assumes that the ANC will be compatible with e-POWER.

To improve the smoothness, Nissan will further optimize the balance between the output characteristics of the engine and battery. When a high-power engine is installed, in particular, the power generated by the engine takes up a large share of driving power, and the output characteristic of the engine affects the smooth drive characteristic. As for engines, Nissan will continuously improve both specific fuel consumption and output characteristics.

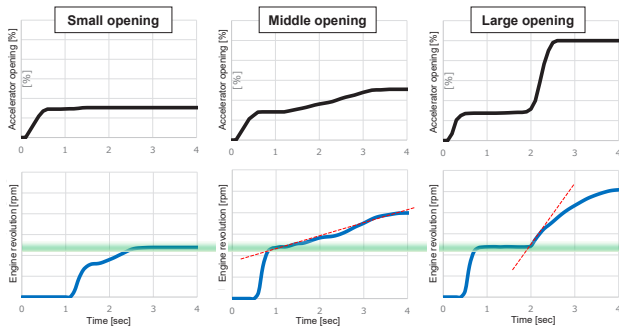


Fig.12 Power distribution when SOC is low

To improve the responsiveness to the driver's intended acceleration as with the BEV, Nissan will suppress shock and vibration and aim to actively control the vehicle posture.

### Explanation of terms

- \*1 EV: Vehicle driven by electric motor only
- \*2 BEV: An EV driven by battery power only
- \*3 EV-ness: Quiet, powerful, and smooth driving feeling unique to electric motor drive
- \*4 EV driving: Driving with e-POWER, operated by battery power only with the engine stopped

## Authors



Tomoyuki Hanyu



Eigo Sakagami



Tomohiro Ito



Isamu Kazama



Yuki Kosaka



## 4. Fuel saving technology that satisfies e-POWER's driving performance

Hiroshi Kuriki\* Shuichi Orita\* Ryuzou Noguchi\*

### 1. Introduction

Nissan developed the electric power train system, e-POWER, which satisfies both fuel economy and the pleasure of a 100% motor drive. In 2016, the system was installed in the compact car, NOTE, for the first time. Since then, additional vehicle models have been added including the mini-van, SERENA in 2018, the SUV, KICKS in 2020, and the new NOTE in 2021.

This article introduces the fuel saving technologies that utilize the characteristics of "e-POWER system" that are inseparable from the electric vehicles in Nissan's power train strategy.

### 2. e-POWER system and operation mode

Fig.1 shows the system configuration of the e-Power. The biggest characteristic is that the power generation system and drivetrain are completely separated from each other. Thus, the operation points of the engine and generator can be flexibly determined regardless of the mode of the drivetrain. Nissan has also developed a new driving mode "e-POWER Drive," which fully utilizes the advantages of 100% motor drive. As shown in Fig.2, in the market, 90% or more of the deceleration is covered by the accelerator pedal to recover deceleration regenerative energy and enable the driver to control the vehicle with only the accelerator pedal, which achieves the feeling of "Fun to drive." <sup>\*(1)</sup>

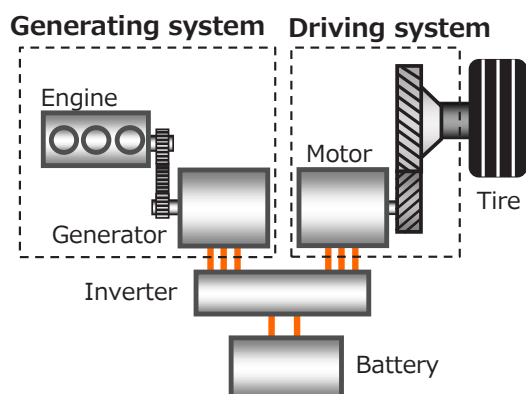


Fig.1 Diagram of system configuration

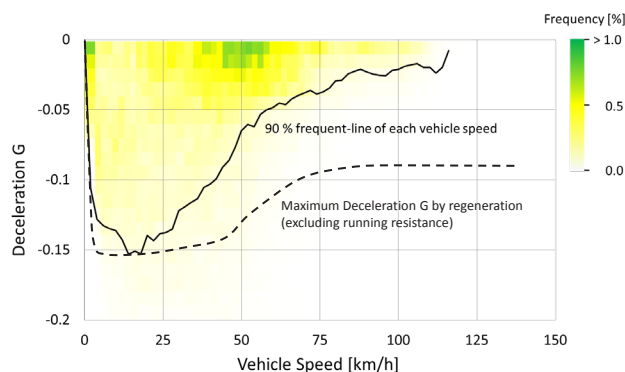


Fig.2 Deceleration frequency in the market and deceleration characteristics of e-POWER Drive

The system's operation is composed of the following six modes: Fig.3 illustrates each mode. Modes (1) to (5) are for basic operation and mode (6) is optional.

- (1) The engine is stopped, and traction is achieved just by the power of the lithium battery.
- (2) The vehicle is driven by the power generated by the engine, and surplus power is used to charge the lithium battery.
- (3) The vehicle is accelerated using the power generated by both the engine and the lithium battery.
- (4) The vehicle is driven by the power generated by the engine.
- (5) The engine is stopped, and the coast deceleration regenerative energy is recovered to the lithium-ion battery.
- (6) The engine is rotated by the generator used as motor to discharge power from the lithium-ion battery (for generating brake M/V negative pressure, performing OBD, and preventing battery overcharge).

### 3. Elements for fuel economy improvement commonly required for e-POWER

e-POWER converts the mechanical power of the engine into electric power by means of a generator and generates traction with the motor using electric power. Because of this mechanism, loss occurs during the conversion between mechanical power and electric power. To improve fuel economy, it is essential to devise measures

\*Powertrain and EV Performance Engineering Department

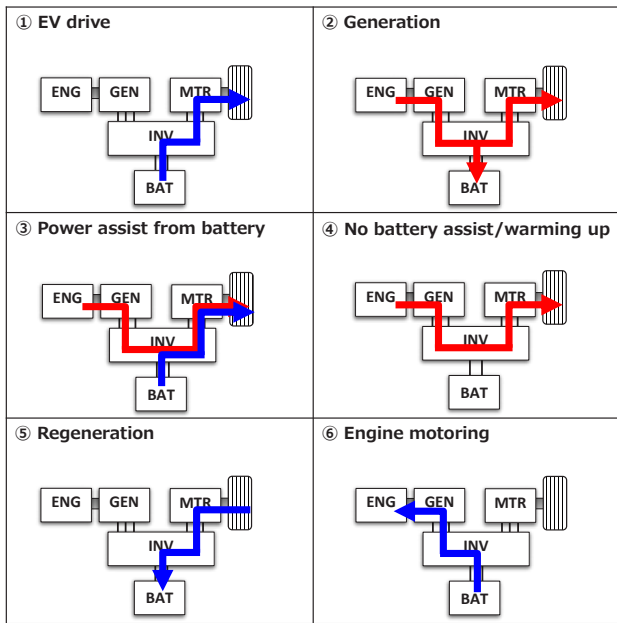


Fig.3 e-Power System operation modes

for efficiently generating power by the engine and improving the efficiency of the entire system at the same time.

Thus, Nissan has thoroughly improved the power generation efficiency of the engine by utilizing the characteristics of e-POWER, based on the operations at set operation points, where the efficiency of the power generating system is high (hereinafter called fixed-point operation (mode (2) in Fig.3).

### 3-1. Fuel economy improvement by fixed-best efficient point operation

Fig.4 shows the line  $\alpha$  connecting the operation points per revolution, where efficiencies reach the highest. Because, in conventional hybrid systems, engine revolution is bound by vehicle speed and required traction, the systems are controlled by tracing this line, and thus, fewer operation points need to be used in the low revolution range.

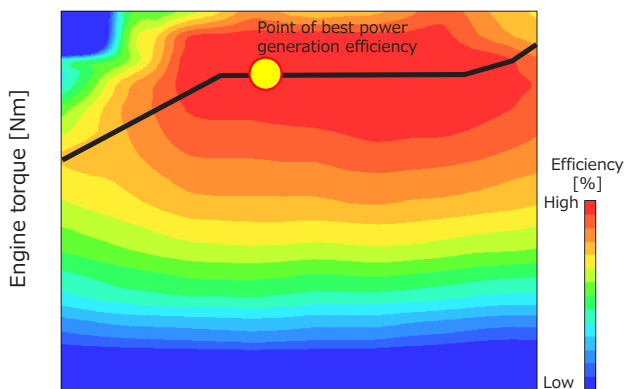


Fig.4 Efficiency characteristic of power generation system

Conversely, because the drivetrain and engine are completely independent of each other in e-POWER, operation is controlled regardless of the mode of the drivetrain. In this way, the most power

generation-efficient operation point is selected within the permissible ranges of various requirements, such as mechanical power, drivability, noise and vibration, emission, heat, air heating, brake negative pressure, component protection, and diagnosis. During the control, the optimum amount of power for motor output is adjusted by charging and discharging to/from the lithium battery, as shown in Fig.5 (modes (2) and (3) in Fig.3)<sup>(4)</sup>.

When driving in cities or similar scenarios where the

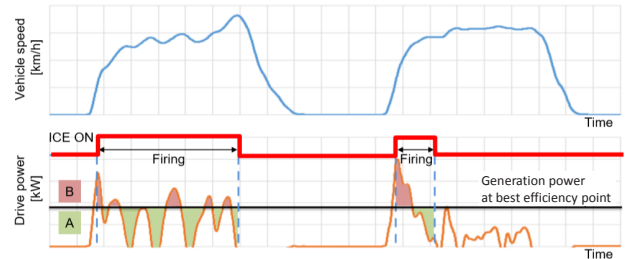


Fig.5 Concept of energy management

required traction is small, the engine is operated at fixed points and surplus power charges the lithium battery (mode (2) in Fig.3). Then, the stored electric energy is used to start the EV drive (mode (1) in Fig.3).

Fig.6 shows the result of fuel economy improvement achieved by switching fixed-point operation and EV drive. The figure shows that the fuel economy has improved to approximately twice that of the operation mode with the engine always on (mode (4) in Fig.3).

In scenarios where the required traction is large, such as when driving at a high speed or accelerating for passing, the electric energy in the lithium-ion battery that has been stored from surplus power is used to supplement the necessary power for acceleration. This maintains fixed-point operation as much as possible and minimizes fuel consumption (mode (3) in Fig.3).

### 3-2. Improvement of power generation system

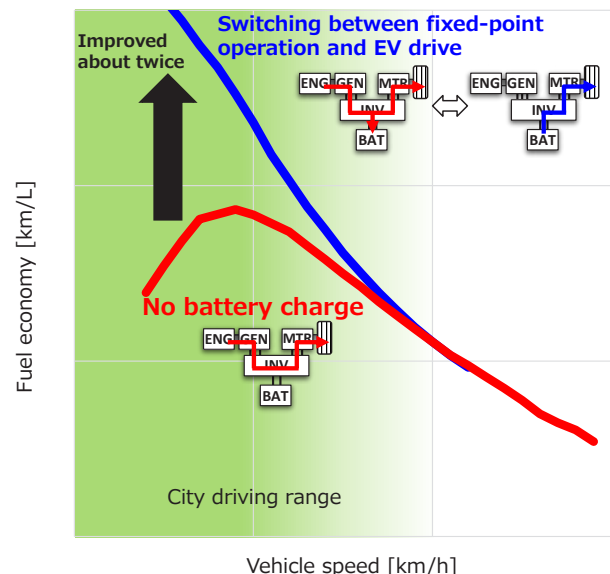
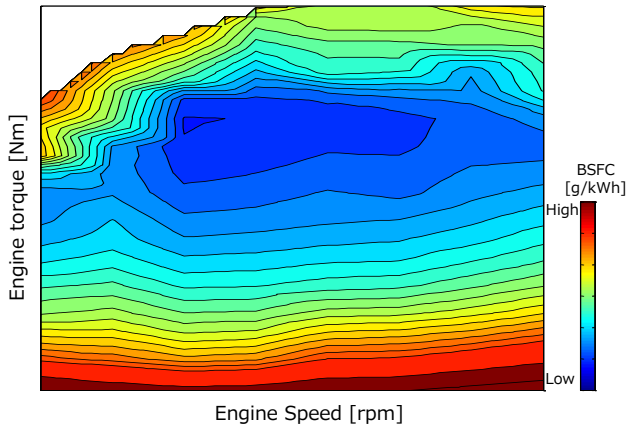


Fig.6 Result of fuel economy improvement achieved by cruising at a constant speed

**(engine + generator)**

Fig.7 shows the characteristics of the specific fuel consumption of the engine. Nissan has developed an engine for e-POWER, based on the 3-cylinder 1.2-L gasoline engine, HR12DE. By adopting cooled exhaust gas recirculation (EGR) and electrified accessories such as water pumps and air compressors, Nissan reduced friction to improve the optimum fuel consumption rate.<sup>\*(2)</sup>

Fig.8 shows the efficiency characteristics of the



**Fig.7 Specific fuel consumption of engine**

generator (overall efficiency including the inverter). The generator has also been tailored to e-POWER to cover the maximum torque and output of the engine.<sup>\*(3)</sup>

Because the high-efficiency ranges of the engine and

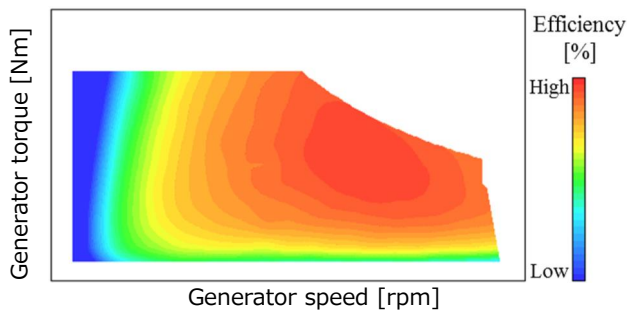


**Fig.8 Efficiency characteristics of generator (including inverter)**

the generator are different from each other, Nissan set 0.6 as the gear ratio of the speed-increasing gear. This is provided in-between the engine and generator to bring power generation efficiency to the maximum within the range of the maximum allowable revolutions of the engine and generator.

**3-3. Improvement of battery system**

Improvement in fuel economy is also attributable to the evolution of lithium battery technology and the following parameters:

- By reducing the internal resistance of the lithium-ion battery, the losses at charging and discharging power were significantly reduced.
- By reducing size and weight, the high-capacity

lithium battery can fit in a compact car. This significantly reduced the frequency of engine starts and enabled longer EV driving with the quietness equivalent to BEV.

- By enhancing the cooling performance, high-power and long charging/discharging became available.

Thus, Nissan have achieved top-level fuel economy and quietness for this class of vehicle.

**4. Engine operation control of improved e-POWER**

As discussed above, e-POWER basically reduces fuel consumption by fixed-point operation during engine operation. Nissan has provided the three measures described below to improve engine operation control and has adopted them in KICKS and the new NOTE.

**4-1. Further reduction of the frequency of engine start**

Nissan focused on the fuel consumed when the engine is started and then reaches the point of fixed-point operation where the efficiency of the power generation system reaches the maximum as well as on the electric energy consumed at the engine start. Nissan reviewed the conditions of engine start based on user data and significantly reduced the frequency of engine starts so that the EV drive is maintained when low-speed driving and short acceleration are expected. Although the fuel economy degrades immediately after the engine is started until it reaches the point of fixed-point operation, the process is completed in an extremely short time. However, because this transition to the point of fixed-point operation occurs every time the engine is started, reducing the frequency of engine start is effective for fuel reduction.

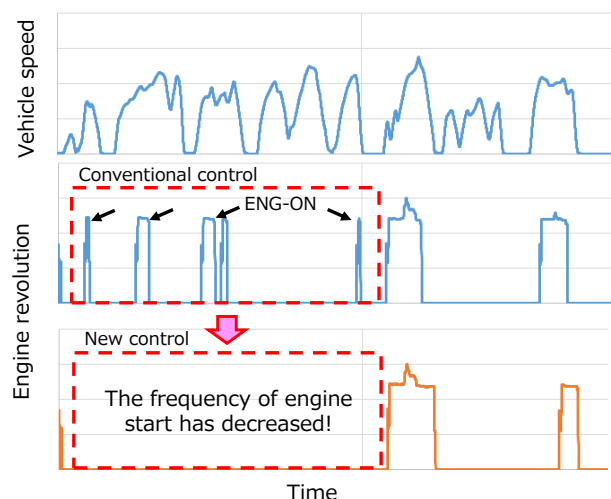


**Fig.9 Reduction of the frequency of engine start**

#### 4-2. Addition of points of fixed-point operation during engine warm-up

For cold starting, Nissan used to generate waste heat to facilitate warm-up, using the operation range where the engine's thermal efficiency was poor. Instead, Nissan has now adopted the point of best power generation efficiency, where a heat source is not required.

In addition, by focusing on the fact that the point of best power generation efficiency varies before and after engine warm-up, Nissan set the points of fixed-point operation for warm-up such that the points of fixed-point operation can be switched according to the warm-up status. As a result, the actual fuel economy at short-distance driving has improved.

#### 4-3. Change of engine operation points for heater operation in winter

e-POWER uses the waste heat from the power-generating engine as a heat source for heating. It is an important issue to efficiently manage the air conditioning environment in the vehicle compartment to maintain comfort.

Conventionally, power generation efficiency is prioritized as a fixed-point operation after engine warm-up, even when the heater was used in winter. Because the engine needed to be continuously powered during heating, when the storage capacity of the lithium-ion battery was exceeded, forced discharge was performed with the engine motoring (operation mode (6) in Fig.3). Accordingly, Nissan could not achieve an optimum fuel economy.

This time however, Nissan controlled the operation point of power generation according to the battery level and heating requirement and secured a minimal amount of heat, so that both heating performance and fuel economy are satisfied.

### 5. Approach for zero emission

Nissan has achieved the top fuel economy in the vehicle class by sharing the evolved technologies of the ICE and EV and providing an energy management system unique to e-POWER. For the new NOTE, Nissan has improved the efficiency of the e-POWER system by improving the thermal efficiency of the engine and adopting a technology that improves the transmission efficiency of the electric components shared with EVs.

In the future, Nissan will strive for further improvement of the e-POWER engine dedicated to power generation for higher thermal efficiency, downsizing and weight reduction, loss reduction, efficient energy generation for heating, and advanced control corresponding to the component evolution. We will also maximize the efficiency of the system through the next-generation of energy management in conjunction with navigation systems and IT/ITS.

Through the innovation of these fundamental technologies, Nissan aims to drastically reduce CO<sub>2</sub> emissions and bring the amount of emission gas to a near-zero level, which will enable us to contribute to global environmental protection. Nissan will continue development so that we can provide more customers with the e-POWER system that delivers pleasant driving with the unique 100% motor drive.

#### References

- 1) 有吉伴弘ほか: 新型電動パワートレイン「e-POWER」とエンジン回転数プロフィールの設計、自動車技術会シンポジウム(2017)
- 2) e-POWER用 新型3気筒HR12DEエンジンの開発、日産技報、No.80(2017)
- 3) 岡野洋二ほか: 小型車向け新型電動パワートレイン用モータおよび発電機の開発、自動車技術会学術講演会予稿集(2017)
- 4) 木村誠ほか: 新型ハイブリッドパワートレイン「e-POWER」、自技会、Vol.72、No.9(2018)

#### Authors



Hiroshi Kuriki



Shuichi Orita



Ryuzou Noguchi

## 5. Noise and vibration technologies of new NOTE supporting the EV-ness of e-POWER

Tetsuya Kawakami\* Hiroataka Kaneko\*\* Yusuke Ienaka\* Kazuhiko Arai\*  
Ryuugo Chiba\* Takanobu Sawada\*\* Toru Nakada\*\*\* Masaya Gotou\*\*\*\*

### 1. Introduction

e-POWER uses common drive motor with battery-driven electric vehicles (hereinafter called BEV<sup>\*1</sup>); hence, it delivers a smooth acceleration feel similar to the BEV and the quietness equivalent to that of high-grade vehicles, particularly from standing start to mid-speed driving, which is driven by the motor only with the engine stopped (hereinafter called EV driving<sup>\*3</sup>).

The following are important factors in individual driving scenarios when pursuing quietness with this system.

In an EV driving scenario, high-frequency noises caused by the motor and speed reducer are dominant. In addition to the reduction of the motor's own exciting force, the radiative characteristics of e-POWER must also be suppressed factoring in the location where the generator and engine are integrated. The BEV does not have this problem.

It is also important to devise measures to muffle the engine operation noise during power generation. Nissan assumed noise and vibration issues would arise in the following operation scenarios and took measures accordingly.

(1) During EV driving: Reduction of the noises of the motor and speed reducer gears

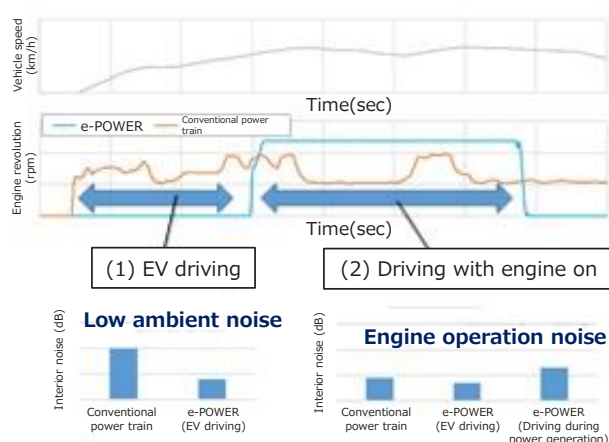


Fig.1 Driving scenarios that hinder the quietness of e-POWER

(2) During driving with the engine on: Reduction of engine noise, rattle noise, and other noises due to the speed increaser gears, and considered quietness at engine start

This article describes the design concept of the e-POWER system considering the key noise and vibration phenomena in the important scenarios above and the technical solutions that have been adopted to the new NOTE.

### 2. Improvement of quietness during EV driving

#### 2.1 Issues during EV driving

During EV driving, the high-frequency noises of the motor and gears that have been masked by engine noise manifest themselves as unpleasant noises. For this reason, a high quietness level equal to that of BEV vehicles is required.

#### 2.2 Motor noise

Motor noise is caused by the electromagnetic force between the stator and rotor. The components of this vibromotive force can be divided into two directions, the circumferential and radial directions of the motor. Their contributions vary according to the frequency range (Fig.2).

While reducing the electromagnetic force over a wide range, Nissan has optically designed a magnetic circuit that satisfies both efficiency and output at a high level. This followed simulation results of hundreds and thousands of design parameter combinations (Fig.3).

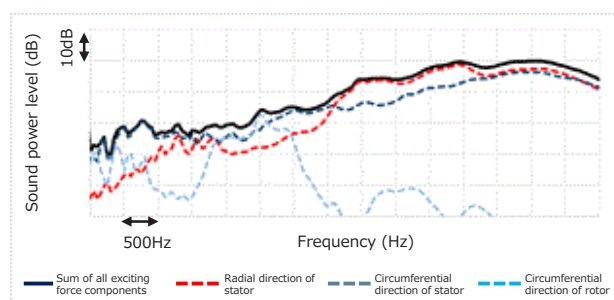
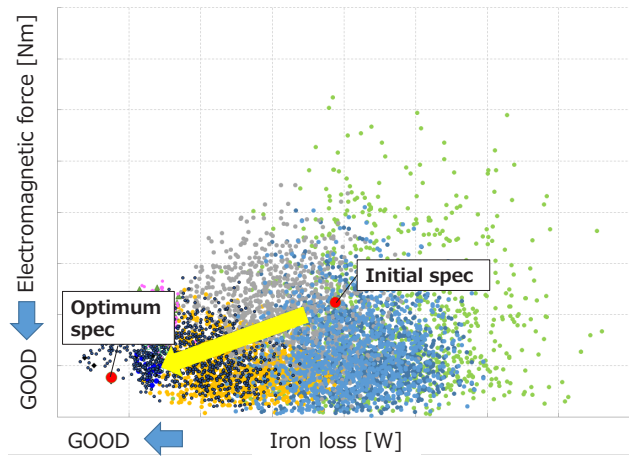


Fig.2 Analysis of the contribution of exciting forces by direction with respect to motor noise levels

\*Powertrain and EV Performance Engineering Department  
\*\*\*Powertrain and EV Electrical Technology Department

\*\*Powertrain and EV Advanced Technology Department  
\*\*\*\*Customer Performance and Vehicle Test Engineering Department No.1

By focusing on reducing the level of the electromagnetic force in the vehicle low-speed range, we have adopted a magnetic circuit for the new NOTE e-POWER that efficiently reduces the components of the vibromotive force in the circumferential direction as well as iron loss.



**Fig.3 Optimum designing of magnetic circuit that satisfies both electromagnetic force and efficiency**

Besides the reduction of the exciting force discussed above, Nissan also carried out further measures to efficiently reduce motor noise. For the structural components of the motor unit, the main cause of motor noise is radiation. Nissan conducted simulations to analyze the major contributors to the radiation noise and found that the inverter was the main contributor. Accordingly, we focused on improving the rigidity of the inverter case (Fig.4).

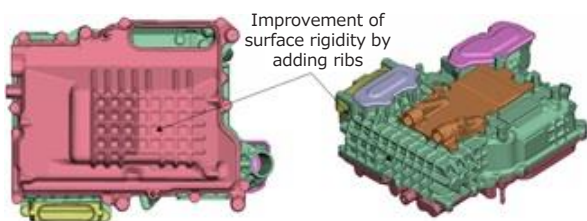


**Fig.4 Measures to improve the rigidity of the inverter case**

### 2.3 Noise of speed reducer gears

To ensure the quietness of the gears at a high speed, Nissan improved the noise level of the speed reducer gears by increasing the face width to enhance the contact ratio and provided additional honing to increase tooth precision.

## 3. Improvement of quietness during engine operation

### 3.1 Noise reduction during engine operation

#### 3.1.1 Guidelines when designing for low noise during engine operation

To efficiently generate power in the e-POWER system, the engine is operated at high-load and low revolutions more often than the engines of conventional vehicles

aiming at higher engine efficiency. Thus, Nissan designed the engine according to the following guidelines.

- (1) Efficient reduction of the vibration level during engine operation in the vibration propagation paths to the vehicle compartment
- (2) Muffling of engine noise by operating the engine in the range where tire noise and other ambient noises are higher

#### 3.1.2 Measures provided for vibration propagation paths

The engine noise propagation paths to the vehicle compartment can be largely divided into two: paths that propagate vibration via parts such as the engine mount and paths that propagate noise by air from the engine compartment.

For the vibration propagation paths, Nissan improved the vibration level by installing the inverter directly above the motor unit to improve packaging efficiency and by adding the minimum necessary parts to significantly improve the rigidity of the entire power train.

Specifically, Nissan fixed the inverter and drive motor with bolts and added a gusset between the inverter and power generation motor to significantly improve the rigidity of the entire motor unit system (Fig.5). For the mount bracket on the left side of the vehicle, Nissan fixed the bracket and the above-mentioned inverter with a small stay by bringing the bolted portions to the top of the motor rear cover. With this improvement, we have greatly reduced the vibration level while controlling the weight increase of the bracket (Fig.6).

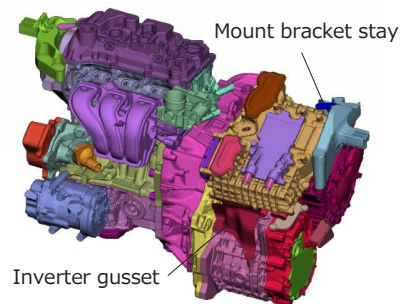


**Fig.5 Major changes in the structural system of new NOTE e-POWER's motor unit**

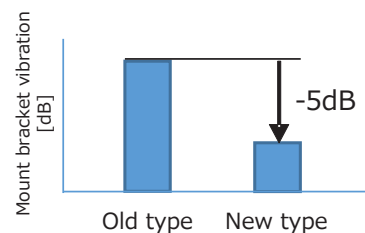


**Fig.6 Vibration reduction by improving the rigidity of inverter case**

### 3.1.3 Conditional control of engine start timing (road surface state discrimination)

Nissan has recently developed a function that controls engine operation by judging the increase in road noise when driving on a rough road surface. This function maintains a sufficient battery level by generating power in scenarios where the engine operation does not bother the driver. Thereby, the driver can enjoy quiet driving, unique to EV driving, more at standing start or when driving on a smooth road surface.

The old NOTE e-POWER was designed to operate the engine at high vehicle speeds, assuming that road noise increased in proportion to vehicle speed. However, in cities where vehicles repeatedly start and stop, scenarios where engine operation does not bother the driver are limited. For this reason, Nissan needed to control the scenarios where the engine operated during low-speed driving.

It is known that the roughness of a road surface affects the level of road noise more than vehicle speed. It is also known that in the driving environment in Japan, many road surfaces cause higher noise levels than the engines. Therefore, Nissan has developed an algorithm for estimating road noise based on the variation of tire revolutions. The algorithm helps control engine operation, which greatly contributes to the improvement of quietness.

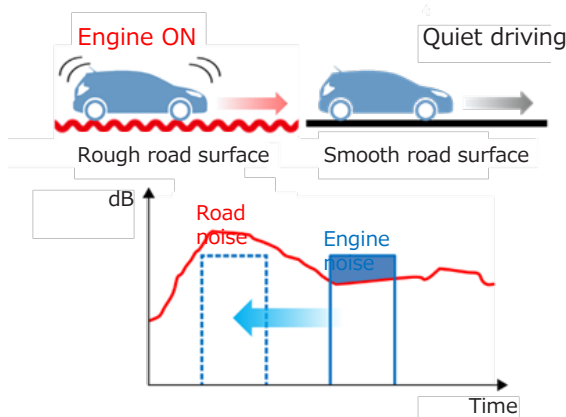


Fig.7 Outline of engine start control based on estimated road noise

## 3.2 Reduction of the rattle noise of speed increaser gears

### 3.2.1 Reduction of the rattle noise of the new NOTE's speed increaser gears

By reducing gear rattle noise with a new, low-rigid torsional damper, the quietness of the new NOTE e-POWER improved from that of the old NOTE e-POWER (Fig.8).

### 3.2.2 Rattle noise of speed increaser gears

The power generation system of e-POWER is composed of an engine, a generator, and a speed increaser. Each component is fixed with a spline, and a gap or backlash is present at each joint and gear meshing portion. In the gap or backlash, the teeth of the spline and gear collide with each other owing to the fluctuation of engine torque

in the low-engine torque range, which generates noise (Fig.9).

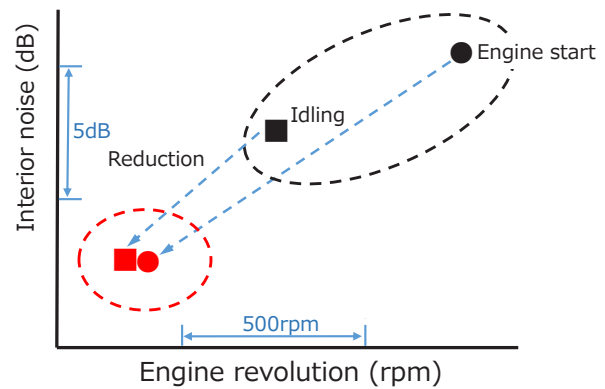


Fig.8 Quietness improvement by revolution reduction

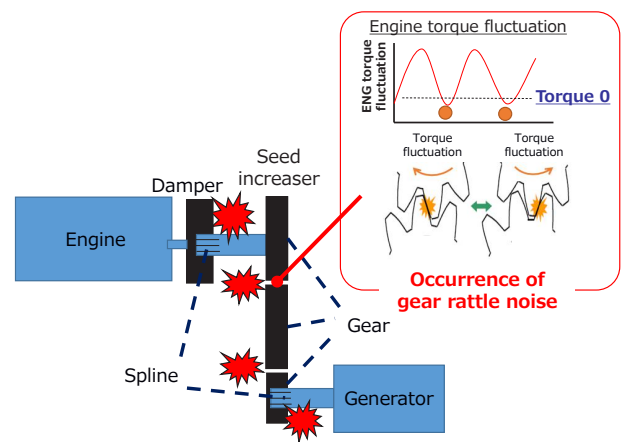


Fig.9 Occurrence mechanism of the rattle noise of speed increaser gears

### 3.2.3 Application of new, low-rigid torsional spring damper

The torsional spring rigidity of the old torsional damper installed between the engine and speed reducer had the characteristics of a single-stage type. However, as a measure to prevent the gear rattle noise discussed above, Nissan has developed a new damper with the characteristics of a double-stage type by reducing the torsional rigidity in the low-engine torque range that causes gear rattle noise (Fig.10). This development has enabled Nissan to significantly dampen the engine torque fluctuation input to the joints and gears and control gear rattle noise (Fig.11).

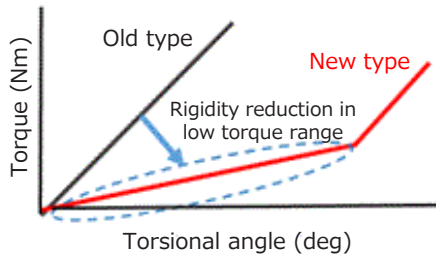
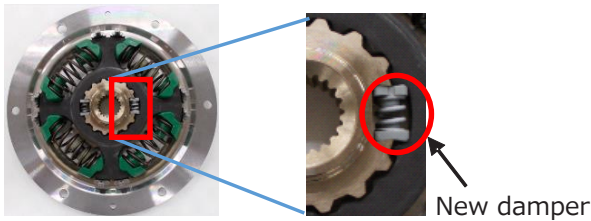


Fig.10 New low-rigid torsional damper

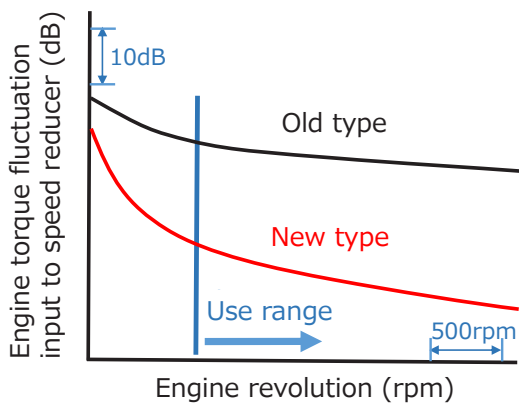


Fig.11 Improvement of the vibration characteristics between engine and speed reducer

### 3.3 Noise of speed increaser gears

Regarding the speed increaser connecting the engine and generator, one of the gears of the intermediate shaft between the engine shaft and generator shaft meshes with the gears of the engine shaft and generator shaft. Accordingly, the gear noise level tends to increase qualitatively. We can reduce the gear noise by optimizing the gear specifications and the layout of the gear shafts in such a way that the meshing phases between these two meshing points are mutually canceled out (Fig.12).

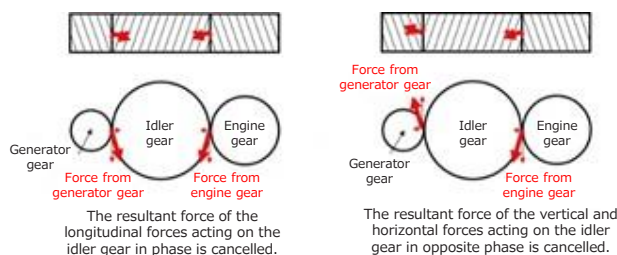


Fig.12 Conceptual diagram of the design for gear meshing phase difference

This design for optimizing phase differences has been adopted in the old and new speed increase of e-POWER so as to further reduce the level in the engine revolution range frequently used.

## 4. Pursuing further quietness

Assuming that e-POWER will be increasingly adopted in higher-power vehicles in the future, Nissan needs to modify the vibration transmission system for noise and vibration performance in accordance with the increase in the existing forces and enlargement of the power train due to the increase in engine and motor torques.

To achieve further quietness and pursuing EV-ness<sup>4</sup>, Nissan aims to improve the quietness while fully bringing out the characteristics of the e-POWER system. This will be achieved by comprehensively designing from the main moving system and body structural system of the power train to the engine mount.

## 5. Summary

To achieve the quietness of high-grade vehicles that is a characteristic of e-POWER, Nissan has taken the following measures: (1) reduction of the high-frequency noise during EV driving, and (2) engine operation in a manner imperceptible to the driver. In addition, Nissan has made further improvements to the old NOTE e-POWER by focusing on controlling the rattle noise of the speed increaser gears.

- High-frequency noise during EV driving: We have reduced the noise level by optimizing the electromagnetic force by redesigning the motor's magnetic circuit, efficiently improving the rigidity of the radiating portions, and improving the precision of the speed reducer gears.
- Noise during engine operation: We have improved the rigidity of the inverter case and newly adopted an engine start/stop control factoring in the driving scenarios where engine noise is muffled by ambient noise. We have also greatly reduced the rattle noise of the speed increaser gears by adopting the newly developed low-rigid damper. In addition, we have optimized the phase differences between two meshing points to address the gear noise caused by the double meshing of the speed increaser.



### Explanation of terms

- \*1 BEV: An EV driven by battery power only\*2
- \*2 EV: vehicle driven by electric motor only
- \*3 EV driving: Driving with e-POWER, operated by battery power only with the engine stopped
- \*4 EV-ness: Quiet, powerful, and smooth driving feeling unique to electric motor drive

### References

- 1) 餌取秀一ほか: e-POWERを支える振動・騒音低減技術、日産技報、No.80, p.39-47(2017)
- 2) 濱野崇ほか: 新開発EVのギヤノイズ低減技術、自動車技術会学術講演会前刷集, Vol.56-11, p.1-4(2011)
- 3) 北條秀樹ほか: 高周波モードを考慮したEV モーターノイズ低減技術、自動車技術会学術講演会前刷集, No.108-12, p.31-34(2012)
- 4) 山本和志ほか: 新型機電一体構造を有する新開発電動パワートレインのモーターノイズ低減技術、自動車技術会論文集, Vol.47, No.6, p.1349-1353(2016)

## Authors



Tetsuya Kawakami



Hiroataka Kaneko



Yusuke Ienaka



Kazuhiko Arai



Ryuugo Chiba



Takanobu Sawada



Toru Nakada



Masaya Gotou



## 6. Electric AWD technology to add value to e-POWER

Ryozo Hiraku\* Eigo Sakagami\*\* Takeji Katakura\*\*

### 1. Introduction

The conventional all-wheel drive (AWD) system functions by distributing the power generated by the internal combustion engine to the front and rear wheels through a mechanical system. However, recent EVs<sup>1</sup> have been adopting electric AWD with motors in both the front and rear, instead of using a single power source that distributes power to the front and rear. When combined with BEV<sup>2</sup>, electric AWD has many advantages in vehicle design, such as fully independent control of the front and rear tractions and highly flexible layout. However, for combining with an internal combustion engine vehicle, electric AWD has some disadvantages such as a high-voltage battery system is required to obtain sufficient power, traction controllability is still limited even if the rear wheels are electric motor-driven because the front wheels are driven by the engine. In contrast, by combining with 100% motor-driven e-POWER equipped with a high-voltage battery system, the issues that arise when combined with conventional internal combustion engine vehicles are solved and the benefits of electric AWD can be gained as with the BEV.

This article discusses the technical direction of the 100% motor-driven AWD system combined with e-POWER, which is scheduled to be launched.

### 2. “e-4ORCE” as the evolution of electric AWD to Nissan

In the 2019 Tokyo Motor Show, Nissan publicized the direction of the evolution of new electric motor AWD, “e-4ORCE” (Fig.1), with the “Ariya Concept”. For the control technology of “e-4ORCE,” Nissan has developed the technologies of four-wheel traction control, chassis control, and electric power train, while combining the knowledge, which Nissan has accumulated over the years. Nissan has the knowledge to maximize the effects of the traction control, brake control, and chassis control acquired from the ATTESA E-TS (Advanced Total Traction Engineering System for All Electronic - Torque Split) of the “GT-R” and the intelligent 4 x 4 system of the “X-Trail”. Furthermore, Nissan has also utilized its

long experience in the development of motor drive and advanced four-wheel drive systems to develop an advanced system “e-4ORCE” equipped with two electric motors.



Fig.1 Ariya Concept in 2019 TMS

The aim of “e-4ORCE” is to bring (1) usability, (2) comfort, and (3) confidence to a level that cannot be achieved by conventional internal combustion engine vehicles, by re-defining the roles of individual vehicle systems based on electric motor drive and maximizing the high potential of the electric motor.

This is not merely the “transformation to AWD” from the front-wheel drive electric vehicles but an evolution aiming at a new direction of vehicle design. Only 100% electric motor-driven BEV and e-POWER can achieve this performance.

### 3. New dynamics control achieved by electric AWD

Basically, vehicles provide their dynamic performance “Run,” “Stop,” and “Turn” by controlling the power generated by the power source, internal combustion engine, and by using the functions of the steering and brake systems, respectively (Fig.2). However, because the electric motor is being used as an alternative power source, it is able to provide functions that the conventional power sources could not provide. For example, some of the functions that used to be provided by the conventional brakes can be covered by the electric motor by properly controlling the regenerative capability of the electric

\*Powertrain and EV Engineering Division

\*\*Powertrain and EV Performance Engineering Department

motor. In addition, unprecedented smoothness and usability can be achieved by properly utilizing the high controllability of the electric motor. One of the applications is the e-POWER drive adopted in the NOTE e-POWER.

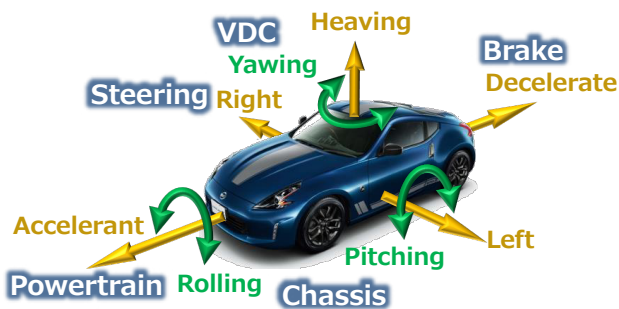


Fig.2 Vehicle's movement and role sharing of systems

Because electric AWD has two electric motors in the front and rear, the variety of movements increases owing to the motors use as power sources. For example, movements such as the vehicle's pitching and yawing can now be controlled by the electric motors to a limited extent, which is not what was expected before (Fig.3).

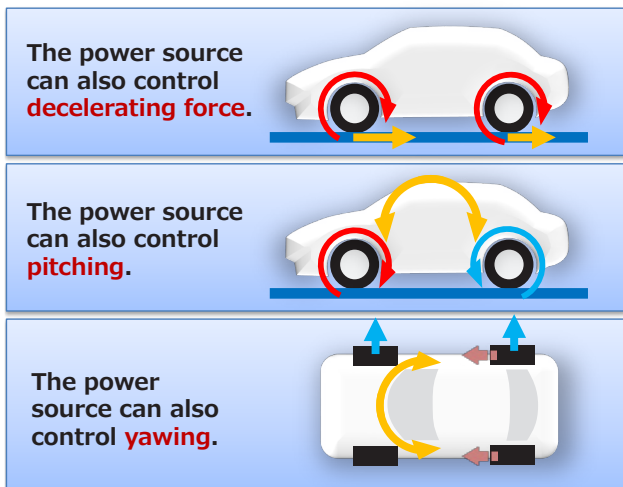


Fig.3 Movements achieved by using electrically driven AWD

#### 4. Values offered by 100% motor-driven AWD

For driver		For occupants
Easy following path as driver's expectation	Confidence anywhere	Comfortable ride for all
Powerful yet smooth		

Fig.3 Movements achieved by using electrically driven AWD

#### 4-1. Easy following path as per driver's expectations

Line traceability and accurate steering can be enhanced by the integrated control of the torques generated by the two electric motors, regenerative braking, and four wheels' hydraulic braking while optimally using individual roles. This control provides the driver with confidence. Such advanced control is particularly effective at cornering. Because the vehicle moves in accordance with the steering operation of the driver, the driver can enjoy smooth and comfortable driving.

For example, Fig.5 compares the behaviors of vehicles slaloming on a snowy road, when traction is properly distributed to the front and rear with integrated control, and when traction is fixed to the front and rear. The figure shows that the integrated control stabilizes vehicle behavior and allows the driver to constantly trace the ideal line as expected.

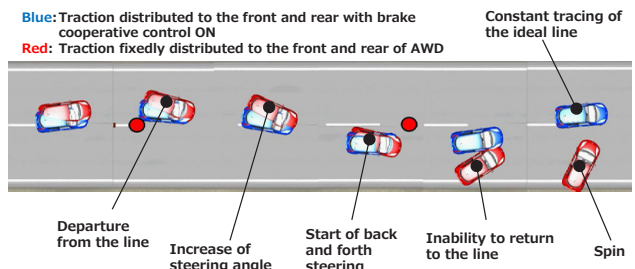


Fig.5 Comparison when slaloming on a snowy road

#### 4-2. Comfortable ride for all

Electric motor-controlled regenerative braking also contributes to a comfortable ride.

Front-wheel-driven e-POWER applies regenerative braking using the electric motor located in the front, so that the front side of the vehicle deeply sinks when decelerated. Electric AWD vehicles optimally control the regenerative braking of the electric motor located in the front and rear to prevent the vehicle from front side sinking and oscillating, respectively, when decelerated (Fig.6). Accordingly, occupants do not feel the oscillations when the vehicle is repeatedly started and stopped or in similar situations, which reduces car sickness and delivers comfortable riding. This control provides not only the driver but also the occupants in the passenger seat and rear seats with stable and smooth ride comfort.

**Without control:  
The head oscillates when decelerated.**



**With control:  
The vehicle decelerates stably.**



Fig.6 Attitude control when decelerated

**4-3. Confidence anywhere**

In scenarios where even an experienced driver feels stress such as when driving on a wet, frozen, or snowy slippery road, the tire's road holding capability is maximized by integrated control of the outputs from the front and rear electric motors and the braking system in a precise manner to help stabilize the vehicle's movement. Thus, even when the driver excessively depresses the accelerator pedal on a slippery road, the vehicle properly controls the outputs so that the driver can securely control the vehicle.

The chart in Fig.7 compares a front wheel drive (FF) vehicle and AWD with or without the integrated control in a scenario where the driver lifts his foot off the accelerator pedal to decelerate the vehicle on a slippery road. By using integrated control, the road holding capability of the front and rear tires can be fully utilized to help secure a stable decelerating force.

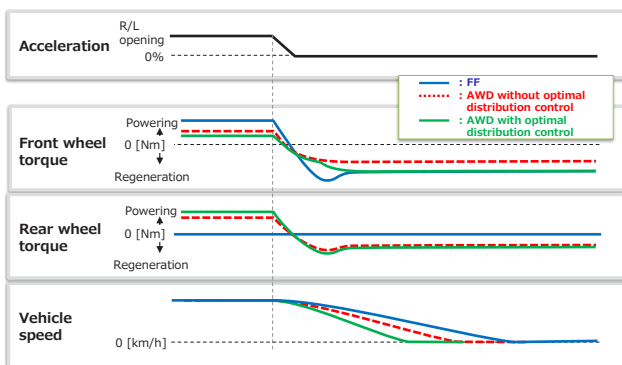


Fig.7 Slip control by motor

**5. Summary**

AWD has been widely known as a mechanism that provides confidence. With the electric AWD to be launched, Nissan not only offers the originally expected performance but also focuses on the performance enhancements “not just for some days but every day”. In other words, we have not only refined rough road performance and limit performance but also enriched the performance that provides average drivers with comfort and ease of driving even during everyday driving on regular roads. We will continuously aim to advance performance toward the Nissan goal, which is ultimate intelligent mobility.

As a combination with e-POWER, the electric AWD combined with the new NOTE e-POWER is the first model, which is scheduled to be launched soon.

**Explanation of terms**

- \*1. EV: vehicle driven by electric motor only
- \*2. BEV: An EV driven by battery power only

## Authors



Ryozo Hiraku



Eigo Sakagami



Takeji Katakura

# Development of estimation and improvement method for Real World Fuel Economy by using a traffic flow simulation (First Report)

Yasuki Fukumoto\* Hiroshi Kuriki\*\* Hajime Miura\*  
Seishi Shimamura\*\* Takahito Nishi\*

**Abstract** Real-world fuel economy is affected by driving style, traffic flow, and other factors. However, quantifying the effects of driving style improvement has been especially difficult thus far because previous traffic conditions have not been clarified. This paper presents a possible means of quantifying the effects of driving style improvement by using a traffic flow simulation with randomized traffic conditions and deviations. In this study, the traffic flow and driving style were modeled by performing a simulation using measured data. It was concluded that the proposed method serves as a promising means of estimating the effects of driving style improvement on real-world fuel economy.

## 1. Introduction

Fuel economy strongly affects the buying motives of many customers in terms of the environmental and economic aspects. It is known that there exists a divergence between the fuel economy values in catalogs and those reported by customers (hereinafter referred to as real-world fuel economy). Real-world fuel economy improvement has been a critical issue for automobile manufacturers. Unlike fuel economy quantification in catalogs, real-world fuel economy quantification is difficult because a wide variety of usage and environmental factors must be considered, such as driving style, travel distance per trip, temperature and other environmental conditions, and surrounding traffic conditions. In this study, the feasibility of quantifying real-world fuel economy was investigated by focusing on the effects of driving style and the traffic environment.

## 2. Simulation configuration and method

### 2.1 Simulation configuration

The software package PTV<sup>1)</sup> Vissim was used to reproduce the traffic flow. Vissim includes an algorithm that varies several parameters such as the vehicle acceleration, target vehicle speed, and number of vehicles by using random numbers. Using this system, deviated traffic flows can be reproduced, and the simulation results can be obtained by fixing random numbers.

For the fuel economy calculation, a power train model created using MATLAB/Simulink by Mathworks was employed<sup>2)</sup>. The inertia of components such as the engine and transmission can be input to this power train model. The calculated operating points of the engine were set to

approach the operating points of an actual engine by inputting a shift schedule in the transmission model. This model has been well proven and used for product development.

As shown in Fig. 1, for the coupled calculations, a cycle was created that outputs the target acceleration and road gradient from Vissim to the power train model of Simulink and then feeds back the effective acceleration calculated in the power train model to Vissim. In the program, the operational cycles of Vissim and MATLAB/Simulink were set to 100 and 1 ms, respectively, to synchronize them.

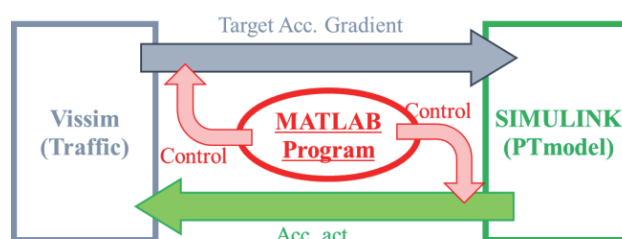


Fig.1 Co-simulation configuration

### 2.2. Traffic flow reproduction

In Vissim, the real-world fuel economy test course in Kanagawa, which is used internally at Nissan Motor Co., Ltd., was reproduced. The course was divided into seven sections, labeled as A–G, to reproduce the traffic flow of each section. An outline of the course is presented in Table 1.

\*Powertrain and EV Advanced Technology Department

\*\*Powertrain and EV Performance Engineering Department

**Table 1 Evaluation course summary**

	Length	Average vehicle speed	Average stop time	Max. Gradient	Road type
Section A	4.0km	22.7km/h	181sec	+6.2%	Urban
Section B	5.5km	16.5km/h	431sec	-7.4%	Congestion
Section C	7.5km	30.6km/h	185sec	+6.0%	Suburb
Section D	6.0km	12.1km/h	697sec	+5.8%	Congestion
Section E	17.5km	73.4km/h	N/A	+6.5%	Highway
Section F	8.0km	24.3km/h	316sec	±5%	Suburb
Section G	2.9km	20.7km/h	163sec	+7.6%	Urban
TOTAL	51.4km	25.7km/h	2110sec	N/A	N/A

To obtain the source data for traffic flow reproduction, the results provided by several in-house drivers who had driven an identical vehicle on an identical course were analyzed and applied. The profiles of the vehicle speed with respect to distance over the entire course are shown in Fig. 2, and the acceleration with respect to distance is depicted in Fig. 3. As the level of traffic flow reproduction, a target of the vehicle speed profile subject to a fuel economy evaluation approaching the average of the results obtained from the above mentioned drivers was set. The average vehicle speed and stop time were utilized as the parameters for traffic flow reproduction. As the vehicle did not stop in section E, which was a high-speed section, the stop time for this section was not reproduced or evaluated.

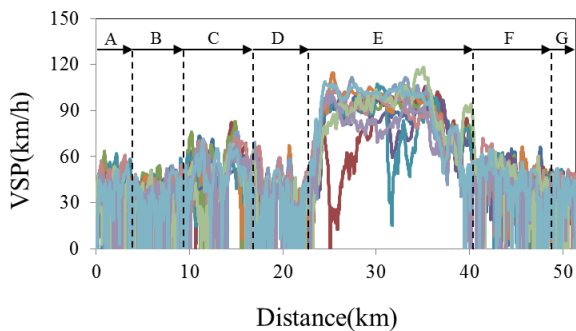


**Fig.2 Actual vehicle speed**

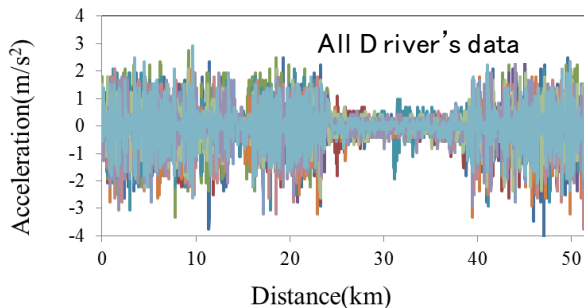


**Fig.3 Actual acceleration, G, of the vehicle**

To adjust the average vehicle speed and stop time in the simulation, the driving styles for all the vehicles, including those subject to the fuel economy evaluation, were reproduced. The target cruising vehicle speeds

during acceleration and deceleration on each road were incorporated as the driving style parameters. For acceleration, the data obtained from actual driving were analyzed, with the aim of reproducing the acceleration profile at startup. The results obtained for the three representative drivers are shown in Fig. 4. The maximum acceleration, G, which is shown in the lower graph in Fig. 4, is approximately 2.0–2.5 m/s<sup>2</sup>; this value is attained at a vehicle speed of 10–20 km/h, as shown in the upper graph in Fig. 4. The results obtained indicate a decrease in acceleration after the maximum G; the acceleration decreases to approximately 1.0 m/s<sup>2</sup> or less at 40 km/h.

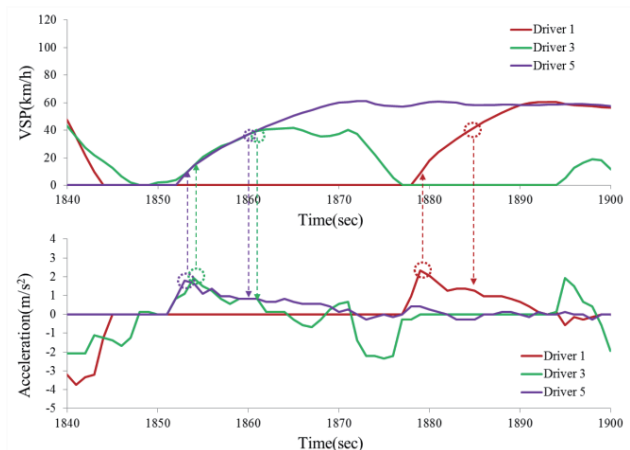


**Fig.4 Actual vehicle speed and G**

To reproduce this acceleration profile, the speed range of 0–100 km/h was divided into 10 km/h intervals, and a common target acceleration for all the vehicle speed zones was set in sections A–G. The deviation of acceleration was determined in the same manner. The values set for the simulation with  $\pm 3\sigma$  as the upper and lower limits are depicted in Fig. 5. The acceleration set was used as the upper-limit acceleration for normal driving in Vissim. When the acceleration of the preceding vehicle is low, such as in a traffic jam, Vissim calculates the appropriate acceleration.

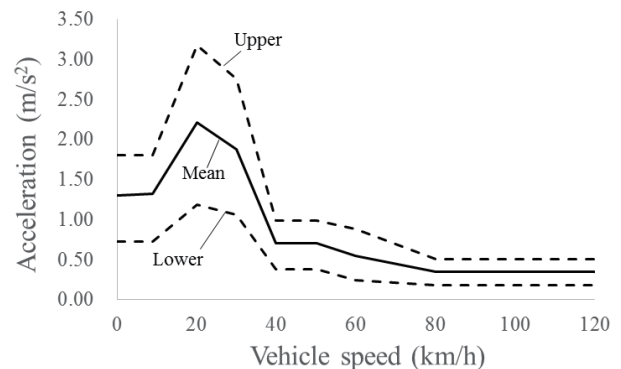


**Fig.5 Acceleration settings**

For deceleration, the maximum deceleration in actual driving exceeds  $-3.0$  m/s<sup>2</sup>. However, this value occurs immediately prior to stopping, and the deceleration from a cruising vehicle speed is approximately  $-3.0$  m/s<sup>2</sup> or less. In the simulation,  $-2.8$  m/s<sup>2</sup> was set as the maximum



deceleration under normal deceleration conditions, excluding emergency braking to avoid a collision and  $-3.0 \text{ m/s}^2$  as the maximum deviation.

The cruising vehicle speed was set for each road in the simulation. Assuming that the drivers set a target cruising vehicle speed at intervals of 10 km/h, the cruising vehicle speed was set at 10 km/h intervals based on the average cruising vehicle speed during actual driving. For heavy-duty trucks and buses, the cruising vehicle speed was set to be less than that of passenger vehicles by 10 km/h. The deviation in the cruising vehicle speed was varied according to the road, and the minimum and maximum speeds were set as 5 and 30 km/h, respectively, considering the median value.

Next, the target traffic flow was reproduced by adjusting the number of vehicles to be driven in Vissim, according to the data from the road traffic census conducted by the Ministry of Land, Infrastructure, and Transport and by adjusting the signal cycles and intersection passing speeds. To evaluate the reproduction, the results of simulations conducted 60 times by varying random numbers were analyzed, considering the median values and deviations of the average vehicle speed and stop time. Thereafter, the results were compared with the actual driving data. For sections prone to traffic jams, the length of the traffic jam in each section was emphasized.

### 2.3. Configuration of the fuel economy calculation section

For the fuel economy calculation section in the Simulink simulation, a powertrain model equivalent to that of the vehicle used for actual driving was employed. The powertrain model included the vehicle mass, air resistance, and tire rolling resistance, which were necessary to calculate the running resistance. The basic specifications of the powertrain model are listed in Table 2.

Table 2 Vehicle specifications

Vehicle type	C segment minivan
Vehicle weight	1760kg(with passengers)
Engine	L4 2.0L N.A.
Trans mission	CVT
Drive line	FF
Tire size	195/60R16

The engine block in the power train model includes parameters such as the fuel economy rate, output, and friction. The calculation of the fuel cut at deceleration is also incorporated. The CVT block includes the friction, torque converter performance, shift schedule, and lock-up timing. In addition to these parameters, the response delay of the powertrain, including the intake response delay, was incorporated to more accurately simulate the behavior of the powertrain in an actual vehicle.

### 2.4. Study of different driving styles

The effects of different driving styles on the real-world fuel economy were studied by reproducing different acceleration levels through a simulation using two types of drivers: one who accelerated the vehicle at a relatively high rate and another who accelerated the vehicle at a lower rate. The acceleration profiles of the different drivers are shown in Fig. 6.

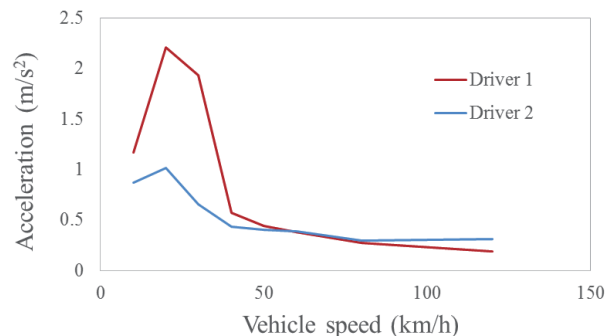


Fig.6 Acceleration profiles of different drivers

## 3. Simulation results

### 3.1. Traffic flow reproduction

The distributions of the average vehicle speeds and stop times obtained from the traffic flow reproduction are presented in Figs. 7–10, and the median values and deviations of these results are summarized in Tables 3 and 4. Here, the objective was to ensure that the median values and deviations of the simulation results are within  $\pm 10\%$  and  $\pm 50\%$ , respectively, of those of the actual driving results.

As shown in Fig. 7, the median value of the average vehicle speed exceeds that of actual driving by 0.3 km/h throughout the test course, and the  $1\sigma$  deviation is less than that of actual driving by 0.6 km/h. Both the median values and deviations are similar to those of actual driving. As depicted in Fig. 8, all the median values and deviations of sections A–F are similar to those of actual driving. However, in section G, the  $1\sigma$  deviation reproduced in the simulation is less than 30% of that of actual driving. The reasons for this difference are as follows: (1) section G includes many off-street stores, and the speed reduction of a vehicle when entering and exiting cannot be sufficiently reproduced; (2) when a vehicle waits for pedestrians to cross a pedestrian crossing before making a left turn, the speed reduction and temporary stop of the vehicle cannot be sufficiently reproduced.

As shown in Fig. 9, the median value of the vehicle stop time is less than that of actual driving by 140 s throughout the test course, and the  $1\sigma$  deviation is less than that of actual driving by 191 s. Thus, the results barely meet the target values. The comparison in Fig. 10 indicates that the errors of the median values are low in sections B, C, and G, as compared to those of actual driving; however, the errors in sections D and F are large at 146 and 121 s, respectively. With the exception of

section G, the  $1\sigma$  deviations of all the other sections satisfy the targets. However, the simulated and reproduced deviation of section G is only 16 s, which is less than 20% of that of actual driving.

According to the results above, it was assumed that the error in the median value of section D was due to the fact that the time per stop in section D was shorter than

that during actual driving. Furthermore, it was assumed that the error in the median value of section F was due to the simulation setting in which a traffic jam readily occurs owing to a vehicle turning right at an intersection. It was also assumed that the cause of the deviation in section G was the same as that determined when studying the average vehicle speed. These traffic flow errors will continue to be improved.

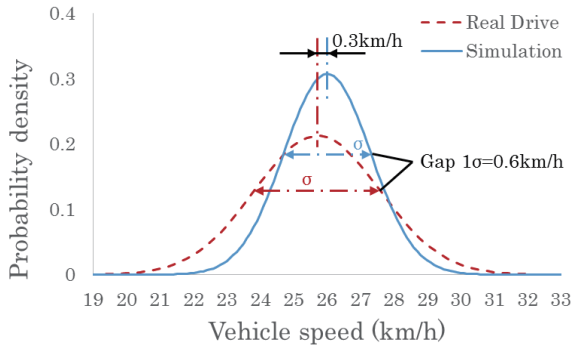


Fig.7 Total average vehicle speed

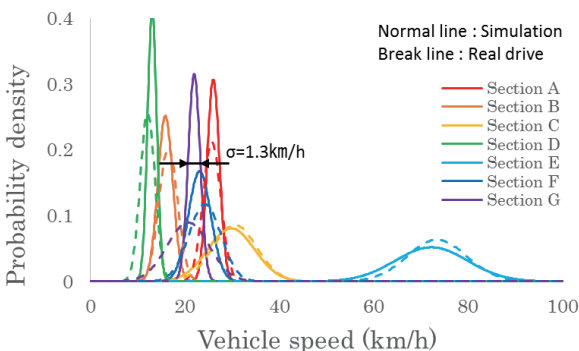


Fig.8 Average vehicle speed by section

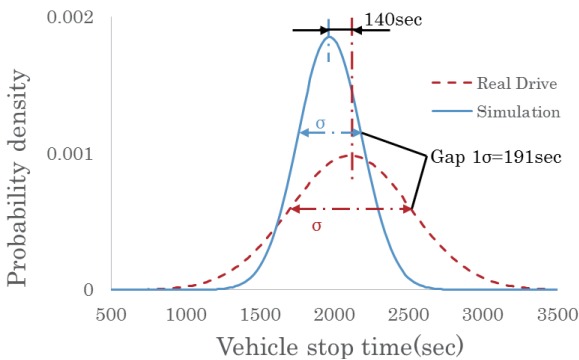


Fig.9 Total vehicle stop time

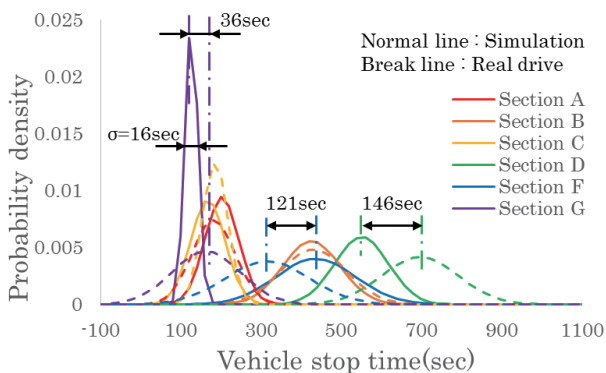


Fig.10 Vehicle stop time by section

Table3 Gap of average value

		Average		
		Real drive (①)	Simulation (②)	Gap (②-①)÷①×100
Average vehicle speed (km/h)	TOTAL	25.7	26.0	1% ○
	Sec. A	22.7	24.2	7% ○
	Sec. B	16.5	15.8	-4% ○
	Sec. C	30.6	29.8	-3% ○
	Sec. D	12.1	13.1	8% ○
	Sec. E	73.4	72.2	-2% ○
	Sec. G	20.7	22.0	6% ○
Vehicle stop time (sec)	TOTAL	2110	1970	-7% ○
	Sec. A	181	202	11% ×
	Sec. B	431	426	-1% ○
	Sec. C	185	167	-10% ○
	Sec. D	697	551	-21% ×
	Sec. E	N/A	N/A	N/A
	Sec. F	316	437	38% ×
	Sec. G	163	127	-22% ×

Table4 Gap of standard deviation value

		Standard deviation		
		Real drive (①)	Simulation (②)	Gap (②-①)÷①×100
Average vehicle speed (km/h)	TOTAL	1.9	1.3	-31% ○
	Sec. A	1.9	2.0	5% ○
	Sec. B	2.0	1.6	-19% ○
	Sec. C	4.7	4.9	6% ○
	Sec. D	1.6	1.0	-38% ○
	Sec. E	6.3	7.7	22% ○
	Sec. F	3.4	2.4	-30% ○
	Sec. G	4.5	1.3	-72% ×
Vehicle stop time (sec)	TOTAL	406	215	-47% ○
	Sec. A	54	42	-22% ○
	Sec. B	82	72	-13% ○
	Sec. C	32	44	38% ○
	Sec. D	96	67	-30% ○
	Sec. E	N/A	N/A	N/A
	Sec. F	105	99	-6% ○
	Sec. G	86	16	-82% ×

### 3.2. Reproduction of the driving style of general vehicles

The simulation results obtained using the acceleration settings in Fig. 5 from Section 2.2 are presented in Fig. 11. According to the results, the maximum G is 2.0–2.5 m/s<sup>2</sup> at 20 km/h, and it decreases to approximately 1.0 m/s<sup>2</sup> at 40 km/h. Thus, an acceleration profile similar to that of an actual vehicle could be reproduced.

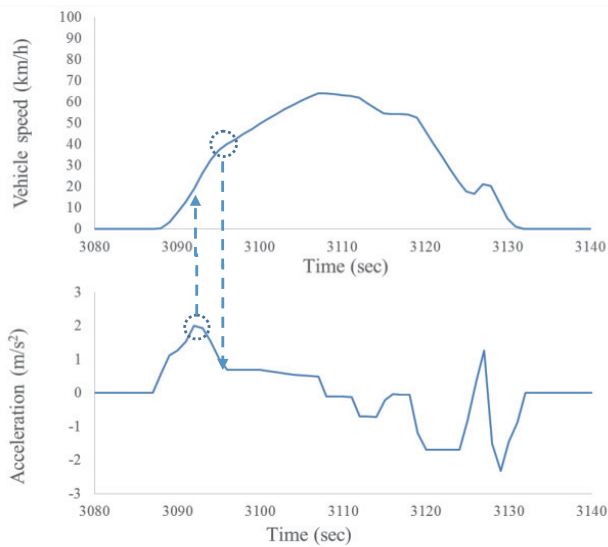


Fig.11 Acceleration setting and simulation results

The simulation results for acceleration and deceleration when the vehicle is driven over the entire course several times are shown in Fig. 12. The deceleration during normal driving is within  $-3.0 \text{ m/s}^2$ , as specified. However, the emergency brakes were applied approximately five times per trip, and the frequency of emergency brakes was high compared to that in the actual driving data. As this characteristic is mainly attributable to the cut-in at the time of lane change and merging, the frequency of emergency brake usage will be reduced.

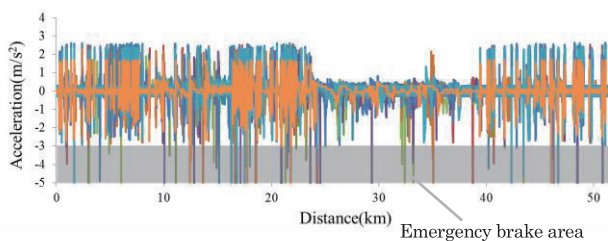


Fig.12 Simulated deceleration

The vehicle speeds obtained from the simulation are depicted in Fig. 13. The characteristics of the cruising vehicle speed with respect to the travel distance are similar to those of actual driving. In particular, under highway scenarios, the vehicle does not operate at a constant speed of 100 km/h; instead, it accelerates and decelerates. Thus, it was possible to bring the deviation in the vehicle speed close to that of actual driving. In certain highway scenarios, the vehicle speed reached a value that would never occur in actual driving. The cruising vehicle speed settings will be reviewed to address this issue.

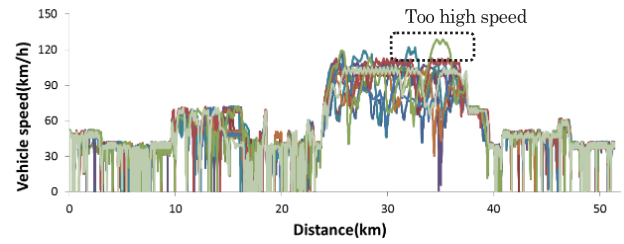


Fig.13 Simulated vehicle speed

### 3.3. Calculated engine operating points

The engine operating points obtained during actual driving are presented in Fig. 14, and the representative engine operating points calculated in the simulation are shown in Fig. 15. In the simulation, the maximum engine speed exceeded 3500 rpm and the maximum engine torque exceeded 150 Nm, which indicates that the operating points in the high-load ranges were reproduced. In addition, the low-load range around 2000 rpm, which appears during acceleration and deceleration in highway driving, is well reproduced. By contrast, the maximum torque of 1500–3000 rpm is low compared to that of actual driving; this likely occurs because the engine load due to the air conditioning compressor when operating the air conditioning system was not reproduced appropriately. Estimating the load of the air conditioning compressor while driving is difficult because it is affected by the ambient temperature and the vehicle driving speed. Thus, this factor was not included in the simulation, and its incorporation will be considered in the future.

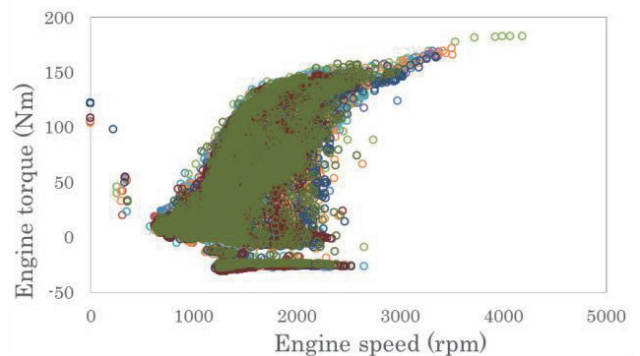


Fig.14 Engine operating points for actual driving data

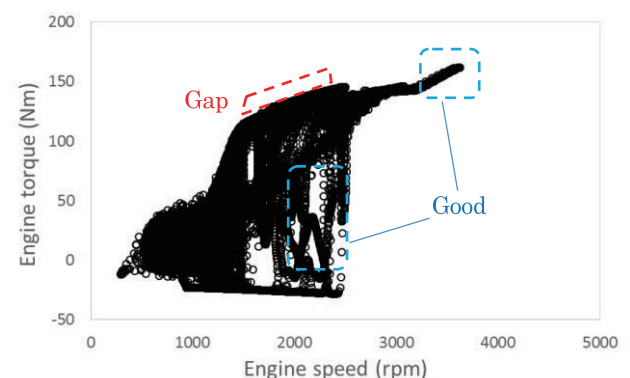


Fig.15 Engine operating points for the simulation data

### 3.4. Calculated fuel economy values

The distributions of the total fuel economy values obtained from the simulation and actual driving are depicted in Fig. 16, and the median value of each section is shown in Table 5.

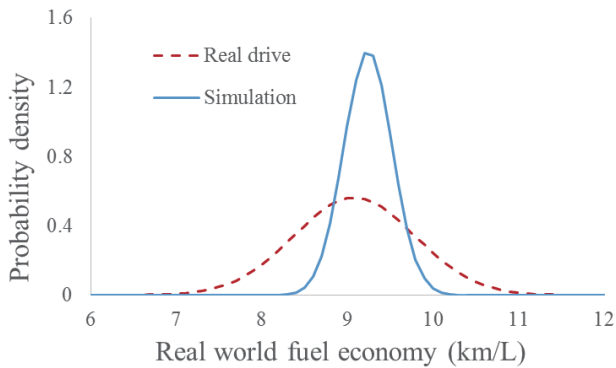


Fig.16 Real-world fuel economy distribution

Table 5 Fuel economy calculation results

	Average			
	Real drive ①	Simulation ②	Gap $(②-①)÷①×100$	
Section A	8.5	8.7	3.1%	○
Section B	8.4	8.3	-2.1%	○
Section C	11.5	10.2	-13.4%	×
Secton D	7.3	6.9	-5.8%	○
Section E	16.6	12.2	-35.3%	×
Section F	10.3	9.9	-3.3%	○
Section G	8.0	9.5	16.3%	×
TOTAL	9.1	9.2	1.7%	○

The objective was to ensure that the simulated fuel economy values are within 10% of those of actual driving. The median of the total fuel economy values during actual driving was 9.1 km/L, whereas that in the simulation was 9.2 km/L. However, as this value does not reflect the load for the air conditioning compressor, as discussed in Section 3.3, the fuel economy in the simulation may decrease further.

The results in sections A, B, D, and F were similar to those of actual driving; however, those in sections C, E, and G diverged by 10% or more. An analysis of the divergence revealed that a traffic jam that occurred from the beginning of section D extended to the latter half of section C. This finding indicates that the simulated length of the traffic jam was greater than the actual length. As indicated in Fig. 17, which depicts the simulated vehicle behavior during high-speed driving in section E, acceleration and deceleration occur repeatedly when following the preceding vehicle, thereby significantly increasing fuel consumption. It was inferred that the result of section G indicates the insufficient reproduction of the traffic flow in Vissim, as discussed in Section 3.1. According to these results, it is necessary to reproduce the fuel economy value of each section

appropriately to reliably judge the total fuel economy value achievable. To realize this objective, it is necessary to make a judgment after improving the accuracy of each section by studying the control indices that are strongly correlated with fuel economy.

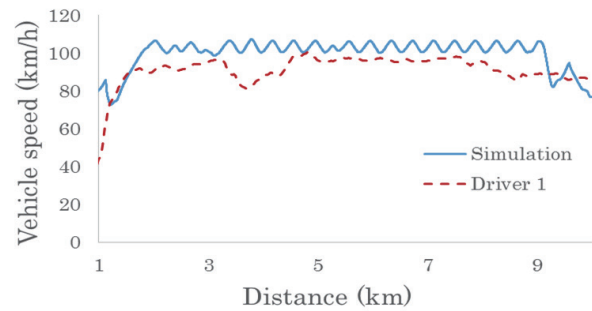


Fig.17 Highway vehicle speed profile

### 3.5. Effects of different driving styles on fuel economy

The simulated fuel economy values obtained from different drivers and the fuel economy values of actual driving are compared in Table 6. The simulation was conducted 15 times.

As shown in Fig. 6 in Section 2.4, Driver 2 exhibited a low acceleration at 50 km/h or less; it was assumed that this would improve the fuel economy, mainly upon starting from a stop. The total fuel economy during actual driving improved by 0.7 km/L, whereas that in the simulation was 0.4. Although the fuel economy varies with the driver, the tendency for higher fuel economy was confirmed.

The simulation results of each section showed that the fuel economy of Driver 2 was higher than that of Driver 1 for all the sections. However, as acceleration from a stop barely occurred in section E, the intended effect could not be confirmed. In actual driving, the fuel economy of Driver 2 was worse than that of Driver 1, because Driver 2 was caught in a temporary traffic jam during high-speed driving. In addition, this effect could not be confirmed in section A. An analysis of the representative results indicated that Driver 2 stopped the vehicle more often than Driver 1, which implies that additional fuel was consumed while starting. Considering the individual sections, it was assumed that it is essential to control the vehicle stopping frequency in sections such as A, where the frequency of accelerating from a stop is low with respect to the section-to-section distance. For sections other than A and E, the simulated fuel economy values of Driver 2 were higher. However, the improvement margin is not uniform with respect to the actual driving. To match the absolute and relative values, as concluded in Section 3.4, it is necessary to improve the accuracy of the traffic flow reproduction and to create control indices that are strongly correlated with traffic flows and fuel economy values.

**Table 6 Gap of different driver fuel economy**

		Driver 1	Driver 2	Gap (Driver 2 - Driver 1)
Section A	Real drive	10.4km/L	9.9km/L	-0.5km/L
	simulation	8.7km/L	8.7km/L	0.0km/L
Section B	Real drive	8.4km/L	9.6km/L	1.2km/L
	simulation	8.0km/L	8.4km/L	0.4km/L
Section C	Real drive	13.3km/L	13.5km/L	0.2km/L
	simulation	11.0km/L	11.3km/L	0.3km/L
Section D	Real drive	6.9km/L	7.9km/L	1.0km/L
	simulation	7.5km/L	8.0km/L	0.5km/L
Section E	Real drive	17.7km/L	17.0km/L	-0.7km/L
	simulation	12.5km/L	12.5km/L	0.0km/L
Section F	Real drive	10.5km/L	10.9km/L	0.4km/L
	simulation	9.9km/L	10.4km/L	0.5km/L
Section G	Real drive	8.3km/L	10.5km/L	2.2km/L
	simulation	9.3km/L	9.8km/L	0.5km/L
Total	Real drive	9.2km/L	9.9km/L	0.7km/L
	simulation	9.0km/L	9.4km/L	0.4km/L

#### 4. Conclusion

Traffic flows and driving styles were reproduced in a simulation. By incorporating a powertrain model in the calculations, the real-world fuel economy while driving in different traffic flows was investigated. Moreover, the effects of different driving styles on the fuel economy were assessed. Although it would be difficult to reproduce the considered driving scenarios repeatedly in real life, they could be reproduced easily using the method proposed herein. However, as the accuracies of the reproduced traffic flows and calculated fuel economy values were insufficient under certain conditions, further work will be conducted to improve the accuracy.

#### References

- (1) <http://vision-traffic.ptvgroup.com/en-us/home/>
- (2) <https://jp.mathworks.com/>

## Authors



Yasuki Fukumoto



Hiroshi Kuriki



Hajime Miura



Seishi Shimamura



Takahito Nishi

# Development of estimation and improvement method for Real World Fuel Economy by using a traffic flow simulation (Second Report)

Yasuki Fukumoto\* Hiroshi Kuriki\*\* Hajime Miura\*  
Seishi Shimamura\*\* Takahito Nishi\*

**Abstract** A real-world fuel economy prediction method using traffic flow simulations was reported in the previous paper. Regarding the relationship between driving style and fuel economy, certain aspects remained unclear. In this study, these aspects were investigated further, and a traffic scene in which mild acceleration results in better fuel economy was identified. Based on these results, a method for improving real-world fuel economy is proposed.

## 1. Introduction

Unlike mode fuel economy values, which are provided in automobile catalogs, the fuel economy values reported by customers (hereinafter referred to as real-world fuel economy values) are difficult to quantify because they are affected by various environmental factors, such as the driving style of the customer and the surrounding traffic conditions. In the previous report<sup>1)</sup>, traffic flow and vehicle fuel economy calculation simulations were combined to develop a method for estimating real-world fuel economy. However, the simulation results obtained by varying the acceleration showed changes in the fuel economy due to differences in the traffic environment and, in certain cases, decreased fuel economy. Thus, the effectiveness of this method for improving fuel economy could not be determined. In this study, the effects of the traffic environment on the acceleration level and the fuel economy were analyzed in detail to determine whether the simulator can effectively monitor changes under driving conditions. In addition, because the traffic environment must be evaluated with an on-board system to realize fuel-efficient driving, traffic jams that can be detected by existing on-board sensors were emphasized, in order to simulate fuel-efficient driving in traffic jams. This paper presents the simulation results.

## 2. Relationship between effects of gradual acceleration and traffic environment on fuel economy

A simulation with the same specifications as those in the previous study was utilized in this work. For the fuel economy calculation, the vehicle fuel economy calculation

model created using MATLAB/Simulink from Mathworks was employed<sup>2)</sup>, and to reproduce the traffic flow, PTV<sup>3)</sup> Vissim was used. In the fuel economy calculation section of Simulink, a powertrain model similar to that of the vehicle used for actual driving was applied. Table 1 lists the basic specifications of the proposed model.

Table 1 Vehicle specifications

Vehicle type	C segment minivan
Vehicle weight	1760kg(with passengers)
Engine	L4 2.0L N.A.
Trans mission	CVT
Drive line	FF
Tire size	195/60R16

As a traffic flow model, a real-world fuel economy test course in Kanagawa was reproduced. This course is described in Table 2.

Table 2 Evaluation course summary

	Length	Average vehicle speed	Average stop time	Max. Gradient	Road type
Section A	4.0km	22.7km/h	181sec	+6.2%	Urban
Section B	5.5km	16.5km/h	431sec	-7.4%	Congestion
Section C	7.5km	30.6km/h	185sec	+6.0%	Suburb
Section D	6.0km	12.1km/h	697sec	+5.8%	Congestion
Section E	17.5km	73.4km/h	N/A	+6.5%	Highway
Section F	8.0km	24.3km/h	316sec	±5%	Suburb
Section G	2.9km	20.7km/h	163sec	+7.6%	Urban

\*Powertrain and EV Advanced Technology Department

\*\*Powertrain and EV Performance Engineering Department

To determine the effects of different driving styles on the fuel economy, a simulation was conducted using two types of drivers: one who accelerated the vehicle quickly (driver 1) and another who accelerated the vehicle gradually (driver 2). The range of 0–120 km/h was divided into 10 km/h intervals to reproduce the acceleration profile and set a common target acceleration for all the vehicle speed zones in sections A–G. The acceleration profiles of drivers 1 and 2 are shown in Fig. 1.

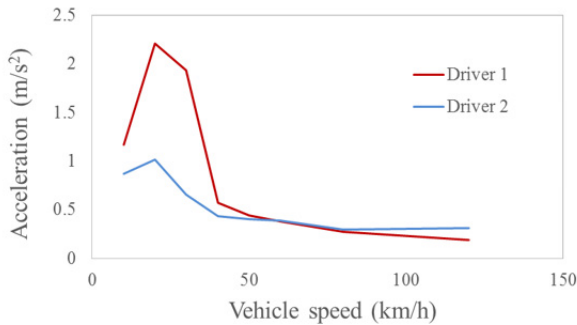


Fig. 1 Acceleration profiles of the two drivers

The simulation was conducted 11 times by varying traffic flows, and the simulation results are presented in Fig. 2.

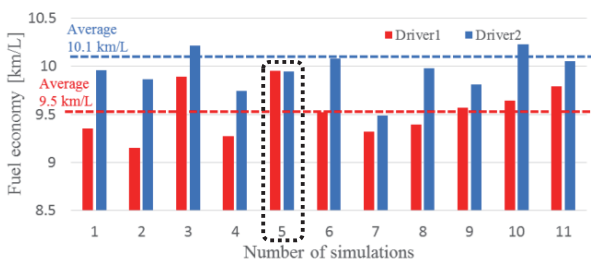


Fig. 2 Fuel economy calculation results

The simulation results show that the driving style (gradual acceleration) of driver 2 is more fuel-efficient; however, the difference from driver 1 is not uniform among the simulation runs. In particular, the result of driver 2 in the fifth simulation run was almost the same as that of driver 1. It was assumed that the unevenness of the fuel economy values was due to the traffic environment. Thus, the results of the fifth simulation run, where the fuel economy values were almost identical, were analyzed. The fuel economy values (in km/L) in each section during the fifth simulation run are listed in Table 3.

Table 3 Fuel economy in each section during the fifth simulation run

No.5	Road type	Fuel consumption [km/L]	
		Driver 1	Driver 2
Section A	Urban	9.2	8.8
Section B	Congestion	9.0	8.3
Section C	Suburb	11.6	10.7
Section D	Congestion	6.9	7.6
Section E	Highway	14.1	13.3
Section F	Suburb	10.5	11.3
Section G	Urban	9.1	9.8

The fuel economy of driver 2 decreases in four sections: A, B, C, and E. Section E was not analyzed in detail because the acceleration levels of drivers 1 and 2 in the high-speed section were almost the same, as shown in Fig. 1. It was assumed that the main cause of the deterioration was the difference between the acceleration and deceleration frequencies caused by the traffic environment, rather than the effect of the different acceleration profiles on the fuel economy. Thus, the remaining three sections, i.e., sections A–C, were analyzed to determine the cause of the decrease in fuel economy.

The fuel economy decreased in sections A and C, which represent urban and suburban roads, respectively, because the vehicle stopped frequently at traffic signals. The vehicle speed profile and signals in section A are depicted in Fig. 3.

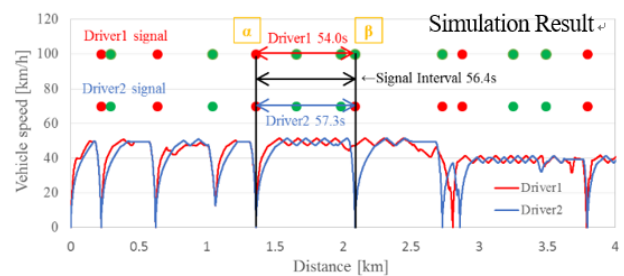


Fig. 3 Velocity profile in section A due to acceleration differences

The red and green dots indicate the signal colors. Both drivers 1 and 2 were at the front when they stopped at signal  $\alpha$ . Thereafter, at the third signal  $\beta$  from signal  $\alpha$ , driver 2 stopped, whereas driver 1 did not stop and instead passed through the intersection.

The running times for drivers 1 and 2 between signals  $\alpha$  and  $\beta$  are 54.0 and 57.3 s, respectively. The time interval from signal  $\alpha$  turning green to signal  $\beta$  turning red is 56.4 s. Accordingly, driver 2, who gradually accelerates the vehicle, stops at this signal. The fuel injection quantities [L] in section A are presented in Fig. 4. According to Fig. 4, the fuel consumptions of drivers 1 and 2 are reversed when driver 2 stops at the signal and then starts the vehicle. It was concluded that this aspect was the main cause of the fuel economy reversal.

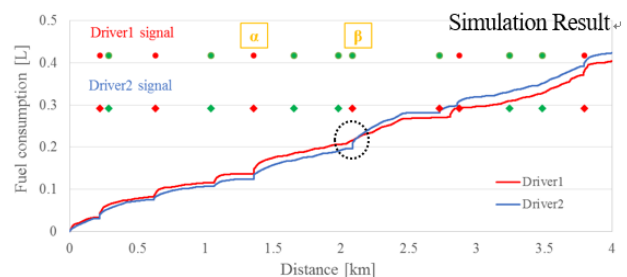


Fig. 4 Fuel consumption in section A due to acceleration differences

Next, an analysis of the results in section B, which represents a traffic jam, is presented. The vehicle speed



profiles and fuel consumption in the relevant section are depicted in Fig. 5. In this section, the arrival times are different due to the different acceleration levels in the previous sections. The vehicle speed profiles of drivers 1 and 2 are significantly different. The fuel economy values of both the drivers were analyzed to elucidate why a higher value was obtained for driver 1. It was found that there were differences in the lengths of traffic jams, stop times, stop frequencies, and fuel-cut times during deceleration.

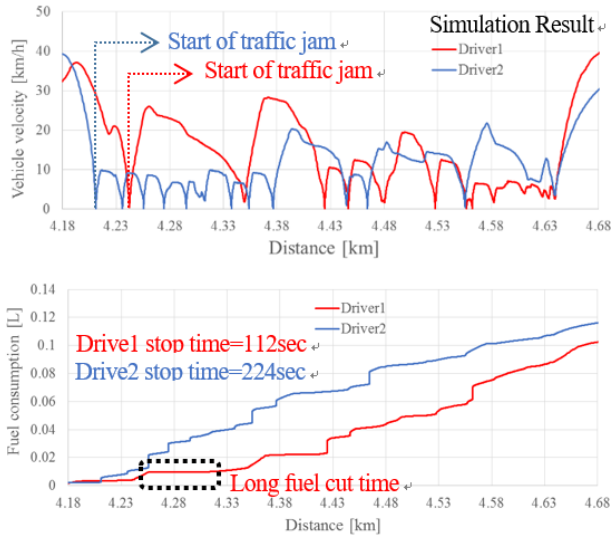


Fig. 5 Velocity profiles and fuel consumption with traffic congestion due to acceleration differences

The causes of the decrease in the fuel economy of driver 2, which is significantly different from that of driver 1, are clarified in Fig. 5. Therefore, it is difficult to determine whether the gradual acceleration of driver 2 directly affects the fuel economy, as it did on the urban and suburban roads.

Further, the simulation runs in which the surrounding traffic environments in a traffic jam were identical were extracted to determine how the gradual acceleration affected the fuel economy in the traffic jam section. The vehicle speed profiles and the fuel consumption of drivers 1 and 2 are presented in Fig. 6.

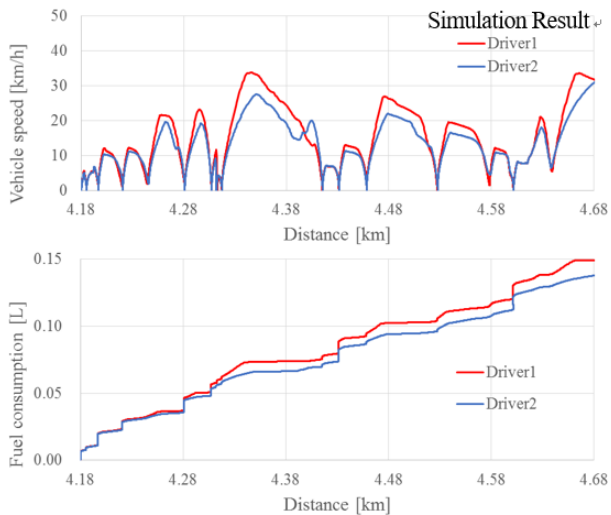


Fig. 6 Velocity and fuel consumption versus distance during traffic congestion due to acceleration differences

The results shown in Fig. 6 indicate that, under the same traffic conditions, better fuel economy is achieved under gradual acceleration. The fuel economy is improved due to the following reasons. In the case of driver 1, who accelerates the vehicle at a high rate, the vehicle speed becomes relatively high in a single trip from start to stop, which presumably consumes a large amount of fuel. By contrast, in the case of driver 2, who accelerates the vehicle gradually, the vehicle begins to decelerate when the vehicle speed is still relatively low, which enables low fuel consumption. In section B, the engine work of driver 1 was 4.55 MJ and that of driver 2 was 4.10 MJ. Engine studies have indicated that, in a traffic jam where a vehicle is frequently stopped and started, fuel economy can be improved by gradually accelerating the vehicle without excessively increasing the vehicle speed.

Through the studies mentioned above, it was confirmed that the fuel economy reversal was caused by the traffic environment rather than simulation failures or other factors. Assuming that real-world fuel economy values can be calculated using this simulation, the following sections describe the measures for further fuel economy improvements, which were investigated with this simulation, that can be proposed to customers.

### 3. Traffic jam detection for higher fuel economy

The studies mentioned above showed that the fuel economy may decrease due to gradual acceleration in uncongested urban and suburban roads with signals. This was determined based on the time interval of the signals and the distance and running time required by a driver to pass through an intersection with an average vehicle speed. However, detecting the time interval of signals is currently difficult, as is detecting the average vehicle speed before passing a signal, because this factor is affected by the surrounding traffic environment. In addition, selecting the acceleration levels for urban and suburban roads is extremely difficult, even for the traffic flow simulation used in this study. This difficulty arises because the lengths of traffic jams vary, as shown in Table 4; the starting point of the low-speed section depends on the simulation case. Thus, this issue was not addressed in this study and remains a subject for future investigations, including vehicle-to-infrastructure and vehicle-to-vehicle technologies.

Table 4 Distance deviations under driving scenes

Distance deviation of driving scene [km]	Driver1		Driver2	
	Max	Min	Max	Min
Traffic congestion	4.3	2.5	5.1	3.1
City and suburb	31.4	29.7	30.9	29

Meanwhile, because gradual acceleration is effective in traffic jams and should be recommended to customers, traffic jam detection was conducted. In traffic jams, vehicles show prominent characteristics, such as an extreme decrease in speed, which is easily detectable by

existing systems. Accordingly, it may be possible to apply these characteristics to utility vehicles.

Currently, navigation systems and smartphone maps offer functions that reflect the results of traffic jam observations based on the traffic information obtained from infrastructure. Highly accurate traffic jam information is required to lead drivers toward eco-driving by means of vehicle behavior control, human-machine interfaces, or ECO Pedal Systems. However, in infrastructure-based traffic jam observations, information update delays and positional inaccuracies occur often. In particular, it was assumed that drivers may experience uncomfortable response delays when they emerge from traffic jams and that the accuracy of the information is insufficient. Therefore, the traffic environment was emphasized to study a method that enables a vehicle to identify traffic jams independently.

First, traffic jams were defined to determine whether the current traffic was congested. Efforts were devoted toward ensuring that drivers do not feel uncomfortable when entering or exiting a traffic jam. To achieve this objective, traffic jams were defined by comparing the speed of the subject or preceding vehicle with the current speed limit information, by using the traffic jam information provided by expressway companies in Japan<sup>4)</sup>.

An analysis of the vehicle speed profiles in Fig. 5 revealed that there are two types of traffic jams: one in which a vehicle repeatedly stops and starts, as in the first half of the trip for driver 2 (short-trip (ST) traffic jam), and another in which a vehicle is continuously operated without stopping (slow-moving traffic jam), as in the latter half of the trip for driver 1. This finding served as the focus for analyzing traffic jams. It was assumed that ST traffic jams easily occur in severe traffic jams on ordinary roads and highways and that slow-moving traffic jams occur during the early stages of traffic jams on highways. These results were used to judge the changes in vehicle behaviors in order to improve the fuel economy in traffic jams, as described later. The measured characteristics of the ST and slow-moving traffic jams are presented in Fig. 7.

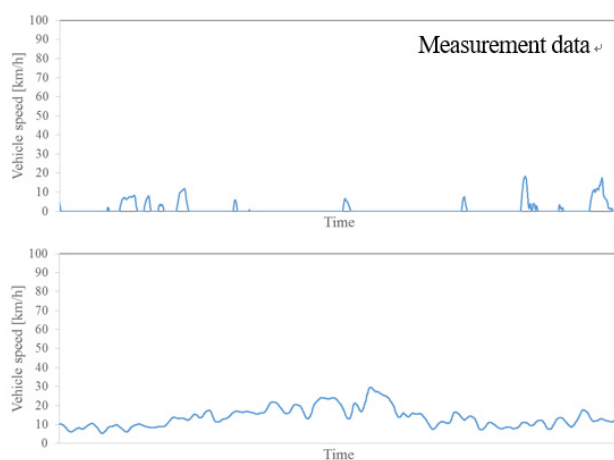


Fig. 7 Vehicle speed profiles for ST traffic jam (upper) and running traffic jam (lower)

To detect and judge traffic jams, apart from the above-described information regarding the vehicle speed limit

and the speeds of the subject and preceding vehicles, information regarding the preceding vehicle was used to determine whether the subject vehicle has emerged from a traffic jam for right/left turning, etc., and information regarding the acceleration of the preceding vehicle was used to immediately determine whether a traffic jam has ended. Moreover, information regarding the distance from the preceding vehicle was utilized. The speed information of the subject vehicle was utilized to determine the type of traffic jam and to control the vehicle speed after identifying the traffic jam.

Two points were set from a high-level perspective when devising the method for detecting traffic jams: versatility improvement and acceptability improvement. Acceptability refers to the condition described above, that is, the condition that a driver does not experience an uncomfortable judgment delay when a traffic jam is detected.

First, to improve versatility, a method that uses only the information regarding the preceding vehicle was designed. Owing to the latest research and development of autonomous driving, vehicles are now equipped with a detection system that provides a 360° view of the surroundings. Thus, an improvement in the detection accuracy was attempted by using the information regarding the vehicles in the next lane.

Considering the possibility that only the lane in which the subject vehicle is operating is congested owing to reasons such as the traffic jam has just started or the lane has a branch ahead, it is necessary to identify traffic jams by simply using the information regarding the preceding vehicle. Moreover, by making a judgment according to the information of the preceding vehicle, a traffic jam on a single-lane road can be detected as well, which improves versatility.

Emergency braking and adaptive cruise control systems have become increasingly common among vehicles in the market; in such vehicles, this traffic detection strategy can be applied easily.

Second, to improve acceptability, the vehicle speed criteria were differentiated to determine whether to enter or exit a traffic jam. Specifically, the vehicle speed was set higher when exiting a traffic jam than that when entering a traffic jam. In addition, the filtered or average vehicle speed information was utilized to identify traffic jams. This approach helped avoid the short-time repetition of entering and leaving a traffic jam, caused by the instantaneous vehicle speed fluctuations. To identify ST traffic jams, the per trip vehicle information based on the immediately preceding start and stop was used. As it was necessary to define one trip of a single vehicle to estimate the average speed of one trip, the speed of the subject vehicle was used instead of that of the preceding vehicle, because the preceding vehicles may change. By contrast, for slow-moving traffic jams, information regarding the preceding vehicle was utilized. For the vehicle speed limit information for a road on which a traffic jam is identified, navigation system data that were recently registered were utilized.

As shown in Fig. 8, a traffic jam determination control model incorporated with the systems described above was configured using MATLAB/Simulink.

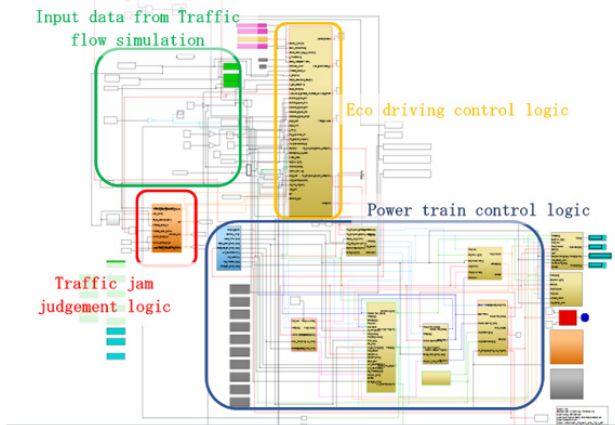


Fig. 8 Simulink model including traffic jam judgment system

#### 4. Results of traffic jam determination control

A traffic jam identification simulation was conducted by inputting the data obtained from actual driving in the MATLAB/Simulink control model mentioned above. The traffic jam detection results are shown in Fig. 9. The timings of entering and exiting the traffic jam, as recorded by the driver, are expressed as jam flags (driver).

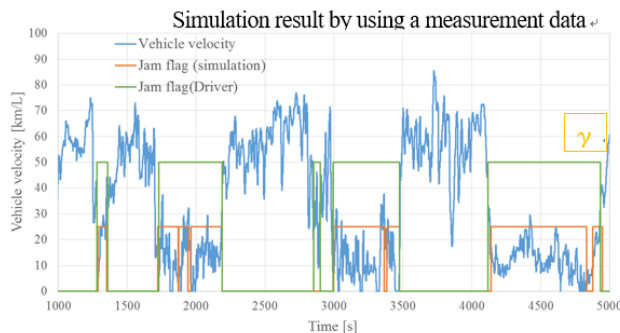


Fig. 9 Calculation results for traffic jam judgment system

These results indicate that the detection accuracy of the control system is 90% with respect to the scenes that the driver judged as traffic jams. Regarding the delay that occurred when exiting a traffic jam, there exists a scene γ in which the delay reaches a maximum of 12.4 s. It was confirmed that the increase in vehicle speed in this scene was approximately 3 km/s, which is an extremely

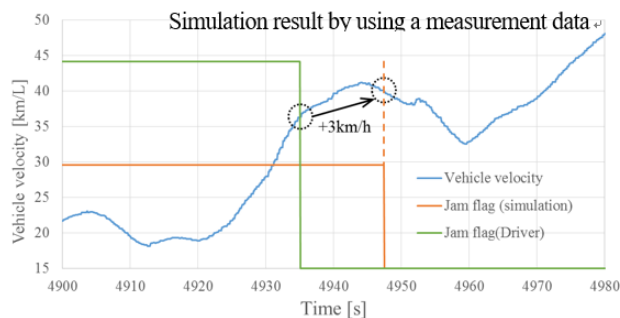


Fig. 10 Magnified view of the simulation results corresponding to exiting the traffic jam

gradual acceleration. The data corresponding to point γ are shown in detail in Fig. 10.

It was estimated that this delay is acceptable because the acceleration is extremely gradual and subsequently shifts to deceleration. However, it will be carefully verified whether this delay is acceptable for drivers in traffic jams.

Regarding the other aspects, it was found that exiting a traffic jam was identified when the preceding vehicle had moved away or accelerated. Thus, it was confirmed that the criteria based on factors other than the vehicle speed were effective.

#### 5. Study of behaviors for higher fuel economy in traffic jams

Next, the vehicle behaviors that improve fuel economy in traffic jams were studied. As described earlier, it was confirmed that fuel economy was improved by gradual acceleration in the traffic jam section. In particular, for an ST traffic jam, when the driver gradually accelerates the vehicle, the vehicle begins to decelerate at a low vehicle speed, as shown in Fig. 6, which helps maintain low fuel consumption.

In a slow-moving traffic jam, it is difficult to detect the stop timing in advance. However, in an ST traffic jam, because the vehicle frequently stops, it is relatively easy to estimate the deceleration and stop timing. It was assumed that, in an ST traffic jam where the deceleration and stop timing could be estimated, the fuel economy would be improved by ending the acceleration at a low vehicle speed and shifting to cruising. Thus, the setting of a speed limit for ST traffic jams was considered next.

It was assumed that the limiting speed would make the driver feel more uncomfortable than gradual acceleration, because the subject vehicle ends the acceleration even when the preceding vehicle is accelerating. Therefore, it is necessary to determine the vehicle speed limit considering the subjective evaluation of the drivers. To determine the fuel economy improvement effect, it was simulated and verified by temporarily limiting the speed to half of the road speed limit. The speed limit was controlled not by adjusting the acceleration but by temporarily changing the target vehicle speed when an ST traffic jam was detected, while also accounting for the vehicle speed overshoot and smooth shifting to the limit speed. However, because the distance from the preceding vehicle would increase if a speed limit was set, a control program was established that canceled the speed limit when the distance reached a certain value and resumed gradual acceleration.

Based on this procedure, gradual acceleration was performed and a speed limit was set when an ST traffic jam was detected. Moreover, gradual acceleration was only performed in a slow-moving traffic jam.

#### 6. Results of behaviors for higher fuel economy in traffic jams

The effect of gradual acceleration on the fuel economy, as shown in Fig. 6, was not considered. Instead, the effect

of the speed limitation was emphasized. The simulation results of the effects of the fuel-saving behaviors in traffic jams on the fuel economy are presented in Fig. 11.

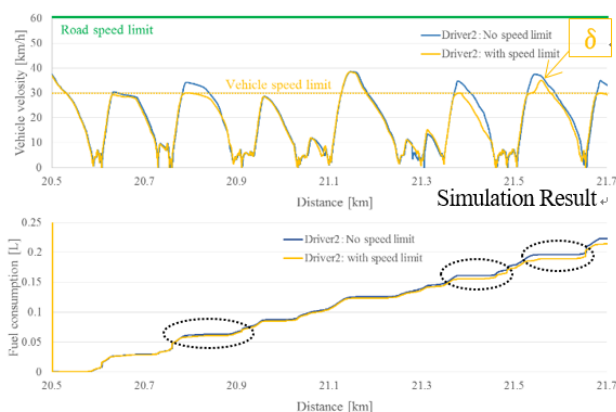


**Fig.11 Result of speed limit control during traffic jam and differences of fuel consumption.**

The scenarios in which the acceleration ends early such that the vehicle speed decreases to half of the road speed limit are denoted in green; these scenarios indicate that an increase in fuel consumption is suppressed. In addition, because the target vehicle speed is altered, the acceleration decreases before the vehicle reaches the speed limit, which also suppresses fuel consumption. Point  $\delta$  in the latter half shows the suspension of the speed limitation and the re-acceleration due to the increase in the inter-vehicular distance. However, when compared to the vehicle speed profile without the speed limitation, deceleration begins at a low speed even after re-acceleration, which indicates that the fuel consumption is low.

## 7. Considerations

- It was found that the traffic jam determination system identifies an exit from a traffic jam when the vehicle speed increases, the preceding vehicle moves away, or the acceleration of the preceding vehicle reaches or exceeds a specified value, which is similar to the perception of drivers.

- The effects of fuel-saving behaviors on the fuel economy in traffic jams demonstrated that, by setting a speed limit, the acceleration ends at a low vehicle speed, which helps maintain low fuel consumption. It was also found that, by setting a speed limit based on the target vehicle speed, the acceleration decreases before the

vehicle reaches the speed limit, which also lowers the fuel consumption. This finding indicates that a fuel economy effect was achieved.

- A scenario in which the speed limitation was suspended because the inter-vehicular distance increased was also identified. The speed limitation was suspended, and acceleration was applied. However, as the deceleration commenced before the vehicle speed increased to that of driver 1, the fuel consumption per trip for the same distance was less than that of driver 1.

## 8. Conclusion

The following conclusions were drawn from the results of this study:

- (1) On urban and suburban roads where vehicles stop at signals, the frequency of vehicle stops increases with gradual acceleration, which lowers the fuel economy of the vehicles that are gradually accelerated. However, the fuel economy of such vehicles is improved in traffic jams.
- (2) The fuel economy values of drivers 1 and 2, who used different rates of acceleration, were reversed in one scenario because of the differences in traffic environments, which enabled a verification of the quantitative effect on fuel economy. Thus, it was possible to estimate real-world fuel economy values in order to create a simulator that verifies the effects of different driving styles on these values.
- (3) Traffic jams could be identified using an existing sensor that detects the preceding vehicle and acquires speed limit information for navigation systems.
- (4) Traffic jams were classified into ST and slow-moving traffic jams; both gradual acceleration and the speed limitation were utilized for ST traffic jams, where vehicles are repeatedly started and stopped. By using these approaches, further fuel economy effects can be expected.

## References

- 1) 福本 泰己: 交通流Simulationを用いた実用燃費予測手法, 自動車技術会学術講演会予稿集(2017)20176175
- 2) Mathworks japan HP :<https://jp.mathworks.com/>
- 3) PTV社HP : <http://vision-traffic.ptvgroup.com/en-us/home/>
- 4) NEXCO中日本HP渋滞の定義は?: <http://highwaypost.c-nexco.co.jp/faq/traffic/rule/345.html>

## Authors



Yasuki Fukumoto



Hiroshi Kuriki



Hajime Miura



Seishi Shimamura



Takahito Nishi

# A Clarification of Relationship Steering Force and Yaw Characteristics to Line Traceability in Small Steering Angle

Mitsunori Tao\*

**Abstract** When driving along a straight roadway, a driver regularly makes minute steering adjustments in order to maintain the vehicle's position within the driving lane. This paper clarifies the quantitative relationship of several steering characteristics in this scenario for accurate line tracing. In this research, the first step was to investigate the driver's behavior when driving along a straight roadway. Then, a driver model consisting of this behavior was created and underwent driving simulations to hypothesize the relationship between line traceability, steering force and vehicle yaw characteristics. Finally, this hypothesis was tested and verified using an actual driving simulator.

## 1. Introduction

When one considers the usual traveling scenario of an ordinary driver, one can imagine that most of the scenario probably consist of driving generally in a straight line, including the moments at which the driver performs minute steering adjustments to control the travel locus. A survey conducted by the author and others in Europe and Japan supports this assumption. According to the survey results, the proportion of the driving scenario at which the steering angle was 5 degrees or less (which was considered to be a minute steering operation) was more than half (51.1%) in all vehicle speed ranges and approximately 80% (79.6%) in the vehicle speed range at or above 80 km/h.

Line traceability, which is the driver's ability to trace the target driving line by performing steering adjustments of the vehicle for minute angles (encountered frequently as described previously), is an important performance for many drivers. Extensive research on steering force characteristics, which is considered to have the largest contribution to this performance, has been conducted<sup>(2)-(4)</sup>, including research on the steering reaction force<sup>(1)</sup>, which is the force that the driver experiences linearly based on Weber's law.

Moreover, research on vehicle movements such as the yaw characteristics, which are considered to have an effect as significant as that by the steering force, has been conducted<sup>(5)-(7)</sup>. Only a very few case studies on the latter research topic clarified the quantitative relationships while including the driver's steering characteristics in the minute angle range. Therefore, in the actual development site, achieving such performance was often dependent on the tuning of the actual vehicle.

We conducted this study based on the concept that designing this performance should enable us to stably provide a target performance to many drivers as well as contribute to reducing the development cost and environmental load by decreasing the dependency on prototype vehicles.

In this study, a scenario was established on a driving course in which the vehicle's travel locus was to be finely adjusted by a minute steering angle (approximately  $\pm 5$  degrees) while the vehicle traveled in a straight line at a constant speed of 80 km/h. The purpose of this study was to clarify the quantitative relationship between the steering force and yaw characteristics with respect to the line traceability using the deviation between the actual trace line and target line as the evaluation index of line traceability.

The first step was to conduct a basic test to ascertain the driver's characteristics in the minute steering angle range. Next, the obtained characteristics were incorporated into the driver model, and an analysis was conducted after combining that model with the vehicle model. Based on the obtained analysis results, a hypothesis of the quantitative relationship between the steering force and yaw characteristics with respect to the line traceability was established. As the final step, the hypothesis was verified in a driving simulator test.

The two tests in this study were conducted with 25 drivers, whose ages were between 20–59 years. They drove cars routinely, for commuting, etc. Informed consent of the contents examined and approved by the Experimentation Ethics Committee of Nissan Motor Co., Ltd. was obtained from the participants of the tests.

\*Mobility and AI Laboratory

## 2. Ascertaining driver's characteristics in the minute steering angle range

A test was conducted to ascertain the two basic characteristics of the drivers, which were considered to be important in the minute steering angle range.

### 2.1 Steering angle at which the driver has perceived an input into the vehicle

For the first characteristic, a test was conducted using a driving simulator fixed onto the floor (Fig.1) to ascertain the minimum steering angle at which the driver perceived that an input had been made into the vehicle."



Fig.1 Fixed-type Driving Simulator

The drivers were instructed to close their eyes, begin steering the steering wheel from its neutral position, and stop at the minimum steering angle at which they perceived that an input had been made into the vehicle.

The drivers were instructed to perform the same operation five times for both the left and right steering operations, and the steering angle was recorded at each trial. In addition, with the assumption that this steering angle was dependent on the predetermined steering force characteristics, the test was conducted with different steering force characteristics. The steering angle–steering force characteristics of a certain C-segment vehicle, traveling at 80 km/h, was set as the reference ("Base" in Fig.2), and four additional specifications were established by multiplying the reference steering force by

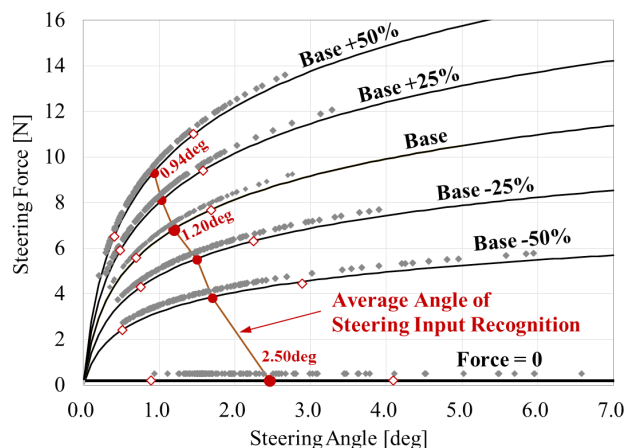


Fig.2 Steering Force Characteristic & Experimental Result

$\pm 25\%$  and  $\pm 50\%$  over the whole range. Another specification, which had zero steering force over the whole range, was added; thus, a total of six specifications of steering force characteristics were used in the test.

The test result is shown in dot data in Fig.2. The average value of the minimum steering angles perceived by all 25 drivers and in all trial times was 1.2 degrees for the base specification. We also confirmed that the value of the minimum steering angle became smaller as the steering force became heavier. When the steering force was increased by +50%, the angle value decreased to 0.94 degrees. In contrast, when the steering force was set to zero, the angle value increased to 2.5 degrees, which was more than twice the angle value for the basic specification.

Outlined rhombus marks indicated the dispersion of each specification, which were approximately  $\pm 0.5$  to  $\pm 1$  degrees.

### 2.2 Yaw rate at which the driver has perceived vehicle movement

The other driver characteristic that was considered important in the minute steering angle range was the minimum yaw rate at which the driver perceived that "the vehicle had moved." The test to ascertain the minimum yaw rate was conducted using a driving simulator<sup>(8)</sup> equipped with a 360° screen and a turntable that could turn in the yaw direction (Fig.3).

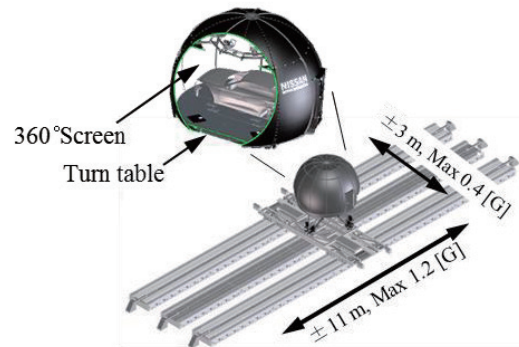


Fig.3 Driving Simulator

As shown in Fig.4 (a), a skidpad with a radius of 300 m and trees planted 10 m apart on its periphery was established as the scenario, and a vehicle was placed at its center. The yaw rate of the turntable was increased from the stopped state in a constant yaw angle acceleration of  $0.05 \text{ deg/s}^2$ , which could not be perceived by the driver. Drivers, while gazing through the front screen, were instructed to press the switch at hand immediately after they perceived the movement in the

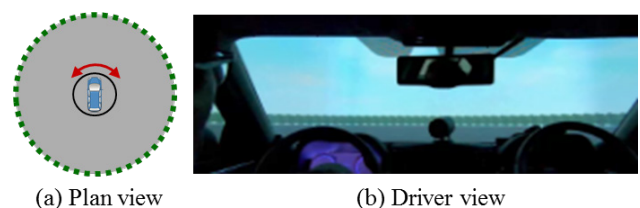


Fig.4 Yaw-rate Sensitivity Experimental Scene

yaw direction. The test was conducted five times for both the right and left directions, and the yaw rate value was recorded at each trial.

The measurement results are shown in Fig.5. The horizontal axis represents the number of the 25 drivers, and the vertical axis indicates the minimum yaw rate each driver perceived. The average value of the minimum yaw rate perceived by all 25 drivers in all trial times was 0.21 deg/s, and the dispersion was  $\pm 0.05$  deg/s.

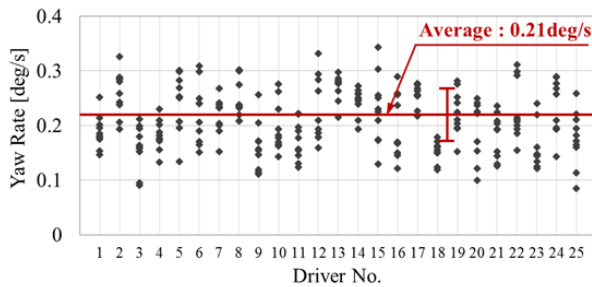


Fig.5 Yaw-rate Sensitivity Experimental Result

The steering angle that generated this yaw rate of 0.21 deg/s was approximately 2 degrees at a vehicle speed of 80 km/h, which is explained in Section 3 using data. Because the steering angle at which a driver perceived that an input had been made into the vehicle was approximately 1 degree, we considered that, within the steering angle range of 1–2 degrees, the driver could not yet perceive vehicle movement and steered via feedforward because the driver could sense only the information of the steering force. This was considered to be one of the reasons the steering force characteristics have been considered as important in the minute steering angle range. This also suggests the importance of properly setting the steering force and yaw characteristics within this steering angle range.

### 3. Hypothesis of the quantitative relationship between steering force and yaw characteristics with respect to line traceability in the minute steering angle range

#### 3.1. Incorporating the driver’s characteristics in the minute steering angle range into the driver model

The look-ahead-point error model<sup>(9)</sup> shown in Fig.6 (a) was used as the driver model. As this study was regarding the minute steering angle of approximately  $\pm 5$  degrees and with the quasi-steady state, slow steering input that was generally at or below 10 deg/s, the simplest function<sup>(9)</sup> that consisted of the proportionality constant ( $h$ ) (between the look-ahead-point error  $\varepsilon$  and steering angle) and dead time ( $\tau_L$ ) (Fig.6 (b)) was used for the driver transmission function. For the base model, the look-ahead-distance ( $L$ ) was set as 33.3 m,  $\tau_L$  was set as 0.3 s, and  $h$  was set as 0.25 rad/m. The two driver characteristics in the minute steering angle range, obtained in the previous section, were incorporated as follows.

As the first revision,  $h$ , which was a constant value in the conventional driver model, was changed depending on the difference in the steering force characteristics. We

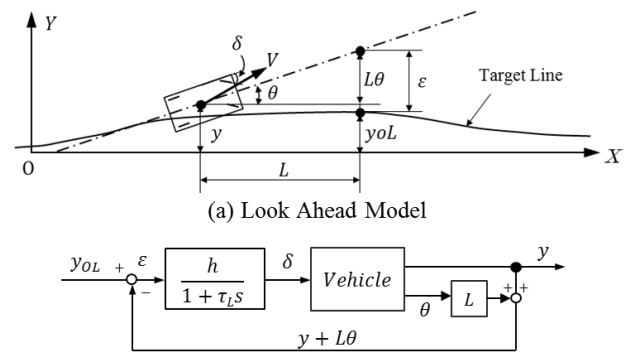


Fig.6 Driver Model

confirmed in the test described in the previous section that the steering angle at which a driver perceived an input had been made into the vehicle varies depending on the difference in the steering force. This is summarized in Table 1, which shows the average value of the perceived steering angles for each specification. The table also shows the amount of driver’s effort that was calculated considering the change in force between the neutral position and the steering angle for each specification, assuming a steering wheel radius of 0.18 m.

Table 1 Driver Work and Definition of Parameter "h"

Spec.	Steering Angle [deg]	Work [ $\times 10^{-2}$ Nm]	h [rad/m]
Base-50%	1.79	1.71	0.50
Base-25%	1.50	1.84	0.33
Base	1.20	1.78	0.25
Base+25%	1.03	1.71	0.20
Base+50%	0.94	1.76	0.17

Although the steering angle perceived by the driver varied considerably depending on the difference in the steering force, the amount of effort required by driver was almost in the same range, between  $1.7\text{--}1.8 \times 10^{-2}$  Nm. From this result, we can deduce that drivers perform the steering input based on the amount of effort rather than on the steering angle itself, at least in the minute steering angle range. Therefore, we assumed that the value of  $h$  of the driver model will change depending on the difference in the steering force and that the change is inversely proportional to the magnitude of the steering force. In more specific terms, the  $h$  value of each specification was set as shown at the right end column of Table 1, with respect to the value of the base specification ( $h = 0.25$  rad/m).

In the conventional driver model, the look-ahead-point was set to move laterally according to the amount of even the slightest movement in the yaw direction. In the test described in the previous section, we confirmed that drivers, on average, do not perceive the vehicle’s movement until the yaw rate of  $r_0 = 0.21$  deg/s occurs. Therefore, as the second revision, the look-ahead-point was changed so that only when this value is attained. In more specific terms,  $L\theta$  of “ $y + L\theta$ ,” which is the feedback from the vehicle in Fig.6 (b), was set at zero if  $r < 0.21$  deg/s.

### 3.2 Incorporation of the dead-band characteristics of the minute steering angle range into the vehicle model

In this study, a two-wheel vehicle model was used. The block diagram(9) is shown in Fig.7, and the precondition parameters are listed in Table 2.

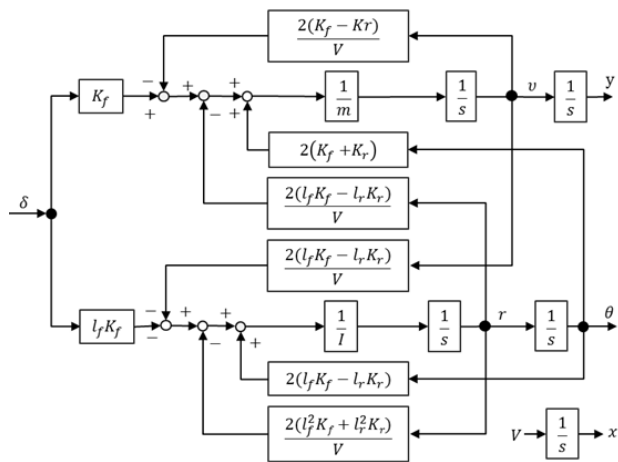


Fig.7 Vehicle Model Block Diagram

Table 2 Vehicle Model Parameter

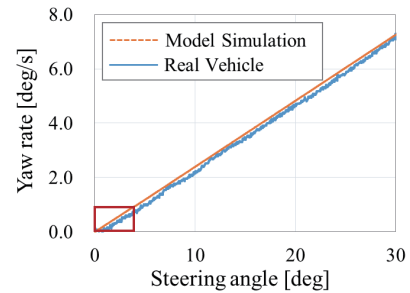
Parameter	Symbol	unit	Value
Vehicle Mass	m	kg	1670
Vehicle Yaw Inertia	I	kgm <sup>2</sup>	2600
Front axle~C.G.	l <sub>f</sub>	m	1.08
Rear axle~C.G.	l <sub>r</sub>	m	1.62
Front Cornering Power	K <sub>f</sub>	kN/rad	62.5
Rear Cornering Power	K <sub>r</sub>	kN/rad	95.5
Steering Gear Ratio	-	-	15.0

A model of the area of the minute steering angle range at which the yaw rate does not occur, which was extracted from the detailed measurements of the actual vehicle, was created and incorporated into the vehicle model in this study.

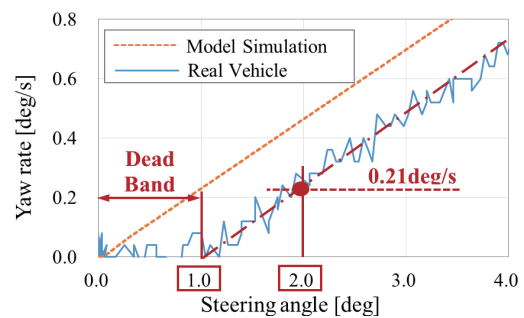
Fig.8, which shows the steering angle in the horizontal axis and yaw rate in the vertical axis, illustrates the comparison between the simulation results of the conventional vehicle model and the measurement results of the actual vehicle in a scenario in which a slow steering input (10 deg/s) was made in a C-segment vehicle that is traveling at a constant speed of 80 km/h. Fig.8 (a) indicates that the simulation generally reproduced the measurement results of the actual vehicle with high accuracy. However, a considerable difference was observed between the two results in the minute steering angle range shown in Fig.8 (b), which shows the enlarged portion surrounded by the rectangular frame in Fig.8 (a). The measurement result of the actual vehicle shows an area in which the yaw rate did not occur until the steering angle was approximately 1 degree, which was probably owing to, for example, friction in the steering or suspension. The enlarged view shows that the minimum yaw rate a driver could perceive ( $r_0 = 0.21 \text{ deg/s}$ , explained in the previous section) corresponded to the steering

angle of approximately 2 degrees. Additionally, this steering angle was considerably affected by the area in which the yaw rate did not occur.

In this study, this area was defined as the “yaw-rate dead band,” and was considered to be a representative characteristic of yaw behavior when investigating the line traceability in the minute steering angle range. In addition, this element was incorporated into the vehicle model. In more specific terms, the setting was adjusted to offset the steering angle, which was input from the driver model into the vehicle model, by the amount of the dead band.



(a) Over View



(b) Enlarged View

Fig.8 Simulation and Real Vehicle Yaw-rate Comparison

Fig.9 shows the driver-vehicle model, which was the combination of the driver and vehicle models, used in this study to investigate the line traceability in the minute steering angle range. The driver characteristics in the minute steering angle range, explained in the previous section, were incorporated into the driver model. The dead band element was incorporated into the vehicle model.

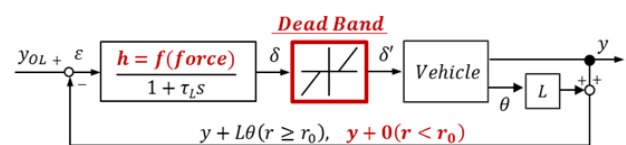


Fig.9 Driver-Vehicle Block Diagram

### 3.3 Defining the evaluation course and evaluation index

The evaluation course was established as shown in Fig.10. The course consisted of two 1200R curves, right and left, and a transition curve. A vehicle traveling in a straight line at a constant speed of 80 km/h was driven in this curved area with the steering input of approximately 5 degrees and mostly less than 10 deg/s.



For the established course as the target drive line, the evaluation index of line traceability was defined as the deviation between the target line and actual trace line when a vehicle traveled from a straight line to 1200R as the driver turned the steering wheel. The deviation between the vehicle's gravity center locus and the target line was measured at a sampling rate of 100 Hz while the vehicle traveled on a 60-m evaluation section. The evaluation section was composed of a 30-m transition curve section, which immediately followed the straight line section and subsequent 30 m of the 1200R steady state curve section. The average value of the sampled data was defined as the "line trace deviation [m]." The inside deviation with respect to the target line was considered to be positive, and the outside deviation was considered to be negative.

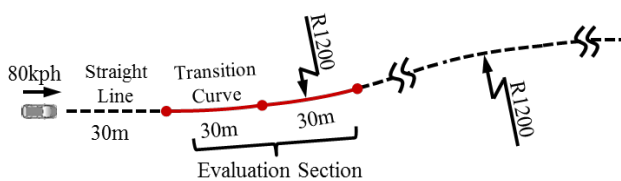


Fig.10 Evaluation Course

### 3.4 Hypothesis of the quantitative relationship between the steering force and yaw rate dead band with respect to the line trace deviation

Based on the aforementioned the driver characteristics and vehicle characteristics in the minute steering angle range, let us consider the steering force and yaw-rate dead band required for a driver to accurately trace the target line. When a driver sees a curve ahead, the driver will begin steering in proportion to the look-ahead-point error. Its proportionality constant is dependent on the magnitude of the steering force. The steering wheel will be turned at a large constant value when the steering force is light and constant value is small and when the steering force is heavy. Although a driver perceives that a steering input had been made into the vehicle for the first time at a steering angle of approximately 1 degree, the driver cannot yet perceive the yaw rate of the vehicle movement. Therefore, while imagining the vehicle's movement, the driver continues to steer via feedforward in proportion only to the increase in the look-ahead-point error that changes along with the change in the target drive line ahead. The driver will finally perceive that the vehicle has moved when the steering angle exceeds approximately 2 degrees. Here, if the magnitude of the dead band is appropriate with respect to the proportionality constant, the driver will perceive the vehicle movement as the one the driver expected, and the vehicle can continue traveling accurately on the target line. However, if the magnitude of the dead band is small with respect to the proportionality constant, the driver will perceive that the vehicle is turning further inside of the target line than the driver expected. In contrast, if the magnitude of the dead band is large with respect to the proportionality constant, the vehicle will already be turning outside of the target line when the driver

perceives the vehicle movement.

In the scenario of traveling on the established evaluation course at 80 km/h, the time at which the driver can perceive yaw rate will be after the vehicle has traveled more than 10 m on the transition curve (the timing will be dependent on the specification). After this timing, the actual timing the feedback steering is input into the vehicle will be after the driver dead time of 0.3 s has elapsed, or after the vehicle has traveled more than 6 m further. Therefore, the important aspect to consider here could be the method of enabling the driver to perceive the vehicle movement the driver has expected before the driver can perceive the vehicle movement while traveling on the feedforward section.

The analysis results using the model used in this study are shown quantitatively in Fig.11. The results for each specification can be observed as follows. For the specification with a -50% steering force of the base specification, an increased proportionality constant, and a dead band reduced to zero degrees, the trace line deviated inside the target line. In contrast, for the specification with a +50% steering force of the base specification, a reduced proportionality constant, and a dead band increased to 2 degrees, the trace line deviated outside the target line. Some other specifications with properly balanced combinations of the steering force and dead band could trace the target line relatively accurately.

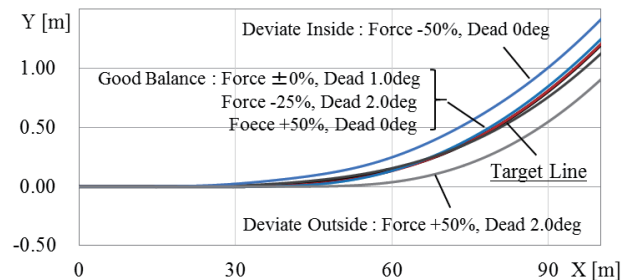


Fig.11 Line Trace Simulation

Fig.12 shows a graph in which the steering force (of the base specification and the base specification multiplied by  $\pm 25\%$  and  $\pm 50\%$ ) is shown in the X-axis, the dead band (changed between 0 to 2 degrees in increments of 0.5 degrees) is shown in the Y-axis, and the line trace deviation (calculated for all 25 specifications) is shown in the Z-axis. The graph shows that, for the specification at the back of the graph, at which the steering force is light and the dead band is small, the line trace deviation value becomes large and positive, which indicates that the vehicle locus deviates inside the target line. For the specification at the front of the graph, at which the steering force is heavy and the dead band is large, the line trace deviation value becomes large and negative, which indicates that the vehicle locus deviates outside the target line. The transition of deviation values for other specifications between these two was smooth. The thick broken line on the  $Z = 0$  plane represents the quantitative relationship between the steering force and yaw rate dead band at which it should be possible to realize the most accurate line traceability with zero line

trace deviation. Based on this hypothesis, tests were conducted for verification.

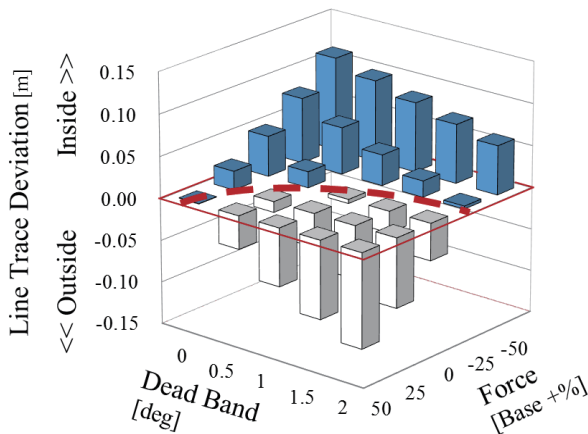


Fig12. Simulation Result of Line Trace Deviation

### 4. Verification of the hypothesis using the driving simulator

#### 4.1 Verification of the accuracy of the driving simulator

The driving simulator shown in Fig.3 was used to verify the hypothesis. This simulator was equipped with a cabin mounted on a hexapod, which was mounted on slide rails with a movable range of 22 m × 6 m. 64 linear motors precisely drove the equipment to enable the actual vehicles and many scenarios to be reproduced with high reproducibility.

Fig.13 shows the comparison results of the steering force and yaw rate characteristics (considering the dead band), which were the focus of this study, between the measurement data of the actual target vehicle (C-segment vehicle) and the measurement data of the driving simulator. High reproducibility by the driving simulator was confirmed for both the steering force and yaw rate.

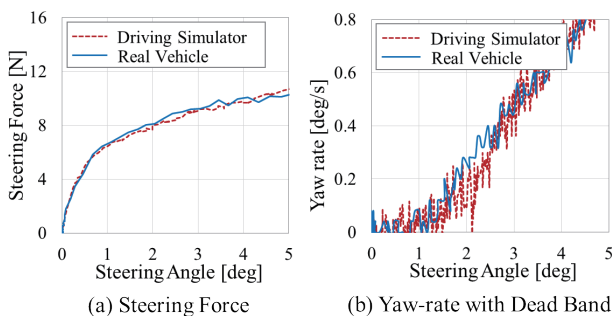


Fig13. Driving Simulator Accuracy Confirmation

#### 4.2 Establishing the evaluation scenario

The driving lanes were established as shown in Fig.14, where the center lane was designed to be according to the evaluation course defined in Fig.10. To reduce the variation between drivers and trials, we set the lane width to 1.8 m, which was almost equal to the vehicle

width. In addition, to reduce the left/right difference between left steering and right steering, we established the scenario in a manner that the vehicle would travel on the center lane of a three-lane road, rather than traveling on one side of a two-lane road.

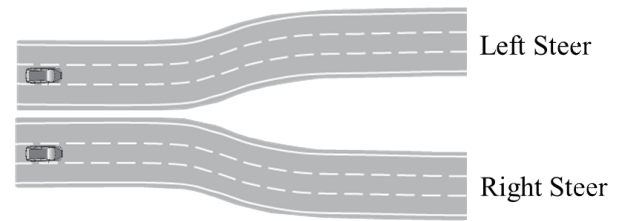


Fig14. Evaluation Course on Driving Simulator

#### 4.3 Test method

The test was conducted with 25 drivers (as the one described in Section 2). The vehicle speed was maintained at 80 km/h, and the drivers were instructed to perform the steering operation only, aiming at the center of the lane. As shown in Table 3, 17 test specifications were selected based on the 25 specifications examined when establishing the hypothesis, considering the test efficiency. The measurements of 17 specifications were conducted one time each on the left and right steering courses, 34 times in total, in the order randomly arranged by the linear congruential generator<sup>(10)</sup>. Sufficient resting time was provided between the tests. The aforementioned measurement steps were repeated three times to obtain three sets of the data for each left and right steering of 17 specifications.

Table 3 Driving Simulator Experimental Specification No.

		Dead Band Angle [deg]				
		0.0	0.5	1.0	1.5	2.0
Steering Force	Base-50%	4	—	17	—	5
	Base-25%	—	11	12	13	—
	Base	16	10	1	6	14
	Base+25%	—	9	8	7	—
	Base+50%	3	—	15	—	2

#### 4.4 Test results

Fig.15 shows the representative examples of measurement results of one of the drivers. The graphs in the figure show the vehicle’s trace line of specifications at the four corners of Table 3, measured for left steering. We confirmed that the results of the graphs generally had the same trend as suggested by the hypothesis. For specification 4, for which the steering force was light and the dead band was small, the vehicle trace line deviated inside the target line. For specification 2, for which the steering force was heavy and the dead band was large, the vehicle trace line deviated outside the target line. For specifications 3 and 5, for the steering force and dead band were well-balanced, the vehicle trace line traced the target line quite accurately.

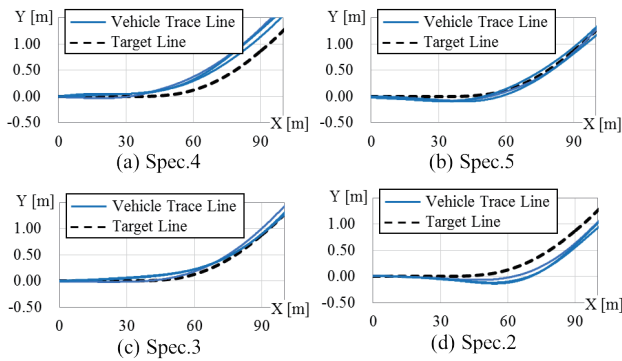


Fig15. Line Trace Experimental Result

Fig.16, which shows the same 3-axis graph as in the hypothesis study, shows the average values of the line trace deviations that were measured with 25 drivers for 17 specifications. Figs. 16 (b) to (z) show the measurement results for each of the 25 drivers. Fig.16 (a) shows the average values of all 25 drivers.

As Figs. 16 (b) to (z) show, variations were observed among drivers in the magnitude of line trace deviation and in the relationship between the steering force and yaw-rate dead band in which the line trace deviation becomes zero. However, a common trend among all drivers was observed. The trace line deviated inward for specifications in which the steering force was light and the dead band was small, and the trace line deviated outward for specifications in which the steering force was heavy and the dead band was large.

The thick broken line on the  $Z = 0$  plane in Fig.16 (a), which shows the average values of all 25 drivers, represents the verification result of the quantitative relationship between the steering force and yaw rate dead band in which the line trace deviation became zero and thus enabled the drivers to realize the most accurate line tracing. This result confirmed that the quantitative relationship established in the hypothesis was almost reproduced, although the broken line tended to shift a little toward the sides of heavier steering force and larger dead band.

The broken line, which represents the specifications for zero line trace deviation, shifted toward the sides of heavier steering force and larger dead band with respect to the broken line examined in the hypothesis. The main reason for this shifting was considered to be because the parameter in the driver model, used to examine the hypothesis, deviated from the parameter of the actual drivers. We consider that accuracy can be increased further in the future by measuring additional data and identifying the parameters.

As described above, the hypothesis on the quantitative relationship between the steering force and yaw rate dead band with respect to the line trace deviation in the minute steering angle range was verified.

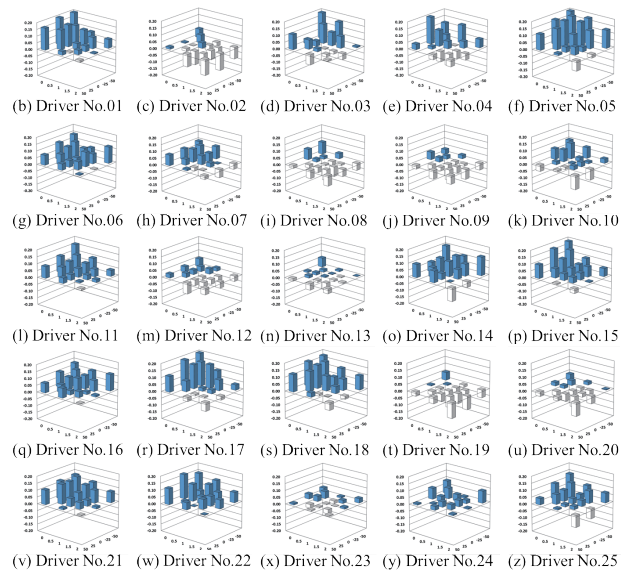
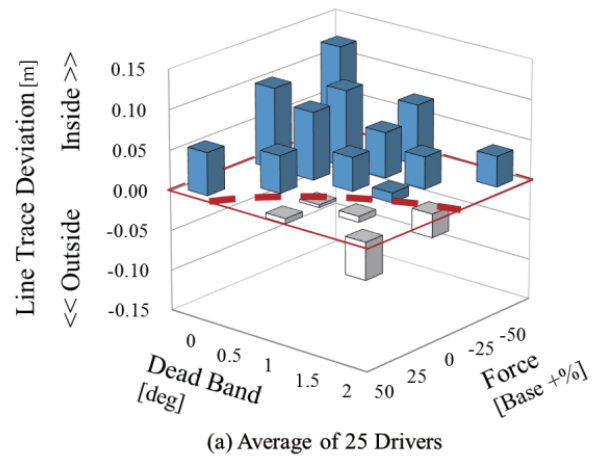


Fig16. Experimental Result of Line Trace Deviation

### 5. Conclusion

After ascertaining the drivers' characteristics regarding the steering force and yaw rate in the minute steering angle range, and after defining the vehicle's yaw rate dead band in the minute steering angle range, those elements were incorporated into the conventional driver-vehicle model. The quantitative relationship between the steering force and yaw rate dead band with respect to the line traceability was clarified by establishing a hypothesis on the line tracing mechanism in the minute steering angle range, conducting quantitative analysis using a new model, and conducting verification tests using the driving simulator.

The results of this study demonstrate that designing the line traceability in the minute steering angle range, which conventionally has been dependent on tuning, is possible by using the steering force and yaw rate dead band.

Note that this study finding is a conclusion derived from the average values of data measured with 25 drivers, and the effects of their dispersion is an issue that requires further investigation.

## References

- (1) 山田大介, ほか: ドライバが知覚する操舵反力の定量化法, 自動車技術会論文集 Vol.47 No.2 pp.437-442 (2016)
- (2) 久代育生, ほか: オンセンターハンドリングの為のステアリングシステム, 自動車技術会論文集 Vol.40 No.2 pp.233-238 (2009)
- (3) 高僧美樹, ほか: 摩擦特性によるオンセンタフィードバックの研究, 自動車技術会 春季大会 学術講演会前刷集No.3-19 pp.1-6 (2019)
- (4) Anna Newberry: Driver Perception of Steering Feel, Journal of Automobile Engineering Vol.221 No.4 pp.405-415 (2007)
- (5) 酒井英樹: 舵の正確さについての一考察, 自動車技術会 秋季大会 学術講演会前刷集No.140-14 pp.7-10 (2014)
- (6) 村岸裕治, ほか: オンセンタでの操舵トルクに対する車両応答解析, 自動車技術会論文集 Vol.41 No.3 pp.575-580 (2010)
- (7) 田尾光規: ドライバが意のままと感じる車両操舵応答特性に関する研究 東京大学 博士論文 (2018)
- (8) 今村昌幸, ほか: 高性能ドライビングシミュレータの開発, 日産技報 ダイナミック・パフォーマンス技術No.83 pp.60-65 (2018)
- (9) 安部正人: 「自動車と運動の制御(第2版)」東京電機大学出版局 (2012)
- (10) Stephen K. Park: Random Number Generator, Communications of the ACM Vol.31 No.10 pp.1192-1201(1988)

## Source

公益社団法人自動車技術会  
自動車技術会論文集  
Vol.51NO.3 文献番号:20204204

## Author



Mitsunori Tao

# Development of NV method that combined engine control model and NV model for electrified powertrain

Masaya Gotou\* Sho Aizumi\* Tadashi Nagami\*\*  
Hisayoshi Matsuoka\* Toshio Enomoto\*\*

**Abstract** The e-POWER system controls engine arbitrarily according to the electric power generation request. Therefore, it is necessary to design noise and vibration performance in various driving scenes of energy request. In order to predict engine noise in cabin, the new model that combined engine control model and NV model using component experiment data is developed. The validity of this model is verified in the early development phase.

## 1. Introduction

In recent years, the increasing awareness of environmental issues has resulted in the diversification of automotive powertrains. We have also adopted the hybrid and e-POWER systems. These powertrains are established by combining the conventional internal combustion engine (ICE) and an electric power unit. Thus, their operations are more complicated than the conventional ICEs because they are electronically controlled.

As a result, it is difficult to solve the trade-offs between multiple performance items. As an example, the e-POWER, which employs an engine as a generator, can be considered. The operating point of the conventional ICE is determined according to the vehicle speed and the accelerator opening. In contrast, only an electric motor provides e-POWER with drive force. This enables an arbitrary setting of the operating point of its engine for fuel efficiency and power. Moreover, the noise and vibration (NV) performance should be comprehensively studied according to the operating point patterns of the engine, which is arbitrarily controlled based on such multiple performance items. Thus, there should be a considerable number of design conditions. /In addition, there are often trade-offs between NV performance, which ensures quietness by controlling engine speed and power/heating performance, which ensures output energy by increasing engine speed.

It is crucial to ensure sufficient hardware potential and develop engine control specifications in an early development stage by ascertaining these trade-offs in the vehicle development stage in advance

Amid globally expanding market, it has also become

more important to predict interior noise virtually under running conditions in each market of electronic powertrain that operates in a complicated manner.

We established the vehicle NV 1D CAE by combining an NV model utilizing experimental data with an engine control model. It allows for the prediction of performance-to-performance trade-offs and interior noise in each market. This report describes the technique developed.

## 2. System configuration example of electric powertrain

The e-POWER system is an electric powertrain that has an engine as a generator, as shown in Fig.1. The system is operated to charge a battery. The electricity stored in the battery is used to drive a motor through an inverter for vehicle running. This configuration prevents coupling of the engine with the drive system, so that the operating point of the engine can be independently controlled. The configuration of the system is shown in



Fig.1 System image

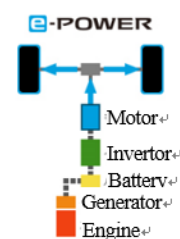


Fig.2 e-POWER System diagram

\*Customer Performance and Vehicle Test Engineering Department No.1

\*\*Advanced Vehicle Performance Engineering Department

### 3. NV issues of electric powertrains

#### 3.1 Engine start request

In conventional ICEs, the power and operating point of the engine required for running are determined according to the accelerator opening, which represents the driver's intention for acceleration. This is because the vehicle's operating conditions are physically determined according to hardware elements such as the engine speed, torque, and vehicle speed. With only design that has taken into account the running conditions according to several patterns, no major problems with NV performance have occurred. On the other hand, as e-POWER adopts motor driving, its engine operating point is determined according to not only the accelerator opening but also the supply of electric power necessary for an acceleration request considering the remaining battery life of the vehicle, and requests from other performance items (heating, emissions, etc.). As the influence of these various generating requests on the NV performance in conventional ICE is negligible, they are not considered so much as design factors. In contrast, the engine operating point of e-POWER varies according to each of these various generating requests, such that. Therefore its NV performance must be comprehensively designed.

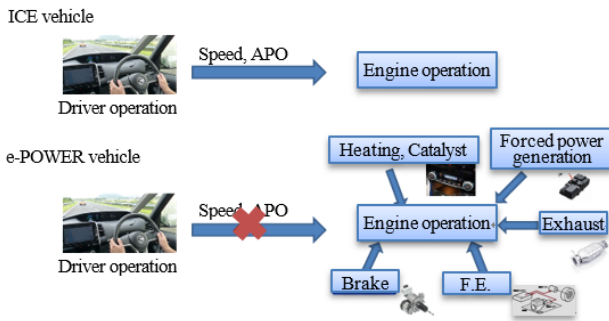


Fig.3 e-POWER engine operation request

#### 3.2 Increase in design scenario

As the generating requests have different effects on NV performance in each running scenario, quantitative examination is required. A specific example is that the engine noise is low in low-speed running in a traffic jam. If the engine suddenly starts due to any request from other performance items (heating, emissions, etc.) in such a running scenario, the engine noise can disturb passengers, causing a problem. In addition, considerable electric generation is required to prevent insufficient power during long-time running at high speed on an ascending road. This means that engine rotation at high speed is required, and the engine speed tends to be higher than that for the conventional ICE. This running scenario is not frequent, but can cause a problem related to engine noise.

As described above, in various cases, generating requests in e-POWER are caused according to the running conditions. In addition, as running conditions increase with the expansion of the market, the

combinations of conditions to be evaluated also increase considerably. Therefore, possible problems should be identified in advance from a wide variety of driving scenes and the NV performance should be designed according to a vast number of patterns for development.

#### 3.3 Trade-off performance items in electric powertrains

The NV performance can be ensured by lowering the engine speed to a certain value for driving scenarios. However, as shown in Fig.4, a reduction in the engine speed can result in insufficient electricity generated and, consequently, a failure to reach the speed requested by the driver, resulting in insufficient power or poor fuel efficiency. Therefore, to improve the total vehicle performance, a well-balanced design should be ensured after taking into consideration influence on other performance items because engine operating point is not determined by only NV performance.

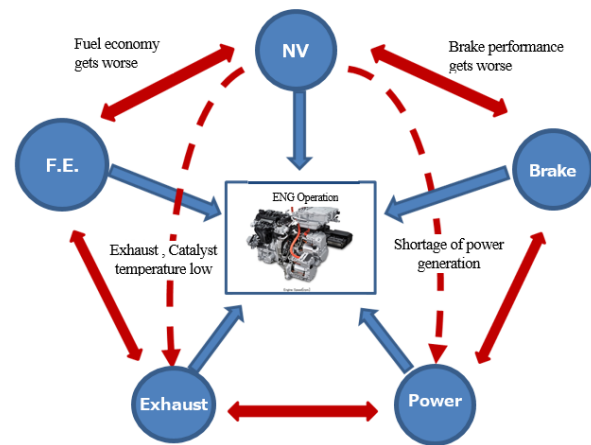


Fig.4 Tradeoff of each performance

### 4. Development of vehicle NV 1D CAE

The targeted engine noise must be predicted to a frequency range higher than idle vibration, booming noise, road noise, etc. However, CAE techniques used in currently developed projects do not have a sufficiently wide frequency range or are not sufficiently accurate. There are partially advanced techniques, but they are not useful from an economic perspective. Accordingly, it was attempted to predict the high-frequency range by utilizing experimental data for model-like behavior. Specifically, as shown in Fig.5, the parameters of engine speed and torque were controlled, engine vibration was measured at each grid, and the measured data were linearly interpolated. In sequence, three-dimensional (3D) map data were obtained, as shown in Fig.6. Thus, a method for incorporating these models into vehicle NV 1D CAE was selected to predict NV performance in the high frequency range. It was also applied to other input paths, such as engine radiation sound, exhaust input, and intake input, other than engine vibration, by measuring experimental data. As described above, a hybrid model was adopted by using a CAE model in the

low frequency range, experimental data in the high frequency range, and data corrected with CAE for partial changes in its design. Then, the 1D CAE model was established by independently calculating these frequency ranges and summing them. The model can predict the range of engine noise under electric generation.

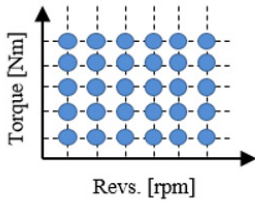


Fig.5 Image of measurement point

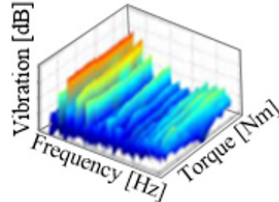


Fig.6 3D map data

Fig.7 shows the 1D CAE model, where the NV model with the hybrid technique and the engine control model are connected. This enables the visualization of trade-offs against other performance items for various running conditions when an engine operating point is controlled.

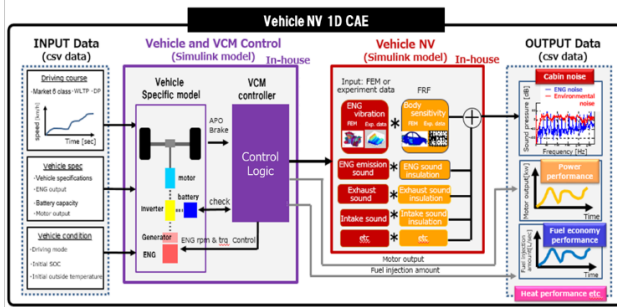


Fig.7 Vehicle NV 1D CAE

The vehicle NV 1D CAE takes into account as input data to the engine control model, running conditions such as the vehicle speed vs. time, and slope angle, vehicle specifications such as battery capacity, and vehicle conditions such as initial SOC and driving mode, and provides output data such as engine speed, torque, and acceleration G. The output data is input into the NV model, which outputs engine noise, consisting of a combination of components through various paths, such as engine, exhaust, and intake. In addition, the engine control model provides fuel consumption/SOC data, so that NV performance and other performance items can be simultaneously verified. Therefore, the study of trade-offs is possible.

The NV model also takes into account various component data such as engine mount characteristics as input data, which provides the characteristics necessary for solving trade-offs.

## 5. Validation of vehicle NV 1D CAE

The vehicle NV 1D CAE described in Section 4 was validated as a simulation tool by verifying its correlation with actual running using a test course. The comparison of the results of the actual running and the 1D CAE in the running scenarios are shown in Fig.8. First, both actual running and 1D CAE were tested under the same condition of vehicle speed. The graph showing time vs. engine speed indicates that the engine operation frequency and the engine speed during the engine operation are in accordance with those in the actual running data. They are also in accordance with the graph showing time and sound pressure level. Consequently, it was considered that the simulation tool was sufficiently effective for designing performance.

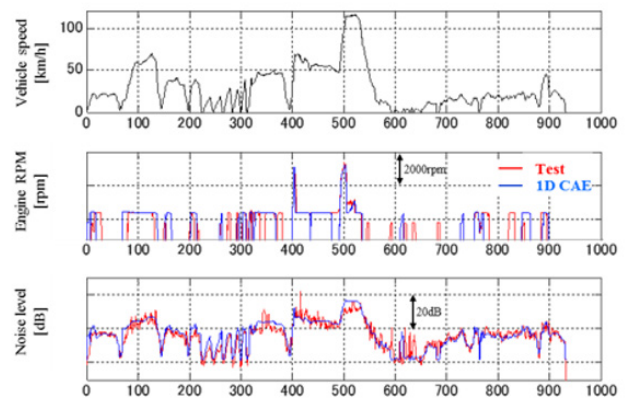


Fig.8 Result of vehicle NV 1D CAE correlation

## 6. Application example of vehicle NV 1D CAE

### 6.1. Prediction of interior noise for each market

It is necessary to create a performance plan for each expanding market. Even in the same categories such as mountainous roads and expressways, running conditions vary according to each market. Therefore, comprehensive predictions regarding markets and courses are necessary. Evaluating the actual running in the field would be inefficient; thus, virtual calculation was applied. Table 1 shows the combinations of markets and scenarios used for the predictions performed with the vehicle NV 1D CAE developed in this report. Additionally, the calculation results of the characteristic cases with “\*” marks in Table 1 are shown in Figs. 9–11.

Table 1. Calculated scene in each market and result

Scene	Market A	Market B	Market C
City	OK	OK	OK
Suburb	OK*	OK	OK
Mountain	OK	OK*	OK
Highway	OK	OK	OK
Traffic jam	OK	OK	CA*
:	:	:	:

Fig.9 shows the results of reproducing a run on the suburban road in Market-A. The high frequency of engine operations due to high-speed running is characteristic. Fig.10 shows the results of reproducing a run on the mountainous road in Market-B. It is observed that the engine keeps running at high speed according to steep slopes, causing a loud noise. Moreover, Fig.11 shows that the interior noise increases with higher engine speed for electric generation on the jammed road in Market-C.

As mentioned above, interior noise predictions in various scenarios enable competitive verifications through comparison with competing vehicles, average sound pressure values in each market, and other approaches. A variety of analyses, such as EV/generating mode time ratio and difference between engine and ambient noises are also available and can be utilized for feedback to parts and/or control specifications.

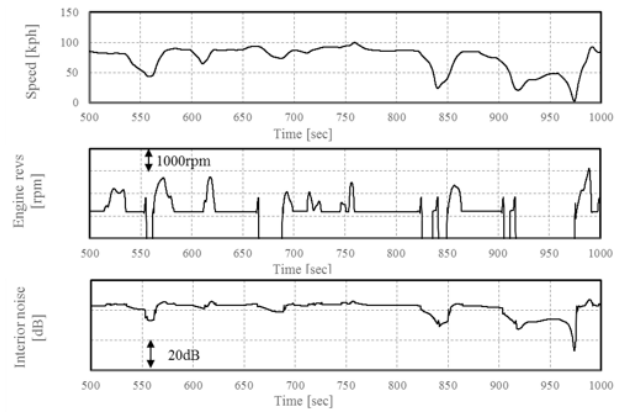


Fig.9 Calculation result in case of market A suburb

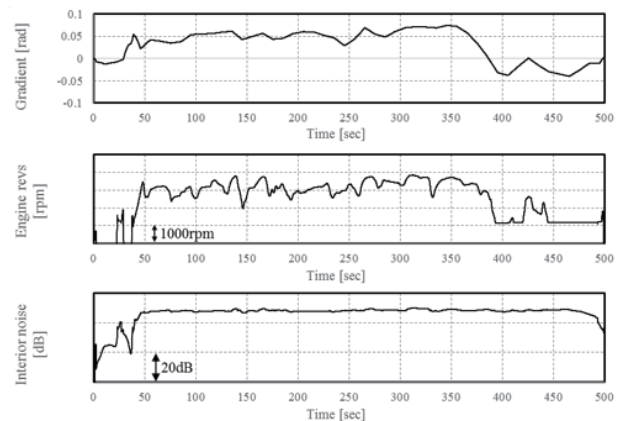


Fig.10 Calculation result in case of market B mountain

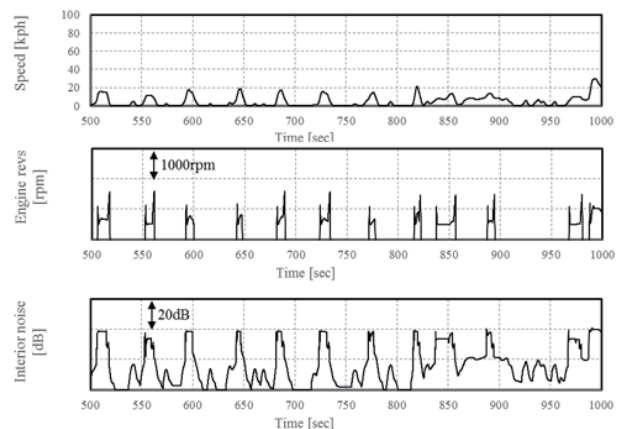


Fig.11 Calculation result in case of market C traffic jam

### 6.2. Prediction of interior noise with changed vehicle specifications

The increase in the number of electric powertrain adoptions has revealed trade-offs between performance items such as NV and heating/fuel efficiency performance. In vehicle development, it is very important to identify any trade-offs between such performance items in the vehicle design phase to ensure the hardware potential necessary for the vehicle and to develop its engine control specifications in an early stage. Fig.12 illustrates the results of interior noise predictions with a change in vehicle mass as a case of vehicle specifications. It



indicates that a 200-kg increase in vehicle mass from the standard causes the engine to often generate electricity under a high-load condition like uphill acceleration, resulting in higher frequency of loud interior noise.

Such predictions of the changed characteristics of parts/systems involved in trade-off relations in an early stage of development can contribute to solving trade-offs at a high level.

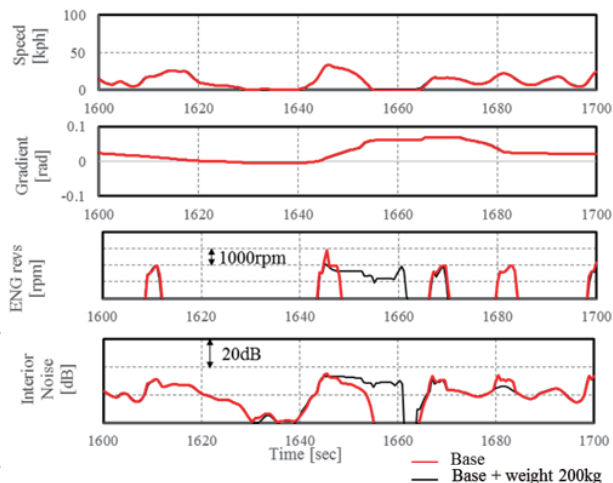


Fig.12 Influence of weight calculated by NV 1D CAE

## 7. Summary

In this study, a vehicle NV 1D CAE was established by integrating a vehicle NV model with an engine control model to cover all designs for various engine operations of electric powertrains with complex engine control, which can predict performance-to-performance trade-offs in advance. The NV model accommodated a hybrid technique to which both the CAE and experimental data-based models are applied to cover the frequency range for designing NV performance.

The 1D CAE established here was considered to be an effective prediction tool based on verification results of the prediction accuracy. This tool was also applied to the predictive calculations of running conditions of many road types in global each market, contributing to efficient development. Additionally, it was confirmed that the tool can also be utilized for the preliminary examination of trade-offs by changing vehicle specifications in an early stage of development.

Future research will focus on the possibility of utilizing the 1D CAE established generally as a preliminary examination tool for new technology introduction and preliminary prediction tool for performance-to-performance trade-offs.

## References

- (1) 餌取秀一: 新型電動パワートレインe-POWERの振動騒音技術, 公益社団法人自動車技術会 春季大会学術講演会講演予稿集, p.1274-1277 (2017)
- (2) 橘秀樹, 矢野博夫: 環境騒音・建築音響の測定, 東京, コロナ社, p.83-90 (2004)
- (3) 金井浩: 音・振動のスペクトル解析, 東京, コロナ社, p.257-260 (1996)

## Source

公益社団法人自動車技術会  
2019年春季大会学術講演会講演予稿集  
No.26-19 文献番号:20195125

## Authors



Masaya Gotou



Sho Aizumi



Tadashi Nagami



Hisayoshi Matsuoka



Toshio Enomoto

# Precise Ego-motion Measurement by High Speed Camera

Hyeongsung Cho\* Hidekazu Nishiuchi\* Hiroshi Satoh\*  
 Shinichi Nishioka\*\* Hiroyuki Sakai\*\* Haruo Matsuo\*

## 1. Introduction

The action planning and control of automated vehicles are performed using information from the ambient environment and the vehicle's behavior. Therefore, the behavior of the vehicle, such as the speed and yaw rate, should be measured.

Methods using various types of sensors have been proposed for measuring the behavior of a vehicle<sup>(1-4)</sup>. A simple method involves the use of a wheel speed pulse to measure the vehicle speed and mileage using the vehicle's wheel revolution speed. However, errors may occur with this method because of external causes such as tire slips; thus, the output of an accurate value may sometimes not be possible<sup>(2)</sup>. A different method, which uses the inertial navigation system (INS) consisting of devices such as acceleration and gyro sensors, determines the vehicle speed and mileage by integrating the acceleration; thus, errors tend to accumulate<sup>(2)(3)</sup>.

In contrast, when measuring the vehicle behavior using images, information regarding the objects and traffic lanes can be obtained from camera images simultaneously; research on this is being conducted<sup>(1)</sup>. Cameras commonly available in the market can obtain images at a rate of 30–60 frames per second (fps). Images of the scenery around the vehicle are used to extract the characteristics of the road structures, such as motionless objects and road surfaces. The amount of inter-frame movement of the characteristics in the actual space is measured using stereo parallax and then used to calculate the behavior of the vehicle. However, the amount of movement of the characteristics becomes large, and the appearance of the same characteristic may change between frames as the traveling speed or turning speed of the vehicle increases, thereby complicating the calculation of the amount of movement of the characteristics.

When measuring the vehicle behavior using images and, in particular, a camera directed towards the front of the vehicle, the movement of the characteristics of motionless objects (road surfaces, white lines, curbs, etc.) near the vehicle can be calculated. This is useful in measuring vehicle behavior because the accuracy of the distance measurement using stereo parallax is high near the vehicle. However, the amount of movement between image frames will be larger when the objects are closer to the vehicle, and changes in the

appearance will also be larger. As the vehicle will be used outdoors, changes in the lighting environment will also occur frequently<sup>(1)(4)</sup>.

This problem can be resolved by implementing either of the two main approaches. One approach is to devise a method of calculating the movements of characteristics when processing an image; many proposals exist for this method<sup>(5)</sup>. Examples of such an approach include correcting the appearance change using affine and similar transformations and simplifying a characteristic if its luminance gradient is constant. The other approach is to use a high-speed camera to decrease the amount of inter-frame movements of characteristics. Proposals for this approach include measuring the movements using a high-speed camera with a rate of 1000 fps<sup>(6)</sup> and using the self-position estimation method using a high-speed camera with a rate of 200 fps<sup>(7)</sup>. However, completing the calculation within the inter-frame time is a problem for this approach.

In this study, a method of measuring the behavior of a vehicle with high accuracy was explored by using a high-speed stereoscopic camera mounted facing forward on a vehicle. The amount of calculation of the optical flow<sup>(8)</sup>, which is the movement of characteristics between image frames, was reduced when programming a field-programmable gate array (FPGA) to perform the calculation within the short inter-frame time of the high-speed camera and complete processing in real time. This study also aimed to establish a method of measuring the behavior of a vehicle using the optical flow obtained from a high-speed camera and

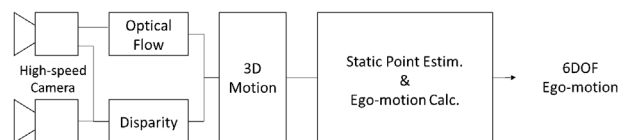


Fig.1 Structure of optical flow calculation by high speed camera

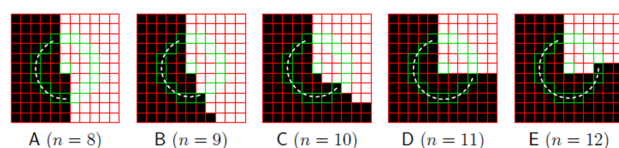


Fig.2 Feature point detection by comparing the brightness values of the central pixel and peripheral pixels by the FAST method

\*Mobility and AI Laboratory    \*\*Prototype and Test Department

calculated up to the vicinity of the vehicle. This method was demonstrated on a test vehicle, and driving tests were conducted to check whether calculating the behavior of the vehicle with high accuracy was possible.

## 2. Measuring the behavior of a vehicle using a high-speed stereoscopic camera

### 2.1. System configuration

The following was considered as the procedure for measuring the behavior of the vehicle using a high-speed stereoscopic camera. First, characteristics that can be easily tracked are extracted from an image captured by a high-speed camera. The optical flow (which is the movement between image frames) and on the parallax (which is convertible into distance at that timing) is then calculated to measure the movement of the extracted characteristics in actual space. Next, the movement coordinates that are calculated from the optical flow of each characteristic, coordinates of the characteristic in the image at each timing, and parallax of the characteristic between images are used to convert the movement into three-dimensional coordinates to calculate the three-dimensional movement in the actual space. The behavior of the vehicle is calculated with the assumption that the three-dimensional movement of the characteristics of the motionless object is based on the behavior of the vehicle. The behaviors of the vehicle in six degrees of freedom (X, Y, Z, pitch, yaw, and roll) are measured; these are the behaviors in the three axial directions (front-rear, left-right, and up-down) and the rotating direction of each axis. The system that measured the behavior of the vehicle, equipped with a high-speed camera that performs this processing, was configured as shown in Fig.1.

In this research, two high-speed cameras were mounted at a pitch of 50 cm. Each camera had a horizontal resolution of 2040 pixels and a vertical resolution of 1088 pixels and could capture 300 images in 1 s. The angle of view of the lens in the horizontal direction was approximately 90°.

The optical flow was calculated by an FPGA using the method described hereafter, and the parallax was calculated by implementing the semi-global matching (SGM) method<sup>(9)</sup> in the graphics processing unit (GPU). In the measurement method used in this research, the characteristics of moving objects were considered to be outliers by random sample consensus when estimating the motionless objects and measuring the behavior of the vehicle, and the three-dimensional movement of characteristics on motionless objects was assumed to be based on the behavior of the vehicle<sup>(10)</sup>. Here, the optical flow for measuring the temporal change was calculated at 300 fps, which was the frame rate of the camera. Parallax calculation, motionless object estimation, and vehicle behavior measurement were calculated at 10 fps.

### 2.2 Optical flow

The optical flow calculation function consisted of a function that extracted the characteristics in the image and a function that tracked the extracted characteristics in the subsequent frame.

The FAST method<sup>(11)</sup> was used to extract the characteristics. The FAST method can extract corners and blobs (for example, small circles that have clear differences in brightness) that can be easily tracked, regardless of direction. As ternarization is used for calculation, this method can be easily installed into hardware such as an FPGA. For all of the pixels in the image, the luminance value of the center pixel was compared with the luminance values of sixteen peripheral pixels that surrounded and were spaced three pixels apart from the center pixel (Fig.2). If peripheral pixels that are brighter or darker than the luminance difference threshold exist, and if such peripheral pixels exist consecutively for a certain angle or more, such a center pixel is considered to be a corner or blob; it was selected as a characteristic that is easy to track. In this research, the judgment criteria angle was set at 135°, which corresponds to 10 pixels. In addition, if multiple candidates of characteristics existed within a local range, the difference in luminance values between the center pixel and peripheral pixels were summed up, and the characteristic with the highest difference was selected as the target characteristic, because such a characteristic was assumed to be easy to track.

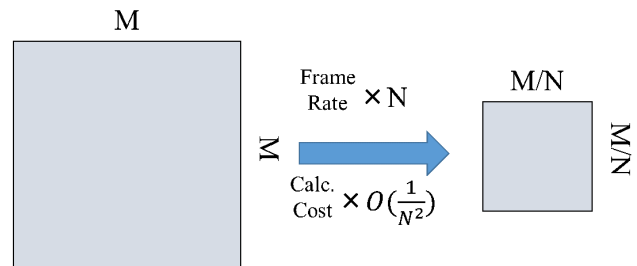


Fig.3 Searching area and calculation cost reduction by increasing frame rate by high speed camera

Next, a description is provided for the function that tracked the extracted characteristic in the next frame. The tracking of characteristics is a process that requires many calculations. To complete these calculations within the inter-frame time, they can be reduced using either of the following two methods.

One method is to utilize the high frame rate and narrow the search range for tracking the characteristic in the subsequent frame because the movement amount of a characteristic in an image is inversely proportional to the frame rate. Fig.3 shows the extent of the search range for tracking a characteristic. If the frame rate is multiplied by  $N$ , the amount of inter-frame movement will be  $1/N$ . Therefore, the search range, which is an area, can be narrowed to  $1/N^2$ . Whereas the number of calculations owing to the increase in the frame rate will increase by  $N$  times, the number of calculations for searching will be multiplied by  $1/N^2$ . As a result, the number of similarity calculations for measuring the movement amount of each characteristic per unit time can be reduced to  $1/N$ . For example, when the movement amount is measured using the 300-fps camera, the number of calculations of each characteristic per unit time can be decreased by 90% compared with that at 30 fps.

The other method is to simplify the similarity calculation of the characteristics. The inter-frame changes of the same

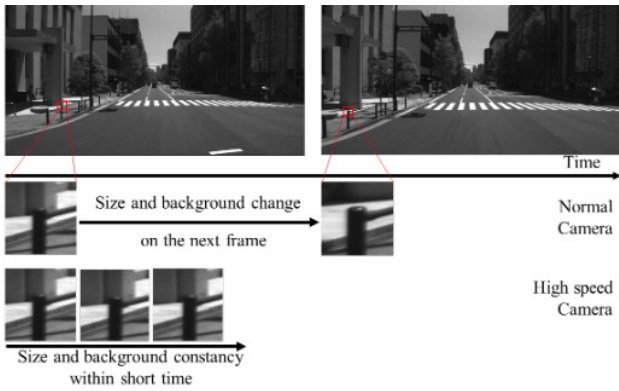


Fig.4 Comparison of reference image near ego-vehicle frame by frame of normal and high speed

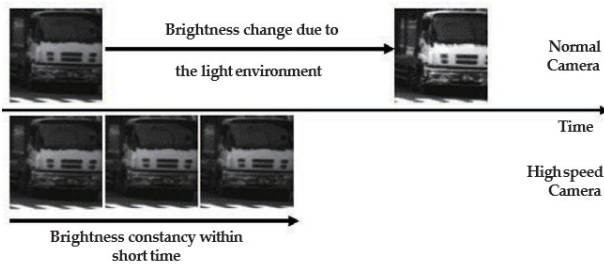


Fig.5 Comparison of reference image frame by frame of normal and high speed camera: brightness change

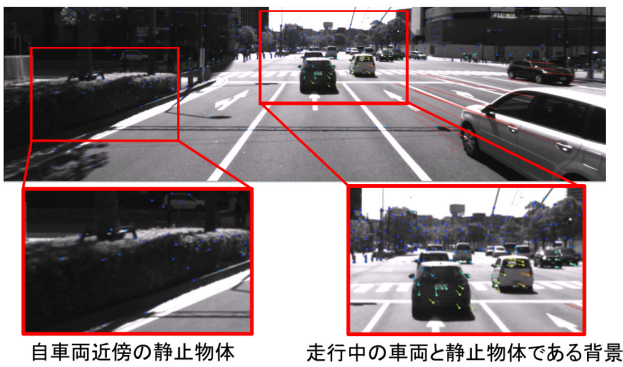


Fig.6 Result of static feature point estimation

object near the vehicle that were captured using the high-speed camera and normal camera are compared in Figs. 4 and 5. As the figures show, the inter-frame changes in the appearance and brightness of the same object, captured by the high-speed camera, were very small; thus, the difference could be ignored.

When a normal camera is used, the brightness between frames will change, as shown in Fig.5, even if the luminance gradient of the target object is constant; thus, correction is performed using indices such as the normalized cross-correlation (NCC), which normalizes the luminance value when performing similarity calculation. Similar to division and calculating the square root, this calculation is difficult to perform in hardware. Therefore, completing the calculation within a short inter-frame time is difficult.

In contrast, if a high-speed camera is used, the change in appearance and brightness can be ignored. Therefore, the similarity calculation can be changed to a simple method such as the sum of absolute difference (SAD) value<sup>(12)</sup>, which is the sum of the luminance difference between pixels. Therefore, installation as the absolute difference in pixel

luminance, which can be easily calculated in the hardware, can be performed.

When performing a similarity calculation of the characteristics using the SAD value, a reference image ( $T$ ) is first established, centered around the extracted characteristic. Subsequently, in the next frame, an image that is centered around the periphery pixel ( $d_x, d_y$ ) of the characteristic's coordinate and has the same size as the reference image is established. Subsequently, the absolute difference between each pixel of that image ( $I$ ) and each pixel of the reference image  $T$  is calculated. In the final step, the periphery pixel ( $d_x, d_y$ ) that has the minimum difference in the sum is set as the pixel with the highest similarity, and it is set as the characteristic in the next frame. As this calculation of the absolute difference between pixels can be performed in parallel, installation into the hardware can be easily performed. With this method, the optical flow, which is the movement of characteristics caused by the behavior of the vehicle, can be calculated.

This optical flow calculation method was installed in the FPGA. Using the results of that calculation and using the parallax calculated by the GPU, the behavior of the vehicle was measured.

### 3. Test method and result

#### 3.1 Evaluation test

The on-vehicle evaluation test was conducted by dividing the test conditions into two types: a simple driving environment and an ordinary road environment. In the former, the background was simple, and only motionless objects were present. Therefore, the extraction of characteristics, calculation of movement, and measurement of the behavior of the vehicle based on the extraction and calculation results were performed. In contrast, the ordinary road environment contained many moving objects. Therefore, the possibility of calculating the behavior of the vehicle by extracting only the characteristics of motionless objects, and the effects of this motionless object extraction on accuracy were investigated. In the simple driving environment test, the maximum vehicle speed was set at 20 km/h. In the ordinary road environment test, the vehicle was driven within the speed limit (maximum 60 km/h). Other moving objects were present in the ordinary road environment; thus, estimating the motionless objects from the extracted characteristics was necessary. Because the accuracy of estimating motionless objects could affect the accuracy of measuring the vehicle's behavior, the results of estimating the motionless objects were checked under ordinary road environment, which contained many moving objects. Four items were evaluated in both environmental conditions: vehicle speed, yaw rate, translational motion error and rotary motion error per unit distance.

#### 3.2 Results of motionless object estimation

To check the results of estimating the motionless objects, we subtracted the vehicle behavior measurements from the optical flow, and the optical flow was displayed for each

characteristic on each frame image. We investigated whether an object moving with respect to the ground can be distinguished correctly. The optical flow that subtracted the behavior of the vehicle is shown in Fig.6.

Fig.6 shows the optical flow of each characteristic using line segments. The magnitude of the optical flow, shown on the screen, is indicated by the length and color of the line segment. The line is blue if there is no velocity, and it turns red as the velocity increases.

The enlarged view at the lower left of the figure shows a shrub. Its characteristics are indicated in blue, which indicates that the shrub was correctly estimated as a motionless object. The enlarged view on the right shows a vehicle moving and as well as the background, which is a motionless object. Only the characteristics that were extracted from the background are indicated in blue, which indicates that the motionless objects were estimated correctly.

### 3.3 Evaluation of the vehicle behavior

The optical flow obtained using the high-speed camera was used to measure vehicle behavior, which was then used to calculate the vehicle speed and yaw rate. The calculated results were compared with the vehicle speed and yaw rate obtained from signals sent from the vehicle. To compare the results of the vehicle speed while the vehicle was traveling, the vehicle speed was compared in the range at or above 5 km/h. To compare the results of the yaw rate in the area in which the vehicle did not travel in a straight line, the yaw rate was compared in the range at or above 2 deg/s. The root mean square error (RMSE) value was obtained as a comparison. To obtain the translational motion error per unit distance, the coordinates of the rectangular plane coordinate system, sent using a real-time kinematic (RTK) GPS signal, were used to calculate the true value, which was then compared with the travel distance calculated using the proposed method to evaluate the translational motion error per 100 m. To obtain the rotational motion error per unit distance, we set the difference between the initial azimuth and final azimuth (calculated from the rectangular plane coordinates) in each test as the true value; this value was then compared with the difference between the initial azimuth and final azimuth (calculated by the proposed method) to obtain the rotational motion error per 100 m of travel distance. Note that the positional accuracy of an RTK GPS satellite signal can decline owing to the signal reception quality. Therefore, the sections with poor positional accuracy were removed from the evaluation. The results of each test environment are discussed in the following.

(1) Evaluation of the vehicle behavior in the simple driving environment

The vehicle was driven for approximately 2.5 km in the simple driving environment, and its behavior was measured and evaluated. Figs. 7 and 8 show some portions of the results of the vehicle speed and yaw rate. The graph in Fig.7 shows the time in the horizontal axis and vehicle speed in the vertical axis and compares the vehicle speed obtained through the signal from the vehicle (blue) with the vehicle speed calculated using the proposed method (orange). The graph in Fig.8 shows the time in the horizontal axis and yaw

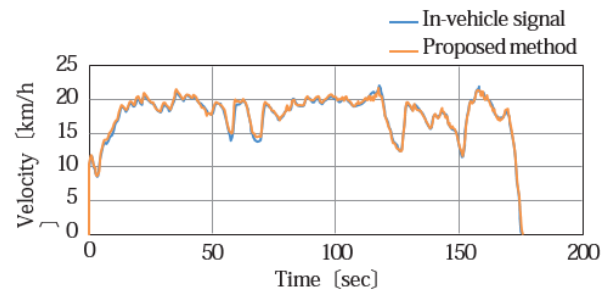


Fig.7 Velocity measured by proposed method in the restricted area

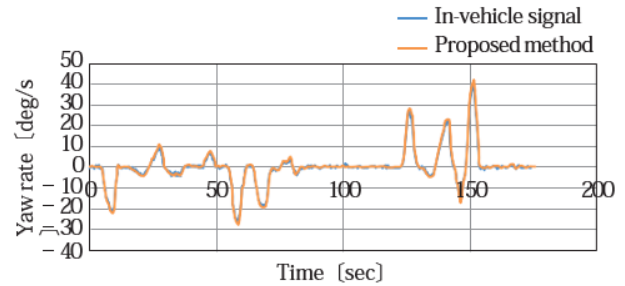


Fig.8 Yaw rate measured by proposed method in the restricted area

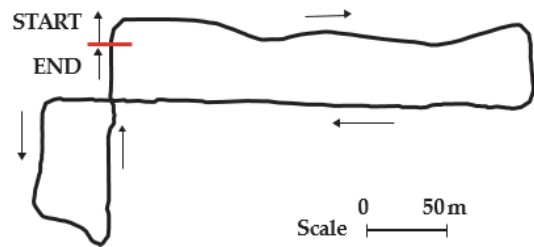


Fig.9 Driven path for a sequence in the restricted area

rate in the vertical axis and compares the yaw rate obtained using the signal from the vehicle (blue) with the yaw rate calculated using the proposed method (orange). Fig.9 shows the travel locus of the test, the results of which are shown in Figs. 7 and 8. Table 1 shows the errors obtained from the entire test.

The results indicated that the vehicle speed and yaw rate were measured with an accuracy equivalent to those obtained from the signals sent from the vehicle. The results also indicated that the behavior of the vehicle, in terms of translational and rotational motions per unit distance, was measured with good accuracy.

(2) Evaluation of the vehicle behavior in the ordinary road environment

In the ordinary road environment, the vehicle was driven for approximately 15 km at a speed at or below the speed limit, and its behavior was evaluated. Figs. 10 and 11 show some portions of the results of calculating the vehicle speed and yaw rate, and Fig.12 shows the travel locus of the test. Table 2 shows the errors obtained for the entire test. Similar to Figs. 7 and 8, the graphs of Figs. 10 and 11 show the time in the horizontal axis and vehicle speed or yaw rate in the vertical axis and compare the vehicle speed or yaw rate obtained using the signal from the vehicle (blue) with the vehicle speed or yaw rate calculated using the proposed method (orange).

Table1 Error of the result

	Error
Velocity (km/h)	0.37
Yawrate (deg/sec)	1.03
Translation motion (m/100m)	1.89
Rotation motion (deg/100m)	0.16

Similar to the results obtained in a simple driving environment, the results indicated that the vehicle speed and yaw rate were measured with an accuracy equivalent to those obtained from the signals sent from the vehicle. The rotational motion error per unit distance was 0.060° per 100 m, which can be considered to be highly accurate considering that the horizontal deviation was somewhat equal to or higher than 1 pixel when the vehicle traveled 100 m. This result confirmed that the vehicle’s turning behavior can also be measured with good accuracy by measuring the optical flow using a high-speed camera. In addition, because the estimation of motionless objects in the ordinary road environment was performed correctly, as is verified in the previous paragraph, we confirmed that the accuracy of measuring the behavior of the vehicle was equivalent to that in a simple driving environment.

Furthermore, the proposed method could measure the vehicle speed even in the low-speed range, in which the measuring accuracy declined if a wheel speed pulse sensor was used. This result is shown in Fig.13. Similar to Figs. 7 and 10, the graph in Fig.13 shows the time in the horizontal axis and the vehicle speed in the vertical axis. The colored portion indicates the range in which the speed was at or below 5 km/h. Because the travel distance within the range shown in Fig.13 was 1 m or longer, the proposed method can be utilized to control the vehicle in the very low speed range.

### 3.4 Optical flow using the high-speed camera

Further investigation was conducted on the calculation of optical flow for the high-speed traveling range, in which the amount of characteristic movement was large. Hence, every second data point of the traveling data, obtained while evaluating the vehicle in the ordinary road environment, was selected to create data that simulates a condition equivalent to traveling at twice the vehicle speed. The generated data were used to calculate the optical flow, and the results were checked.

Fig.14 shows the calculation results of the optical flow that was obtained using the high-speed camera used to measure vehicle behavior.

The optical flow results shown in Fig.14 show the flow

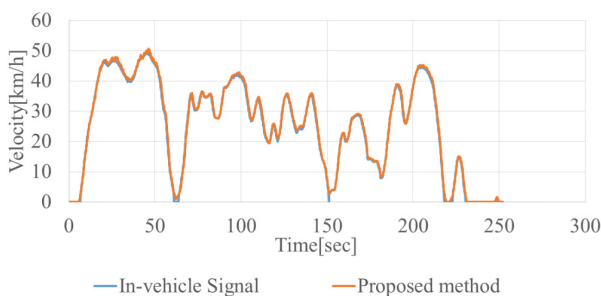


Fig.10 Velocity measured by proposed method on the public road

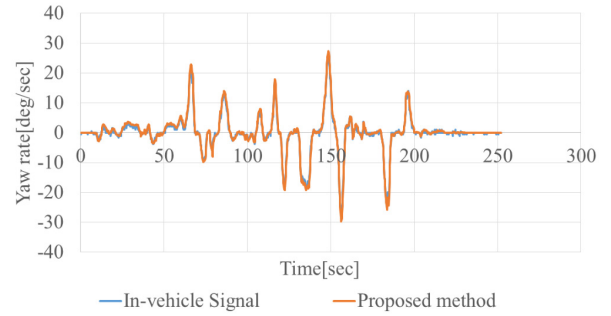


Fig.11 Yaw rate measured by proposed method on the public road

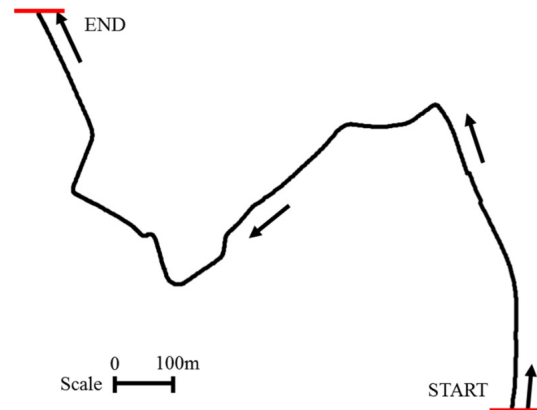


Fig.12 Driven path for a sequence

Table2 Error of the result

	Error
Velocity (km/h)	0.94
Yawrate (deg/sec)	1.02
Translation motion (m/100m)	2.05
Rotation motion (deg/100m)	0.060

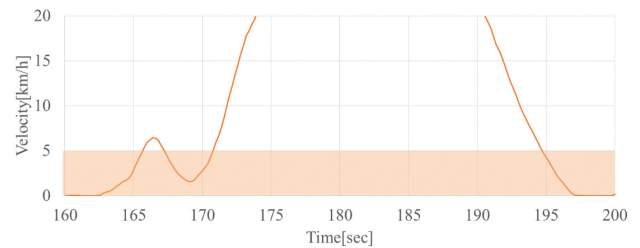


Fig.13 Velocity measured by proposed method on the low vehicle speed (below 5km/h, colored)

calculated from the data that simulated a vehicle speed of 94 km/h. The left figure shows the results calculated using the normal camera (30 fps), and the right figure shows the results calculated using the high-speed camera (300 fps). The red frame located at the lower left portion indicates the position close to the vehicle, and its enlarged view is shown below each figure. In each characteristic, the length of the line segment represents the magnitude of the optical flow, and the color represents the orientation. In the results shown in the left figure, the optical flow at the lower left portion was either not calculated or the calculated flow was not correct. For the results shown in the right figure, we confirmed that the calculation was performed correctly.

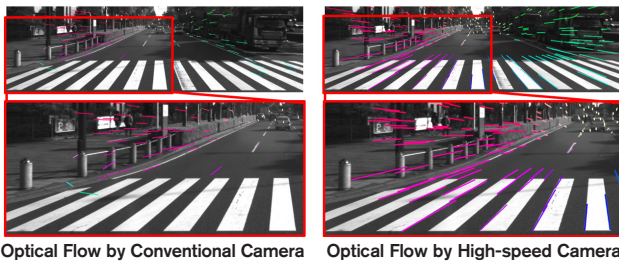


Fig.14 Comparison of calculated optical flow

#### 4. Conclusion

A method of measuring the behavior of a vehicle using the optical flow obtained using a high-speed camera was proposed and demonstrated. An on-board evaluation was conducted under a simple driving environment and an ordinary road environment.

The use of a high-speed camera to calculate the optical flow enabled the number of calculations per unit time to be reduced because the range for searching for the movement of characteristics in the subsequent frame can be decreased. In addition, by simplifying the similarity calculation, programming an FPGA and calculating up to the vicinity of the vehicle in real time became possible. These methods enabled the tracking of the characteristics near the vehicle, for which the distance accuracy of the stereo parallax is high. This enabled a highly accurate measurement of the movement of characteristics in actual space, and enabled a highly accurate measurement of the vehicle behavior; this measurement was performed by calculating the aforementioned measurement results backward. As, in particular, measuring the optical flow even when the vehicle was turning became possible, the accuracy of measuring the behavior of the vehicle in the turning direction has become higher. We confirmed that measurement is also possible in the low-speed range, in which the measurement accuracy declines if a wheel speed pulse sensor is used. As a system, measuring vehicle behavior in real time and with high accuracy was enabled by adopting the following methods: measuring the optical flow (which tracks the temporal position change of characteristics) in real time, with high accuracy, and up to large movements by the devised use of the high-speed camera; and calculating the parallax, which was performed to obtain the three-dimensional position simultaneously, at a longer interval.

Future research will focus on verifying the efficacy of this system against various actual environmental conditions such as the behavior conditions of the vehicle, including various speed ranges, rotary motions, and inclined roads,

various lighting environments, various weather conditions, and changes in complexity owing to the number of moving objects in an urban area.

#### References

- (1) Mohammad OA Aqel et al.: Review of visual odometry: types, approaches, challenges, and applications, SpringerPlus, 5:1897 (2016).
- (2) Borenstein, Johann et al.: Mobile robot positioning: Sensors and techniques, Journal of robotic systems, 14.4, pp.231-249 (1997).
- (3) Woodman, Oliver J.: An introduction to inertial navigation. University of Cambridge, Computer Laboratory, No. UCAM-CL-TR-696(2007)
- (4) Nistér, David, Oleg Naroditsky, and James Bergen: Visual odometry, Proceedings of the 2004 IEEE Computer Society Conference on Computer Vision and Pattern Recognition, CVPR 2004, Vol. 1 (2004).
- (5) Fortun, Denis, Patrick Bouthemy, and Charles Kervrann: Optical flow modeling and computation: A survey, Computer Vision and Image Understanding, 134, pp. 1-21 (2015).
- (6) Idaku Ishii et al.: High-frame-rate optical flow system, IEEE Transactions on Circuits and Systems for Video Technology, 22.1, pp.105-112 (2011).
- (7) Peter Gemeiner, Andrew Davison, and Markus Vincze: Improving Localization Robustness in Monocular SLAM Using a High-Speed Camera, Robotics: Science and Systems (2008).
- (8) Berthold KP Horn, and Brian G. Schunck: Determining optical flow, Artificial intelligence, 17.1-3, pp.185-203 (1981).
- (9) Hirschmuller, Heiko: Stereo processing by semiglobal matching and mutual information, IEEE Transactions on pattern analysis and machine intelligence, 30.2, pp.328-341 (2007).
- (10) Andreas Geiger, Julius Ziegler, and Christoph Stiller: Stereoscan: Dense 3d reconstruction in real-time, 2011 IEEE intelligent vehicles symposium (IV), pp. 963-968 (2011)
- (11) Rosten, Edward James: High performance rigid body tracking, Diss. University of Cambridge (2006)
- (12) Richardson, Iain E.: H.264 and MPEG-4 video compression: video coding for next-generation multimedia, John Wiley & Sons (2004)

#### Source

公益社団法人自動車技術会  
自動車技術会論文集  
Vol.50NO.3 文献番号:20204214

#### Authors



Hyeongsung Cho



Hidekazu Nishiuchi



Hiroshi Satoh



Shinichi Nishioka



Hiroyuki Sakai



Haruo Matsuo



# Environmental Impact Assessment of Battery Electric Vehicles Considering Air Pollutants from Thermal Power Plants

Gen Saitou\* Hiromi Asahi\*

**Abstract** In order to evaluate the impact of air pollutant emissions from power plants caused by battery electric vehicle (BEV) increase, we assumed vehicle type and power-generation mix in the urban area (Kanto area) in 2030, based on the total mileage of BEV and internal combustion engine vehicle (ICEV). The increase or decrease in average atmospheric concentration of air pollutants was estimated. The reduction of NO<sub>x</sub> concentration in the atmosphere was confirmed, which was due to the introduction of BEV and ICEV fuel economy improvement. In particular, the biggest effect was BEV increase. That is, it can be said that BEV is effective in reducing NO<sub>x</sub>. On the other hand, in urban areas, tropospheric ozone concentrations slightly increased because the sensitivity regimes in urban area were VOC- sensitive.

## 1. Introduction

Although a battery electric vehicle (BEV) does not emit air pollutants when running, the generation of electric power for its functioning bring about air pollutant emissions such as thermal power plants emissions. Therefore, these emissions must be considered when assessing the influence of BEV increase on the atmospheric concentration of air pollutants. However, few reports include this source of emission in their analysis. Therefore, this report estimated the atmospheric concentration of air pollutants, considering emissions originating from BEVs and assuming the composition of automotive types and electric power sources in the Kanto region, for the present situation and a projection for 2030. The estimation assumed that 16% of the current passenger cars would be replaced with BEVs. The applied BEV spread at a rate of 16% is presented in the Prospect of Introduction/Spread of Next-Generation Vehicles in 2030, Long-term Energy Supply and Demand Outlook, Ministry of Economy, Trade and Industry (1). In this estimation, ADMER-PRO Ver. 1.0 (2), developed by the National Institute of Advanced Industrial Science and Technology, was used as a chemical transport model for estimating the atmospheric concentration.

## 2. Assessment method

### 2.1. Assessment procedure

The procedure shown in Fig.1 is used to estimate the atmospheric concentration.

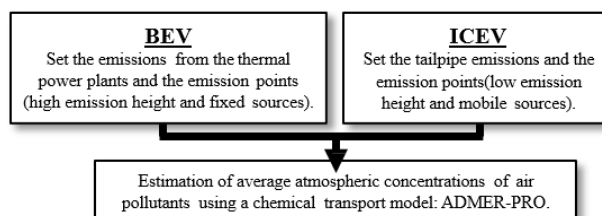


Fig.1 Evaluation procedure for air pollutants from BEV and ICEV

### 2.2. Settings for evaluation

Table 1 presents settings for evaluation in this report.

Tbl.1 Settings for evaluation

Area	Kanto area
Year	2017, 2030
Emission source	ICEV: Tailpipe emissions as mobile sources in ADMER-PRO. BEV: Emissions from thermal power plant chimneys as fixed sources in ADMER-PRO.
Emissions	Create emission data for 2017 and 2030 by setting the increase/decrease rate based on 2005 emission data built into ADMER-PRO.
Weather pattern	Estimated for the top 15% of the annual weather data (4 patterns).
Air pollutants	Primary air pollutants: SO <sub>x</sub> (SO <sub>2</sub> ), NO <sub>x</sub> (NO + NO <sub>2</sub> ). Secondary air pollutants: Sulfate, Nitrate, Tropospheric ozone.

### 2.3. Evaluation cases

For evaluation, four cases, detailed in Table 2, were established: 1. a representation of the present (2017); 2. replacement of 16% of passenger cars with BEVs; 3. BEVs spread by 16%, assuming future conditions such as

\*Technology Planning Department

the improvement of emission intensities and fuel efficiency of ICEVs in 2030; and 4. BEVs will not spread in the future.

The quantitative assessments were made: the effect of BEVs' spread in the present social structure (indicating annual automotive mileage, ICEV fuel efficiency/emission performance, BEV power consumption, emission intensities representing electric generation emission performance, and electric power source composition) by comparing Cases 1 to 2; the effect of BEVs' spread in the present and in the future by comparing Cases 2 to 3; and the effect of BEVs' spread in the social structure assumed in the future by comparing Cases 3 to 4. In addition, we attempted to determine and compare changes in concentration when one BEV runs 1 km to compare the effects of BEV introduction between the cases (various conditions are different between the cases).

Tbl.2 Evaluation cases

Case1	The values for 2017 were taken into consideration: total annual vehicle mileage, power-generation mix (thermal power generation ratio is approximately 65%), and emission intensity. All passenger cars are ICEV.
Case2	16% of the passenger vehicles in Case1 were replaced with BEV from ICEV.
Case3	The values for 2030 were taken into consideration: total annual vehicle mileage (3% decrease for passenger vehicles and 19% increase for freight vehicles compared to 2017), power-generation mix (ratio of thermal power generation is 56%), emission intensity. 16% of passenger cars were replaced by BEV from ICEV.
Case4	All passenger vehicles were ICEV in Case3.

### 3. Setting the amount of emission in each case

#### 3.1. Setting the amount of air pollutant emissions from ICEVs

The amount of air pollutant emissions from ICEVs (air pollutants from mobile emission sources) was determined using Formula (1) based on the annual automotive mileage, fuel efficiency, and air pollutant emission factors of vehicles in each case. The amount of emission was used to set the increase/decrease rate of emissions for SOx and NOx from large-scale emission sources in ADMER-PRO.

The annual automotive mileage was set based on the number of vehicles owned, number of average trips, and trip distances by vehicle type based on CO<sub>2</sub> emissions estimation data (3) by the Transportation Department of the Ministry of the Environment.

The automotive fuel efficiency was set from fuel consumption and annual mileage data for 26 types of vehicle and by fuel based on the Automotive Fuel Consumption Investigation (6) by the Ministry of Land, Infrastructure, and Transport. The average fuel efficiency of stock vehicles in 2017 was determined by vehicle type assuming gasoline for light passenger cars/passenger cars and diesel fuel for others. The total mileage in 2030 was set based on the annual mileage in 2017, considering a reduction of 3% for passenger cars and an increase of

19% for trucks, indicated in the Long-term Energy Supply and Demand Outlook (2). The fuel efficiency in 2030 was determined by applying a fuel efficiency improvement rate of 32.4%, indicated in the Assessment of Future Fuel Efficiency Improvement Rate according to New Fuel Efficiency Targets (7). Table 3 illustrates the total mileage and fuel efficiency of each vehicle.

The automotive emission factors in 2017 and 2030 were set based on the data of emission factors (for NOx, volatile organic compounds – VOC, SO<sub>2</sub>, and CO) and spread rates by fuel type and by vehicle body size in Japan contained in the database of IIASA's GAINS Asia (8). Table 4 presents the emission factors of each vehicle.

$$\text{Emissions} = \sum (\text{ICEV total mileage} \div \text{fuel efficiency} \times \text{emission factor}) \quad (1)$$

Tbl.3 ICEV total mileage and fuel economy

2017年	車種・燃料仮定	軽乗用車	乗用車	バス	軽貨物	小型貨物	普通貨物	特種車
		100%ガソリン	100%ガソリン	100%軽油	100%軽油	100%軽油	100%軽油	100%軽油
総距離	千台km	36,118,143	104,763,708	2,256,927	18,975,783	13,436,820	15,215,079	6,236,776
燃費	台km/L	14.1	11.3	3.6	8.7	9.7	3.9	4.0
低位発熱量	MJ/ton	44,005	44,005	42,582	42,582	42,582	42,582	42,582
密度	kg/L	0.740	0.740	0.820	0.820	0.820	0.820	0.820
燃費	台km/MJ	0.434	0.348	0.102	0.248	0.248	0.111	0.114
2030年	車種・燃料仮定	軽乗用車	乗用車	バス	軽貨物	小型貨物	普通貨物	特種車
		100%ガソリン	100%ガソリン	100%軽油	100%軽油	100%軽油	100%軽油	100%軽油
総距離	千台km	34,881,221	101,175,910	2,179,635	23,493,826	16,636,062	18,837,717	7,721,723
燃費	台km/L	20.9	16.8	5.3	12.8	12.8	5.8	5.9
低位発熱量	MJ/ton	44,005	44,005	42,582	42,582	42,582	42,582	42,582
密度	kg/L	0.740	0.740	0.820	0.820	0.820	0.820	0.820
燃費	台km/MJ	0.642	0.515	0.152	0.367	0.367	0.165	0.168

Tbl.4 ICEV emission factors

2017年	車種・燃料仮定	軽乗用車	乗用車	バス	軽貨物	小型貨物	普通貨物	特種車
		100%ガソリン	100%ガソリン	100%軽油	100%軽油	100%軽油	100%軽油	100%軽油
NOx排出係数	ton/TJ	0.032	0.032	0.193	0.031	0.031	0.143	0.143
VOC排出係数	ton/TJ	0.037	0.037	0.017	0.020	0.020	0.017	0.017
CO排出係数	ton/TJ	0.513	0.513	0.246	0.112	0.112	0.246	0.246
SO2排出係数	ton/TJ	0.00045	0.00045	0.00047	0.00047	0.00047	0.00047	0.00047
2030年	車種・燃料仮定	軽乗用車	乗用車	バス	軽貨物	小型貨物	普通貨物	特種車
		100%ガソリン	100%ガソリン	100%軽油	100%軽油	100%軽油	100%軽油	100%軽油
NOx排出係数	ton/TJ	0.026	0.026	0.112	0.030	0.030	0.086	0.086
VOC排出係数	ton/TJ	0.030	0.030	0.013	0.020	0.020	0.013	0.013
CO排出係数	ton/TJ	0.484	0.484	0.016	0.112	0.112	0.016	0.016
SO2排出係数	ton/TJ	0.00045	0.00045	0.00047	0.00047	0.00047	0.00047	0.00047

#### 3.2. Setting the amount of air pollutant emissions from BEVs

The amount of air pollutant emissions from BEVs, that is, from power plants was determined using Formula (2) based on the automotive annual mileage (3) (passenger cars, trucks, etc.) for each case found in 3.1, BEV power consumption (assumed to be 8.3 km/kWh), BEVs' spread rate (16%), the amount of electricity generated by thermal power plants (demands other than BEVs), and emission intensities (Table 5). This amount of emission was used to set the increase/decrease rate of emissions for SOx and NOx from large-scale emission sources in ADMER-PRO.

Table 5 shows the settings of the emission intensities and the amount of electricity generated by thermal power plants (4, 5), whose values are from the area controlled by Tokyo Electric Power Company. The composition of electric power sources in 2030 was set based on the rate of thermal power generation described in the Long-term Energy Supply and Demand Outlook. The emission intensities of thermal power plants in 2030 were set with a regression formula based on the data of emission intensities until 2018 by the Tokyo Electric Power Company. Based on these data, the amount of emission in 2030 was determined.

$$\text{Emissions} = \sum \left( \begin{array}{l} \text{total mileage} \div \text{BEV power consumption} \\ \times \text{power plant emission intensity} \\ + \text{thermal power plant output} \\ \text{(demands other than BEVs)} \\ \times \text{power plant emission intensity} \end{array} \right) \quad (2)$$

Tbl.5 Emission intensity and electricity generation from thermal power plants.

Year	Emission intensity [g/kWh]		Electricity generation [TWh/year]
	SOx	NOx	
2017	0.03	0.09	184.2
2030	0.026	0.051	129.5

## 4. Results of estimated average atmospheric concentrations

### 4.1. Average atmospheric concentrations of SOx and sulfate

Fig.2 shows the results for SOx and sulfate. The change in social structure from Cases 1 and 2 to Cases 3 and 4 caused a reduction of approximately 10% in the average atmospheric concentrations of SOx and sulfate. The results of the distribution of the average atmospheric concentrations (Case 3) in Figs. 3 and 4 indicate that the higher concentrations of SOx and sulfate are mainly in the suburbs of Tokyo, where large-scale emission sources (power plants) are concentrated, along the coast of Tokyo Bay.

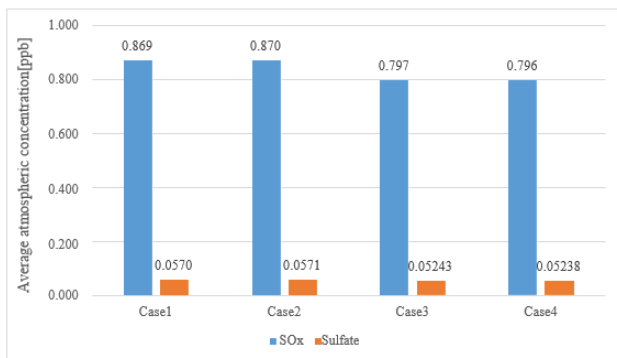


Fig.2 Average atmospheric concentration (SOx, Sulfate)

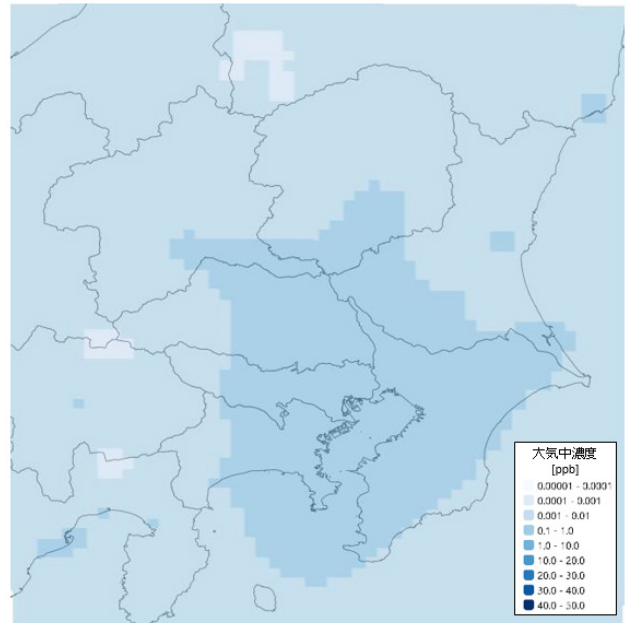


Fig.3 Average atmospheric concentration (Case 3 | SOx)

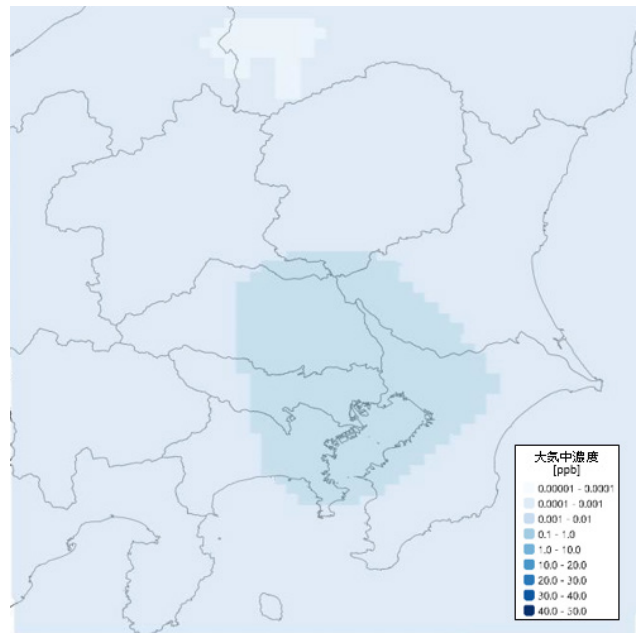


Fig.4 Average atmospheric concentration (Case 3 | Sulfate)

### 4.2. Average atmospheric concentrations of NOx and nitrate

Fig.5 shows the results for NOx and nitrate. The change in social structure from Cases 1 and 2 to Cases 3 and 4 caused a reduction of approximately 20% in the average atmospheric concentrations of NOx and nitrate. Additionally, the lowest result was observed for Case 3, in which BEVs are introduced considering the composition of electric power sources in 2030. The distribution of the average atmospheric concentrations (Case 3) is shown in Figs. 6 and 7. As a result, the concentration of NOx was higher on the coast of Tokyo Bay, and that of nitrate was higher over the suburbs of Tokyo, probably because the sources of NOx are large-scale and mobile emission sources, which are in a wider range compared to the

emission sources of SO<sub>x</sub>, resulting in the higher concentration of nitrate over a wider range.

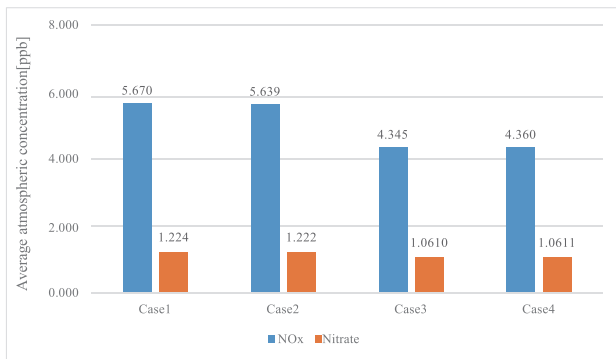


Fig.5 Average atmospheric concentration (NOx, Nitrate)

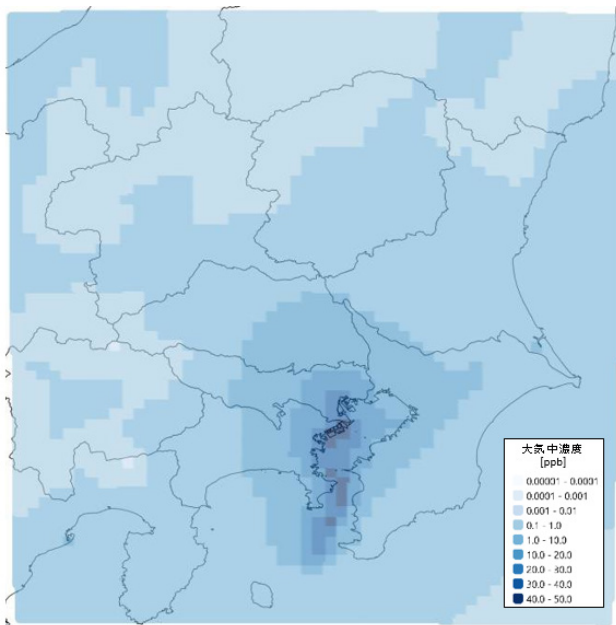


Fig.6 Average atmospheric concentration (Case 3 | NO<sub>x</sub>)

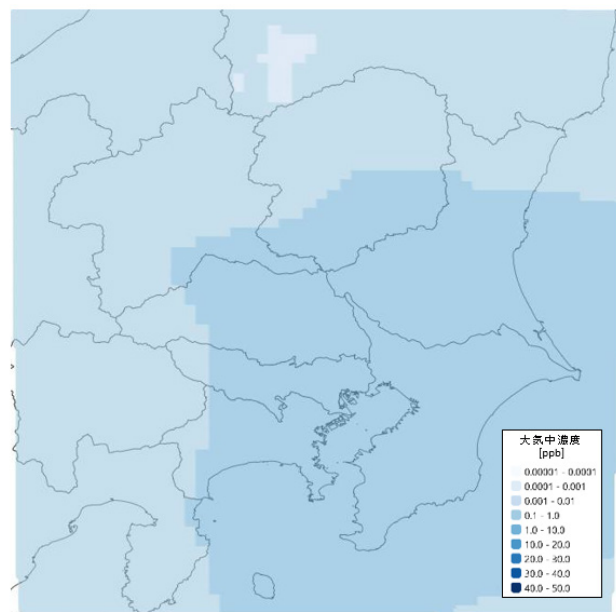


Fig.7 Average atmospheric concentration (Case 3 | Nitrate)

### 4.3. Average atmospheric concentration of tropospheric ozone

As shown in Fig.8, the average atmospheric concentration of tropospheric ozone was higher for Case 3, in which BEVs are introduced considering the composition of electric power sources in 2030. The results of the distribution of the average atmospheric concentrations (Case 3) in Fig.9 indicate that the concentrations are lower on the coast of Tokyo Bay, probably because the concentration of ozone, a secondary product, is higher at destinations, unlike the concentrations of NO<sub>x</sub> and SO<sub>x</sub>, which are higher near the sources.

The estimated concentrations of NO<sub>x</sub> and VOC plotted on the graph by referring to the isoline map of ozone production (9, 10) shown in Fig.10 indicate that the sensitivity regime of Tokyo Metropolis is VOC-sensitive, the sensitivity regime of Gunma Prefecture is Transition, and Tokyo Metropolis exhibits a relationship in which a reduction in the concentration of NO<sub>x</sub> causes an increase in the concentration of ozone.

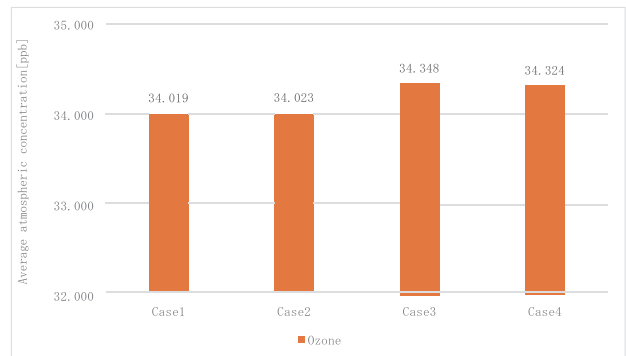


Fig.8 Average atmospheric concentration (O<sub>3</sub>)

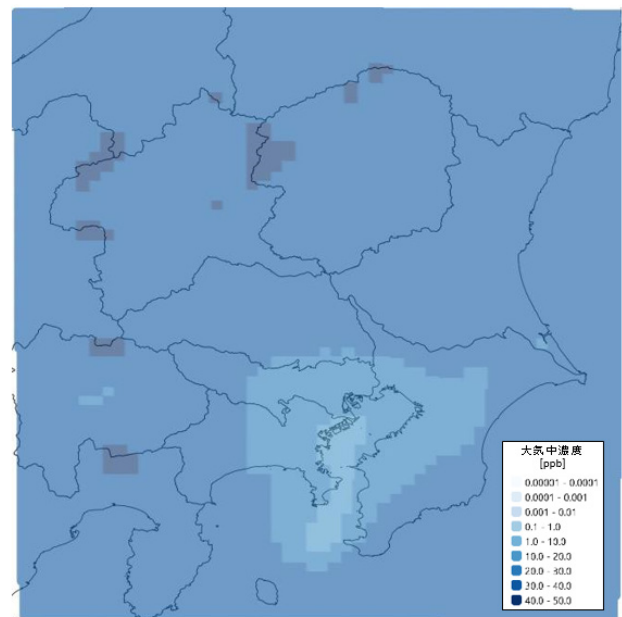


Fig.9 Average atmospheric concentration (Case 3 | O<sub>3</sub>)

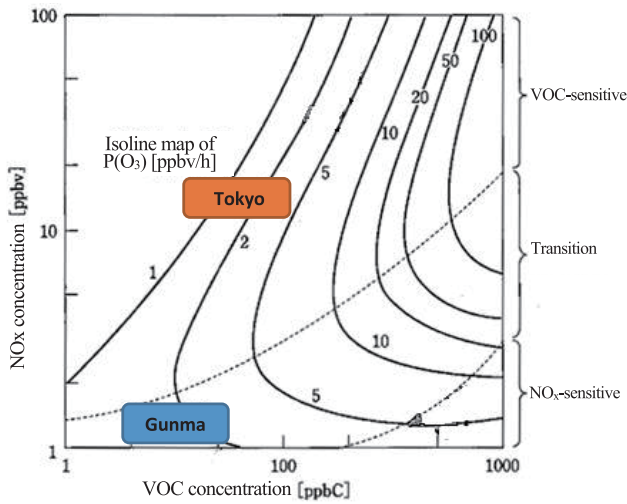


Fig.10 Ozone isopleth diagram

#### 4.4. Analysis of average atmospheric concentration changes per km for one BEV

To measure the effect of BEV introduction in each case, the amount of average atmospheric concentration change per 1-km running for one BEV,  $\Delta C$  [ppb/km for a car], was determined with Formula (3) and the results are shown in Table 6.

For NO<sub>x</sub>, if 16% of passenger cars are replaced with BEVs under the current conditions (changing from Cases 1 to 2),  $\Delta C = -1.8 \times 10^{-12}$  [ppb/km for a car]. Similarly, under future conditions,  $\Delta C = -9.4 \times 10^{-13}$  [ppb/km for a car]. Therefore, in the future, a smaller reduction in the concentration of NO<sub>x</sub> will be caused by BEV introduction. This is probably because this calculation does not include the prospection of BEV power consumption improvement, whereas ICEV fuel efficiency improvement is expected in the future.

For tropospheric ozone, if 16% of passenger cars are replaced with BEVs under the current conditions,  $\Delta C = 2.6 \times 10^{-13}$  [ppb/km for a car]. Similarly, under future conditions,  $\Delta C = 1.5 \times 10^{-12}$  [ppb/km for a car]. Therefore, in the future, a larger increase in the concentration of tropospheric ozone will be caused by BEV introduction. It seems that from the present to the future, NO<sub>x</sub> emissions will reduce in VOC-sensitivity state and the concentration of tropospheric ozone will increase.

$$\Delta C = \text{average atmospheric concentration } C_{\text{BEV}} - \text{average atmospheric concentration } C_{\text{ICEV}} \quad (3)$$

The average atmospheric concentration  $C_{\text{BEV}}$  refers to the average atmospheric concentration in Cases 2 or 3; the average atmospheric concentration  $C_{\text{ICEV}}$  refers to the average atmospheric concentration in Cases 1 or 4.

Tbl.6 The changes in average atmospheric concentration

Year	$\Delta C$ [ppb/vehicle-km]	
	NO <sub>x</sub>	O <sub>3</sub>
2017	$-1.8 \times 10^{-12}$	$2.6 \times 10^{-13}$
2030	$-9.4 \times 10^{-13}$	$1.5 \times 10^{-12}$

## 5. Conclusion

### 5.1. Conclusion

The results indicate that the average atmospheric concentrations of SO<sub>x</sub>, sulfate, NO<sub>x</sub>, and nitrate tend to decrease due to factors such as BEV introduction, ICEV fuel efficiency improvement, and annual automotive mileage reduction, whereas the average atmospheric concentration of tropospheric ozone increases. As shown in Fig.11, the results of the comparison between present and future situations (Cases 1 to 3) indicated that the concentration of NO<sub>x</sub> decreases by approximately 23%, whereas the concentration of the tropospheric zone increases by approximately 1%. This is because the relationship between VOC and NO<sub>x</sub> concentrations for the concentration of tropospheric ozone in urban areas is VOC-sensitive. Therefore, it could be confirmed that a reduction in NO<sub>x</sub> causes an increase in the concentration of tropospheric ozone.

### 5.2. Future challenges

In this report, air pollutants originating from automotive running were examined; therefore, VOC emissions originating from evaporation during refueling, manufacturing industry, and other sources were not considered. In the future, it is necessary to examine emissions from all the related industries to a more precise estimate of the atmospheric concentration of air pollutants.

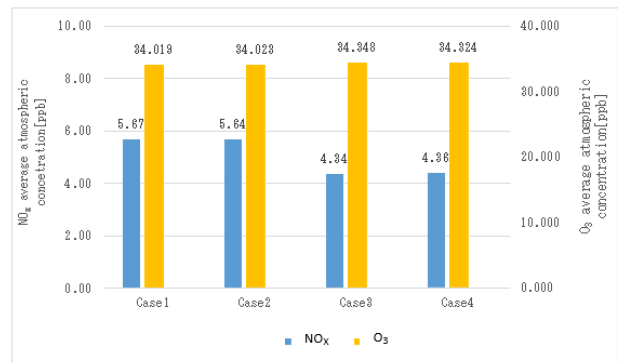


Fig.11 Average atmospheric concentration (NO<sub>x</sub>, O<sub>3</sub>)

It also seems necessary to study the target of VOC emissions from every emission source so that a reduction in the concentration of tropospheric ozone can also be achieved in the future, as NO<sub>x</sub> emissions will be controlled by the BEVs' spread.

In addition, the concentrations of SO<sub>x</sub>, NO<sub>x</sub>, and tropospheric ozone found in this report were annual average values, which cannot be directly compared with the daily and hourly average concentrations of the air quality standards. Consequently, it is necessary to analyze the peak concentration of tropospheric ozone during the daytime in summer.

## References

- (1) 経済産業省,長期エネルギー需給見通し 参考資料(2015),p38
- (2) 二次生成に対応した広域大気モデル ADMER-PRO Ver.1.0 (著作権登録管理番号 H24PRO-1397)
- (3) 環境省,運輸部門(自動車)CO<sub>2</sub>排出量推計データ(2019)
- (4) 東京電力,TEPCO 統合報告書 2018
- (5) 東京電力,1kWhあたりのSO<sub>x</sub>排出量(火力発電所)及び1kWhあたりのNO<sub>x</sub>排出量(火力発電所)
- (6) 国土交通省 「自動車燃料消費量調査」 (2017)
- (7) 国土交通省 「新燃費基準による今後の燃費改善率の評価」 (2017)
- (8) 国際応用システム分析研究所・オーストリア(IIASA), GAINS Asia
- (9) 詳細リスク評価書シリーズ24 オゾン
- (10) Sillman Snaford (1999). The relation between ozone, NO<sub>x</sub> and hydrocarbons in urban and polluted rural environments

## Source

公益社団法人自動車技術会  
2020年春季大会学術講演会講演予稿集  
No.86-20 文献番号:20205195

## Authors



Gen Saitou



Hiromi Asahi

# Development of 0W-8 low viscosity engine oil for fuel efficiency improvement

Seichi Nakano\* Hiroki Saito\* Yusuke Koike\*\*  
Sachiko Okuda\* Takumaru Sagawa\*

**Abstract** Low viscosity engine oil lower than 0W-16 has been needed for improving fuel efficiency in the Japanese market. However, it generally has negative points in regards to anti-wear performance and volatility control with lower viscosity oil. The technical challenges are to reduce viscosity while keeping anti-wear performance and volatility level as 0W-20 oil. They have been solved by focusing on MoDTC and base oil characteristics. This paper describes a new engine oil that provides good fuel efficiency while keeping the reliability.

## 1. Introduction

In order to improve fuel efficiency, energy-efficient powertrains such as electric vehicles (EVs) and hybrid EVs have been introduced in the market, mainly in Japan, the United States, Europe, and China. However, vehicles with traditional internal combustion engines are still the mainstream in the global market. Therefore, the fuel efficiency improvement of internal combustion engines remains a very important issue from the perspective of CO<sub>2</sub> reduction.

In recent years, several approaches to fuel efficiency improvement by applying a low-viscosity oil to reduce the stirring resistance have been proposed. Consequently, 0W-16 fuel-saving engine oils<sup>(4)</sup> have been introduced into the market. In addition, in the SAE J300 viscosity classification, low-viscosity grades such as SAE 12 and SAE 8, which have lower viscosity than the existing SAE 16, were established<sup>(1)</sup> in 2015. As no official quality standards were applied to SAE 12 and SAE 8, the standardization was studied according to requests from Japanese automotive manufacturers.

Prior to this, we examined a 0W-8 low-viscosity fuel-saving engine oil. There are two issues related to lower engine oil viscosity: (1) evaporativity deterioration and oil consumption increase due to lower-viscosity base oil, and (2) friction increase caused by more contact in sliding sections due to thinner oil film.

Thus, two subjects were examined in this report: (1) application of a gas-to-liquids (GTL) base oil<sup>(3)</sup> for lower viscosity while controlling oil consumption to comply with the standards of JASO GLV-1; and (2) friction reduction and abrasion resistance improvement by optimizing base-oil viscosity and utilizing MoDTC (friction modifier).

## 2. Experiment method

### 2.1. Actual-engine oil consumption test

Applying a direct-injection NA 2.0-L L4 engine, oil consumption was evaluated with an automatic lubricating oil/ consumption measuring system. In this study, an evaluation was performed in the high-speed and the 6000-rpm full-load modes, in which evaporativity is thought to have a significant effect due to high oil temperature.

### 2.2. Chain wear test

Table 1 shows the test conditions simulating the wear of a silent chain. Fig.1 illustrates the tester (TCM-55M by TOKYO METER CO., LTD.). The distance between the two shafts was adjustable. Each shaft has a sprocket that can let a chain go round at any tension, temperature, or rotation speed. In this study, an evaluation was performed at a high tension and high temperature considering a thinner oil film due to a low-viscosity oil.

Table1 Chain wear test mode

Chain type	Silent chain
Speed	6000rpm
Oil temperature	110±1°C
Oil supply	Splash
Oil	Oil with 0.4mass% carbon black Average particle size from 0.1 to 0.3µm

\*Materials Engineering Department

\*\*Powertrain and EV Mechanical system Technology Department

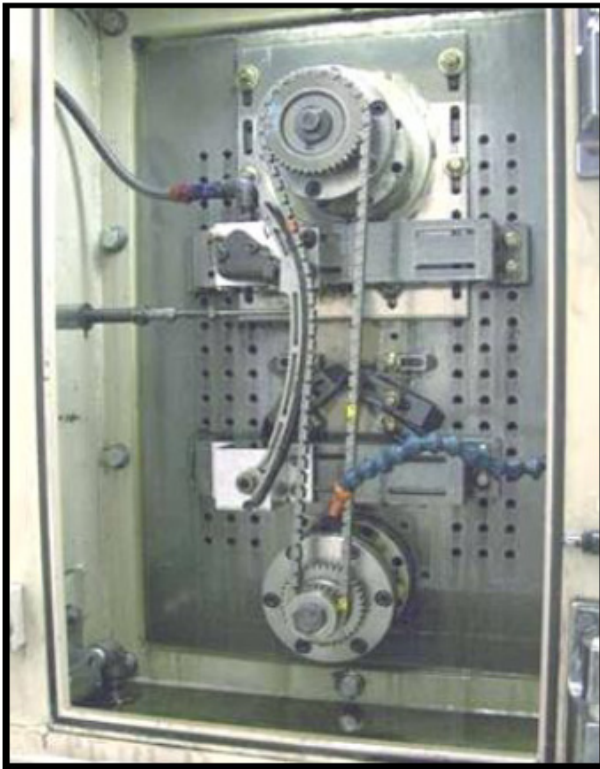


Fig.1 Silent chain wear test

### 2.3. Oil film thickness test

The outline of the equipment (EHD2 Ultra-Thin Film Measurement System by PCS Instruments) is shown in Fig.2. It allows an oil film thickness to be measured at any setting of oil temperature, load, and speed. In this study, the effect of lower viscosity on oil film thickness was verified by changing the sliding speed under high-temperature conditions

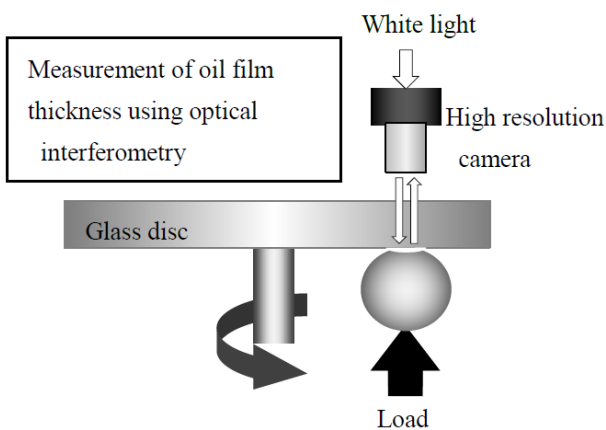


Fig.2 Oil film thickness measurement equipment

### 2.4. Engine motoring torque test

The outline of the equipment is shown in Fig.3. In this study, MR20DD (direct injection, NA, 2.0 L, L4) was applied, and the friction torque was measured using a torque meter with an engine driven by a motor to evaluate the friction characteristics of various oil materials<sup>(4)</sup>.

Measurements were performed at an engine speed of 650 to 2800 rpm and at two test temperature levels: 50°C for simulating the low temperature of the fuel efficiency evaluation mode, and 80°C for simulating the high temperature.

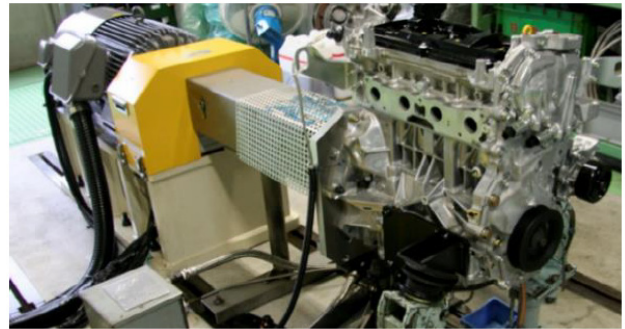


Fig.3 Engine motoring torque test

## 3. Test results

### 3.1. Examination of base oil

#### 3.1.1. Selection of optimal base oil type

Lower viscosity is essential for improving fuel efficiency. An attempt to lower the viscosity with a blend retaining the same viscosity index as the current OW-16 oil requires a lower-viscosity base oil. In this case, the evaporativity standards of JASO, NOACK 250°C, 15% or less, are widely exceeded. Accordingly, the application of a GTL base oil with low evaporativity and an optimized blend for viscosity were studied.

Based on the same viscosity modifier (VM) and additive package, the relationship between evaporativity and kinematic viscosity was verified using OW-8 oils whose oil evaporativity (NOACK) levels were adjusted by changing the base oils (two types of the existing Gr. III and GTL Gr. III base oils), base oil viscosities, and the amount of additional VM. Fig.4 illustrates the relationship between NOACK and kinematic viscosity.

At the equivalent viscosity, GTL Gr. III base oil has an approximately 5% lower NOACK value than the existing Gr. III base oil at 250°C. This is thought to be caused by the narrower molecular weight distribution of GTL Gr. III base oil components and consequent smaller number of low-molecular-weight components, which are more evaporable.

Fuel efficiency (estimated JC08 mode value) was also evaluated by applying the motoring torque test and using an oil with this GTL Gr. III base oil blended. Fig.5 illustrates the results of the fuel efficiency evaluation with different NOACK values. Within the range of oil evaporativity applied, the higher the NOACK value, the better the fuel efficiency, which indicates a trade-off relationship between the evaporativity and fuel saving performance. This result is thought to reveal that the application of the GTL base oil for lower viscosity and fuel efficiency improvement provides both fuel efficiency improvement and reduction in NOACK, thereby controlling the deterioration of oil consumption.



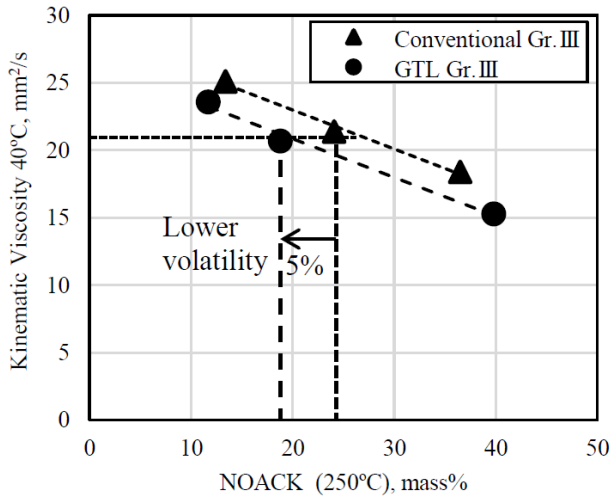


Fig.4 Relationship between volatility and kinematic viscosity

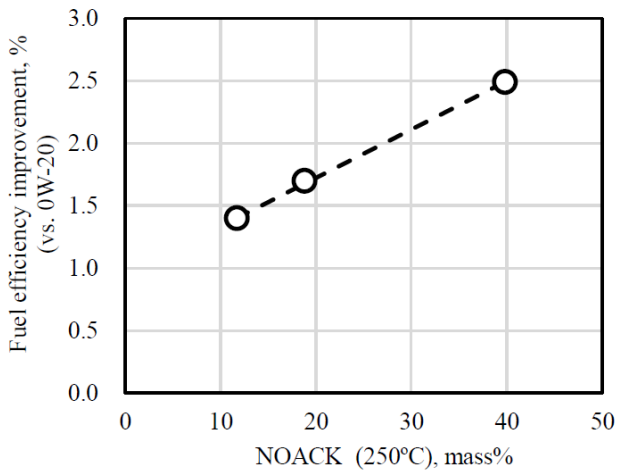


Fig.5 Relationship between estimated fuel efficiency and NOACK in GTL base oil

### 3.1.2. Actual-engine oil consumption verification

Table 2 shows the oils used in this test. The 0W-8 oil complies with the evaporativity standards and its blend contains a GTL Gr. III base oil; the 0W-20 A oil complies with the evaporativity standard of NOACK 250°C, 15% or less. The results of the oil consumption test are shown in Fig.6. In the high-speed and 6000-rpm full-load modes, the 0W-8 oil with the GTL Gr. III base oil blended exhibited an equivalent or lower oil consumption compared to the 0W-20 oil meeting the evaporativity standards. It is thought that the use of GTL Gr. III base oil resulted in a NOACK equivalent or lower than that of the 0W-20 oil and the control of the actual engine oil consumption.

Table2 Characteristics of test oil for oil consumption test.

	SN/GF-5 0W-20 A	GTL base oil 0W-8
Base oil type	Gr. III	GTL Gr. III
Additive package	PKG A +MoDTC	PKG B +MoDTC
NOACK (mass%)	250°C	
	12.6	11.7

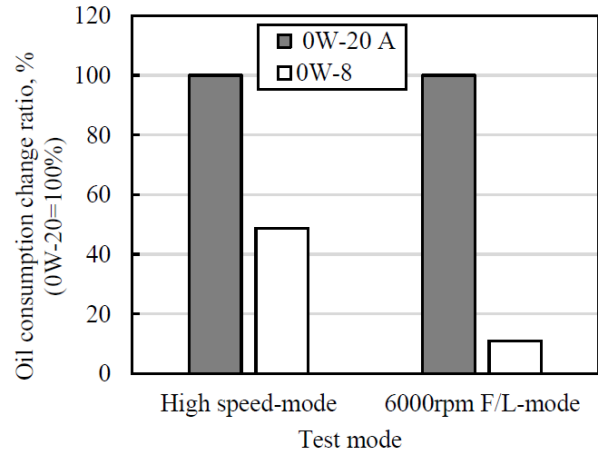


Fig.6 Results of oil consumption test

## 3.2. Examination of abrasion resistance

### 3.2.1. Examination of wear prevention by ensuring oil film thickness

The silent chain of a valve operating system, which is related to the lower viscosity of engine oil, exhibits mixed to boundary lubrication in the sliding sections between the pins and plates, which are wear sections. To ensure oil films, it is thought that the effect of VM is small and the effect of base oil viscosity is dominant<sup>(5)</sup>. Consequently, to verify the abrasion resistance of a 0W-8 oil in a silent chain, oil film thicknesses were measured by applying oils with a viscosity grade of 0W-20 B and 0W-8, and whose viscosities were almost equal at 100°C. Table 3 shows the properties of the oils used in this test. Measurements were performed in a high temperature range, in which oil films become thinner and it is difficult to avoid abrasion. The results of the oil film thickness test are shown in Fig.7. In the range of 0.5 m/s or less of slip speed, the oil film thicknesses are similar, and the abrasion resistance is thought to have a similar performance as that of the 0W-20 oil.

**Table3 Oil characteristics for oil film thickness measurement.**

	SN/GF-5 0W-20 B	GTL base oil 0W-8
VM addition	STD	Reduction
Additive PKG	MoDTC PKG	←
Kinematic Viscosity (mm <sup>2</sup> /s)	100°C	7.8
	40°C	32.4
HTHS 150°C(mPa·s)	2.6	1.7

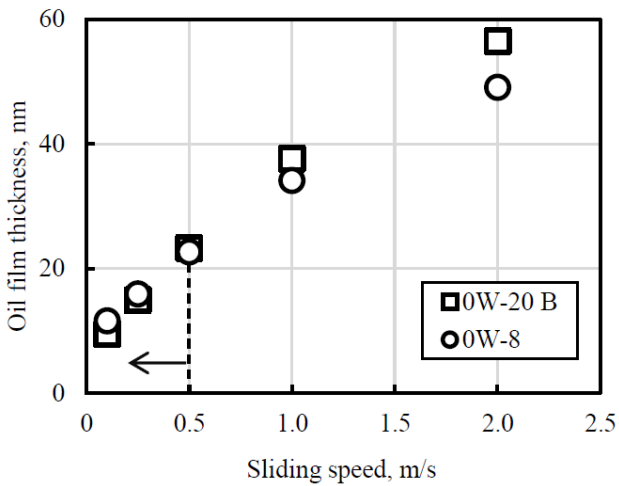


**Fig.7 Results of oil film thickness measurement.**

**3.2.2. Silent chain wear test**

The wear test of a silent chain was performed with the oils used in 3.2.1, whose properties are detailed in Table 4. The chain wear test was performed using the same base oil and additive package as the 0W-20 B oil and using a 0W-8 oil whose viscosity was adjusted with VM. Fig.8 shows the results using these oils and also actual results using the SM/GF-4 5W-30 oil with no MoDTC added for comparison, as this is an oil applied to our engines with silent chains. The chain elongation rate for the 0W-8 oil was equivalent to that for the 0W-20 B oil, and a reduction in chain elongation rate of 50% compared to the 5W-30 oil was verified. The reason of this reduction is thought to be the difference in the additive package and the formation of MoO<sub>3</sub> films<sup>(6)</sup> originating from the MoDTC.

**Table.4 Oil characteristics for silent chain wear test.**

	SN/GF-5 0W-20 B	GTL base oil 0W-8	SM/GF-4 5W-30
Additive package	PKG B +MoDTC	←	PKG C
Kinematic Viscosity (mm <sup>2</sup> /s)	100°C	7.8	10.1
	40°C	32.4	57.4
HTHS 150°C (mPa·s)	2.6	1.7	2.9

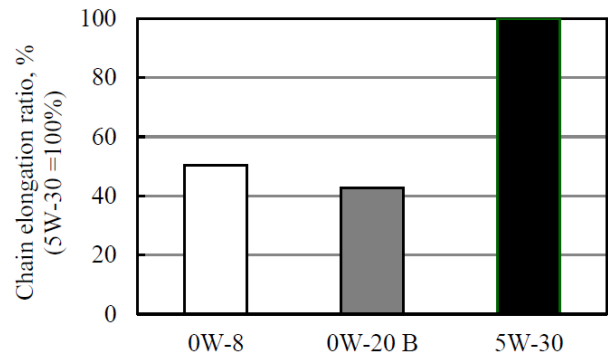


**Fig.8 Results of silent chain wear test**

**3.3. Verification of fuel saving effect**

Table 5 shows the properties of the 0W-8 and API SN 0W-16 oils used in the motoring torque test. Fig.9 illustrates the results of this test with an MR20DD engine (direct injection, NA, 2.0 L, L4). The test was performed to determine the rate of fuel efficiency improvement in the WLTC fuel efficiency certification mode (Japanese mode). There is no change in torque at 650 rpm, but the higher the engine speed, the lower the torque. Therefore, it is thought that stirring resistance reduction due to lower viscosity caused torque improvement.

Fig.10 illustrates the effects of torque reduction on fuel efficiency improvement<sup>(4)</sup> in the WLTC mode. The use of the 0W-8 oil meeting NOACK 250°C, 15% or less (a challenge) resulted in a prospective fuel efficiency improvement of 0.57% in the WLTC mode compared to the API SN 0W-16 oil.

**Table5 Oil characteristics for motoring fuel efficiency test.**

	SN 0W-16	GTL base oil 0W-8
Additive package	PKG D +MoDTC	PKG B +MoDTC
Kinematic Viscosity (mm <sup>2</sup> /s)	100°C	6.2
	40°C	27.2
HTHS 150°C (mPa·s)	2.3	1.7
NOACK (mass%)	250 °C	13.5
		11.7

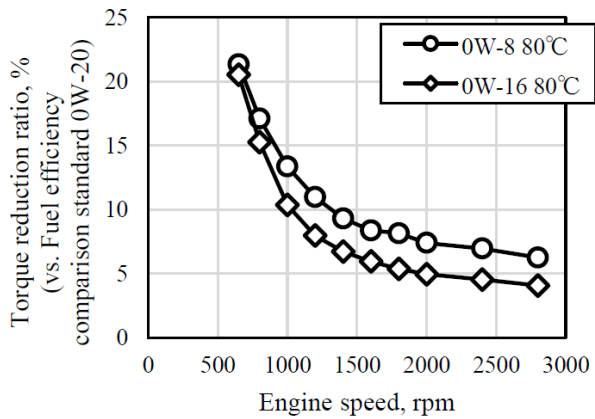


Fig.9 Result of torque improvement ratio with motoring fuel efficiency test.

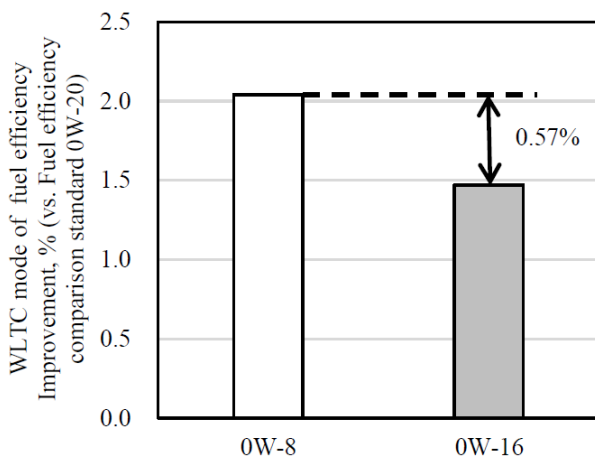


Fig.10 Fuel efficiency improvement results of WLTC mode evaluated by motoring fuel efficiency test.

## 4. Conclusion

The results of examining a fuel-saving blend for spreading and deploying 0W-8 fuel saving oils indicated the following:

- (1) By applying a GTL-base oil while attempting lower viscosity, the 0W-8 oil met NOACK 250°C, 15% or less, which is the evaporativity requirement of the standard JASO GLV-1;
- (2) It was verified that maintaining the viscosity of the base oil and reducing VM ensured the oil film thickness in the range of mixed to boundary lubrication and the abrasion resistance equivalent to that of the current oil;
- (3) It was verified that a fuel efficiency improvement effect of 0.57% in the WLTC mode can be expected in comparison with the current API SN 0W-16 oil.

## 5. Acknowledgements

We would like to offer our special thanks to Mr. Sato from Shell Lubricants Japan K.K., who made enormous contributions to sample adjustments, property verifications, and in the preparation of this abstract.

## References

- (1) 美藤 洋平;仲野 誠一;鈴木 理佳;小池 裕介;楠原 慎太郎;佐川 琢円:API SN 0W-16低粘度省燃費エンジン油, 2016年春季大会 学術講演会 講演予稿集, No.72-16S p.1787 (2016)
- (2) (公社)自動車技術会:JASO 自動車用ガソリン機関潤滑油, JASO M364 (2019)
- (3) (株)潤滑通信社:潤滑経済2018年2月号(第634号)p.19~23
- (4) (公社)自動車技術会:JASO自動車用ガソリン機関潤滑油-モータリング燃費試験方法, JASO M365 (2019)
- (5) Takumaru Sagawa, Seiichi Nakano, Yohei Bito, Yusuke Koike, Sachiko Okuda, Rika Suzuki: Development of Low Viscosity API SN 0W-16 Fuel-Saving Engine Oil Considering Chain Wear Performance, SAE Int. J. Fuels Lub. 10(2):469-477, 2017

## Authors



Seiichi Nakano



Hiroki Saito



Yusuke Koike



Sachiko Okuda



Takumar Sagawa

# Clarification of Resin Impregnation Mechanism in CFRP C-RTM Forming

Rieko Yamaguchi\* Atsushi Mizutani\* Ryoichi Takatsu\* Kiyohito Yanagibashi\*

**Abstract** In recent years, efforts to alleviate environmental problems have required vehicles with reduced weights. As a result, it has become challenging to apply super-high tensile strength steel and light-weight materials using aluminum, carbon fiber reinforced plastic (CFRP), etc. CFRP allows weight reduction by approximately 50% compared to steel, but its practical application is limited. To expand its application, issues such as cost reduction and productivity improvement must be solved. Accordingly, the compression resin transfer molding (C-RTM) method has been applied for reduction of form cycle, solving one of the issues. Unlike the conventional RTM, after a carbon-fiber forming object is placed into a mold in C-RTM, a slight space is allowed for injecting resin without completely closing the mold to allow resin to quickly flow into it. In this study, the mechanism of resin flows within the space between a mold and a carbon-fiber layer in the forming process of C-RTM is clarified, and a simulation method in which interface resistance between resin and a fiber layer is considered as viscosity resistance is reported.

## 1. Introduction

Although automobiles have eased people's lives and have been considerably developed, they are limited by environmental problems. As a result, maintaining a sustainable society becomes more important. Our company has set target values based on the Nissan Green Program: compared to 2000, a 40% reduction in CO<sub>2</sub> emissions by 2022, and a 90% reduction by 2050. The CO<sub>2</sub> controls of various countries have become gradually stricter, and Europe will have even stricter controls in 2025. The route for achieving the targets is by accelerating electrification. However, motors and/or inverters used for electrification may increase vehicle weights. Therefore, a further weight reduction in vehicle bodies is required. To reduce vehicle body weights, super-high tensile strength steel and/or aluminum have been applied. In some models, carbon fiber reinforced plastic (CFRP) has been applied. To reduce vehicle body weight in the future, multi-material applications are being considered, in which multiple materials are applied to appropriate sections, thus utilizing most of the characteristics of various materials such as steel, aluminum, and CFRP. Among such materials, CFRP is used in aircrafts and other applications, provides superior specific tensile strength and specific stiffness, and allows for approximately 50% weight reduction. Although our company has already employed CFRP for some models such as GT-R NISMO, the cost of CFRP is approximately ten times the cost of steel parts, which limits its application. However, CFRP is important for weight reduction in the future. Thus, the following issues for cost reduction should be addressed: rational structural designs appropriate for composite material, material cost

reduction with innovative material manufacturing methods for carbon fibers, and productivity improvement. With regard to productivity improvement, conventional major forming methods, such as the hand lay-up and the autoclave methods, require a long forming time of approximately 3 to 4 h. In recent years, to significantly reduce the forming time, development/application cases of multiple forming methods have been performed, focusing on resin transfer molding (RTM).

## 2. Purpose of development

As described above, as the most important challenge for productivity improvement is to reduce its cycle time, the focus was driven to a forming method known as compression-RTM (C-RTM). This forming method allows the resin to flow into a mold faster than in the conventional RTM, with the mold slightly opened.

In C-RTM, to optimize resin injection points and/or flow assisting grooves when a mold is designed, techniques to grasp resin flows to predict any points with no resin impregnation are important. Conventionally, the optimization process was based on repeating prototyping and mold modifications, but simulation-based evaluations can minimize development process repetitions. However, in the current conditions, significant differences between actual forming results and simulation results are observed. Thus, improving the simulation accuracy has been an issue that needs to be resolved.

In a previous study, Pham et al. built a new model considering the mass balance and pressure of resin during compression to improve the accuracy of C-RTM<sup>1)</sup>. In addition, Serge represented the effect of a space on flows at the edges in a model<sup>2)</sup> to improve accuracy. Gauvin, Young, and others experimentally found a space

\*Production Engineering Research and Development Center

impregnation coefficient<sup>3)</sup> and represented it in an analysis.

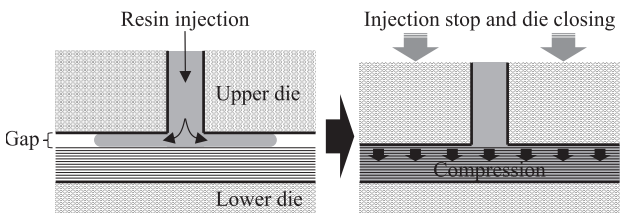
This study clarified the mechanism of resin flows in a small space before a mold is closed in the forming process of C-RTM; moreover, it addressed a technique of modeling the mechanism and incorporating it into a resin impregnation simulation.

### 3. Experiment method

#### 3.1 Summary of C-RTM method

Fig.3 Shape of experimental mold and positions of mold temperature sensors

A summary of the C-RTM method used in this study is shown in Fig.1. A space provided between a fiber layer and a mold during resin injection allows the resin to flow and spread quickly. Closing the mold just after the resin is filled causes the resin to be impregnated in the direction of the plate thickness, resulting in faster resin impregnation than that in the conventional method.



Gap space = Low flow resistance Assist impregnation by die closing

Fig.1 Summary of C-RTM method

#### 3.2 Summary of base simulation software used in this study

We first describe the analysis software program used in the simulation (PAM-RTM by ESI Japan Ltd.). This software program simulates the resin flow between carbon fibers to predict the time period from flowing to hardening of the resin and non-impregnated areas and is used to determine resin injection positions when a mold is designed.

As shown in Fig.2, impregnation coefficients, which represent fluidity in consideration of fiber orientation in “X,

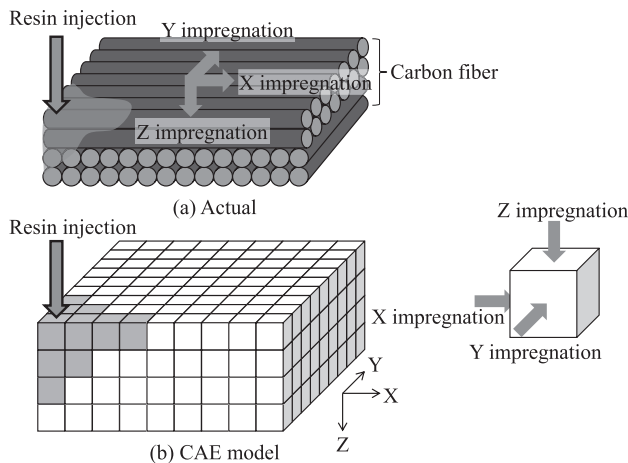


Fig.2 Summary of simulation

Y, and Z” directions, are input into cells of each mesh to calculate the resin flow into an adjacent cell. The impregnation coefficients are determined from the flow velocity, viscosity, and pressure difference based on Darcy’s law.

#### 3.3 Experimental mold and forming conditions

The experimental mold, shown in Fig.3, was used to perform a forming experiment for flow behavior. Temperature sensors were fitted to four points on the lower mold to read changes in temperature during the flow of the injected resin to measure the time of resin flow. The forming conditions, including mold temperatures, resin viscosities, and laminating conditions, are shown in Table 1.

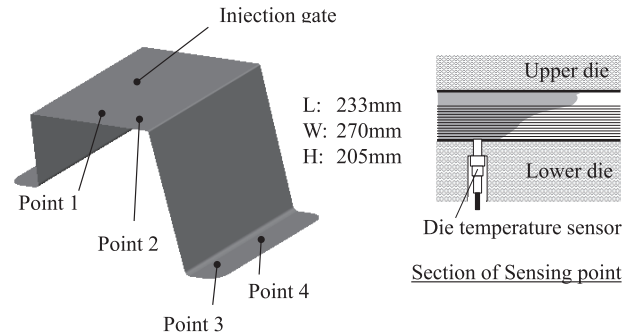


Fig.3 Shape of experimental mold and positions of mold temperature sensors

Table 1 Material properties and viscosity characteristics

Molding thickness	2.6[mm]
Fiber areal weight	305[g/m <sup>2</sup> ]
Fiber density	1.8[g/cm <sup>3</sup> ]
Quantity of ply	8PLY
Fiber orientation	[±45/0/0/0]s
Material lamination	[NCF/UD/UD/UD]s
V <sub>f</sub>	50[%]

#### 3.4 Modeling and input conditions for simulation

The RTM impregnation simulation used as a base uses a model for predicting resin flows into a fiber layer (impregnation) with a completely closed mold. For C-RTM, there is a space between the mold and the fiber layer in the stage of resin injection, which is the initial stage of forming. Accordingly, as shown in Fig.4, two zones were set by considering the space between a carbon-fiber base material (hereinafter referred to fiber layer) and a mold as Zone 1 and the part of the fiber layer as Zone 2, and a model was applied, in which the resin flow in Zone 1 is more prominent than in Zone 2.

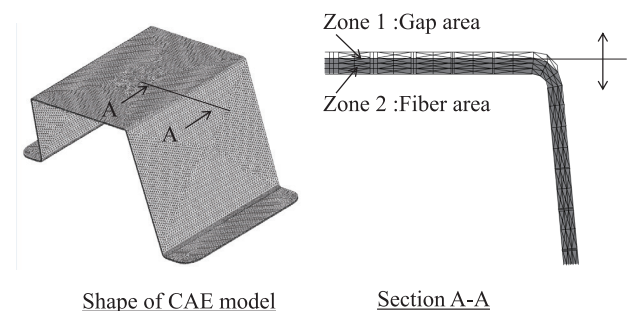


Fig.4 Zoning of simulation model

A problem was identified in the simulation, which is the input condition for the impregnation coefficients in Zone 1. Resin impregnation simulation is calculated by inputting the impregnation coefficients into each cell element, but the space has no fiber layer. Then, as shown in Fig.5, the experimental results for the relationship between the fiber density and the impregnation coefficient were used to estimate the impregnation coefficient of resin flowing within a space. Table 2 shows the plate thickness and impregnation coefficients for Zones 1 and 2 used in the simulation.

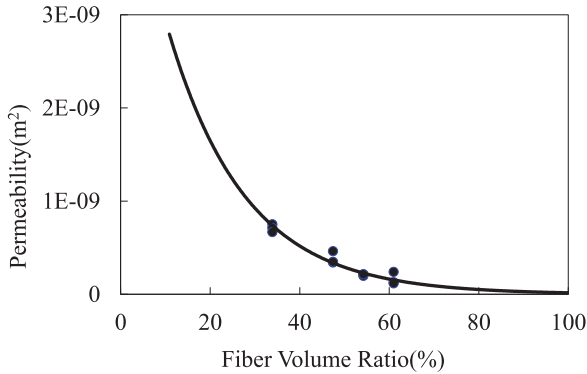


Fig.5 Relationship between fiber density and impregnation coefficient

Table 2 Impregnation coefficients for CAE in the initial stage

Molding thickness	2.6[mm]
Zone 1 permeability	x:1.5E-07[m <sup>2</sup> ]
(i.e. Gap permeability)	y:1.5E-07[m <sup>2</sup> ]
	z:1.5E-07[m <sup>2</sup> ]
Gap height	1[mm]
Zone 2 permeability	x:4.9E-11[m <sup>2</sup> ]
	y:3.6E-11[m <sup>2</sup> ]
	z:1.9E-12[m <sup>2</sup> ]

### 3.5 Comparison between simulation and experimental results

The simulation and experimental results are shown in Fig.6. Numbers “1” to “4” on the x-axis represent the positions of the temperature sensors placed on the mold shown in Fig.3. As the resin flows in the order of 1 to 4, the time for the resin to pass the points was measured as the resin impregnation time. As a result, it was revealed

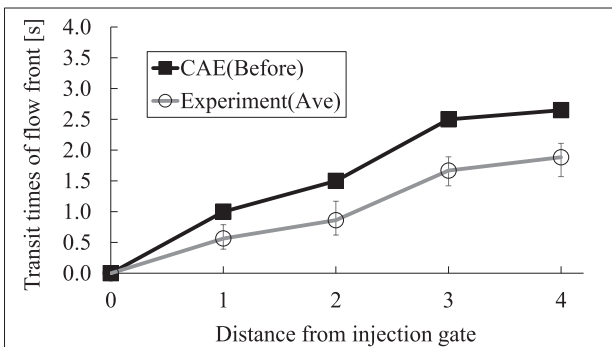


Fig.6 Simulation and experimental results

that the simulation deviated from the experimental results by approximately 40% (the average value of 12 cases); the resin slowly reached the temperature sensors placed on the lower mold, resulting in slow impregnation.

## 4. Accuracy improvement of simulation

### 4.1 Identification of factors affecting simulation accuracy

The factors that caused the simulation to deviate from the experiment were identified. To identify factors affecting resin flows among input conditions including 20 items or more, experiments were performed according to L18 orthogonal table composed of affecting factors, as shown in Table 3. The effects of these factors are shown in Fig.7. As a result, the contribution rate of the impregnation coefficient setting for space (C) in Zone 1 was the highest, and the resin injection speed (D) also has an effect. In contrast, no effect on the fiber density (A) and the plate thickness (B) related to Zone 2 was observed.

Table 3 Affecting factors

	Factor	Unit	Level 1	Level 2	Level 3
A	Carbon fiber permeability	m <sup>2</sup>	Vf dependence	Thickness dependence	-
B	Carbon fiber thickness	mm	2.6	2.7	2.8
C	Gap permeability	m <sup>2</sup>	Without viscosity	With viscosity	-
D	Resin injection speed	cc/sec	80	90	100
E	Die closing timing	sec	0	1	2

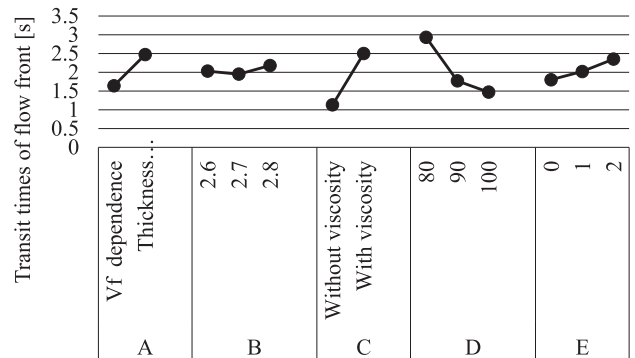


Fig.7 Contribution rates from the factor effect diagram

### 4.2 Clarification of resin flowing mechanism in space parts

From the results of the quality engineering method described in Section 4.1, a problem regarding the modeling of resin flows in a space with no fibers in Zone-1 was revealed; therefore, efforts were made to clarify the mechanism. Using the visualized mold shown in Photo 1, flows on the metal and the fiber layer surfaces were evaluated. As a result, it was confirmed that there is a flow difference between the metal surface and the fiber layer surface, as shown in Fig.8, and the flow on the fiber layer surface is slower by approximately 25%. Because

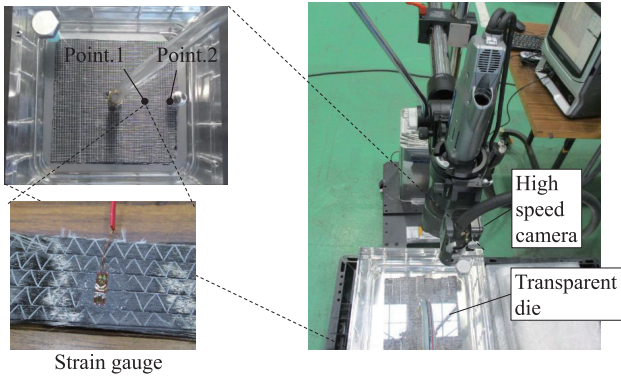


Photo 1 Visualized mold

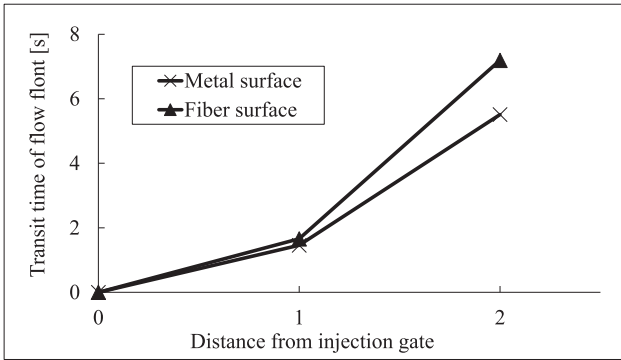


Fig.8 Resin-flowing time difference between metal and fiber surfaces

fibers are bundled into a fabric, the surface of the fiber layer is fluffy. In addition, as the carbon-fiber surface is sizing-treated to improve carbon fiber-to-resin adhesion, the carbon-fiber surface has a high surface energy, hindering the flow of the resin.

Based on the above results, it was assumed that the resin flowing in a space is affected by the viscosity resistance of the fiber-layer surface. Thus, as shown in Fig.9, it was supposed that accuracy improvement could be achieved by finding a viscosity resistance from the shearing force in the parallel flow and substituting it into the input conditions of the simulation as a coefficient of fluidity in Zone 1. Additionally, the viscosity resistance was calculated by substituting the resin viscosity determined from the material properties and the measured pressure difference between the two points into the equation. A specific measurement method was applied, in which pressure sensors were set at the two points, as shown in Photo 1, to measure the pressure difference between the resin flowing on the metal and the resin flowing on the fiber layer. The results are shown in

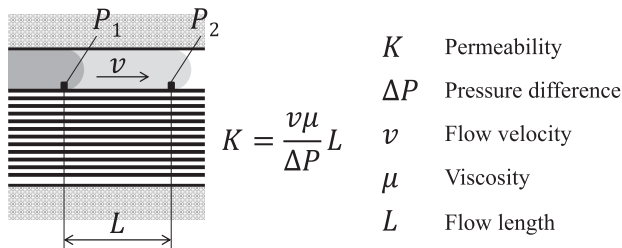


Fig.9 Calculation method of viscosity resistance of flow between flat plates (between mold and fiber)

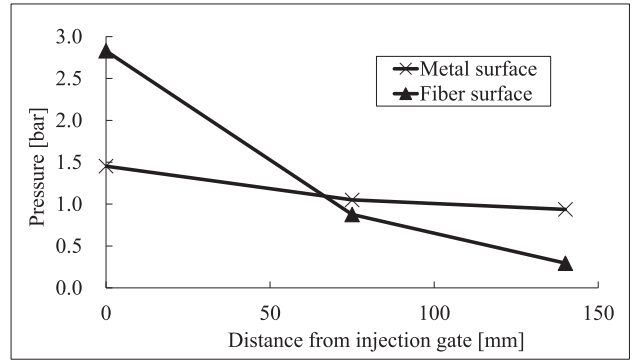


Fig.10 Pressure difference of resin flowing between mold and fiber

Table 4 CAE parameters after consideration of viscosity resistance

Molding thickness	2.6[mm]
Zone 1 permeability	x:5.0E-09[m <sup>2</sup> ]
(i.e. Gap permeability)	y:5.0E-09[m <sup>2</sup> ]
	z:5.0E-09[m <sup>2</sup> ]
Gap height	1[mm]
Zone 2 permeability	x:4.9E-11[m <sup>2</sup> ]
	y:3.6E-11[m <sup>2</sup> ]
	z:1.9E-12[m <sup>2</sup> ]

Fig.10. As the hat-shaped carbon fiber has eight plies, measurements were performed with the height of the space area fixed at 1 mm.

### 4.3 Accuracy improvement of prediction of resin flow

Figure 11 illustrates the results of the simulation, in which viscosity resistance is considered for resin flows in a space area. It was verified that the analysis results almost conform to the experimental values. It was supposed that, after the viscosity resistance between the resin flowing in the space part and the fiber layer was considered, the amount of resin flowing in the space part was reduced; the amount of resin impregnated into the fiber layer increased; the resin was impregnated faster in the direction of the plate thickness, and the time required to reach the sensors on the lower molds shortened. This means that the consideration of the viscosity resistance caused a reduction in the value of the impregnation coefficient in Zone 1 to approximately 1/3. Moreover, the

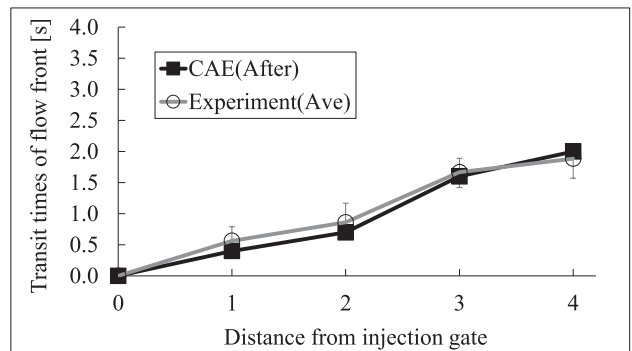


Fig.11 Simulation and experimental results



amount of resin flowing in the XY direction of the space part decreased, and the amount of resin to the fiber layer in the Z direction increased, resulting in the improvement of impregnation. Based on this, the accuracy was improved by normalizing the impregnation coefficients.

#### 4.4 Accuracy verification of prediction of positions with no resin impregnation

In addition to the resin flow, the accuracy of analyzed positions where no resin impregnation occurred was verified. As shown in Fig.12, the side face of the hat shape (Fig.13) was segmented with an interval of 20 mm, and the conformity rate of the experimental and simulation results was verified. Resin-impregnated areas are shown in purple, and non-resin-impregnated areas are shown in black. As a result, the initial analysis had a conformity rate of approximately 73% in area ratio. As shown in Section 4.4, the accuracy improvement of the resin flow simulation caused the conformity rate to improve to approximately 90%, and the accuracy improvement of the non-impregnation occurrence positions and their areas was also verified.

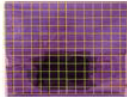
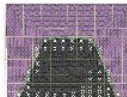
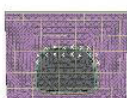
	Dry spot result	Impregnated area	Matching rate
Experiment		494[cm <sup>2</sup> ]	-
CAE (Without viscosity)		360[cm <sup>2</sup> ]	73.8[%] (124/168 cells)
CAE (With viscosity)		482[cm <sup>2</sup> ]	90.4[%] (152/168 cells)

Fig.12 Positions of non-impregnation occurrence in simulation and experiment

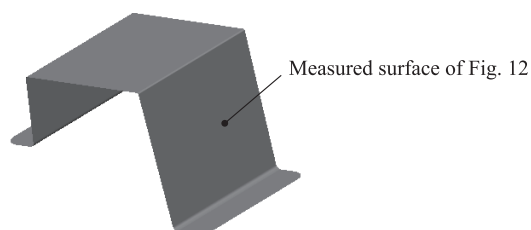


Fig.13 Evaluation section of non-impregnation occurrence positions

## 5. Conclusion

In this study, by applying the resin impregnation simulation using the C-RTM method, the mechanism of resin flows in a space part between a mold and a fiber layer in the initial stage of forming was clarified, and the modeling considering the viscosity resistance was verified. This consideration also improved the accuracy of

the impregnation simulation. The results obtained and perspectives for future work are listed below.

1. The impregnation simulation of C-RTM forming was performed by using the RTM impregnation simulation software as a base. Resin flows were divided into a space part and a fiber layer, and the fiber layer was allowed to take over the resin flow from the space part.
2. From the experiments of fiber densities and impregnation-system coefficients, it was found that resin flows in a space part in the initial stage of forming cannot be reproduced with the impregnation coefficients of the space part estimated; it was also found that the resistance received from the interface when resin flows on the fiber layer must be considered as viscosity resistance.
3. It was shown that the viscosity resistance received by the resin in a space part can be determined by substituting an experimentally measured pressure difference between two points into the calculation formula for the viscosity resistance of the flow between parallel plates; the calculation can be performed by replacing the viscosity resistance with the resin fluidity in the simulation.
4. Regarding the viscosity resistance of resin flowing in a space part, which was clarified in this study, its effects caused by the differences in the height of the space part or the types of carbon-fiber base materials (fiber layer) will be verified in future work.

## 6. Acknowledgements

We would like to offer our special thanks to ESI Japan Ltd., Kanazawa Institute of Technology, and all related departments of our company, who provided experimental support and knowledge for the progress of this study.

## 7. References

- 1) X-T. Pham, F. Trochu, J.-F. Remacle and R. Gauvin, *Trans. Eng. Sci.* 21, pp.87-96 (1998).
- 2) Serge Abrate, *Appl. Mech. Rev.* 55-6, pp.579-599 (2002).
- 3) Young WB and Lai CL, *Composites A-28*, pp.817-822 (1997).
- 4) 日産自動車ニュースルーム:車体軽量化に向けた炭素繊維強化プラスチック(CFRP)部品の量産化技術を開発(2020)

## Authors



山口 りえこ



水谷 篤



高津 亮一



柳橋 清人

# Analysis and measurement of PCB heating due to abnormal current and safety conditions

Tsutomu Horikawa\* Shingo Inagawa\* Tsuneaki Yamuchi\*

## 1. Abstract

In electronic equipment, there is a slight probability of accidental short-circuit failures in electronic devices even with high-quality design. A typical method to interrupt an abnormal current in such a case is the blowout of a fuse. However, in 12-V power source systems used for vehicles, an electronic board may cause abnormal heating with a current lower than the fusing current of a fuse. This study indicates that a simple calculation model of heat transfer can represent actually measured heating characteristics of a phenomenon where an abnormal current causes a pattern on the printed circuit board (PCB) to generate heat and/or fuse. A method to estimate the safety range of an overheated PCB that must prevent carbonization from spreading, leading to smoke/fire generation, was presented as a design technique.

## 2. Framework of safety design

The flow of a safety design against an abnormal current due to an accidental failure is shown in Fig.1. If an abnormal current occurs, the copper foil generates heat first. The generated heat flows into and heats the substrate. The heated substrate exceeds its glass transition point, gets overheated, and causes thermal decomposition. In the area where thermal decomposition progresses into carbonization in this process, insulation of the substrate cannot be expected. Therefore, estimating a carbonized area is necessary to prevent a secondary short circuit between power and the ground. Any gas generated during thermal decomposition may ignite with a spark caused by fusing; thus, estimating the ignition area, checking the fire power by testing, and designing the fire resistance of the case are required.

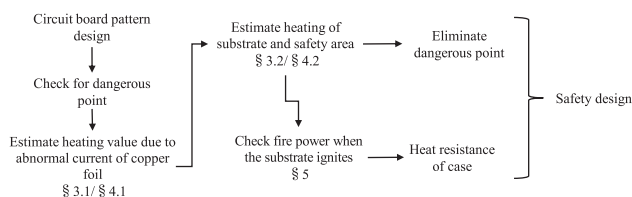


Fig.1 Safety design flow against abnormal current

## 3. Calculation model

An abnormal current flowing through a PCB causes a copper foil to generate heat, which heats the substrate. This mechanism is illustrated in Fig.2 using a heat flow. Due to this heat flow, a calculation model was created. The model was divided into two steps: heat generation of the copper foil and heating of the substrate. Using the model, the fusing characteristics of the copper foil and the carbonization area of the substrate were predicted. In the model of this study, thermal radiation is not considered to simplify the calculation.

### 3.1. Heat generation model of copper foil

Assuming that the heat transfer route is as shown in Fig.3, the temperature rise  $\Delta T_{Cu}$  caused by energizing the copper foil with a heat capacity of  $C_{Cu}$  for  $s$  seconds can be expressed by Eq. 1.

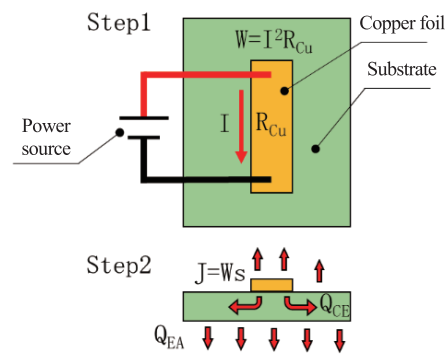


Fig.2 Diagram of the model

$$\Delta T_{Cu} = \frac{(I^2 R_{Cu} - Q_{CA} - Q_{CE} - Q_{CC})s}{C_{Cu}} \dots Eq. 1$$

Here, heat flow  $Q_{CE}$  from the copper foil to the substrate can be expressed by Eq. 2 using the substrate's thermal resistance  $\theta_{CE}$ .  $\Delta T_{CE}$  is the temperature difference between the copper foil and the substrate.

\*System Integration and EE Architecture Engineering Department

$$Q_{CE} = \frac{\Delta T_{CE}}{\theta_{CE}} \dots \text{Eq. 2}$$

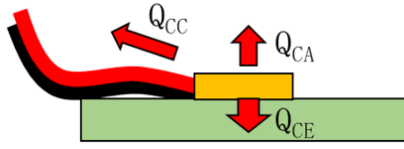


Fig.3 Heat transfer route of heat generated in copper foil

In addition, heat radiation  $Q_{CA}$  due to convection from the copper foil to the air is expressed in Eq. 3.

$$Q_{CA} = \Delta T_{CA} h A \dots \text{Eq. 3}$$

Here,  $h$  refers to the convection heat transfer coefficient, and  $A$  refers to the area of the copper foil. The heat transfer to the cables  $Q_{CC}$  was considered as a constant to provide a good agreement with the results of actual measurement.

Eq. 1 can be re-expressed as Eq. 4 with a fusing time  $s_m$  until the copper foil reaches a fusing temperature  $T_m$ .

$$s_m = \frac{C_{Cu} \Delta T_m}{I^2 R_{Cu} - Q_{CA} - Q_{CE} - Q_{CC}} \dots \text{Eq. 4}$$

At this point, fusing limit current that causes an equilibrium state between heat radiation and heat generation can be a condition for Eq. 5. Under this condition, the copper foil is heated at fusing temperature.

$$I^2 R_{Cu} - Q_{CA} - Q_{CE} - Q_{CC} = 0 \dots \text{Eq. 5}$$

### 3.2. Heating model of substrate

Heat  $Q_{CE}$  flows from the heating copper foil to the substrate beneath the foil. The heat that flew in is divided into the heat radiated into the air  $Q_{EA}$  and the heat transferred through the substrate  $Q_{EE}$  (see Fig.4).

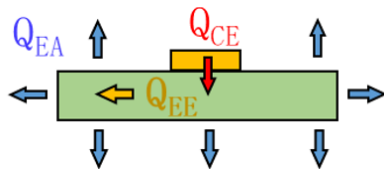


Fig.4 Transfer route of heat flow into substrate

Here, discretizing the volume of the substrate can provide numerical solutions without the need to solve heat conduction equation. Fig.5 illustrates the inputs and outputs of heat  $Q_{CE}$  that flows into the substrate beneath the copper foil.  $Q_{CE}$  is given by Eq. 2. Thermal resistance  $\theta_{CE}$  is determined by Eq. 6 from thermal conductivity  $\lambda_{EP}$ , contact surface area  $A_0$ , and substrate thickness  $t$ .

$$\theta_{CE} = \frac{t}{\lambda_{EP} A_0} \dots \text{Eq. 6}$$

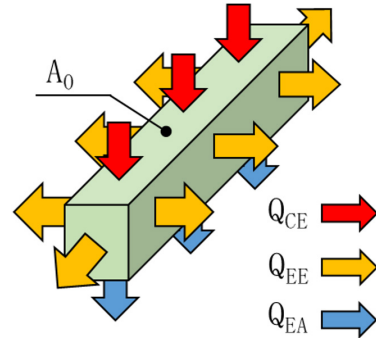


Fig.5 Inputs/outputs of the heat flow into the substrate beneath the copper foil

Then, assuming that the thickness of the adjacent volume is  $\delta$ , heat  $Q_{EE}$  flow into the adjacent volume with contact area  $A_1$  (Fig.6) is given by Eq. 7. Here,  $\Delta T_{E01}$  is the temperature difference between the substrate beneath the copper foil and its adjacent volume.

$$Q_{EE} = \Delta T_{E01} \frac{\lambda_{EP} A_1}{\delta} \dots \text{Eq. 7}$$

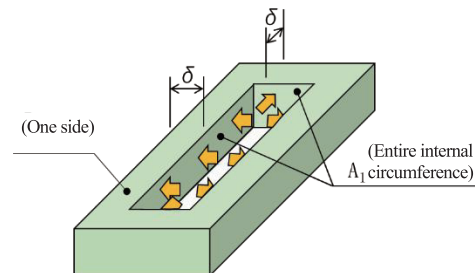


Fig.6 Discretized substrate volume in inner circumference direction

In addition, the radiation from the  $i$ -th volume into the air is given by Eq. 8, in which the area exposed to the air is expressed as  $B_i$ . Here, it was assumed that the convection heat transfer coefficients of the upper/lower surfaces were the same.

$$Q_{EAi} = \Delta T_{EAi} h B_i \dots \text{Eq. 8}$$

By discretizing the substrate volume through which heat is transferred, the heat conduction of the substrate can be solved as a thermal resistance ladder (see Fig.7) between the temperature of copper foil  $T_{Cu}$  and ambient temperature  $T_{am}$ .

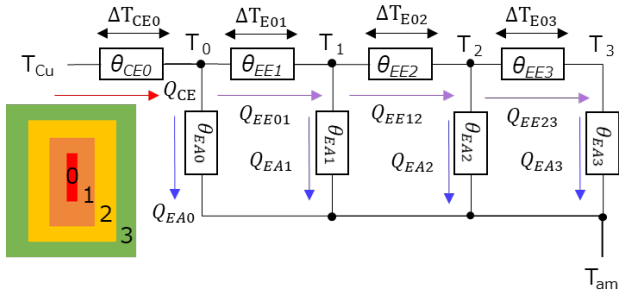


Fig.7 Thermal resistance ladder for four-way split discretization

### 4. Comparison between actual measurement and model calculation

The sample shown in Fig.8 was energized at room temperature until the copper foil was fused. The fusing time was compared with that of the model calculation.

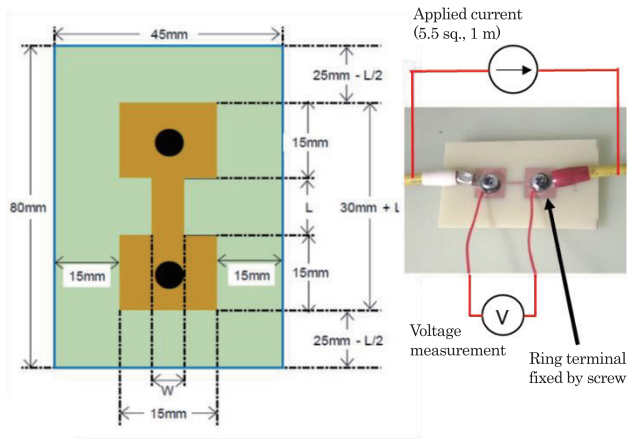


Fig.8 Shape of sample

Here, as a sample substrate, Panasonic R-1566 with a thickness of 1.6 mm was used. The fusing characteristics of the copper foil and the width of the substrate carbonized area (Fig.9) were adopted as comparison items between the calculation model and the actual measurement. In this case, a detailed investigation is necessary to verify whether a black-discolored area was thermally decomposed into carbonization. However, in this study, a black-discolored area was considered to be carbonized.



Front side Back side

Fig.9 Example of carbonized substrate after being fused

#### 4.1. Fusing characteristics of copper foil

Eq. 4 is used to determine fusing time when current is applied. The parameters used for calculation are listed in Table 1. Here,  $Q_{CE}$  and  $Q_{CA}$  values were obtained by an

approximation calculation using a value of constant at the maximum heat flow at the melting point temperature of Cu foil. In addition, cable-related parameter  $Q_{CC}$  and the net heat capacity of the test board  $C_{Cu}$  were adjusted based on the test results considering the effect of the cable fixing points. The resistivity of copper foil  $\rho$  was determined using Eq. 9 and  $V$  and  $I$  measured.

$$\rho = \frac{RA}{L} = \frac{VA}{IL} \quad \dots Eq.9$$

The resistivity of the copper foil while fusing was in agreement with the resistivity at the melting point temperature of Cu (1085°C), and it fused when reached the melting point. Thus, it is thought that Cu has a significant change in resistivity as it changes from solid to liquid state, as the melting area is locally heated, and a spark is generated.

Table 1 Calculation parameters

	t: 35 $\mu$ m L: 10 mm W: 1 mm	t: 35 $\mu$ m L: 10 mm W: 0.5 mm	t: 18 $\mu$ m L: 10 mm W: 0.5 mm	
$Q_{CE}$	4.11	2.05	2.05	[W]
$Q_{CA}$	0.13	0.06	0.06	[W]
$Q_{CC}$	3.1	3.1	2.1	[W]
$C_{Cu}$	1	0.5	0.25	[J/K]
$\rho$	10.8	8.76	8.71	[10 <sup>-8</sup> $\Omega$ m]
$\lambda_{EP}$	0.62	←	←	[W/mK]
$h$	0.0012	←	←	[W/cm <sup>2</sup> K]
$I_{limit}$	15.8	10.2	6.6	[A]

The calculation results, represented as dotted lines, and the actual measurement results, represented as plotted dots, are shown in Fig.10. It was verified that even with a simple calculation considering only the amount of the heat transferred from the copper foil can sufficiently represent fusing characteristics. Here, the vertical solid lines represent fusing limit current  $I_{limit}$  for calculation, which is a current value determined by making the denominator in Eq. 4 zero. At the fusing limit current value, the copper foil does not fuse, and the PCB remains heated.

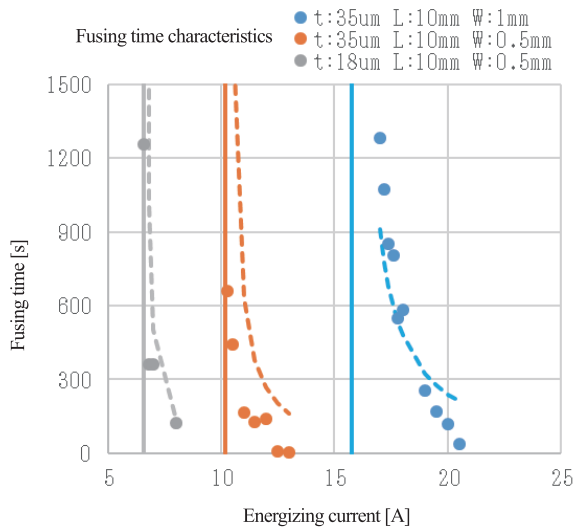


Fig.10 Dependence of current on fusing time

#### 4.2 Width of carbonized substrate

The heating of the substrate can be estimated by solving the simultaneous equations of the thermal resistance ladder illustrated in Fig.7. Here, it was considered that heating was continued at the fusing limit current, which was regarded as the maximum condition under which carbonization occurs. Then, a system in an equilibrium state at the Cu melting point temperature was used for calculation (see Fig.11).

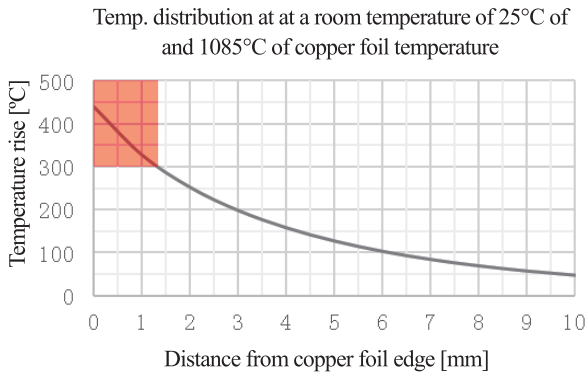


Fig.11 Estimated result of heating of substrate

Here, as the calculation conditions, for the copper foil of  $1 \times 10$  mm and discretization width of 1 mm, to determine  $\delta$ , an area over  $300^\circ\text{C}$  of substrate decomposition temperature was estimated to have approximately 1.3 mm as a carbonization width. In this case, the carbonization width as a result of calculation is one-side distance from the copper foil edge, thus two times the carbonization width should be added to the copper foil width to determine actual carbonization width (see Fig.12). Therefore, net carbonization width was estimated to be 3.6 mm. Fig.13 shows the actual measurement results of the substrate carbonization width with a fused copper foil ( $1 \times 10$  mm and  $35 \mu\text{m}$  thick).

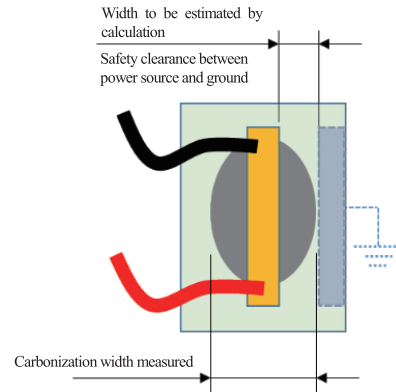


Fig.12 Calculated estimation and carbonization width measured

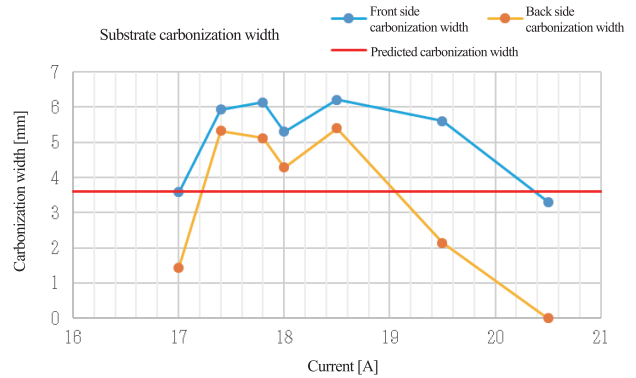


Fig.13 Fusing current and substrate carbonization width

The peak of the carbonization width appeared at a slightly higher current than the fusing limit current (15.8 A), which is a condition for continued heating. It was verified that carbonization width becomes narrower because fusing time becomes shorter after the peak. The case where ignition occurred during the test was excluded from the data because carbonization width cannot not be measured.

### 5. Behavior at ignition of substrate

Fire resistance of a casing that is resistant to fire power when the substrate is ignited is required for safety, and it is necessary to verify fire power by testing. In this study, the behavior during ignition was investigated.

Fig.14 illustrates the heating characteristics until the substrate was ignited. The characteristics were measured with thermocouples attached on the back side of the substrate. Here, a copper foil ( $35 \mu\text{m}$  thick and  $2 \times 10$  mm) was adopted as a sample.

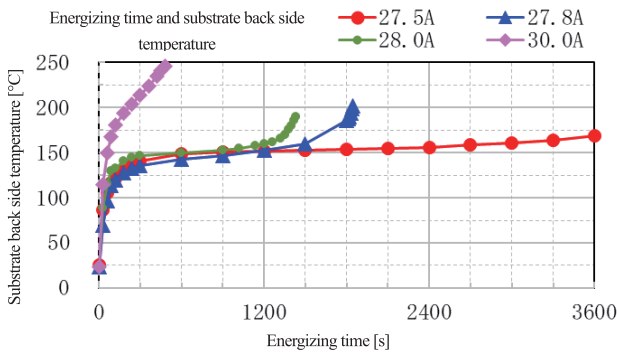


Fig.14 Heating characteristics of substrate

From the results of measuring temperatures, it was verified that an increase of only 0.3 A from 27.5 to 27.8 A causes the heating characteristics to sharply change. In addition, at 27.8 A or more, the temperature starts to rise sharply after it is heated to approximately 150°C. This sharp temperature rise is thought to be the heating mode causing the substrate to ignite.

Considering the process until ignition occurs, it is thought that the epoxy resin is heated, the molecular chains of the high polymers are gradually cut and thermally decomposed into a combustible gas that is ignited by a spark while fusing of copper foil (Fig.15).

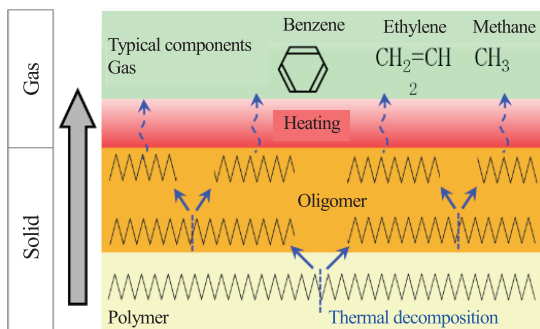


Fig.15 Thermal decomposition process of substrate

Fig.16 shows the conditions for ignition occurrence during the measurement of fusing characteristics. The marks colored in red indicate the occurrence of ignition. Because the ignited samples appear to be at random, it is thought that the ignition of the PCB due to fusing current is not directly caused by heating over the fire point, but by a mode where combustible gas is ignited by a spark while fusing.

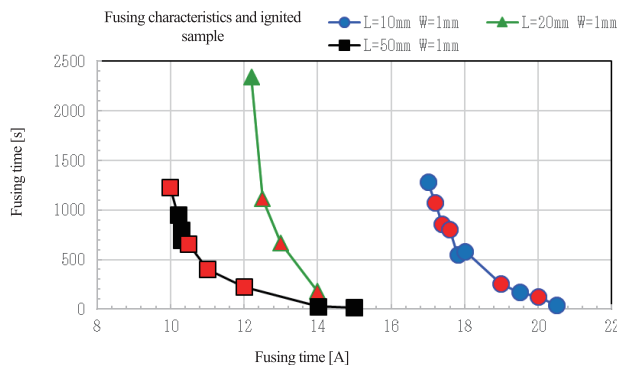


Fig.16 Fusing time characteristics and ignition presence/absence

## 6. Future prospects and conclusion

This study presents a method to estimate a dangerous current area. The model improves calculation accuracy by considering the heat radiation from the copper foil and the substrate. With a sample for this time, a heat radiation of approximately 1 W was estimated. Additionally,  $Q_{CE}$  and  $Q_{CA}$  were determined by approximating them as constants in this study, but  $Q_{CE}$  and  $Q_{CA}$  can be dynamically handled by discretizing time and temperature distribution, which improves the calculation accuracy of the fusing characteristics and carbonization widths. The calculation flow for discretizing time is shown in Fig.17. When this flow is used for calculation, it is necessary to repeatedly solve thermal resistance ladder; thus, a dedicated calculation tool should be prepared.

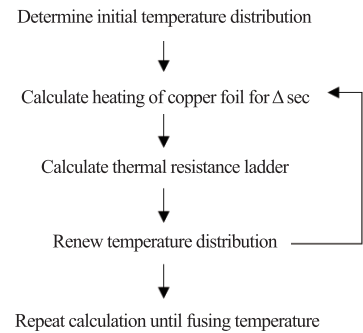


Fig.17 Calculation flow including transient analysis

In order to secure the safety of printed circuit board, it is crucial to estimate a dangerous current region. And it is also important to take measures for design that ensures sufficient safe region by reviewing fuse capacity and detecting any abnormal current/heating based on correct estimation results.

## 7. References

- ・ パナソニック 電子回路基板材料 総合カタログ
- ・ 熱物理学 丸善株式会社 チャールズ・キッテル (著)
- ・ サーキットテクノロジー Vol.3 No3 「直流電流によるプリント配線板導体箔の溶断過程」首藤 克彦、鶴見 策郎

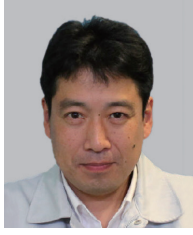
### Source

一般社団法人エレクトロニクス実装学会  
第34回春季講演大会予稿  
講演番号:3B2-01、2020年

## Authors



Tsutomu Horikawa



Shingo Inagawa



Tsuneaki Yamuchi



# Method of Driving Style Adaptation for Automated Vehicle

Machiko Hiramatsu\* Hwaseon Jang\* Yuki Ito\*\*  
Masaru Yamazaki\*\* Takashi Sunda\*\*\*

**Abstract** In the market penetration phase of automated vehicles, adapting automated vehicle control to individual driving styles is assumed to contribute toward the feelings of security and acceptability. This study developed a modeling method involving few parameters for adapting the distance to the preceding vehicle during automated vehicle control to the driving style of an individual. An experiment using an actual vehicle on a proving ground showed the effectiveness of this method in terms of increasing the feelings of security and acceptability of the driver.

## 1. Introduction

Over recent years, the research and development of automated driving has accelerated owing to its advantages, such as reducing accidents and driver workload and providing assistance to people suffering from mobility difficulties. Although the development of this technology is anticipated, many drivers still perceive automated driving as unreliable <sup>(1)</sup>. Hence, promoting the feelings of security and acceptability among drivers is necessary for the penetration of this technology into society. For everyday drivers, the standards of appropriate driving are based on their respective driving styles. Therefore, adapting automated driving control to individual driving styles is important in terms of promoting the feelings of security and acceptability toward the technology.

A few previous studies have focused on adapting the vehicle control to individual driving styles. These include a study to investigate the relationship between scores on the driving style questionnaire (DSQ) developed by Ishibashi et al. <sup>(2)</sup> and the distance to the preceding vehicle and the braking behavior in a car-following situation <sup>(3)</sup>, as well as a study to investigate the individual differences in the deceleration behaviors on ordinary roads <sup>(4)</sup>. These studies revealed individual differences in terms of the distance to the preceding vehicle and the deceleration behavior with respect to the preceding vehicle or the intersection. It is considered that there exist large individual differences in the driving styles under situations without imminent collision risks; therefore, most users would expect automated driving to adapt the control parameters to their own driving styles in such situations.

To this end, this study developed a method of modeling individual driving styles to realize automated driving that learns the driving styles of individuals during manual driving and adapts the automated driving control accordingly. In this work, “driving style” is defined as the personal characteristics of driving behavior. The car-following situation was the focus of this study, and a method of modeling the personal characteristics of the distance to the preceding vehicle was devised.

The following steps were performed in this study: collecting driving data for ordinary roads, identifying driving situations in which the personal characteristics of distance to the preceding vehicle are well observed, determining a variation factor such as a driving environment characteristic, proposing a method for modeling the personal characteristics corrected by the variation factors, and validating the proposed method by using a test vehicle equipped with an automated driving function on a proving ground.

It should be noted that the experiments reported herein were approved by the human research ethics committee of Nissan Motor Co., Ltd., and were performed with participants to whom the experimental conditions were explained and who signed written consent forms in advance.

## 2. Collection of driving data on a public road

### 2.1. Selection of participants

Several drivers with various driving styles were selected before data collection using the DSQ <sup>(2)</sup>. The DSQ consists of 18 questions to assess eight driving styles. It was previously reported that the distance to the preceding vehicle was correlated with scores of “impatient driving tendency” and “careful driving tendency” <sup>(3)</sup>. Therefore,

\*Mobility and AI Laboratory

\*\*Prototype and Test Department

\*\*\*AD/ADAS Advanced Technology Engineering Department

the DSQ survey was attempted by 19 employees who drove frequently, and five participants who had different tendencies in the two scores were selected. Their ages ranged from 25 to 59 years.

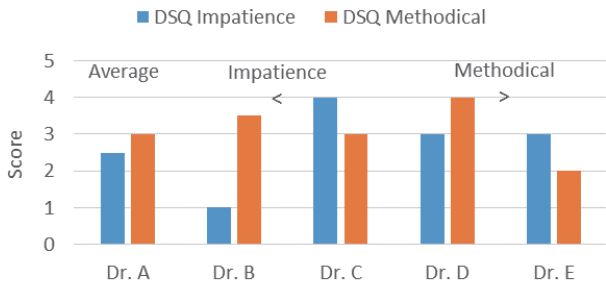


Fig.1 DSQ score of participants

The DSQ results of the five participants are shown in Fig. 1. Driver A has average impatient and careful tendencies; driver B has a lower impatient tendency, whereas this tendency is higher for driver C; and driver D has a higher careful tendency, whereas this tendency is lower for driver E.

### 2.2. Driving route

Data collection was performed on a 32 km circular route between our facility in Atsugi City, Kanagawa, and SOTETSU Sagamino Station in Ebina City via Route 246, which took 1–1.5 h. The course was considered to include various environmental factors that affect the driver’s distance to the preceding vehicle, such as road type; speed limit; number of lanes; and presence of traffic lights, curves, and sloping roads. As Route 246 is an arterial road with considerable traffic involving large vehicles, situations in which the preceding vehicle was a large vehicle or traffic congestion were also included.

### 2.3. Measurement method

Driving data were collected using a standard passenger vehicle equipped with measurement instruments (hereinafter referred to as the “measurement vehicle”). CAN, GPS, camera recognition, and video images (front view, side views, rear view, driver face, and foot area) were synchronously collected. Output data from a forward radar for the ACC were used to measure the distance to the preceding vehicle. The road type; speed limit; number of lanes; and presence of intersections, curves, and slopes were identified using location data and map information. Traffic congestion was identified as the number of vehicles detected by the front camera within 50 m ahead. The indications of traffic signals ahead and the types of preceding vehicles were manually classified using the images captured by the front camera.

The drivers first drove through the course with an operator to familiarize themselves with the measurement vehicle and the course. Thereafter, they were asked to complete six trials by themselves as everyday driving to collect the driving data.

## 3. Method of modeling the distance to the preceding vehicle

### 3.1. Extraction of distance data

Data were extracted in the car-following situation to capture the personal characteristics of distance to the preceding vehicle. The car-following situation was defined as a situation in which a preceding vehicle had existed continuously for 5 s, the relative speed was 2 m/s or less, and the steering angle was 15° or less; this was to eliminate transient situations involving the temporary existence of preceding vehicles, such as cutting in/out, lane changing, or driving on a curved road. The data were extracted in 1 s intervals when the required situational characteristics were present. In addition, data were extracted once the measurement vehicle completely stopped covering the stopping scene in the car-following situation.

### 3.2. Distance while stopping

The distance to the preceding vehicle while stopping was investigated, and the results for each driver are shown in Fig. 2. The most frequent distances for each driver range from 3 to 5 m, and all the distances range from 2 to 8 m.

Driver C, who has a higher impatient tendency, and driver D, who has a prevailing careful tendency, have shorter stopping distances than the other drivers. Driver D also had the lowest standard deviation. These results are similar to those of a previous study <sup>(3)</sup>.

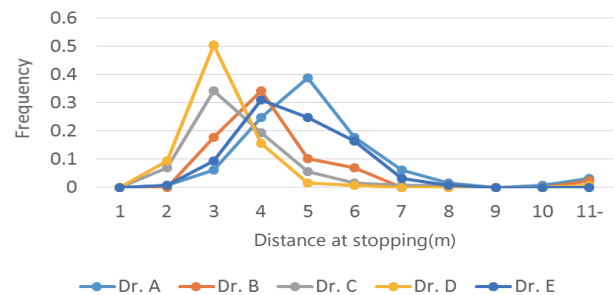


Fig.2 Frequency of distance at stopping (N=5)

### 3.3. Distance while moving

As it is known that the distance to the preceding vehicle depends on the traveling speed, the relationship between speed and distance was investigated first. A previous study showed that the distance to the preceding vehicle at low or medium speeds was different between cruising and starting/accelerating scenarios <sup>(5)</sup>. Therefore, the distance data were classified into three phases: cruising, accelerating, and decelerating. Cruising was defined as moving with no braking and an acceleration less than 0.05G, accelerating was defined as moving with an acceleration of 0.05G or more, and decelerating was defined as moving with braking.

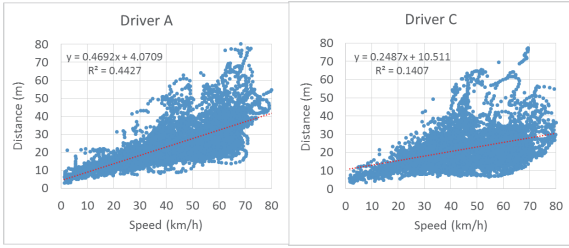


Fig. 3 Distance during cruising (drivers A and C)

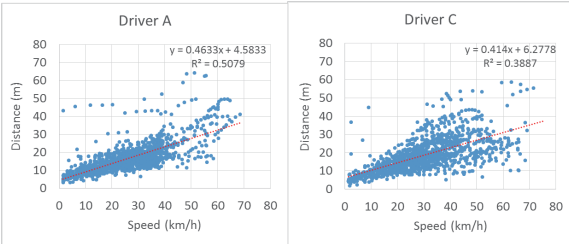


Fig. 4 Distance during acceleration (drivers A and C)

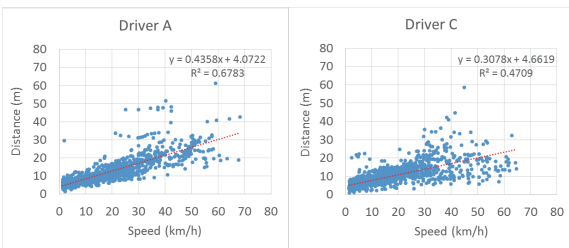


Fig. 5 Distance during deceleration (drivers A and C)

The results for drivers A and C are shown in Figs. 3–5. The distance while decelerating in Fig. 5 exhibits less variation than the cruising distance in Fig. 3 and the distance while accelerating in Fig. 4. The regression line for driver C, who had an impatient tendency, has a smaller slope than that of driver A, who had average tendencies. The slopes are remarkably different during cruising, followed by deceleration. The coefficient of determination,  $R^2$ , for the regression increases in the order of decelerating, accelerating, and cruising, which was consistently observed for all five participants.

It is considered that drivers actively apply braking to maintain a constant distance to the preceding vehicle during deceleration in a car-following situation, as compared to cruising or accelerating. The results show that the target distance to the preceding vehicle during deceleration is clearly different among the individuals.

### 3.4. Proposed model for the distance to the preceding vehicle

From the results in Sections 3.2 and 3.3, it is considered that the distance to the preceding vehicle during stopping or deceleration reflects personal driving characteristics; therefore, the data obtained during stopping and

deceleration were used to model the personal target distance characteristics. It should be noted that only the data corresponding to stopping distances between 2 and 8 m were used for modeling; this was to exclude deceleration or stopping at a red signal at the intersections, which was observed in the video analysis, as most of the outlier data deviated from the regression line, as shown in Fig. 5.

The basic model of individual vehicle speed,  $V_f$ , and distance to the preceding vehicle,  $D_f$ , can be expressed as shown in Equation (1):

$$D_f = a V_f + b \quad (1)$$

Here, the slope  $a$  represents the time to travel the distance ( $D_f - b$ ), and the intercept  $b$  corresponds to the stopping distance. Thus, the time gap ( $a$ ) to point  $D_f - b$  and the stopping distance ( $b$ ) are personal characteristics. Hereinafter, the coefficient  $a = (D_f - b)/V_f$  is described as the time gap.

To include variation factors such as the road environment in the basic model of Equation (1), a multiple regression model was proposed, as expressed in Equation (2):

$$D_f = (a_0 + a_1x_1 + a_2x_2 + \dots) V_f + (b_0 + b_1y_1 + \dots) \quad (2)$$

### 3.5. Candidate factors affecting the distance to preceding vehicle

It is assumed that the distance to the preceding vehicle varies with both the internal factors of the driver, such as their sense of hurriedness, and the external factors, such as the road or traffic environments. Nine independent variation factors were selected from all the possible factors that were encountered or had an influence on the distance-keeping behavior: trip, number of lanes, traffic light indication, preceding vehicle type, slope, curve, presence of congestion, distance to intersection, and turn signal condition at an upcoming intersection (going straight or turning right/left). Multiple levels for each factor were set, and the distributions of the distance to the preceding vehicle were compared among the levels. As the distance depends on the traveling speed, a t-test for the difference in average values was performed for the stopping distance and the distance during deceleration.

### 3.6. Factors affecting stopping distance

The t-test results for the difference in the average stopping distance for each variation factor and each driver are presented in Table 1. The asterisks in the table represent the significance levels of the t-test. It was decided to incorporate the distance to the intersection in the model as a variation factor, as it exhibits a significant influence over three of the five drivers (denoted by the shaded cells in the table).

Drivers A and E had longer stopping distances when the distance to the intersection was longer, but driver D had the opposite results. The stopping distance distributions of drivers A and E are shown in Fig. 6. Both the drivers exhibit tendencies to have longer stopping distances at a distance to the intersection of 100 m or more. It is considered that drivers tend to use larger

stopping distances to better assess the situation in front or to accommodate lane changing when the distance to the intersection is longer, which is caused by traffic congestion, parked vehicles on the shoulder, or the anticipation of unexpected circumstances.

**Table 1 Factors affecting stopping distance (N = 5)**

\*\*\* p<.001, \*\* p<.01, \* p<.05

Factor	Influence	Dr. A	Dr. B	Dr. C	Dr. D	Dr. E
Trip	Difference between trip		*			
Lane number	Single lane vs. Multiple lanes	** <				*** <
Signal	Red signal vs. Others					
Type of preceding vehicle	Normal vs. Truck	* <				
Slope	Uphill vs. Downhill	* >				
Curve	Curve vs. Straight					
Congestion	Few vs. Congestion					** <
Distance to intersection	Close vs. Far	** <			*** >	* <
Turning at intersection	Turning vs. Straight	** <	** <			

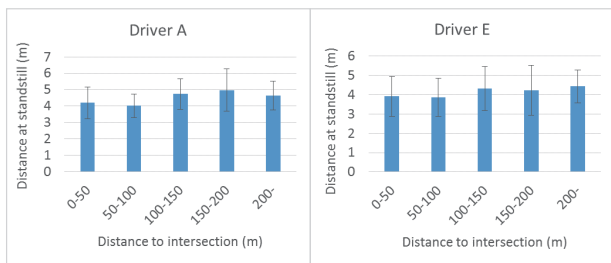


**Fig. 6 Stopping distance versus distance to intersection (drivers A and E)**

**3.7. Factors affecting the time gap during deceleration**

The variation of the average time gap during deceleration with respect to each factor was examined in the same manner as that of the stopping distance. Data regarding the deceleration for reasons other than the preceding vehicle were excluded prior to calculating the time gap, which was determined based on the difference between the distance to the preceding vehicle and the average stopping distance of each driver, divided by the traveling speed when it was 10 km/h or higher. Data corresponding to traveling speeds less than 10 km/h were also excluded because the time gap became unstable.

The test results, which indicate significant differences in the time gap during deceleration with respect to the variation factors, are shown in Table 2. Significant differences with respect to the trip are observed for drivers A–C and E. It is considered that these difference are caused by both the internal factors of drivers, such as their state of hurriedness, and the environmental factors, such as weather conditions. A previous study revealed that the time gap was shortened during hurried driving (6), and some drivers could have been in a hurried driving state during the data collection. There was only one rainy trip, in which the time gap was longer than those under other conditions.

The effects of the number of lanes are illustrated in Fig.

7. Drivers A and E had longer time gaps in the case of multiple lanes, as compared to those in the case of a single lane. Driver C had the opposite results. It is possible that drivers A and E may have been preparing for other vehicles to cut in from the adjacent lanes. Meanwhile, driver C, who has a prevailing impatient tendency, appeared to intend to prevent other vehicles from cutting in; thus, shorter time gaps were noted even during deceleration in the case of multiple lanes.

Drivers A, C, and D had longer time gaps at red traffic lights. It is considered that these drivers take margins in situations that required complete stops. By contrast, their time gaps were reduced in certain situations other than red signals owing to unexpected situations or the requirement for temporary deceleration. Drivers A, D, and E had shorter time gaps with respect to large preceding vehicles, as compared to that with standard-sized vehicles. Drivers A–D had longer time gaps for a greater degree of congestion. Furthermore, drivers A and E had longer time gaps at points far from the intersection, whereas drivers B and D showed opposite results. Drivers A and E also had shorter time gaps for the turn signals (right/left turns), whereas driver C had the opposite results.

From the abovementioned observations, the following seven factors were incorporated, for which three of the five drivers exhibited differences in the model: trip, number of lanes, type of preceding vehicle, congestion, traffic light, distance to intersection, and turn signal conditions at the approaching intersection. The distance data used in this study may have included data corresponding to events of braking unintentionally applied by the drivers. Developing exclusion criteria for unintentional braking events will be the focus of future work.

**Table 2 Factors affecting the time gap during deceleration (N = 5)**

\*\*\* p<.001, \*\* p<.01, \* p<.05

Factor	Influence	Dr. A	Dr. B	Dr. C	Dr. D	Dr. E
Trip	Difference between trip	**	***	***		***
Lane number	Single lane vs. Multiple lanes	*** <		*** >		** <
Signal	Red signal vs. Others	*** >		*** >	*** >	
Type of preceding vehicle	Normal vs. Truck	*** >			*** >	* >
Slope	Uphill vs. Downhill					
Curve	Curve vs. Straight					** <
Congestion	Few vs. Congestion	*** <	** <	*** <		* <
Distance to intersection	Close vs. Far	** <	*** >		** >	** <
Turning at intersection	Turning vs. Straight	** <		*** >		** <

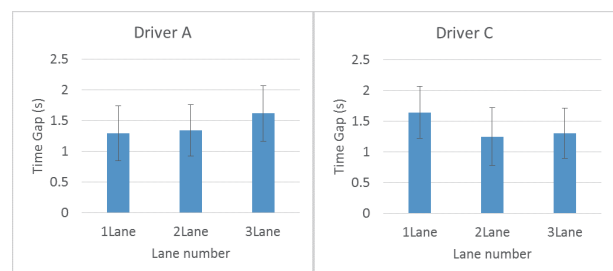


**Fig. 7 Comparison of time gaps with different numbers of lanes (drivers A and C)**

### 3.8. Modeling of distance to the preceding vehicle considering the variation factors

A multiple regression model of Equation (3) was developed using the selected variation factors.

$$Df = (a_0 + a_1x_1 + a_2x_2 + a_3x_3 + a_4x_4 + a_5x_5 + a_6x_6) Vf + (b_0 + b_1y_1) \quad (3)$$

A value of 1 or 0 is assigned to each factor from  $x_1$  through  $x_6$  and  $y_1$  according to whether or not the factor exists. The coefficients of the terms were defined as follows:

- $a_0$ : Standard value of the time gap in each trip
- $a_1$ : Correction coefficient in the multilane case
- $a_2$ : Correction coefficient when there is a red traffic light ahead
- $a_3$ : Correction coefficient when the preceding vehicle is large
- $a_4$ : Correction coefficient when there is dense traffic
- $a_5$ : Correction coefficient when the distance to the intersection is less than or equal to a predefined threshold
- $a_6$ : Correction coefficient when a signal is operated before an intersection
- $b_0$ : Standard value of the distance to the preceding vehicle at stopping
- $b_1$ : Correction coefficient when the distance to the intersection is less than or equal to a predefined threshold

Modeling was performed by determining the average value of  $a_0$  with no variation factors ( $a_1$  through  $a_6$ ) for each trip and applying all the driving data regarding  $a_1$  through  $a_6$ ,  $b_0$ , and  $b_1$ .

The coefficients of the multiple regression model are listed in Table 3.  $R^2$  is presented in the bottom row, and the number of datasets used to create the model is provided above.  $R^2$  is within the range of 0.74–0.84 for all five drivers, which indicates the validity of the model. The P-values of  $a_0$ ,  $a_2$ , and  $b_0$  are less than 1%, and those of  $a_0$ ,  $a_2$ ,  $a_3$ , and  $b_0$  are less than 10% for all five drivers. The P-values of the other coefficients are less than 10% for three or four drivers. Thus, the results indicate that the influencing factors differ among the drivers.

The range of the time gap was 1.42–1.76 for single-lane roads and 0.97–1.51 for multilane roads. The time gap of driver C, who showed an impatient tendency, was the longest on the single-lane roads. On multilane roads, the time gap of driver C was the shortest, followed by that of driver D, who had a careful tendency. These results are consistent with those of previous studies.

**Table 3 Model of the distance to the preceding vehicle (N = 5)**

		Factors	Dr. A	Dr. B	Dr. C	Dr. D	Dr. E
Time Gap (sec)	$a_0$	Individual baseline	1.42	1.58	1.76	1.42	1.62
	$a_1$	Multiple lanes	0.03	-0.11	-0.79	-0.11	-0.11
	$a_2$	Red signal in front	0.19	-0.14	0.20	0.29	0.34
	$a_3$	Behind truck	-0.22	0.09	0.17	-0.25	-0.09
	$a_4$	Congestion	-0.18	0.10	0.56	0.23	0.13
	$a_5$	Close to intersection	0.00	0.12	-0.18	0.12	-0.08
Distance at standstill (m)	$a_6$	Turning at intersection	-0.46	0.29	-0.14	-0.06	-0.16
	$b_0$	Individual baseline	4.36	3.87	3.42	2.06	4.66
	$b_1$	Close to intersection	-0.32	-0.39	0.02	0.12	-0.85
Number of data			1519	1283	1008	935	1027
Prediction accuracy $R^2$			0.80	0.84	0.74	0.81	0.77

## 4. Evaluation of the modeling method with an automated test vehicle

### 4.1. Test vehicle

To validate the modeling method presented in Section 3, evaluation experiments with an automated test vehicle were performed on a proving ground.

The automated test vehicle was an electric vehicle with right-hand drive, and it was possible to switch between automated and manual driving. The driver could override the automated driving function by steering and/or braking at any time. An operator in the passenger seat could also perform an override by using a brake pedal installed on the passenger-side. The longitudinal and lateral control functions could be turned on/off independently; in this study, the lateral control function was turned off, but the longitudinal control function was turned on to eliminate the effect of the automated lateral control on drivers who evaluated the longitudinal control, including the speed and distance control.

### 4.2. Proving ground

A course comprising simulated city roads at the Japan Automobile Research Institute was used, and the route shown in Fig. 8 was set as a test route such that the long straight sections could be used. Only one preceding vehicle was included in the test route, and the automated test vehicle always followed this vehicle during the test drive. The test route contained single- and double-lane roads in each direction, a signalized intersection, and a stop sign intersection for the experiment. The traffic signal at the intersection was controlled to turn red when the automated test vehicle approached such that it always stopped at the intersection; this was to learn the distance to the preceding vehicle while decelerating as well as that at the stop sign intersections.

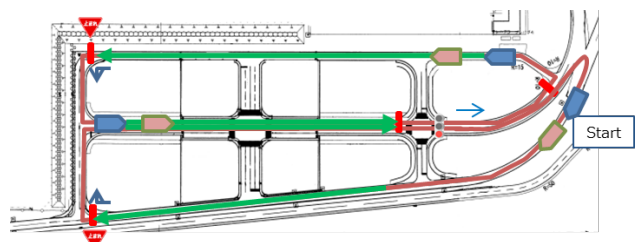


**Fig. 8 Test course used to evaluate the personal distance model (JARI city road)**

### 4.3. Evaluation method

Based on the survey results of the DSQ, which was conducted as described in Section 2, 10 employees with different driving styles were selected as the participants for the experiments.

The evaluation procedure was as follows: the participant manually drove through the test route for approximately 15 min while following the preceding vehicle in order to acquire learning data; a personal distance model was created using the method detailed in Section 3, and various coefficients were applied to the distance control parameters of the automated test

vehicle. Subsequently, the distance to the preceding vehicle was evaluated using the automated test vehicle, to which the personal distance model had been applied.

Because a variation factor other than the number of lanes could not be applied to the personal distance model owing to the limitations of the test course, a simplified version of the multiple regression model, as shown in Equation (4), was used; this only included the number of lanes (a1) as a variation factor:

$$Df = (a0 + a1x1) Vf + b0 \tag{4}$$

Automated following was performed only in the straight sections, which are represented in green in Fig. 8, and the participants turned on the automated following function using a steering wheel switch when the designated speed was achieved in the straight sections. The preceding vehicle set the speed within the range of 30–50 km/h according to the length of the straight section.

Subjective ratings were assigned by the participants. The distance to the preceding vehicle during automated car following was verbally rated when driving through each straight section, with seven stages ranging from very short to very long while stopping. In addition, the feeling of conformity to the distance used by the driver, the feeling of security, and the acceptability were rated based on seven stages after a set of test drives had been completed. For the acceptability rating, the participants were asked to evaluate how pleased they were with the level of conformity.

After the model of automated car following reflecting the personal distance was evaluated, a model of car following considering the time gap offset was assessed. The time gap was set to 0.2 s shorter or 0.2 s longer if the evaluation results of the personal distance model were moderate/long or short, respectively.

#### 4.4. Evaluation results

The personal distance models for the 10 participants are shown in Table 4. R2 is listed in the bottom row, and the number of data sets used for model creation is listed in the next higher row. R2 ranges from 0.82 to 0.96 for all the models. The P-values of coefficients a0 and b are less than 5% for all the drivers, and those of a1 are less than 5% for seven drivers. The standard value of the time gap and the distance to the preceding vehicle while stopping exhibit individual differences, ranging from 1.28 to 2.67 s and 1.38 to 4.38 m, respectively.

Thereafter, the subjective ratings were calculated as average values according to the speed range and for each participant, as shown in Fig. 9. “Slightly short but acceptable,” “moderate,” and “slightly long but acceptable” corresponded to conformity ratings of 3, 4, and 5, respectively, and the results for all the drivers were within the acceptable range, regardless of the speed conditions. It was revealed that the automated car following the personal distance model conformed to the feelings of each participant.

A comparison of the personal models and the models with offset time gaps is presented in Fig. 10. Eight participants had time gaps that were 0.2 s shorter than the actual time gaps of the drivers. For the condition of

30–40 km/h, two participants, C and I, changed their evaluations from “slightly long” to “moderate,” while participant A changed the evaluation from “moderate” to “slightly short.” For the condition of 40–50 km/h, two participants, A and J, changed their evaluations from “moderate” to “slightly short.” Two participants, B and G, had time gaps that were 0.2 s longer, and they did not change their evaluation. The results indicated that some drivers could distinguish time gaps that were 0.2 s shorter than those during their own driving, and they indicated that a shorter distance may be unacceptable.

Subsequently, the relationship between the feeling of conformity, feeling of security, and acceptability was investigated. The results are shown in Fig. 11. Here, the evaluation results of both the personal and offset models are incorporated to include various conformity levels from high to low. In Fig. 11, the left side shows the relationship between the feeling of conformity and the feeling of security, whereas the right side shows the relationship between the feeling of conformity and acceptability. Both display positive correlations, revealing that higher conformity leads to a stronger feeling of security or acceptability.

Table 4 Model of distance to the preceding vehicle (N = 10)

Factors	A	B	C	D	E	F	G	H	I	J
a0 Time Gap baseline	1.84	1.28	2.67	1.96	2.22	2.16	1.72	1.34	2.32	1.33
a1 Multiple lanes	-0.08	0.05	-0.26	0.13	0.39	0.22	0.29	0.30	0.42	0.15
b Distance at standstill	3.34	2.66	3.61	3.24	1.93	1.89	1.38	2.57	2.88	4.38
Number of data	75	109	41	59	43	72	67	75	73	99
Prediction accuracy R <sup>2</sup>	0.92	0.88	0.96	0.83	0.92	0.89	0.82	0.90	0.92	0.82

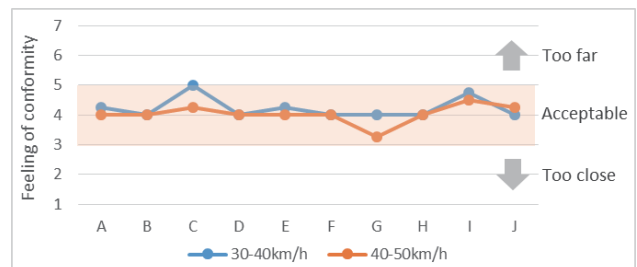


Fig. 9 Feeling of conformity during automated following (N = 10)

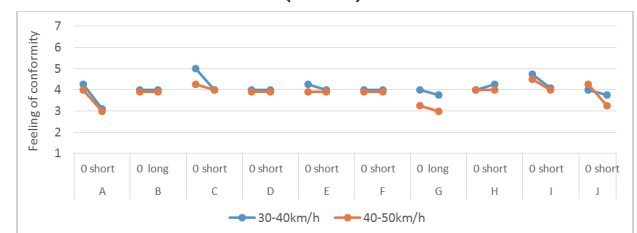


Fig. 10 Feeling of conformity during offset following (N = 10)

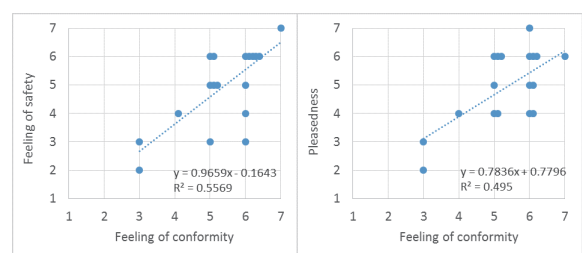


Fig. 11 Feeling of conformity versus feeling of security and acceptability

## 5. Conclusion

In this study, a method for modeling the personal characteristics of distance to a preceding vehicle were examined to realize automated driving that learns the driving style of an individual during manual driving and adapts the automated driving control accordingly.

Data pertaining to driving on ordinary roads were collected from drivers who had different driving styles, and it was found that the distance from the preceding vehicle in the stopping/decelerating phase reflected the personal driving styles. Thus, the distance data from this phase is expected to be appropriate for modeling personal distance-keeping behaviors.

Because the distance to the preceding vehicle depends on the individual vehicle speed, the time gap was examined to investigate the factors affecting the distance model. It was revealed that the time gap was affected by factors such as the trips, number of lanes, traffic light, and distance to an intersection. The effects of these variation factors differed between the drivers. These factors were further simplified into a few variables, and a multiple regression model reflecting personal characteristics and environmental variation factors was developed.

Evaluations with an automated test vehicle on a proving ground were performed to validate the modeling method; the results showed that automated car following reflecting the personal distance model conformed with the driving feelings of the participants. In addition, it was found that a higher conformity improved the feelings of security and acceptability. Furthermore, some drivers could distinguish time gaps that were 0.2 s shorter than those during their own driving; for such drivers, a shorter distance to the preceding vehicle may be unacceptable.

As the next step, further evaluations of the personal distance model under various driving conditions and different environments are necessary. The extension of this method to other personal characteristics and the development of more sophisticated detection methods for environmental variation factors in order to improve the accuracy of modeling remain as topics for future works.

## References

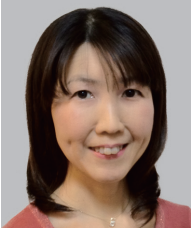
- (1) 三井住友海上火災保険, あいおいニッセイ同和損害保険, インターリスク総研: 自動運転車および公道実証実験に関する消費者の意識調査, [http://www.ms-ins.com/news/fy2016/pdf/0907\\_1.pdf](http://www.ms-ins.com/news/fy2016/pdf/0907_1.pdf) (参照2017.08.01)
- (2) 石橋基範, 大桑政幸, 赤松幹之: 運転スタイル・運転負担感受性の個人特性指標と運転行動, 自動車技術, Vol.58, No.12, p.34-39 (2004)
- (3) 石橋基範, 大桑政幸, 土居俊一, 赤松幹之: 運転スタイルの指標化と追従運転行動, 自動車技術会論文集, Vol.39, No.1, p.121-126 (2008)
- (4) 倉橋哲郎, 大桑政幸, 坂口靖雄, 名切末晴, 瀬口裕章, 大日方五郎: 一般路走行時におけるドライバの減速行動の分析, 自動車技術会論文集, Vol.39, No.2, p.363-368 (2008)
- (5) 中野英茂, 荒木秀夫, 伊東敏夫: 追従発進時の車間距離特性

- に関する研究, 自動車技術会学術講演会前刷集, No.54-04, p.13-16 (2004)
- (6) ポンサトーン・ラクシンチャラーンサク, 飯島健, 道辻洋平, 前田公三, 永井正夫: 市街地走行データベースに基づく急ぎ運転状態検出アルゴリズム, 自動車技術会論文集, Vol.41, No.3, p.751-758 (2010)

## Source

公益社団法人自動車技術会  
自動車技術会論文集  
Vol.49NO.4 文献番号:20184466

## Recipients



Machiko Hiramatsu



Hwaseon Jang



Yuki Ito



Masaru Yamazaki



Takashi Sunda



# Study of Engine-Out PM Emission Mechanism under Low-Temperature Transient Condition and PN Reduction Technology for Direct Injection Gasoline Engines

Yoshihiro Imaoka\* Takao Inoue\* Taisuke Shiraishi\*

**Abstract** The mechanism of in-cylinder phenomena, which are the main sources of particulate matter (PM) emission under low-temperature transient conditions before a warm-up, was analyzed in this study. As a result, a key parameter for the particulate number (PN) under low-temperature transient conditions was clarified. A larger cycle-to-cycle carryover fuel film on the combustion chamber wall results in a higher PN, which was confirmed via PN evaluations considering transient conditions. For PN reduction, a cycle-to-cycle carryover fuel film should be considered. Therefore, a carryover fuel prediction tool was developed, and countermeasures were subsequently identified based on these phenomena.

## 1. Introduction

Over recent years, emission regulations have become more stringent, including those pertaining to actual driving emissions. The particulate number (PN), which is one of the regulated factors, has attracted increasing interest. In particular, for direct-injection engines particulate matter (PM) suppression and PN reduction are significant concerns.

According to previous studies, the main causes of PM generation in direct-injection gasoline engines are pool fires<sup>(1)</sup>, caused by the fuel on the wall surface and the combustion at locations where the fuel in the air–fuel mixture is locally rich<sup>(2)</sup>. Given that the processes of PM generation and emission are complicated, these phenomena have been actively studied in recent years. Many studies have focused on these phenomena, including investigations of the effects of fuel<sup>(3-5)</sup> and oil<sup>(6)</sup> on the PM/PN and PM behaviors in exhaust pipes<sup>(7)</sup>.

Before an engine warms up, as the temperature of engine oil, coolant water and the inner walls of the engine cylinders are low, the fuel directly injected into the cylinders adheres to the inner walls of the cylinder, and a fuel-rich air–fuel mixture is easily formed locally on these walls. It has been reported that, when this fuel-rich air–fuel mixture formed as detailed above is exposed to burned areas, pool fires are created, resulting in PM generation<sup>(8)</sup>.

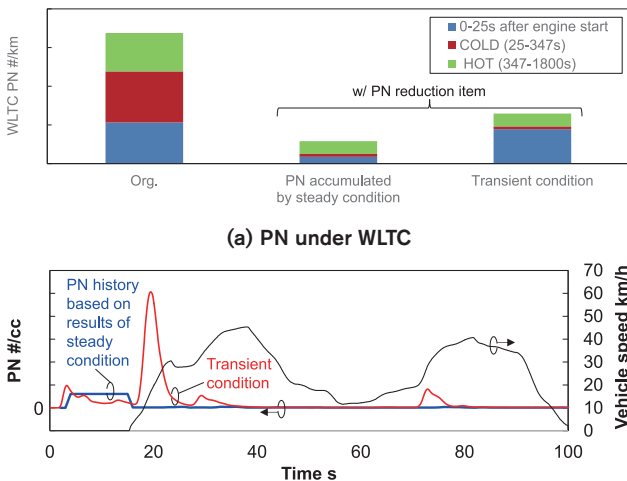
With regard to PM generation, various technological developments for operation under conditions involving low temperatures of the engine oil and coolant have been studied, such as multi-stage fuel injection<sup>(9)</sup> and increasing the fuel pressure to suppress the adhesion of fuel onto walls.

As the wall temperature increases, reduced the adhesion of fuel onto walls leads to lower PM generation. However, this does not imply that the PM emissions are completely eliminated. It has been confirmed that the generation mechanism of injector tip-soot is a major cause of PM emissions during operation (hot) after warm-up and also the key parameter for reducing soot, by analyzing the phenomena occurring inside engine cylinders<sup>(10-12)</sup>.

Most previous studies on PN reduction technology have focused on means of understanding and reducing the phenomena under steady engine operation conditions. However, an increase in the PN has been identified under actual engine operation conditions, including transient conditions<sup>(13)</sup>; this was not considered in previous studies, and thus far, there are no detailed reports on this aspect. An example of this phenomenon is presented in Fig. 1; the PN from an engine under the Worldwide harmonized Light duty driving Test Cycle (WLTC) and its distribution are shown in Fig. 1(a). The state prior to applying PN reduction technology is represented by the leftmost bar. The bar at the center represents the state after applying the PN reduction technology that was proven under steady operation conditions and involves calculating the PN in the operating mode of WLTC by accumulating the results under steady conditions. Furthermore, the rightmost column represents the state after applying the same technology as that applied to obtain the center column under transient conditions. The PN behavior under transient conditions at the first peak of the WLTC and the PN generation history for each operation condition/coolant temperature, which was calculated from a test under steady conditions, are shown in Fig. 1(b). Under actual engine operation conditions, the PN increases when the engine starts in a manner that is not

\*Powertrain and EV Advanced Technology Department

assumed under steady conditions. Consequently, technologies to reduce the transient PN in this situation have been studied using the following approaches: visual evaluation of the in-cylinder state under low-temperature transient conditions, evaluation of the transient state of an actual engine under these conditions, and investigation of the generating mechanism and key parameters.



(a) PN under WLTC  
(b) PN under WLTC: first hill  
Fig.1 Example of PN under WLTC

## 2. Test method

Considering that the results of previous studies on the increase in the PN, as described in the previous section, might have been affected by inappropriate control or incorrect evaluation methods, the operations and evaluation methods were assessed prior to commencing this study.

As a result, it was confirmed that the operation and control of each engine device were assumed as those under steady conditions and that the results were not affected by incorrect evaluation methods or measurement variations. Accordingly, it was concluded that the PN increase under low-temperature transient conditions in the engine cylinders occurs due to phenomena that are not assumed under steady conditions, which are the cause of PM generation and emission. The following evaluations were conducted to elucidate the abovementioned unknown phenomena and identify the reasons for the increase in the PN.

### 2.1 Evaluation of the engine under transient conditions

In this study, the PN from an actual multi-cylinder engine during low-temperature transient operation under the WLTC was assessed to simulate the actual operation conditions. The PN measurement was performed at the tailpipe. The PN was measured using the HORIBA MEXA-2300SPCS and evaluated via direct sampling. Table 1 lists the specifications of the engine used in this study. When using a 4-cylinder, 1.6 l direct-injection turbo engine, the effects of various settings, such as the fuel injection settings and the valve and ignition timings, on PN are visualized and verified. Vehicle-equivalent driving is evaluated using an engine

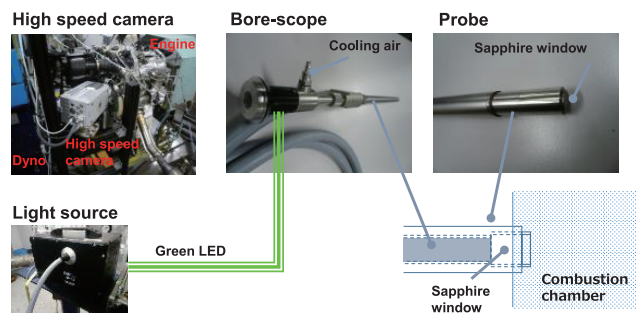
bench that enables driving under transient conditions. For the operation, a CVT-equipped conventional vehicle weighing 1470 kg was used. Initially, the engine water temperature was set as that at the start of the cooling facility, and during the engine evaluation, temperature was controlled in the same manner as for a vehicle. Gasoline, with a research octane number of 95 and a PM index of 1.85, was used for the evaluation.

### 2.2. Borescope observation of in-cylinder luminous flames under transient conditions

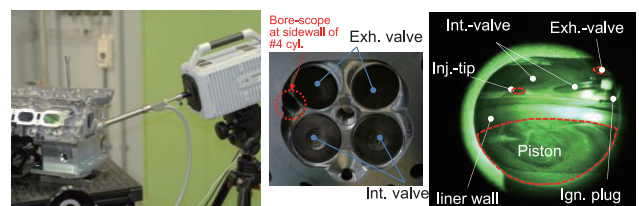
To evaluate the behavior of the PN emitted from the engine under different conditions, including the transient conditions, a borescope was installed on the multi-cylinder engine mentioned above, and a visual evaluation of the in-cylinder state was conducted using a high-speed camera (Photron FASTCAM SA-X). The engine used for the visual evaluation and the visualization system are depicted in Fig. 2. A borescope system (SMETEC BS-NIR) that allowed for coaxial irradiation was employed, and a green LED (SMETEC LED-P40) was used as the light source. The borescope was set on the sidewall of cylinder No. 4 of the multi-cylinder engine by using a probe (SMETEC NIR-PROBE), in order to ensure a suitable field of view for observing the top of the piston, bore, intake valve, ignition plug, and injector tip inside the engine cylinder.

Table 1. Engine specifications

Engine Type	Inline 4
Displacement cc	1618
Bore x Stroke	79.7 x 81.1
Compression Ratio	10.5:1
Fuel Supply System	Direct Injection (side)
Injector Type	Multihole
Max. Fuel pressure (MPa)	20
Aspiration	Turbochager



(a) Visualization system



(b) Layout of the borescope and in-cylinder view

Fig. 2 Visualization system

### 3. Clarification of the PN increase under low-temperature transient conditions

#### 3.1 Occurrence of luminous flames under transient conditions

To elucidate the in-cylinder state of the engine under low-temperature transient conditions, it was observed under different conditions, including the transient conditions, by using the visualization system described in Section 2.2. A visualization test of the in-cylinder state was conducted, focusing on the state after the engine started and that during the first acceleration (one-peak acceleration) under the WLTC driving conditions, as shown in Fig. 1. The in-cylinder states of the engine under transient and steady conditions are compared in Fig. 3. The in-cylinder state under transient conditions is shown in Fig. 1, where the PN increases during the first acceleration under the WLTC. Under steady conditions, the in-cylinder state remains the same as that in the steady operation case, with the revolution, load, and water temperature equivalent to those used to obtain the PN increase visualized above. In this evaluation, vigorous luminous flames were observed in the broad area of the top of the piston under transient conditions. By contrast, almost no luminous flames were observed under the steady conditions. To understand the occurrence of luminous flames under transient conditions, in-cylinder luminous flames were observed under the PN increase conditions mentioned above on a time-series basis. The time-series visualization results are presented in Fig. 4. Photographs of the in-cylinder state were captured at 2000 fps for one cycle when the PN increased. The results for every five frames are displayed. After ignition, vigorous and broad luminous flames occurred in the cavity of the piston near the top dead center. Subsequently, the luminous flame range moved downward as the piston moved downward. According to the evaluation results, it was found that the luminous flames originate from the top of the piston, particularly at the cavity, during the period from combustion to the expansion stroke.

#### 3.2. Hypothesis for the PN increase mechanism

Next, a hypothesis explaining the mechanism of PN increase under low-temperature transient conditions was analyzed. As strong luminous flames occurred in the piston cavity, it was assumed that a large amount of fuel film adhered to the piston cavity. Furthermore, because almost no luminous flames were observed under the steady conditions, it was concluded that the generation of the fuel film was specific to the transient conditions.

Thus, the following hypothesis was developed. Immediately after the engine is started, the wall temperature of the combustion chamber is similar to the temperature of the environment. Accordingly, it was assumed that the fuel that temporarily adhered to the wall of the combustion chamber did not completely evaporate within one cycle until approximately 15 s after the start of the engine owing to the slow evaporation and thus remained until the next cycle. The number of cycles during idling was 100 or more. Therefore, it was assumed that the amount of the fuel film

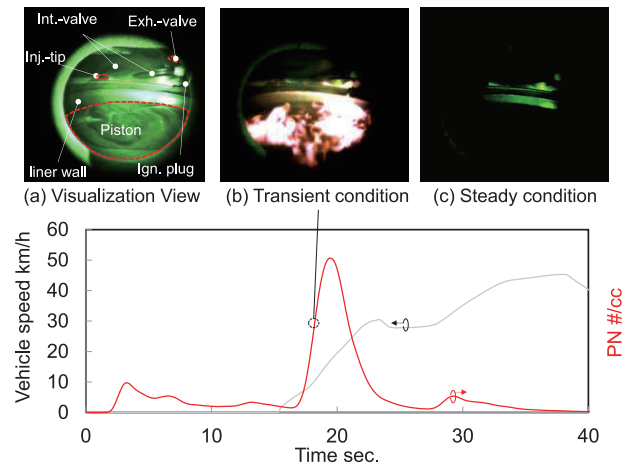


Fig. 3 Comparison of in-cylinder visualization between transient and steady conditions

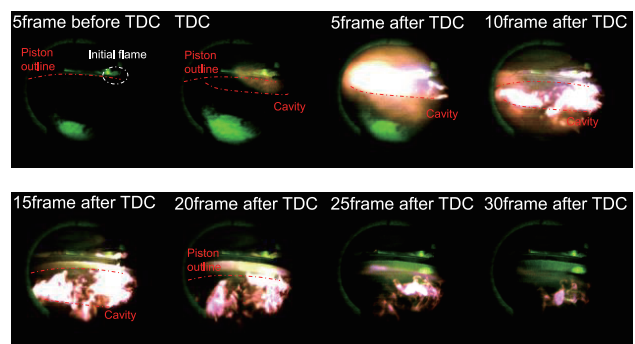


Fig. 4 Luminous flame at first acceleration under transient conditions (camera speed: 2000 fps)

accumulated during this period would reach a certain level, based on the fuel injection volume per cycle. It was assumed that a large amount of the accumulated fuel film could lead to strong luminous flames during acceleration, that is, PM generation. This hypothesis that the accumulated fuel film before acceleration affects the acceleration also agrees with the fact that no luminous flames were observed under the steady conditions. This hypothesis is illustrated schematically in Fig. 5. It was also hypothesized that the PN increases when the fuel (carryover fuel) that accumulates on the wall over multiple cycles immediately after the engine starts results in a pool fire during the first acceleration.

#### 3.3. Verification of the hypothesis for the PN increase under low-temperature transient conditions

To verify the hypothesis for the PN increase mechanism, which is detailed in Section 3.2, it was determined whether the carryover fuel was responsible for PN generation by varying the injection patterns and their durations during the transition. The injection patterns used for this verification are listed in Table 2. When fuel is injected after the piston has ascended during the compression stroke, the amount of the adhered fuel film increases because the sprayed fuel directly collides with the piston wall. By contrast, when fuel is injected after the piston has descended and reaches the bottom dead center during the intake stroke, the amount of fuel adhered to the piston wall decreases.

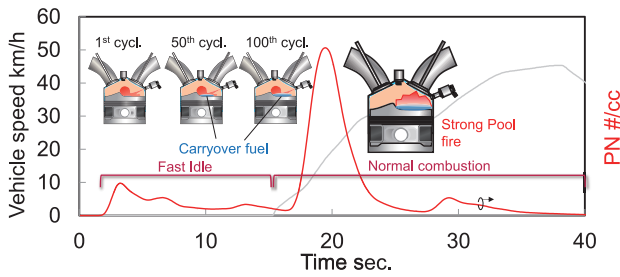


Fig. 5 Hypothesis of PN emission mechanism under low-temperature transient conditions

Table 2 Injection timing under idle conditions immediately after engine start

	Case1	Case2
Injection timing 1	80 deg. ATDC	80 deg. ATDC
Injection timing 2	300 deg. ATDC	110 deg. ATDC
Timing chart		

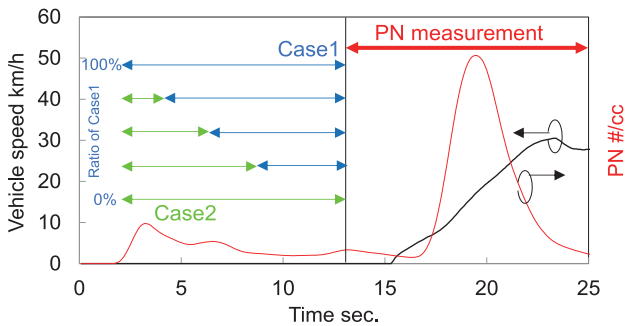


Fig. 6 Duration ratio for each injection pattern

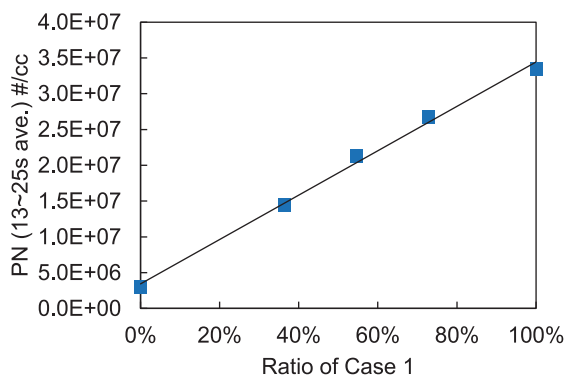


Fig. 7 PN emission for each injection pattern ratio

Consequently, verification was conducted by combining two injection patterns in an actual engine: in case 1, fuel was injected during the compression stroke, and in case 2, fuel was injected only after the piston had descended during the intake stroke. A schematic comparison of the injection settings used in this verification is shown in Fig. 6. During the idling before acceleration, the durations after engine start in cases 1 and 2 were varied and combined in order to verify the PN behavior during subsequent acceleration. The evaluation results are presented in Fig. 7, where the horizontal axis represents the time rate for case 1; the closer

the value to 100%, the longer is the injection pattern in case 1, whereas the closer the value to 0%, the longer is the time rate in case 2. The vertical axis shows the PN at the first acceleration (13–25 s). The rate in case 1 is large when the compression-stroke injection is performed. In other words, the greater the amount of fuel adhered to the piston wall, the higher is the PN generated during the first acceleration. The verification results clearly indicate that the fuel injection conditions before acceleration (0–13 s) affect the PN during acceleration (13–25 s). In addition, based on the result that the PN during acceleration increases linearly with respect to the time rate in case 1, it was confirmed that the carryover fuel at low temperatures was the key parameter that led to an increase in the PN.

### 3.4. Analysis of transient condition with a fuel film prediction tool

A tool for predicting the carryover fuel was configured with the objective of predicting the PN emitted by an engine under transient conditions. This tool predicts the amount of fuel film using 0-dimensional models, according to the injector tip position and the injection direction layout.

#### 3.4.1. Outline of models for carryover fuel prediction tool

The models used for the prediction tool and the tool itself are described in this section. The configuration of the fuel film prediction tool models is shown in Fig. 8. The tool consists of a spray model, spray evaporation model, and fuel film mode. The calculations are outlined in Fig. 9. The amount of fuel film adhered to the wall per cycle was calculated using the layout, with the direction and timing of the injection employed as input values. The calculations were performed in three stages. (I) First, the collision rates of the fuel spray droplets were calculated according to the spray calculation and the geometric relationship. (II) Next, the adhesion rate of the fuel film was calculated based on the fuel film model. (III) Finally, the evaporation rate of the fuel film was calculated. In the first stage, based on the calculation of the collision rates in (I), the subsequent fuel spray calculation was performed. The spray breakup length and spray droplet breakup within the breakup length were calculated using the Kelvin–Helmholtz model<sup>(14)</sup>, and the spray particle size distribution in the slipstream of the breakup length was calculated using the Nukiyama–Tanasawa equation<sup>(17)</sup>. Subsequently, the amount of evaporation for each droplet was calculated using the Ranz–Marshall model<sup>(15)</sup>. In addition, the spray number density in each spray penetration region was calculated by accounting for the conservation of momentum by using Hiroyasu’s equation<sup>(18)</sup> and Wakuri’s equation<sup>(16)</sup> in order to calculate the collision with the wall geometrically. The entire amount of fuel does not adhere to the wall upon collision; instead, some splashing occurs due to reflection and other factors. Therefore, the wall adhesion amount in (II) was calculated using the Senda model<sup>(19)</sup>, while accounting for the amount of splash. Thereafter, for determining the amount of evaporation of the fuel film in (III), experimental sensitivity was used. The evaporation amounts for each wall and the environmental temperature were measured when the fuel

spray collided with the fuel film formed in a constant-volume vessel, and temperature-specific amounts of evaporation were compiled in a database.

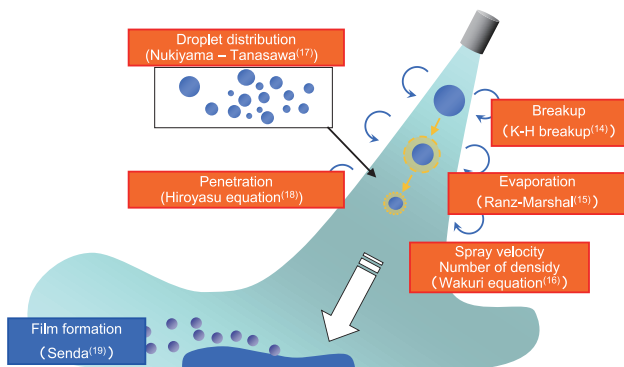


Fig. 8 Model configuration

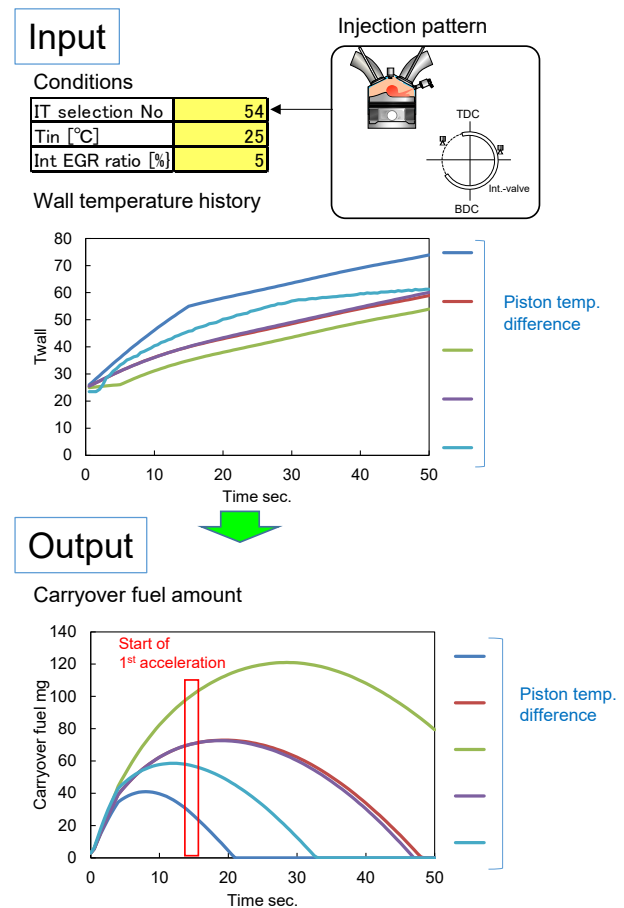


Fig. 9 Carryover fuel prediction tool

The database of the evaporation velocities of the fuel film, which was obtained based on the intake temperature, the residual burned gas inside the cylinders, and the history of the piston wall temperature after starting the engine in order to calculate the residual carryover fuel on the piston wall during acceleration after several cycles, was assessed. An example of the calculation results based on the difference in the wall temperature history is shown in Fig. 9. It was confirmed that the slower the increase in

the piston wall temperature, the greater is the amount of carryover fuel approximately 15 s after starting the engine.

### 3.4.2. Verification of carryover fuel by Hydrocarbon (HC) measurements at low temperature

A measurement method for qualitatively determining the amount of carryover fuel in an actual engine was derived. Idling continued for 15 s, which was similar to the initial idle time after the engine started under the WLTC. Thereafter, fuel injection was cut. It was concluded that the HC emitted after cutting the fuel injection was the unburned HC contained in the residual gas, the HC from the carryover fuel remaining as liquid fuel, or from other oils. In addition, it was determined that the HC emission from oil and other sources was approximately 400 ppm, which was equivalent to that before the engine started, and the HC emission from residual gas was 100 ppm or less. Accordingly, it was concluded that the carryover fuel accounts for a large portion of the HC emissions after cutting the fuel injection; thus, it was used for a qualitative comparison. An example of the results of this evaluation is shown in Fig. 10. Because the HC emission after the fuel cut increased with the decreasing water temperature (T<sub>w</sub>), it was assumed that its tendency was the same as that of the carryover fuel.

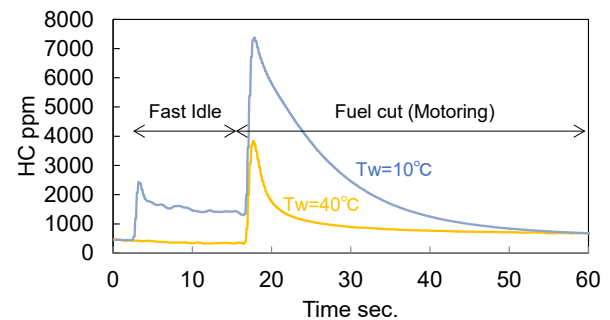


Fig. 10 HC emission after fuel cut

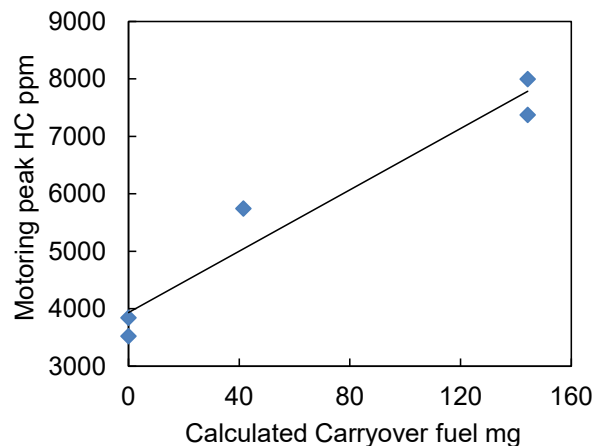


Fig. 11 Comparison between calculated amount of carryover fuel and measured HC

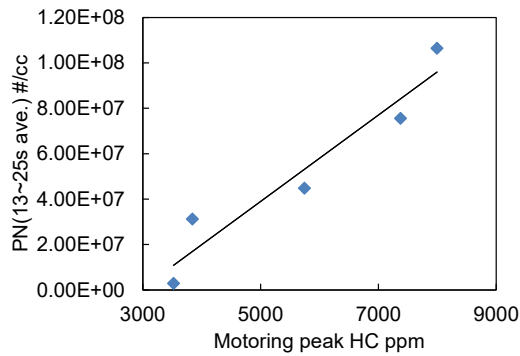


Fig. 12 Relationship between motoring peak HC and WLTC PN during 13–25 s

### 3.4.3. Verification of the prediction tool using measured carryover fuel

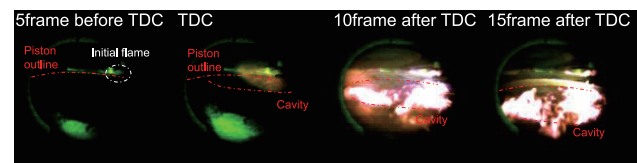
The results of the measurement method described in the previous section and those of the carryover fuel prediction tool detailed in Section 3.4.1 were compared and verification was performed. The comparison results are shown in Fig. 11. The horizontal axis represents the calculated carryover fuel amounts, whereas the vertical axis indicates the peak HC emissions after the fuel cut, as obtained from a test/evaluation. The calculated amounts of the carryover fuel showed an almost linear correlation with the actual peak HC emissions of the engine after the fuel cut, that is, the residual HC during idling. Fig. 12 shows the relationship of the peak HC after the fuel cut with the PN during the first acceleration (13–25 s) when driving under the WLTC, where the same injection settings as in the peak HC measurement conditions were applied to the initial idling. As is evident, both the parameters are almost linearly correlated with each other. Based on these results, the validity of the proposed prediction tool was confirmed. The results also showed that the measured peak HC can be used as an interim index describing the amount of carryover fuel and that the low-temperature transient PN at one-peak acceleration can be predicted by setting the carryover fuel as a parameter.

## 4. Transient PN reduction technology and verification

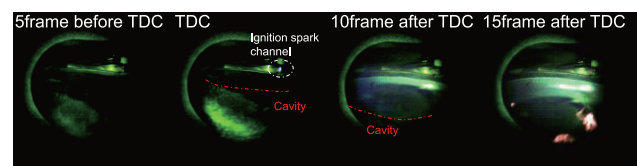
It was confirmed that the carryover fuel was the key parameter affecting the transient PN. In this section, measures for reducing the PN under low-temperature transient conditions are presented. The two following measures were studied: measures for suppressing PM generation during acceleration, assuming that there exists a fuel film due to the carryover fuel at low temperatures, and measures for reducing the carryover fuel itself prior to acceleration.

The first measure, i.e., PN reduction, is an example of reducing the PN during acceleration, assuming the existence of carryover fuel. When a fuel film was present at the top of the piston due to the carryover fuel, it was concluded that this film caused a severe pool fire and then resulted in PM generation, as described in Section 3.2. To suppress this PM generation, the fuel film must be kept away from the flame;

alternatively, the amount of PM must be reduced even if a pool fire occurs due to a temperature reduction or other factors. In the former case, the occurrence period of pool fires can be reduced by retarding the ignition timing in order to delay the hot flame from reaching the top of the piston. In the latter case, PM generation can be suppressed by reducing the combustion temperature of the exhaust gas recirculation (EGR)<sup>(20)</sup>. To confirm these effects, the in-cylinder state was visualized, and the PN emitted from the engine under the WLTC when the ignition timing at one-peak acceleration was retarded by 17° was evaluated. Furthermore, the valve overlap was increased by 40°, thereby increasing the amount of residual gas. The visualized in-cylinder states with one-peak acceleration prior to implementing these measures and after modifying the engine as described above are presented in Fig. 13. A comparison with the state prior to implementing the measures demonstrates that the in-cylinder flame propagation is delayed, the occurrence timing of the luminous flame at the top of the piston is retarded, and the occurrence of the luminous flame is suppressed.



(a) Without transient PN reduction technology



(b) Ignition retardation and larger overlap

Fig. 13 In-cylinder visualization for ignition retardation with 17° CA and larger overlap with 40° CA during the first acceleration under transient conditions (Frame speed: 2000 wfps)

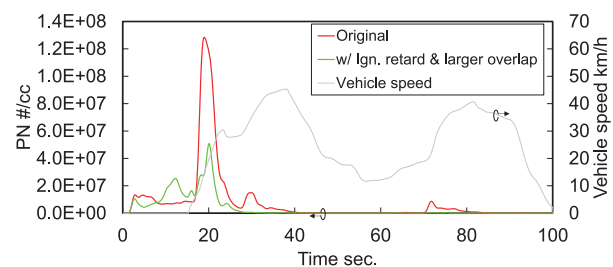


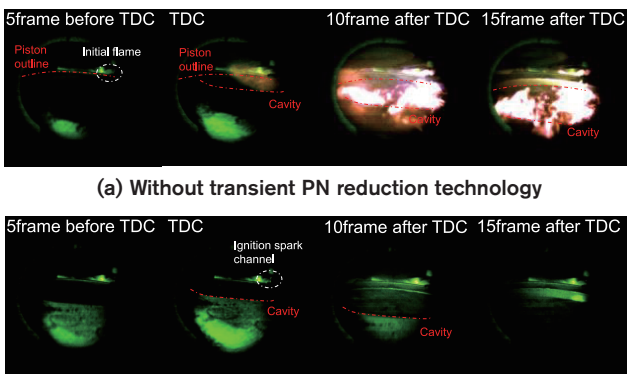
Fig. 14 PN emission for ignition retardation with 17° CA and larger overlap with 40° CA during the first acceleration

The PN generation history with one-peak acceleration is shown in Fig. 14. As visualized in the figure, the peak PN at one-peak acceleration is significantly reduced.

In addition to the abovementioned measures, this effect was verified by reducing the carryover fuel itself. Using the carryover fuel prediction tool, the fuel injection settings that cause the amount of carryover fuel to reduce to zero were analyzed. Accordingly, the fuel injection conditions were set, and the carryover fuel amount was

set to zero, for the idling condition of an actual engine. Next, the in-cylinder state was visualized under the WLTC, and the PN emitted by the engine was measured. The results obtained for the visualized in-cylinder state with one-peak acceleration before and after implementing the measures are compared in Fig. 15. On modifying the engine as described above, almost no luminous flame was observed at the top of the piston. The PN generation history with one-peak acceleration is presented in Fig. 16. The peak PN, which is unique to one-peak acceleration, almost disappears after the engine is started.

The ignition, fuel injection, and valve timing settings for each PN reduction measure are shown in Fig. 17. The settings varied between idling or acceleration. Because the ignition timing and fuel injection with acceleration vary according to the rotational load, a schematic diagram for typical conditions is presented. The effects of PN reduction under the WLTC are shown in Fig. 18. The state after applying the PN reduction technology under steady conditions is represented by the leftmost bar, and the state after retarding the ignition timing with acceleration and increasing the valve overlap is represented by the bar at the center. The state after setting the carryover fuel amount to zero, as in the idling condition, is represented by the rightmost bar. Compared to the leftmost state, before implementing measures where the PN unique to the transient condition was not considered, PN was reduced by 40% on retarding the ignition timing and increasing the valve overlap and by 65% on setting the carryover fuel amount to zero. The PN was significantly reduced when considering the carryover fuel through the measures for reducing the PN with one-peak acceleration and reducing the amount of the carryover fuel during idling after starting the engine.



(a) Without transient PN reduction technology

(b) Minimum wall wet fuel injection while idling

Fig. 15 In-cylinder visualization with minimum wall wet fuel injection while idling under transient conditions (frame speed: 2000 fps)

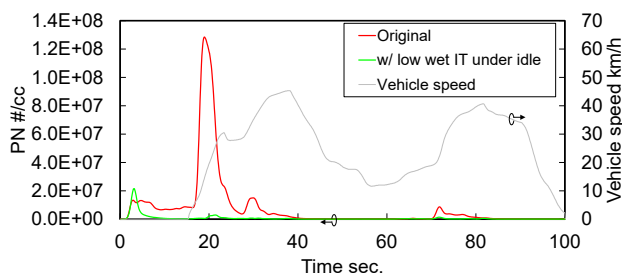


Fig. 16 PN emission with minimum wall wet injection while idling

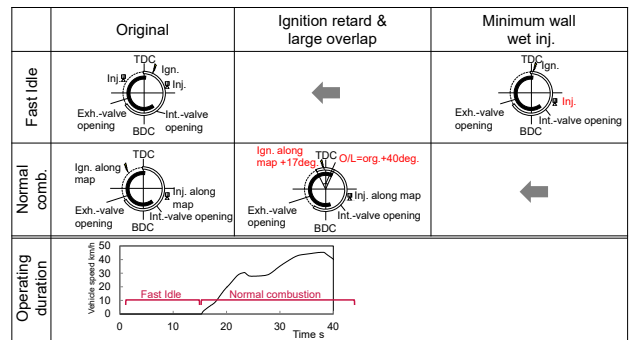


Fig. 17 Timing of each device operating under each set of operating conditions

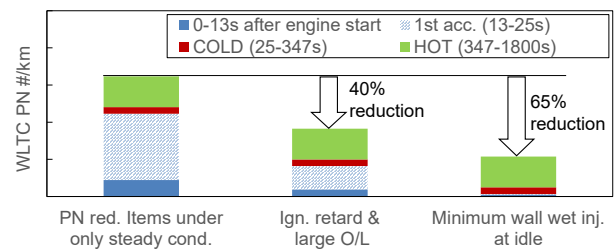


Fig. 18 PN emission with each PN reduction item

## 5. Conclusion

The following insights were obtained by evaluating the effects of the key parameters for clarifying the causes of the increase in the PN under transient conditions in direct-injection engines:

- (1) During the acceleration after low-temperature idling, a notable PN increase was identified; this increase did not occur under any other acceleration conditions.
- (2) Through visualization with a borescope, the PM generation/emission from the top of the piston during the first acceleration after starting the engine was observed. This phenomenon is unique to actual engines under transient conditions and was not observed in the evaluation under steady conditions.
- (3) It was clarified that the key parameter affecting the PM generation/emission from the top of the piston during the first acceleration after starting the engine is the fuel film (carryover fuel); this fuel film accumulates over several cycles when the piston is cold during the idling before one-peak acceleration.
- (4) After elucidating the PM generation/emission phenomena caused by the carryover fuel and by visualizing the in-cylinder state and evaluating the PN emitted from an engine, it was demonstrated that the amount of PN can be significantly reduced by introducing the following PN reduction technologies: retarding the ignition timing at acceleration and reducing the combustion temperature, and reducing the amount of carryover fuel during idling after starting the engine.

To reduce the PN further in order to achieve zero-emission, it is essential to reduce the low-temperature transient PN. Consequently, technologies must be

developed to reduce the amount of carryover fuel, which is the key parameter influencing the low-temperature transient PN. In addition, to further reduce emissions and promote the creation of innovative technologies, mechanism-based technologies must be developed by quickly and flexibly utilizing measurement and analysis technologies, as stated when explaining the reduction of the PN from the injector tip-soot under hot conditions in a previous report<sup>(10)</sup> and when explaining the reduction of PN under low-temperature transient conditions herein.

### References

- (1) Ketterer, J.K. and Cheng, W.K., "On the Nature of Particulate Emissions from DISI Engines at Cold-Fast-Idle", SAE Technical Paper 2014-01-1368 (2014).
- (2) Sukegawa, Y., Kumano, K. and Ogata, K., "Estimation of Particulate Matter in Direct Injection Gasoline Engines by Non-Combustion CFD," SAE Paper 2014-01-1142 (2014).
- (3) Tanaka, D., Uchida, R., Noda, T., Allen A., and etc. "Effects of Fuel Properties Associated with In-Cylinder Behavior on Particulate Number from a Direct Injection Gasoline Engine," SAE Technical Paper 2017-01-1002 (2017), doi:10.4271/2017-01-1002.
- (4) Aikawa, K., Sakurai, T., and Jetter, J., "Development of a Predictive Model for Gasoline Vehicle Particulate Matter Emissions," SAE Int. J. Fuels Lubr. Vol. 3, No. 2, pp.610-622 (2010), doi:10.4271/2010-01-2115.
- (5) 橋本 淳, 足立 久也, 伊藤 朋晃, 高橋 美沙紀, 田上 公俊, "Toluene Reference Fuel火炎における芳香族炭化水素の生成特性," 自動車技術会論文集, Vol.48, No.6, pp.1201-1206 (2017)
- (6) Hadler, J., Franzen, C. L., Gohl, M., Mink, T., "Influencing Factors on Particle Formation under Real Driving Conditions," MTZ, Vol. 77, pp.50-58 (2016)
- (7) Ericsson, P., Samson, A., "Characterization of Particulate Emissions Propagating in the Exhaust Line for Spark Ignited Engines," SAE Technical Paper 2009-01-2654 (2009).
- (8) 秋濱一弘, "Soot: 微粒子の科学と技術 (1) 粒子状物質 (PM): 自動車排出ガス規制と PM 生成モデリングの必要性: 直噴ガソリンエンジン/乗用車を中心に," 日本燃焼学会誌, Vol. 59, No. 187, pp.49-54(2017).
- (9) Imaoka, Y., Shouji, K., Inoue, T., and Noda, T., "A Study of a Multistage Injection Mechanism for Improving the Combustion of Direct-Injection Gasoline Engines," SAE Int. J. Engines Vol. 8, No. 3, pp.1080-1087(2015), doi:10.4271/2015-01-0883.
- (10) 今岡 佳宏, 橋詰 豊, 井上 尊雄, 白石 泰介, "直噴ガソリンエンジンのPN低減技術の研究(第1報)-Tip-sootの発生メカニズムとそのキーパラメータ-," 自動車技術会2017年秋季大会 学術講演会, 講演予稿, No.139-17, pp.784-790 (2017)
- (11) Kufferath, A., Wiese, W., Samenfink, W., Degeforde, H., Knorsch, T. and Jochmann, P., "Assessment of feasible system solutions for future particle emission requirements,"IMECHE - Fuel Systems for IC Engines, 2015
- (12) 板谷 隆樹, 熊野 賢吾, 前川 典幸, 大須賀 稔, 三宅 威生, 小倉 清隆, 安川 義人, 吉村 一樹, "インジェクタの流れ解析を用いたPN低減手法の検討," 自動車技術会論文集, Vol.49, No.2, pp.181-186 (2017)
- (13) Whitaker, P., et al. "Measures to reduce particulate emissions from gasoline DI engines." SAE International Journal of Engines Vol. 4, No. 1, pp.1498-1512 (2011)
- (14) Beale, J. C. and Reitz, R. D., "Modeling spray atomization with the Kelvin-Helmholtz/Rayleigh-Taylor hybrid model," Atomization Spray 1999, Vol. 9, PP. 623-640.
- (15) Ranz, W. E., and Marshall, W. R., "Evaporation from drops—Parts I and II", Chem. Eng. Prog., Vol. 48, No. 3, p. 141 (1952)
- (16) Wakuri, Y., et al. "Studies on the penetration of fuel spray in a diesel engine." Bulletin of JSME Vol. 3, No. 9, pp.123-130 (1960)
- (17) Nukiyama, Y., and Tanasawa, Y. "Experiment of liquid droplet atomization." Transactions of the Japan Society of Mechanical Engineers Vol. 5, No. 18, pp. 136-143 (1939)
- (18) Hiroyasu, H., and Arai, M., "Structures of fuel sprays in diesel engines." SAE transactions, pp.1050-1061 (1990)
- (19) Senda, J., Ohnishi, M., Takahashi, T., Fujimoto, H., Utsunomiya, A. and Wakatabe, M., "Measurement and Modeling on Wall Wetted Fuel Film Profile and Mixture Preparation in Intake Port of SI Engine," SAE Technical Paper 1999-01-0798, (1999)
- (20) Alger, T., Gingrich, J, Khalek, I. A. and Mangold B., "The Role of EGR in PM Emissions from Gasoline Engines," SAE Technical Paper 2010-01-0353 (2010)

### Source

公益社団法人自動車技術会  
自動車技術会論文集  
Vol.50NO.3 文献番号:20194324

### Recipients



Yoshihiro Imaoka



Takao Inoue



Taisuke Shiraiishi



# Evaluation of Equivalent Temperature in Vehicle Cabin by a Mesh-free Simulation (First Report)<sup>※</sup>

Hajime Oi\* Yasushi Ichikawa\*\* Akira Matsumoto\*

**Abstract** This report describes the equivalent temperature (teq), the measurement of the equivalent temperature in a vehicle cabin, and the development of a numerical thermal manikin. A method for measuring teq using a clothed thermal manikin was examined. Thereafter, teq measurements were conducted in a vehicle cabin, considering the effects of air temperature, air velocity, and radiation. In addition, a numerical thermal manikin, including a clothing model, was developed and used to calculate teq, as detailed in the second report. The teq measurement results were also used as validation data to confirm the simulation accuracy, as stated in the second report.

## 1. Introduction

ISO 14505-2<sup>(1)</sup> defines equivalent temperature as an index for evaluating the thermal environment in a vehicle cabin. It is a type of sensible temperature that expresses the key factors of the thermal environment in a vehicle cabin, that is, the air temperature, air velocity, and radiation effect, through a single index. Owing to its usability, equivalent temperature was recently adopted by the Architectural Institute as an environmental standard<sup>(2)</sup>. The use of equivalent temperature has also been increasing in the construction industry<sup>(3), (4)</sup>.

In the automobile industry, implementing simulation-based evaluations of the equivalent temperature during the design phase before vehicle prototyping is useful for improving the technological developments related to the efficiency and quality of air conditioning. However, ISO 14505-2 only covers equivalent temperature measurements based on thermal manikins and does not provide sufficient information regarding the methods of calculating the heat transfer of clothing, which is required when performing a simulation. Thus far, there has been no report comparing the equivalent temperature obtained from measurements in vehicles using clothed thermal manikins with the equivalent temperature obtained from ISO 14505-2-based precise simulations in vehicle environments. Shinozuka et al.<sup>(3)</sup> and Yumino et al.<sup>(4)</sup> measured and simulated equivalent temperatures using clothed thermal manikins. However, because the setting was a room under moderate conditions, the analysis environment was different from that inside a vehicle cabin.

Meanwhile, Nilsson<sup>(5)</sup> measured and simulated equivalent temperatures using a clothed thermal manikin for a vehicle cabin. However, because the

thermal manikin used in the simulation was fabricated by combining 18 cubic blocks and the shape was considerably different from that of an actual manikin, the simulation results cannot be compared with the measurement results directly. Kawanago et al.<sup>(6)</sup> studied a model for the heat transfer of clothing in a vehicle cabin but did not apply the model to a simulation of a vehicle cabin. Thus, the objective of this study was to establish a method for simulating the equivalent temperature in a vehicle cabin under clothed conditions.

This study yielded two reports. The first report (this report) describes an equivalent temperature measurement experiment performed using a vehicle and the development of a thermal manikin model incorporated with a practical clothed heat transfer model in order to reproduce the clothed thermal manikin used in the experiment.

The second report discusses the equivalent temperatures simulated in a vehicle cabin by using the thermal manikin described in the first report. For the simulation, a mesh-free simulation that did not require filling or the deletion/correction of unnecessary shapes was utilized. The accuracy of the simulation was verified by comparing the results with the experimental results obtained in the first report.

This paper was prepared by revising a speech<sup>(7)-(9)</sup> presented at the JSAE Spring Congress in 2018. This study was a collaborative work with AGC Inc.

## 2. Definition of equivalent temperature

Equivalent temperature is defined as the air temperature in a standard environment (under quiescent air flow in which the average radiant temperature is equal to the air temperature), where the sensible heat loss (convection + radiant heat loss) from a human body at a certain skin temperature becomes equal to the

\*Integrated CAE and PLM Department \*\*Advanced Materials and Processing Laboratory

※ This technical award is result based on the collaborative investigation with AGC inc.

environment of the evaluation object. The equivalent temperature,  $t_{eq}$ , according to ISO 14505-2 is defined in Equation (1)<sup>(1)</sup>. The variable names and units used in this work are collectively listed at the end of this paper.

$$t_{eq,n} = t_{sk,n} - \frac{Q_{sk,n}}{h_{cal,n}} \quad (1)$$

According to ISO 14505-2, the parameters of Equation (1) are measured using a thermal manikin. A thermal manikin is a human-shaped thermal measurement instrument. By splitting a thermal manikin into body segments, the body segment-specific equivalent temperatures can be measured and used to evaluate the nonuniform environment in a vehicle cabin.

Among all the parameters in Equation (1), the skin surface temperature of the manikin,  $t_{sk,n}$ , and the sensible heat loss from the manikin surface,  $Q_{sk,n}$ , can be measured by placing the thermal manikin in a vehicle cabin. The heat transfer coefficient between the manikin surface and a standard environment,  $h_{cal,n}$ , can be measured by setting the thermal manikin in an environment that satisfies the conditions of a standard environment. For accuracy, the value of  $h_{cal,n}$  varies according to the relationship between the skin surface temperature of a manikin and the environmental conditions. However, given that it can be considered as a constant if the clothing and posture remain the same, a body segment-specific constant was used in this research.

### 3. Experimental measurement of equivalent temperature

#### 3.1. Experimental method

##### 3.1.1. Experimental overview

To verify the accuracy of the equivalent temperature simulation (second report), an equivalent temperature measurement experiment was conducted using an actual vehicle in a climate chamber. An R/H middle-sized crossover SUV was used as the experimental vehicle, and a thermal manikin was set in the driver seat. Photographs of the experimental setup are shown in Fig. 1.

The thermal factors in the vehicle cabin were measured once per second. The following instruments were used: (1) a K-type thermocouple to measure the air temperature in the vehicle cabin and around the thermal manikin (30 mm from the surface) (33 points), the temperatures at the air conditioner outlets (8 points), and the surface temperatures of individual portions inside and outside the vehicle cabin (26 points); (2) a heat flux sensor to measure the heat flux at the vehicle cabin surfaces (9 points); and (3) a hot-wire anemometer to measure the air velocities around the thermal manikin (30 mm from the surface) (22 points).

Two types of experimental conditions were set: summer cooling conditions and winter heating conditions, as shown in Table 1. Under both sets of experimental conditions, measurements were taken until the

measurements of the environment in the vehicle cabin and thermal manikin became steady, and the average value obtained from the last 3 min of the experiment was used for the analysis.

#### 3.1.2. Equivalent temperature measurement

The equivalent temperatures were obtained from Equation (1). The sensible heat loss  $Q_{sk,n}$  was obtained using the thermal manikin set in the vehicle cabin. The thermal manikin was split into 24 body segments. Eighteen body segments other than those in contact with the seat were analyzed. The thermal manikin was dressed in a T-shirt (short sleeve), dress shirt (long sleeve), trunks, cotton pants, socks, and shoes. The surface of the thermal manikin was controlled to remain at a constant temperature of 34 °C.



Fig.1 Vehicle (left) and thermal manikin (right) used for the experiment.

Table1 Experimental conditions

	Cooling	Heating
Outside temperature	35°C	0°C
Relative humidity	50%	Not controlled
Solar lamp	OFF	OFF
Vehicle speed	IDLE	IDLE
A/C temperature setting	25°C	24°C
Blower fan speed	MAX	MAX
Mode	VENT	FOOT
Air flow direction	Neck	Neck
REC/FRE	Recirculation	Fresh

As explained in Section 2,  $h_{cal,n}$  can be directly measured from the thermal manikin; however, Equation (2) is suggested herein to calculate this value based on the database of the thermal insulation of clothes. In this equation, a temperature difference of 1 °C between the manikin surface and the environment and the convective heat transfer coefficient/radiant heat transfer coefficient in a standard environment are assigned<sup>(10)</sup>, which are conditions that describe the sensible heat loss of a human body.

$$h_{cal,n} = \frac{1}{I_{cl,n} + \frac{1}{f_{cl,n} \cdot (h_{cs,n} + h_{rs,n})}} \quad (2)$$

In this study, a common value of 8.1 W/m<sup>2</sup>°C was set for the total heat transfer coefficient in a standard environment, i.e.,  $h_{cs,n} + h_{rs,n}$ , regardless of the body segment. Equation (3) was used for the assumption of the area factor, i.e., the surface area difference with clothing,  $f_{cl,n}$ .

$$f_{cl,n} = 1.0 + 1.94 \cdot I_{cl,n} \quad (3)$$

For obtaining Equation (3), the units of the equation for  $f_{cl}$  from literature<sup>(10)</sup> were converted into the equivalent SI units. By assigning  $h_{cs,n} + h_{rs,n} = 8.1$  and using Equations (2) and (3),  $h_{cal,n}$  can be expressed as a function of the thermal insulation of clothing.

### 3.1.3. Measurement of the thermal insulation of clothing

For Equation (2), an experiment was conducted to obtain the thermal insulation of clothing, which is required to determine  $h_{cal,n}$ . In a climate chamber, under a radiant temperature that was approximately equal to the air temperature ( $\sim 20^\circ\text{C}$ ) and an air velocity less than 0.2 m/s, the thermal manikin wearing the clothing used for the vehicle experiment (hereinafter referred to as the clothed manikin) and a naked thermal manikin (hereinafter referred to as the naked manikin) were placed; in this manner, the thermal resistance between the manikin surface and the environment was measured. Subsequently, the thermal insulation of the clothing was calculated based on the thermal resistances of the clothed and naked manikins. The surface of the thermal manikin was maintained at a constant temperature of  $34^\circ\text{C}$ .

Equations (4) and (5) were used to obtain the thermal resistances between the manikin surface and the environment of the clothed and naked manikins:

$$R_{cm,n} = (t_{sk,cm,n} - t_{a,cm,n})/Q_{sk,cm,n} \quad (4)$$

$$R_{nm,n} = (t_{sk,nm,n} - t_{a,nm,n})/Q_{sk,nm,n} \quad (5)$$

To obtain the thermal insulation of clothing in a simple manner, the difference between these values was calculated (Equation (6)):

$$I_{cl,n} = R_{cm,n} - R_{nm,n} \quad (6)$$

However, because the increase in surface area due to the clothing is not considered in this calculation method, the thermal insulation of the clothing would be underestimated. Accordingly, in this research, the thermal insulation of the clothing was calculated by considering the increase in surface area due to the clothing. The heat transfer models of the clothed and naked manikins are presented in Fig. 2. Assuming that the thermal resistance between the clothing surface and the environment of the clothed manikin (per unit clothing surface area) is equivalent to the thermal resistance between the manikin surface and the environment of the naked manikin (per unit body surface area), the thermal insulation of the clothing considering the increase in surface area can be expressed as shown in Equation (7):

$$I_{cl,n} = R_{cm,n} - R_{nm,n}/f_{cl,n} \quad (7)$$

By solving Equations (3) and (7) as a set of simultaneous equations, the thermal insulation of clothing could be obtained, as shown in Equation (8):

$$I_{cl,n} = \frac{1.94 \cdot R_{cm,n} - 1 + \sqrt{(1 - 1.94 \cdot R_{cm,n})^2 - 7.76(R_{nm,n} - R_{cm,n})}}{3.88} \quad (8)$$

## 3.2. Experimental results and considerations

### 3.2.1. Thermal insulation of clothing

The thermal insulation of the clothing according to the body segment, as obtained from Equations (6) and (8), is shown in Fig. 3. For symmetric body segments (such as the right and left upper arms), the average values of the right and left segments were used.

The comparison results show that the thermal insulation of clothing when neglecting the increase in surface area (Equation (6)) was underestimated by 16% on an average, as compared to the thermal insulation of clothing obtained when considering the increase in surface area (Equation (8)). This finding indicates that the sensible heat loss from the thermal manikin is overestimated by approximately 8% when the conditions of the “thermal insulation of clothing” and “thermal resistance between clothing surface and environment” are at the same level. This error further increases when the thermal resistance between the clothing surface and the environment is low (i.e., when the air velocity is high).

This report and the subsequent report describe the use of the thermal insulation of clothing, where the increase in the surface area due to clothing is considered (Equation (8)). Considering the increase in the surface area due to clothing enables the calculation of the heat transfer and the equivalent temperature under actual environmental conditions.

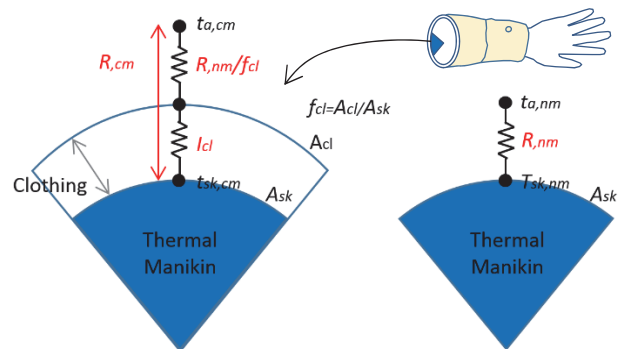


**Fig.2** Cross-sections of a part of manikin, indicating the heat transfer between the manikin surface and the environment when the air temperature is equal to the radiant temperature: clothed manikin (left) and naked manikin (right).

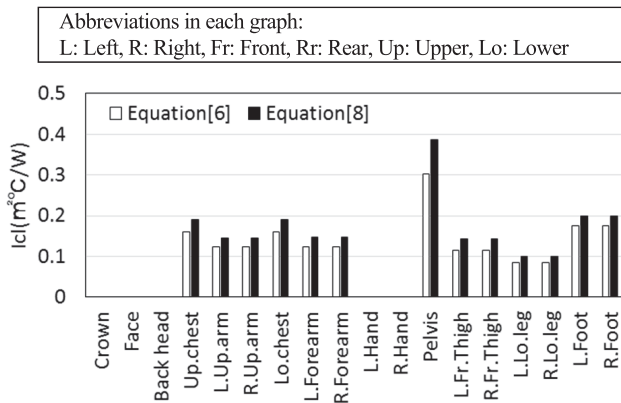


Fig.3 Clothing insulation on each body segment

### 3.2.2. Equivalent temperatures

Figs. 4–7 show the distributions of the air temperatures and air velocities around the thermal manikin, the surface temperatures of individual interior components in the vehicle cabin, and the equivalent temperatures of individual body segments of the thermal manikin, respectively. The measurement results for summer cooling and winter heating conditions are described in the following subsections. First, the measurement results for each thermal element are presented; thereafter, the validity of the measured equivalent temperature results is assessed by comparing them with the air temperature.

#### 3.2.2.1. Summer cooling conditions

Under summer cooling conditions, the air temperatures at the feet of the thermal manikin (Fig. 4) are slightly higher than those at the upper body segments; however, no significant difference is observed among the body segments. By contrast, the air velocities around certain body segments of the thermal manikin (Fig. 5) exhibit significant differences. High air velocities (>1.5 m/s) were measured at the face, chest, left upper arm, and left hand; however, the air velocities at the lower body segments remained low and equivalent to those under natural convection. Generally, the surface temperatures of individual interior components of the vehicle cabin (Fig. 6) exceed the air temperatures around the thermal manikin, owing to the influence of the ambient temperature.

The equivalent temperatures (Fig. 7) vary widely among the body segments. The equivalent temperatures at the feet are higher than the air temperatures. This difference was likely because, although the air velocities at the feet were close to zero and the effect of convection was relatively weak, the surface temperatures of the individual interior components in the vehicle cabin were higher than the air temperatures and radiation increased the equivalent temperatures.

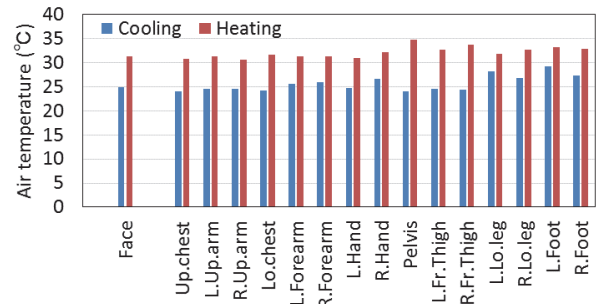


Fig.4 Air temperature around each body segment

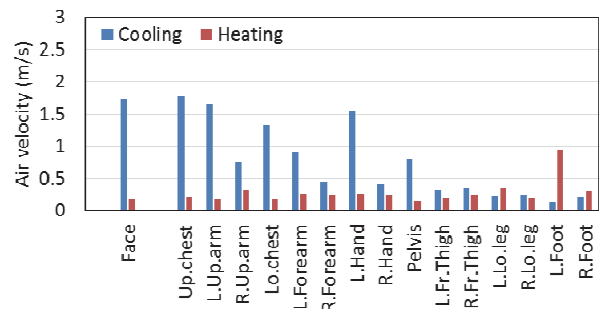


Fig.5 Air velocity around each body segment

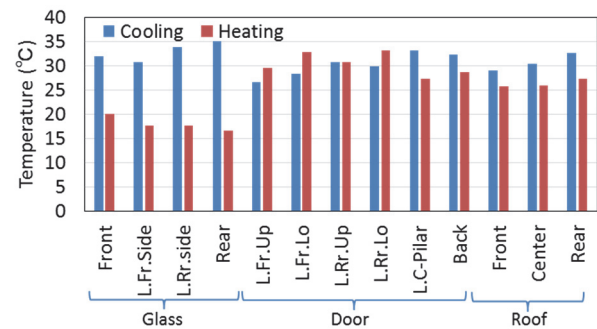


Fig.6 Inner surface temperature of each component

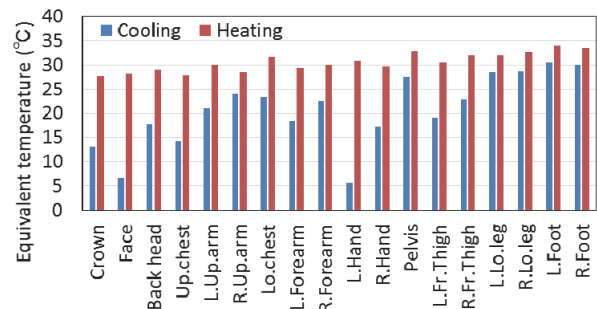


Fig.7 Equivalent temperature around each body segment

For the upper body segments, the equivalent temperatures are low, as compared to the air temperatures, and the temperatures vary among the body segments. In particular, the equivalent temperatures of the face, upper chest, and left hand, which were exposed to high air velocities, are significantly decreased. It is assumed that the equivalent temperatures are low owing to the cooling effect of convection.



Fig.8 Measurements using 3D Handy laser scanner

Furthermore, radiation likely increased the equivalent temperatures at the upper body segments. However, it is assumed that, because the air velocities at the upper body segments were high, the lowering of the equivalent temperatures due to convection surpassed the effect of radiation, and the equivalent temperatures remained lower than the air temperature. Based on the abovementioned findings for summer cooling conditions, body segment-specific equivalent temperatures that appropriately reflected the effects of air temperature, air velocity, and radiation could be measured.

### 3.2.2.2. Winter heating conditions

Under winter heating conditions, the air temperatures around the lower body elements of the thermal manikin (Fig. 4) are slightly higher than those around the upper body segments; however, no significant difference is observed among the body segments. The air temperatures at the lower body segments are approximately 33–35 °C, which are similar to the surface temperature of the thermal manikin (34 °C). The overall air velocities around the thermal manikin (Fig. 5) are low and close to zero; however, the value at the left foot is measured to be approximately 1 m/s because it was exposed to the air from the outlet. Generally, the surface temperatures of individual portions in the vehicle cabin (Fig. 6) are lower than the air temperatures around the thermal manikin, owing to the influence of the ambient temperature. In particular, the surface temperature of the glass is approximately 15–20 °C, which is lower than the air temperature of 15 °C.

The equivalent temperatures (Fig. 7) do not vary among the body segments as much as those under the summer cooling conditions. However, the equivalent temperatures at the upper body segments are lower than

the air temperatures, which likely because the surface temperature of the glass is lower than the air temperature and the upper body segments are affected by the cold radiation from the glass. Unlike those under the summer cooling conditions, the equivalent temperatures under the winter heating conditions are almost identical, regardless of the air velocity. It is assumed that this similarity is observed because the surface temperature of the body segment of the thermal manikin exposed to high air velocities (i.e., the left foot) is almost the same as the surrounding air temperature, and the heat loss due to convection remains relatively constant, even when the air velocity is high. Based on the abovementioned findings under the winter heating conditions, body segment-specific equivalent temperatures that appropriately reflected the effects of air temperature, air velocity, and radiation could be obtained.

## 4. Modeling of clothed thermal manikin

For the simulation-based calculation of the equivalent temperature, the manikin used in the experiment was reproduced as a digital model.

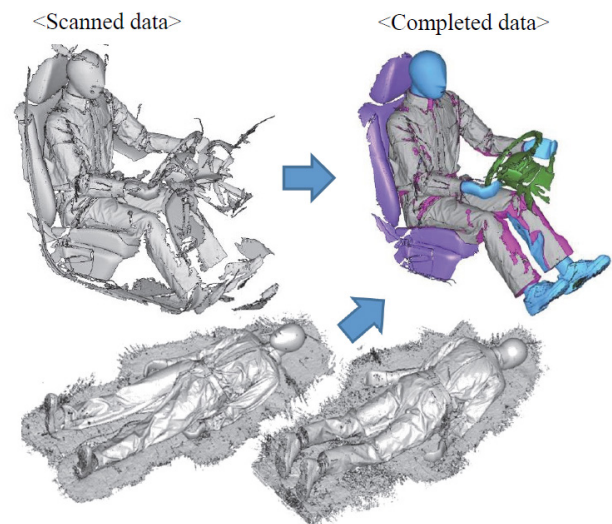


Fig.9 Modeling of clothed manikin (example)

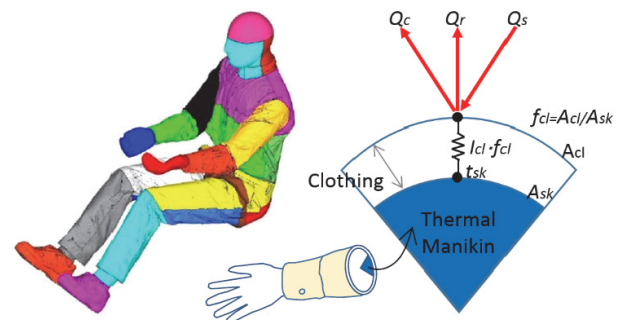


Fig.10 Geometric model of the manikin

Fig.11 Heat transfer model for the numerical thermal manikin

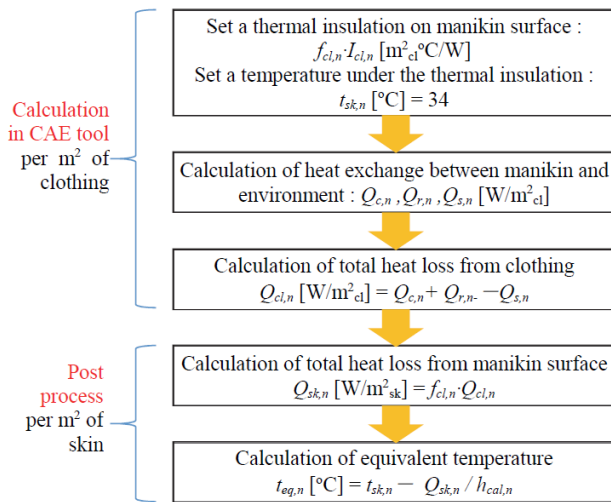


Fig.12 Equivalent temperature calculation procedure

#### 4.1. Creation of a geometric model via 3D laser measurements

A geometric model was created by measuring the shape of the clothed thermal manikin used in the experiment, with a precision of 1 mm. The laser scanner (Ametek 3D HandySCAN 700) used for the measurements and the measurements conducted using a vehicle are depicted in Fig. 8. As a distance of approximately 20–30 cm from the target is required during the measurements, some areas of the manikin, such as the feet, could not be measured in the vehicle. Accordingly, the shape of the manikin was measured separately by laying it on its back and on its abdomen, as shown in Fig. 9, in order to compensate for the areas that could not be measured in the vehicle. Subsequently, the details were added, the manikin was split into body segments (24 segments) in the same manner as in the experiment, and a geometric model of the manikin was created, as depicted in Fig. 10.

#### 4.2. Heat transfer calculation model

In the simulation, it was difficult to reproduce and analyze the multi-layer structure formed by the manikin surface and clothing and the inner structure of the clothing; therefore, a practical heat transfer calculation model was developed based on two parameters: the thermal insulation of the clothing,  $I_{cl}$ , and the area factor, i.e., the surface area difference due to the clothing,  $f_{cl,n}$ . In this method, the heat transfer between the clothing surface and the environment is calculated by considering the clothing surface as a boundary surface. Subsequently, the result is converted into the heat transfer from the manikin surface via post-processing.

Fig. 11 shows the heat transfer model with the clothing surface as the boundary surface. As the thermal insulation of the clothing,  $I_{cl}$ , is the thermal resistance of

the manikin per unit surface area, it was converted into the thermal insulation of the clothing per unit surface area ( $=f_{cl,n} \times I_{cl,n}$ ) to be used as an input to the thermal manikin model. The heat capacity of the clothing was set to zero. The temperature under the thermal insulation of the clothing was fixed at 34 °C, which was the surface control temperature of the thermal manikin; this was to calculate the convective heat loss from the clothing surface,  $Q_{c,n}$ ; the radiant heat loss from the clothing,  $Q_{r,n}$ ; and the solar heat absorption of the clothing,  $Q_{s,n}$ , in the simulation. Thereafter, the total heat loss from the clothing surface,  $Q_{cl,n}$  was calculated using Equation (9) and converted into the heat loss from the manikin surface,  $Q_{sk,n}$ , using Equation (10). Here,  $f_{cl,n}$  was determined using Equation (3).

$$Q_{cl,n} = Q_{c,n} + Q_{r,n} - Q_{s,n} \quad (9)$$

$$Q_{sk,n} = f_{cl,n} \cdot Q_{cl,n} \quad (10)$$

#### 4.3. Equivalent temperature calculation

The clothed thermal manikin model described in this section enables the evaluation of the equivalent temperature in the simulation. The equivalent temperatures can be calculated using Equation (1), based on ISO 14505-2. The equivalent temperatures of the individual body segments can be calculated using Equation (1) by assigning  $t_{sk,n} = 34$  °C,  $Q_{sk,n}$  obtained from Equation (10) based on the simulation results, and  $h_{cal,n}$  obtained from Equation (2). Fig. 12 shows the steps involved from parameter setting to the developed thermal manikin model and up to the calculation of the equivalent temperature.

The second report describes the application of the clothed thermal manikin model discussed in this section to the 3D geometry of the vehicle cabin used for the experiment detailed in Section 3; the second report also presents the calculations of the thermal environment and equivalent temperatures in the vehicle cabin. In addition, the results are compared with the experimental results in Section 3 to verify the simulation accuracy.

### 5. Conclusion

- (1) A method of measuring the thermal insulation of clothing while considering the area factor, i.e., the increase in surface area due to the clothing, was developed, and the thermal insulation of the clothing used for the experiment was measured.
- (2) A method of obtaining  $h_{cal}$  (the heat transfer coefficient between the manikin surface and a standard environment) from the thermal insulation of clothing measured in (1) was also proposed.
- (3) The equivalent temperatures in a vehicle were measured using (1) and (2). In this manner, equivalent temperatures that appropriately reflected the effects of air temperature, air velocity, and radiation could be

determined. These experimental results were used to verify the simulation accuracy, as described in the second report.

- (3) The thermal manikin used for the experiment was converted into a digital model using 3D laser scanning measurements, in order to develop a thermal manikin model incorporated with a clothed heat transfer model. This model was used to simulate the equivalent temperatures, as described in the second report.

### References

- (1) ISO 14505-2: Ergonomics of the thermal environment -- Evaluation of thermal environments in vehicles -- Part 2: Determination of equivalent temperature, Geneva, International Organization for Standardization (2006)
- (2) AIJES-H0005-2015: サーマルマネキンを用いた室内温熱環境評価法規準・同解説建築学会基準, 東京, 日本建築学会 (2015)
- (3) 篠塚貴志ほか: 暖房時窓近傍の温熱環境に関する基礎的検討 (その2) サーマルマネキンによる顕熱損失量と全身温冷感の評価, 2017年度日本建築学会大会 学術講演梗概集 環境工学II, pp.259-260 (2017)
- (4) 弓野沙織ほか: 暖房時窓近傍の温熱環境に関する基礎的検討 (その3) 数値サーマルマネキンを用いた顕熱損失量の対流・放射割合の評価, 2017年度日本建築学会大会 学術講演梗概集 環境工学II, pp. 261-262 (2017)
- (5) Nilsson, H.O.: Comfort climate evaluation with thermal manikin methods and computer simulation models. Stockholm, National Institute for Working Life (2004)
- (6) 川中子貴紀ほか: 着衣サーマルマネキンの伝熱特性予測手法に関する研究, 自動車技術会2015年秋季大会 学術講演会 講演予稿集, No.49-15S, pp.1159-1162 (2015)
- (7) 大井元ほか: メッシュフリーシミュレーションによる車室内の等価温度解析(第1報), 自動車技術会2018年春季大会 学術講演会 講演予稿集, No.80-18, 文献番号 20185361 (2018)
- (8) 米津豊作ほか: メッシュフリーシミュレーションによる車室内の等価温度解析(第2報), 自動車技術会2018年春季大会 学術講演会 講演予稿集, No.80-18, 文献番号 20185362 (2018)
- (9) 尾関義一ほか: メッシュフリーシミュレーションによる車室内の等価温度解析(第3報), 自動車技術会2018年春季大会 学術講演会 講演予稿集, No.80-18, 文献番号 20185363 (2018)
- (10) ASHRAE: ASHRAE Handbook of Fundamentals, Chapter 8 Thermal Comfort, Atlanta, American Society of Heating, Refrigerating and Air-Conditioning Engineers Inc. (2001)

### Symbols and unit

Symbol	Term	Unit
$A_{cl}$	Clothing surface area	m <sup>2</sup>
$A_{sk}$	Skin surface area	m <sup>2</sup>
$f_{cl}$	Area factor (ratio of clothing surface to manikin surface area)	-
$h_{cal}$	Total heat transfer coefficient in a standard environment	W/m <sup>2</sup> °C
$h_{es}$	Convective heat transfer coefficient in a standard environment	W/m <sup>2</sup> °C
$h_{rs}$	Radiant heat transfer coefficient in a standard environment	W/m <sup>2</sup> °C
$I_{cl}$	Thermal insulation of clothing	m <sup>2</sup> C/W
$Q_c$	Convective heat loss from clothing	W/m <sup>2</sup>
$Q_{cl}$	Total heat loss from clothing surface	
$Q_{sk}$	Total heat loss from manikin surface	W/m <sup>2</sup>
$Q_r$	Radiant heat loss from clothing	W/m <sup>2</sup>
$Q_s$	Solar heat absorption on clothing	W/m <sup>2</sup>
$R$	Thermal resistance	m <sup>2</sup> C/W
$t_a$	Air temperature	°C
$t_{eq}$	Equivalent temperature	°C
$t_{sk}$	Skin surface temperature of a manikin	°C
$cm$	Suffix: clothed manikin	-
$n$	Suffix: Segment number of a manikin	-
$nm$	Suffix: naked manikin	-

### Source

公益社団法人自動車技術会  
自動車技術会論文集  
Vol.50NO.4 文献番号:20194578

## Recipients



Hajime Oi



Yasushi Ichikawa



Akira Matsumoto



# Evaluation of Equivalent Temperature in Vehicle Cabin by a Mesh-Free Simulation (Second Report)<sup>※</sup>

Hajime Oi\*   Yasushi Ichikawa\*\*   Akira Matsumoto\*

**Abstract** This report (i.e., the second report) provides an outline of the proposed mesh-free simulation method; it also presents comparisons between the equivalent temperature (teq) obtained via calculations and measurements under summer cooling and winter heating conditions, based on the mesh-free simulation of the 3D laser scanned clothing surface of a thermal manikin in a vehicle cabin. Overall, the calculations results for teq and the thermal environment of the cabin well reproduced the measurements. The key factors for evaluating the value of teq for each body segment of the clothed thermal manikin under cooling and heating conditions are also discussed.

## 1. Introduction

An increasing number of studies have focused on evaluating the thermal environments as well as the thermal sensation and comfort of occupants in a vehicle cabin through numerical simulations. These simulations have been widely used, ranging from the early design stage before vehicle prototyping to the final stage, for purposes such as evaluating the streamlining of air conditioning technology development and improving fuel/electric economics. Various models and methods have been proposed for studying the thermal sensations of occupants, including (1) human thermal models in which the thermoregulatory function of a human body is modeled to evaluate the skin temperature, other physiological quantities, and the thermal sensation indices, and (2) methods that evaluate heat loss,

equivalent temperature, and other physical quantities by modeling the control of thermal manikins. Equivalent temperature is a physical quantity that is distinct from human physiological quantities, and its measurement and evaluation methods are defined in ISO 14505-2<sup>(1)</sup>. Owing to its usability, it has been widely employed not only in the automobile industry but also in other industries such as the construction and aircraft industries. However, ISO 14505-2 only covers the measurement of the equivalent temperature based on thermal manikins and does not include sufficient clear information regarding the measurements when applied in simulations. Although simulations of the equivalent temperatures in a vehicle cabin have been performed previously<sup>(2)-(8)</sup>, few researchers have compared the simulated equivalent temperatures in a vehicle cabin with the experimental values. Thus, the validity of the

numerical calculation results has not been sufficiently verified. Moreover, an appropriate method for handling clothing has not been reported thus far.

Nilsson<sup>(2)</sup> measured and simulated equivalent temperatures using clothed thermal manikins in a vehicle cabin. However, because the thermal manikin used in the simulation was expressed by combining 18 cubic blocks and the shape was significantly different from that of an actual manikin, it is difficult to use the results for a close comparison with the experimental results. To study the air conditioning system in a low-pressure aircraft cabin, Stancato et al.<sup>(3)</sup> calculated the body segment-specific equivalent temperatures using a numerical thermal manikin, for which the skin temperature was set as 34 °C, and the amount of clothing was specified for each body segment. However, they used an occupant composed of cubic blocks and did not compare the results with the experimental results. Using computational fluid dynamics (CFD), Kaushik et al.<sup>(4)</sup> studied the effects of cooler air on the body segment-specific equivalent temperatures by varying the manner in which the body segments were exposed to cooler air, and they compared the results with experimental values. They also modeled the shape of an occupant and analyzed it by applying the thermal insulation of clothing in order to demonstrate that the sensitivity of the experiment was ensured under each condition. However, they did not refer to the validity of the human body shape or consider the clothing shape; instead, they only applied the thermal resistance. For the heat transfer of clothing in a vehicle cabin, Nagano et al.<sup>(5)</sup> modeled the clothing shape to study the heat transfer mechanism; however, they did not apply the model to the simulation of a vehicle cabin. Thus, none of the previous studies have reproduced the human body and clothing shapes to closely compare the

\*Integrated CAE and PLM Department   \*\*Advanced Materials and Processing Laboratory

※ This technical award is result based on the collaborative investigation with AGC inc.

experimental summer and winter vehicle equivalent temperature results with simulation results on a body segment basis.

The objective of this study was to establish a method for simulating the equivalent temperatures in a vehicle cabin under clothed conditions. The first report described an equivalent temperature measurement experiment based on a vehicle and the modeling of a clothed thermal manikin. This report provides an analysis of the equivalent temperatures in a vehicle cabin by means of a mesh-free simulation, which is to be proposed in a separate report, and closely compares the results with the experimental results in order to verify the simulation accuracy. The accuracy of the equivalent temperature prediction with respect to the heat loss from the clothing surface was also assessed.

This paper was prepared by revising the speech<sup>(9)-(11)</sup> presented at the JSAE Spring Congress in 2018. This research was a collaborative work with AGC Inc.

## 2. Overview of mesh-free simulation

Typically, analyses with conventional CFD code require the deletion/correction of unnecessary shapes by filling or using tools such as a lapping tool, which increases the workload and time. By contrast, the developed method enables analyses even if holes or unnecessary shapes are present. Accordingly, users do not need to explicitly consider the creation of the fluid meshes required for regular CFD code, which significantly reduces the analysis workload.

The discretization of the Navier–Stokes equations using one of the typical CFD code, the finite volume method (FVM), requires the vertex coordinates (vertex) and vertex connectivity (connectivity), as shown in Fig. 1 (a). However, this method is described using the area and normal line vectors at the interface of the control volume depicted in Fig. 1 (b), such that it does not require the vertex coordinates and vertex connectivity of regular mesh information. Therefore, the flow can be analyzed by automatically generating information regarding the control volumes and their interfaces (area and normal line vectors) with the point cloud (particles) automatically arranged in the space.

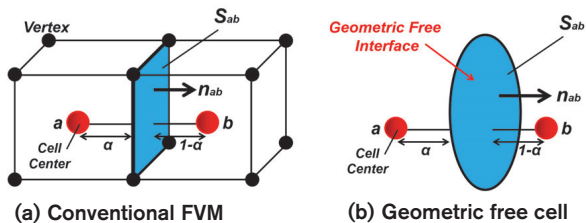


Fig.1 Comparison of control volume between conventional FVM and geometric free cell

In this method, as shown in Fig. 2, the control volumes can have any shape. This free shape can be applied to equation systems that express all the fields, including the flow field. In this method, control volumes are generated

in such a manner that a given control volume and an adjacent control volume satisfy the geometric conditional equation, i.e., Equation (1), to fulfill the conservation law of physical quantities between themselves. Thus, they satisfy laws such as the conservation of mass, momentum, and energy and always behave naturally. Because the automatically generated point cloud of particles is fixed, this method is different from conventional particle methods such as the moving-particle semi-implicit method<sup>(12), (13)</sup>. For further details and a verification of the validity, refer to separate reports<sup>(14), (15)</sup> and patents<sup>(16), (17)</sup>.

$$\sum_{i=1}^m [(n_i \cdot n_p) \cdot S_i] = 0 \quad (1)$$

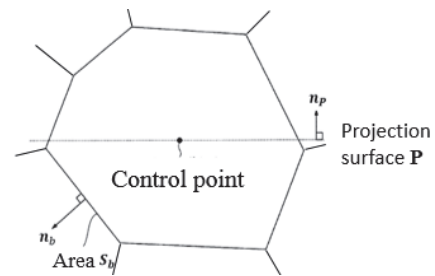


Fig.2 Conservation law for control volume

## 3. Equivalent temperature analysis

A clothed thermal manikin shape was set in the three-dimensional computer-aided design (3D-CAD) of a middle-sized crossover SUV. The interior thermal environments under summer cooling and winter heating conditions in an environmental experiment chamber were analyzed by performing a mesh-free simulation. The equivalent temperature distribution for the occupant in the driver seat was also assessed through a coupled calculation with the clothed thermal manikin model that was described in the first report.

### 3.1. Vehicle body and clothed thermal manikin shapes

For the vehicle body shape, the vehicle body surface data based on the 3D-CAD vehicle body shape were utilized, as shown in Fig. 3. An analysis was conducted by utilizing the features of the mesh-free simulation, without correcting the 3D-CAD data and including the deletion of the surface crossings and protrusions. For the clothed manikin shape, a clothed thermal manikin shape obtained via 3D laser measurements was used; this model was obtained after reproducing the arrangement in the experiment by placing the clothed thermal manikin in the driver's seat of the experimental vehicle. When obtaining the shapes via 3D laser measurements, the shapes of other components nearby, such as the seats and steering wheel, were also acquired in addition to the shape of the clothed thermal manikin. The shape data obtained from the 3D laser measurements do not necessarily agree with the 3D-CAD vehicle shape data.

To reproduce the experimental conditions, part of the 3D-CAD vehicle body shape data pertaining to the side of the vehicle body was moved/corrected based on the 3D data obtained from the 3D laser measurements. Both these sets of data were integrated in this work, and the experimental conditions were reproduced.

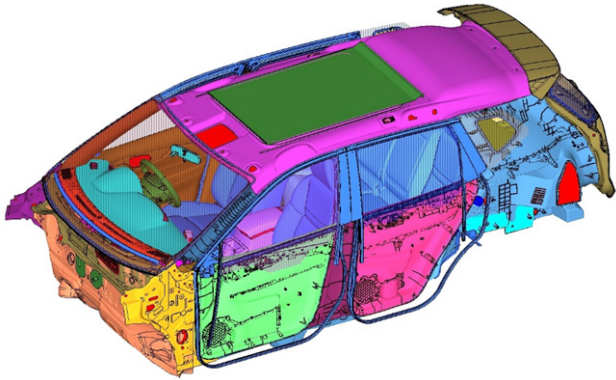


Fig.3 Surface data of the vehicle cabin

### 3.2. Analysis conditions

As described in the first report, an analysis was conducted under summer and winter conditions, as listed in Table 1. Under the summer cooling conditions, the ambient temperature was set to 35 °C, which was the temperature during the experiment; furthermore, the vent recirculation mode was set, and the cooling air flow rate was set to the maximum level. As the inflow conditions, the duct shapes were set to reproduce the state in which air is blown into the vehicle cabin according to the shape and orientation of the vent louver. Discharge air flow rates were set for the ducts at four of the front vents and one rear vent. The discharge temperatures measured under stable conditions were specified for individual ducts. As an outflow condition, the air outflow rate was set equal to the air inflow rate from the HVAC blower. Moreover, the outflow air flowed out from the cabin through the HVAC blower.

Table1 Experimental conditions

	Cooling	Heating
Outside temperature	35°C	0°C
Relative humidity	50%	Not controlled
Solar lamp	OFF	OFF
Vehicle speed	IDLE	IDLE
A/C temperature setting	25°C	24°C
Blower fan speed	MAX	MAX
Mode	VENT	FOOT
Air flow direction	Neck	Neck
REC/FRE	Recirculation	Fresh

For the thermal conditions of the vehicle body members, the surfaces of the inner vehicle body members were divided into the floor, front and rear, right and left doors, roof, etc., according to their thermal performance.

Each member was specified using a heat transfer condition (thermal conductance) under one-dimensional heat flow in the thickness direction, accounting for the structure in which various members are stacked over each other. For the surfaces of the outer vehicle body members, heat transfer conditions were set considering the air velocities at the outer panels of the members. The thermal conductance of the air layer inside the vehicle body members was set according to the direction of heat flow. To analyze the equivalent temperature at each body segment of the manikin, the clothing surface of the manikin was divided into 24 sections. To adjust the manikin control conditions to match those in the experiment, the temperature of the manikin skin surface was set to 34 °C, which was the temperature used in the experiment. For the thermal insulation of the clothing at each body segment of the manikin, the thermal resistance measured considering the increase in surface area due to the clothing, as described in the first report, was specified for each body segment.

Under winter heating conditions, the ambient temperature was set to 0 °C, which was the experimental temperature. The foot fresh-air mode was set, and the heating air flow rate was set to the maximum level. For the inflow conditions, the duct shapes were set in the same manner as those under the cooling conditions, in order to reproduce the state in which air is blown into the vehicle cabin according to the shapes of the foot and defroster ducts. Discharge air flow rates were applied to individual ducts. The discharge temperatures that were measured under stable conditions were specified for individual ducts. With regard to the outflow condition, the leakage of warm air through the gaps in the vehicle body must be considered because the ventilation is set in the fresh-air mode. Therefore, a vehicle body leakage ratio was introduced to model the leakage from the gaps in the vehicle body.

The thermal conditions of the members were set in the same manner as those under the cooling conditions. However, because the door and roof feature door ventilation and the sunroof, respectively, the thermal conductance obtained from the heat flux was set for their thermal conditions. The manikin conditions were the same as those specified for the cooling conditions. When comparing the manikin measurements and analysis values, 18 body segments excluding those in contact with the seat were evaluated, as described in the first report.

### 3.3. Analysis method

The temperature and airflow properties in the vehicle cabin were analyzed using the mesh-free simulation, as described in Section 2. This simulation can analyze thermal liquids by automatically generating information on the control volumes and their interfaces (area and normal line vectors) with the point cloud (particles) automatically arranged in the space. For the surfaces of the vehicle body members, a thermal fluid analysis was coupled considering thermal radiation. In the thermal radiation analysis, the S2S method based on view factors was used<sup>(18)</sup>, and in the thermal fluid analysis, a standard

$k-\varepsilon$  two-equation model was used<sup>(19)</sup>. Regarding the thermal manikin, the heat balance of the clothed thermal manikin was reproduced using a heat transfer model, considering the thermal insulation of the clothing and the area factor. The equivalent temperature at each body segment was calculated based on ISO 14505-2. The steps ranging from the parameter setting to the development of the thermal manikin model and the measurement of the equivalent temperature are summarized in Fig. 4.

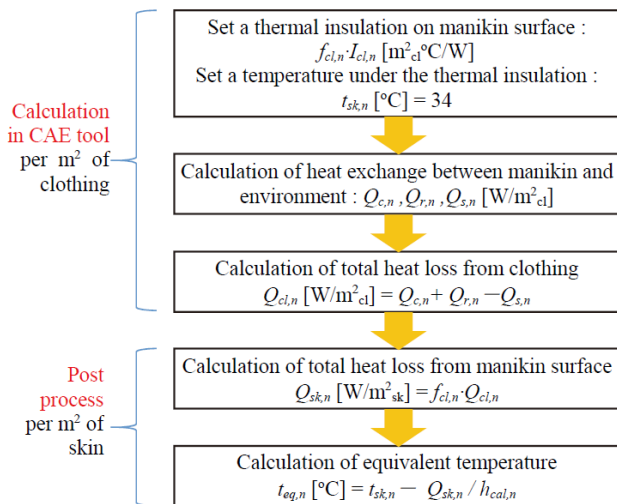


Fig.4 Calculation procedure of equivalent temperature

## 4. Equivalent temperature analysis results

The physical quantities and the equivalent temperatures at individual body segments of the manikin, as obtained from the thermal fluid analysis with the mesh-free simulation, were compared with the experimental results described in the first report in order to verify the accuracy of the simulation-based analysis.

### 4.1. Thermal environment in a vehicle cabin

The velocity distribution and isosurface at a scalar velocity of 3 m/s under the summer cooling conditions are presented in Fig. 5. As the cold air from the vent outlet blows toward each occupant, high velocities are distributed, centering on the front seats. When the recirculation mode is used, the air returns to the foot area. The distribution of the surface temperatures of the individual portions in the vehicle cabin is depicted in Fig. 6. The temperatures are low at the front seats, which are exposed to cold air, whereas those at the rear seats tend to be high.

The velocity distribution and isosurface at a scalar velocity of 2 m/s under the winter heating conditions are presented in Fig. 7. Warm air rises from the foot area at the front seats; as the fresh-air mode is used, the velocity distribution flows toward the rear. The distribution of the surface temperatures of the individual portions in the vehicle cabin is shown in Fig. 8. High temperatures are centered on the front seats, which are exposed to warm air, whereas the temperatures at the rear seats tend to be lower. However, the temperature reduction at the rear seats is suppressed due to the rear seat foot heater.

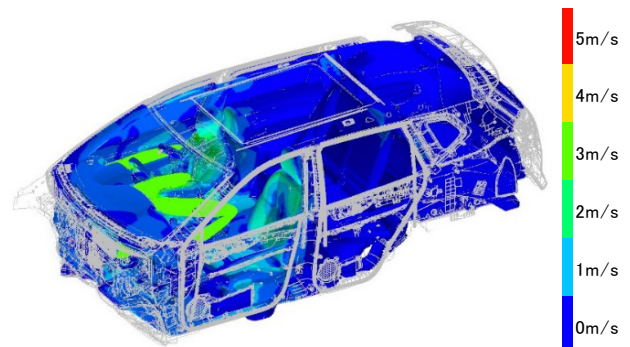


Fig.5 Scalar velocity distribution (cooling)

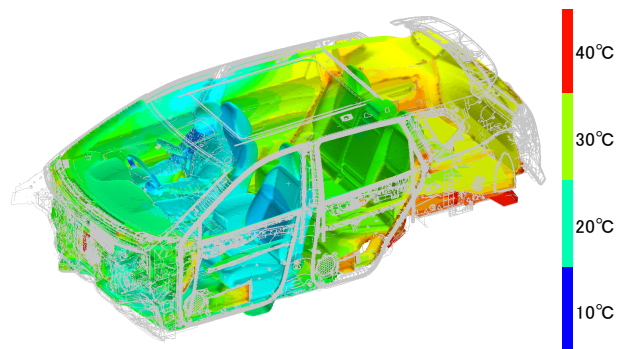


Fig.6 Inner surface temperature distribution on each body part (cooling)

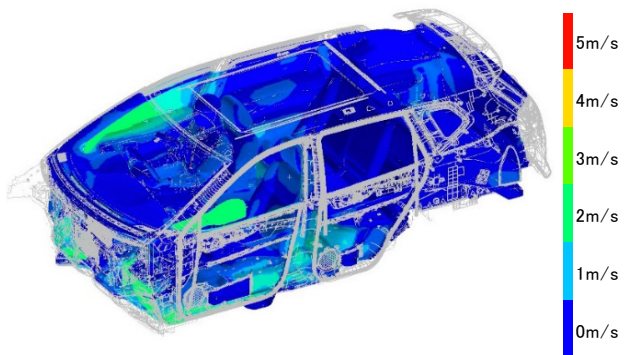


Fig.7 Scalar velocity distribution (heating)

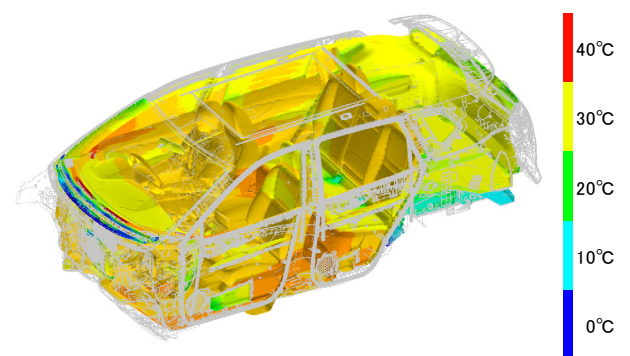


Fig.8 Inner surface temperature distribution on each body part (heating)

### 4.2. Comparison between analysis and experimental results

The surface temperatures of individual portions in the vehicle cabin under the summer cooling conditions are compared in Fig. 9. The analysis values for the door are generally high and differ from each other; however, the values of the glass and roof show a relatively good agreement with each other.

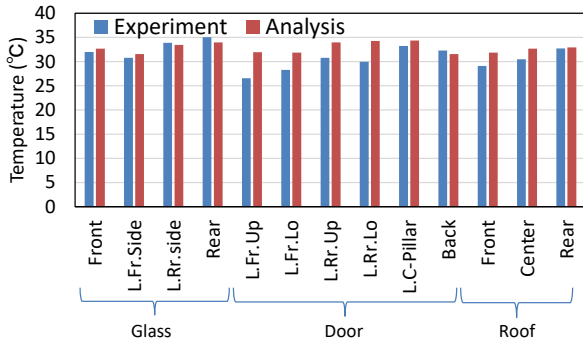


Fig.9 Inner surface temperature on each part (cooling)

The temperatures around the thermal manikin are shown in Fig. 10. The analysis values were obtained from the same points as those measured in the experiment. Although the air temperatures at the lower body segments are slightly higher, the difference in the air temperatures of the other body segments is relatively small. Considering these and other circumstances, the analysis values correspond with the experimental values.

The air velocities around the thermal manikin are

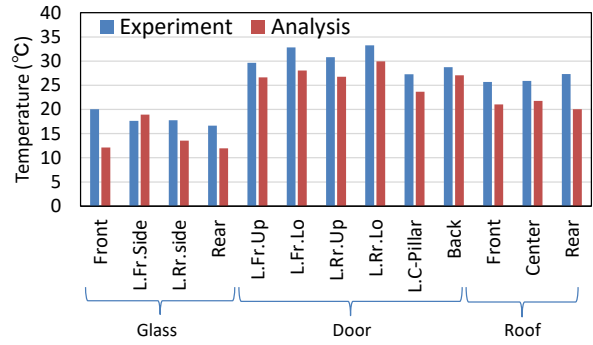


Fig.13 Inner surface temperature on each part (heating)

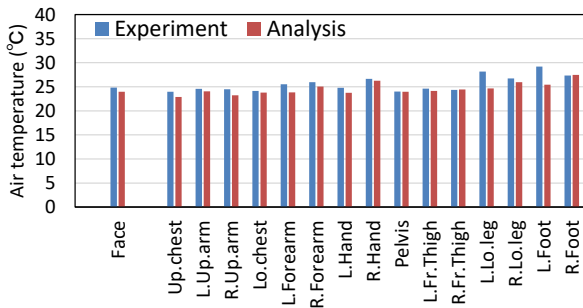


Fig.10 Air temperature around each body segment (cooling)

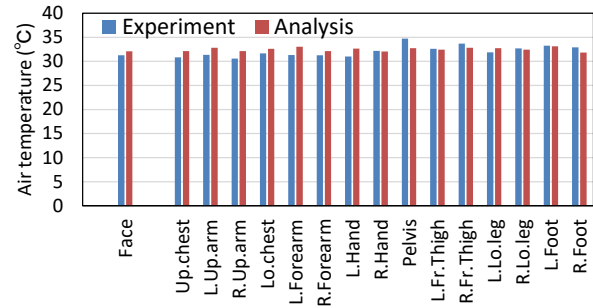


Fig.14 Air temperature around each body segment (heating)

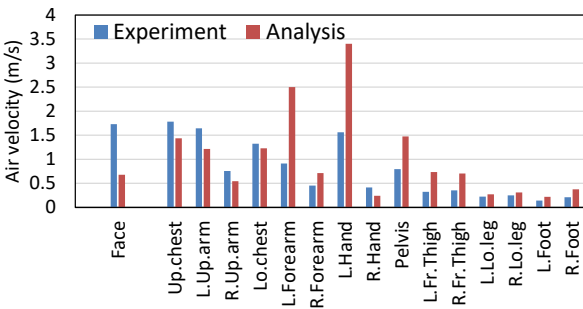


Fig.11 Air velocity around each body segment (cooling)

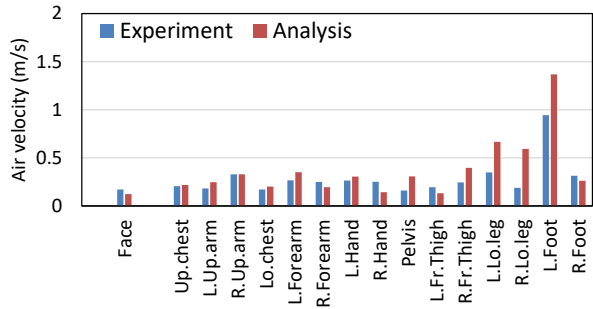


Fig.15 Air velocity around each body segment (heating)

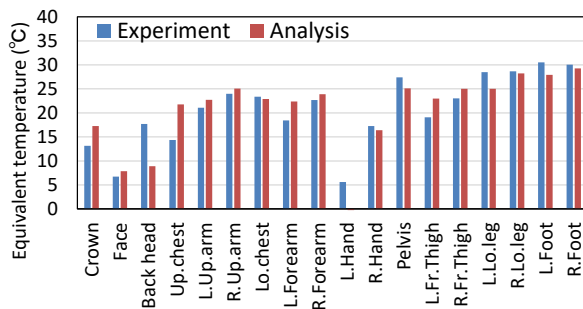


Fig.12 Equivalent temperature around each body segment (cooling)

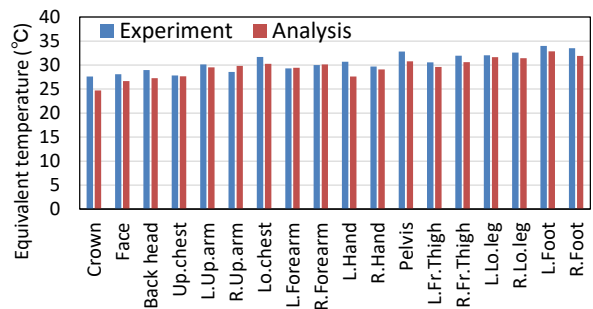


Fig.16 Equivalent temperature around each body segment (heating)

depicted in Fig. 11. Although the air velocities for the face, left hand, and left forearm do not correspond, the characteristics of vent-mode cooling air conditioning, in which the velocities at the upper body segments are relatively high and those at the lower body segments tend to be low, are reproduced well in the calculation. Considering these and other circumstances, the values generally correspond with each other. It was assumed that the differences for the left hand and left forearm occurred because the left hand and left forearm were located close to the vent outlet when the steering wheel was held; thus, they were significantly affected by the direction of the airflow from the vent outlet. It was assumed that the face was affected by the small differences in the orientation of the vent outlet.

The equivalent temperatures are compared in Fig. 12. Considering the distribution tendency and other circumstances, the analysis values correspond relatively well with the experimental values. The abovementioned findings indicate that the analysis values correspond with the experimental values. In particular, considering that the equivalent temperature differences are 3 °C or less, the thermal sensation votes could be predicted with an accuracy of one-point on the seven-point ISO scale.

The surface temperatures of individual portions in the vehicle cabin under the winter heating conditions are presented in Fig. 13. The analysis values of the door are slightly lower than the experimental values. The probable reason for this difference is as follows. In the experiment, warm air flowed toward the back of the door trim from the vehicle cabin, and the sunroof-type roof was affected by this. It was assumed that the windshield was affected by the set temperature of the defroster outlet.

The temperatures around the thermal manikin are shown in Fig. 14. The temperatures are slightly higher at the feet, which are exposed to warm air, and the distribution is generally small. Considering these and other circumstances, the values correspond well with each other.

The air velocities around the thermal manikin are depicted in Fig. 15. Considering the distribution tendency of the air velocities and other circumstances, the analysis values correspond well with the experimental values.

The equivalent temperatures are compared in Fig. 16. Although the distribution is generally small, as compared to that under the summer cooling conditions, the temperature tends to increase from the head toward the feet. Considering these and other circumstances, the analysis values correspond well with the experimental values. These findings indicate that, as in the case of the summer cooling conditions, the analysis values correspond well with the experimental values under the winter heating conditions. In particular, considering that the differences in the equivalent temperature are less than 1 °C, the thermal sensation votes could be predicted within a one-point level.

## 5. Consideration

The differences between the clothing surface temperatures of the upper body segments of the manikin and the air temperatures in the surrounding area were large under the cooling conditions, as compared to those under the heating conditions. In addition, under the cooling conditions, the amount of convective heat transfer varies easily owing to the large fluctuations in the convective heat transfer coefficients due to the airflow of the vent. Accordingly, it was assumed that the back of the head and the upper chest were likely to be affected by components such as the vent outlet, which easily resulted in differences between the experimental and analysis values. For a higher prediction accuracy, the orientation of the vent outlet, the analysis resolution including particle arrangements, and the turbulence model must be improved.

For the shapes that need to be analyzed because the positional relationship between the manikin and the vehicle body is adjusted by the 3D laser measurements, it was assumed that the predicted configuration factors were not significantly different from those under the actual conditions. Meanwhile, the differences between the surface temperatures of the manikin and the individual members were small, as compared to the air temperature differences. Accordingly, it was assumed that the effect of the prediction accuracy of the amount of radiant heat transfer on the equivalent temperatures was relatively weak.

Under the heating conditions, the differences between the clothing surface temperatures of the manikin and the air temperatures in the surrounding area were small. In addition, because the air velocities around the manikin were generally low, except for the feet exposed to warm air, the convective heat transfer coefficients were also small. Thus, the effect of the convective heat transfer on the prediction accuracy of the equivalent temperatures was relatively weak. The feet were directly exposed to warm air from the foot duct, which could easily affect the convective heat transfer coefficients. However, because the differences between the clothing surface temperatures of the manikin and the air temperatures in the surrounding area were small, it was assumed that the effect on the amount of convective heat transfer was generally weak.

Meanwhile, considering the differences between the surface temperatures of the members and the skin surface temperature of the manikin, the differences for the door area were small, whereas those for the glass area were large. Thus, it was assumed that the prediction accuracy of the amount of radiant heat transfer at portions where the surface temperatures varied significantly affected the equivalent temperatures. In this study, the calculated door area and windshield (WS) area were rather low. However, for the door glass area, in which the view factors of the manikin were relatively large and the temperatures were considerably different from those of the manikin, the analysis values for the surface temperatures corresponded well with the

experimental values. Accordingly, it was assumed that the differences between the equivalent temperatures of the analysis and the experimental values were small.

In general, the differences between the surface temperatures of individual components in a vehicle cabin and the skin surface temperature of a manikin increase under heating conditions. Therefore, it was assumed that the following aspects were important: (1) the prediction accuracy of the surface temperatures of the glass area, where the surface temperatures were low and the view factors were large, and the roof, where the view factors were relatively large; and (2) the positional relationship with the manikin centered on the feet, which are located close to the outlet of warm air.

## 6. Conclusion

- (1) In a mesh-free simulation, a clothed thermal manikin shape was set in an SUV shape to analyze the thermal environment and equivalent temperatures in a vehicle cabin under summer cooling and winter heating conditions.
- (2) General information regarding mesh-free simulations was provided.
- (3) The analysis and experimental results were compared under the summer cooling and winter heating conditions. The equivalent temperatures of the individual body segments of the thermal manikin were reproduced with sufficient accuracy; this enabled the prediction of the thermal sensation votes of the individual body segments of the thermal manikin within a one-point level.
- (4) The prediction accuracy of the equivalent temperatures was considered based on the heat loss from the clothing surface of the thermal manikin. The prediction accuracy of the amount of convective heat transfer from the upper body segments affected the equivalent temperatures under the summer cooling conditions, whereas that of the amount of radiant heat transfer affected the equivalent temperatures under the winter heating conditions.

## References

- (1) ISO14505-2: Ergonomics of the thermal environment - Evaluation of thermal environments in vehicles - Part 2: Determination of equivalent temperature, Geneva, International Organization for Standardization (2006)
- (2) Nilsson H.O.: Comfort climate evaluation with thermal manikin methods and computer simulation models. Stockholm, National Institute for Working Life (2004)
- (3) Stancato F., Conceicao S., Papa R. and Santos L.: CFD Thermal Comfort in Aircraft Cabin, a Comparative Study, SAE Paper 2015-01-2561 (2015)
- (4) Kaushik S., Han T. and Chen K.H.: Development of a Virtual Thermal Manikin to Predict Thermal Sensation in Automobiles, SAE Paper 2012-01-0315 (2012)
- (5) Nagano H., Kobayashi Y., Kawanago T., Kohri I., Matsunaga K.: Prediction of Convective Heat Transfer

- Coefficient for Ruck and Asperity of Clothing Surface, Proceedings of Ambience14 & 10i3m, ID 118 (2014)
- (6) Hepokoski M., Curran A. and Schwenn T.: A Comparison of Physiology-Based Metrics to Environment-Based Metrics for Evaluating Thermal Comfort, SAE Paper 2013-01-0844 (2013)
  - (7) Chen K.H., Kaushik S., Han T., Ghosh D. and Wang M.: Thermal Comfort Prediction and Validation in a Realistic Vehicle Thermal Environment, SAE Paper 2012-01-0645 (2012)
  - (8) Ghosh D., Wang M., Chen K.H., Kaushik S. and Han T.: Energy Efficient HVAC System with Spot Cooling in an Automobile - Design and CFD Analysis, SAE Paper 2012-01-0641 (2012)
  - (9) 大井元ほか:メッシュフリーシミュレーションによる車室内の等価温度解析(第1報),自動車技術会2018年春季大会 学術講演会 講演予稿集, No.80-18, 文献番号 20185361 (2018)
  - (10) 米津豊作ほか:メッシュフリーシミュレーションによる車室内の等価温度解析(第2報),自動車技術会2018年春季大会 学術講演会 講演予稿集, No.80-18, 文献番号 20185362 (2018)
  - (11) 尾関義一ほか:メッシュフリーシミュレーションによる車室内の等価温度解析(第3報),自動車技術会2018年春季大会 学術講演会 講演予稿集, No.80-18, 文献番号 20185363 (2018)
  - (12) 越塚誠一:粒子法,日本計算工学会編,丸善株式会社,(2005)
  - (13) Koshizuka, S and Oka, Y : Moving-Particle Semi-Implicit Method for Fragmentation of Incompressible Fluid, Nucl. Sci. Eng., 123, 421-434 (1996).
  - (14) H. Sato, et.al.: Thermal Fluid Analysis by A Mesh Free Simulation, Part1 Analysis of the thermal fluid field in a headlamp based on the real 3D-CAD model, No. 2011-28-0135, APAC-16 (2011)
  - (15) M. Inoue, et.al.: Thermal Fluid Analysis by A Mesh Free Simulation, Part2 Analysis of the indoor climate in a vehicle cabin based on the 3D-CAD model, No. 2011-28-0136, APAC-16 (2011)
  - (16) 斉藤恒洋ほか,国際公開番号 WO 2010/150758A. 物理量計算方法、数値解析方法、物理量計算プログラム、数値解析プログラム、物理量計算装置および数値解析装置
  - (17) 柳原一貴ほか,国際公開番号 WO 2014/069421A. シミュレーション装置、シミュレーション方法およびプログラム
  - (18) 尾関義一ほか:複雑な内部形状を有する大規模メッシュ対応型放射伝熱計算手法に関する研究,空気調和・衛生工学会論文集, No.62, 101-110 (1996)
  - (19) 尾関義一ほか:実験用実大アトリウム内の熱伝達・気流性状に関するCFD解析(第1報)-CFD・2波長放射連成シミュレーションにおけるサッシュのモデリングに関する研究,空気調和・衛生工学会論文集, No.68, 65-75 (1998)

**Source**

公益社団法人自動車技術会  
 自動車技術会論文集  
 Vol.50NO.4 文献番号:20194579

**Symbols and unit**

Symbol	Term	Unit
$A_{cl}$	Clothing surface area	$m^2$
$A_{sk}$	Skin surface area	$m^2$
$I_{cl}$	Thermal insulation of clothing	$m^2\text{°C/W}$
$Q_c$	Convective heat loss from clothing	$W/m^2$
$Q_{cl}$	Total heat loss from clothing surface	$W/m^2$
$Q_{sk}$	Total heat loss from manikin surface	$W/m^2$
$Q_r$	Radiant heat loss from clothing	$W/m^2$
$Q_s$	Solar heat absorption on clothing	$W/m^2$
$R$	Thermal resistance between manikin surface and environment	$m^2\text{°C/W}$
$S_{ab}$	Abuttal area between $V_a$ and $V_b$	$m^2$
$V_a, V_b$	Control volume	$m^3$
$f_{cl}$	Area factor (ratio of clothing surface to manikin surface area)	-
$h_{cat}$	Total heat transfer coefficient in a standard environment	$W/m^2\text{°C}$
$h_{cs}$	Convective heat transfer coefficient in a standard environment	$W/m^2\text{°C}$
$h_{rs}$	Radiant heat transfer coefficient in a standard environment	$W/m^2\text{°C}$
$\mathbf{n}_{ab}$	Normal vector	-
$t_{eq}$	Equivalent temperature	$\text{°C}$
$t_{sk}$	Skin surface temperature of a manikin	$\text{°C}$
$cm$	Suffix: clothed manikin	-
$n$	Suffix: Segment number of a manikin	-
$nm$	Suffix: naked manikin	-

**Recipients**


Hajime Oi



Yasushi Ichikawa



Akira Matsumoto



# Development of the First Active Torque Rod in the World

Masahiko Kondo\* Koji Tanimura\*\* Ryosuke Yamauchi\* Yuta Oana\*\*\*

## 1. Description of technological development

### 1.1 Introduction

Downsizing turbo (DST) and high compression ratios have been increasingly adopted as measures of improving the fuel economy of future high-efficiency powertrains. However, because they increase the exciting force of the engine, the mount weight must be increased under conventional technologies, which, in turn, decreases the fuel economy. Therefore, it has become necessary to create a new mount that suppresses the weight input into the body.

Torque rods strongly affect the booming and acceleration noises that influence vehicle ride comfort. This study developed an active torque rod that utilizes the resonance of the torque rod itself to prevent high-frequency engine exciting forces and addresses the trade-off peak resonance by providing a damping force for the reciprocal actuator.

This work can be summarized as follows. (1) Various functions required for a torque rod were realized in a balanced manner by employing independent design variables. (2) Simple, automatic, and robust controls were implemented by incorporating the acceleration-integrating function of the controller into the actuator in order to realize direct velocity feedback for the damping rod resonance.

### 1.2 Effects of fuel economy improvement technologies on vibration noise characteristics

Many well-known approaches exist for improving the fuel economy of internal combustion engines, such as downsizing by replacing a V-type six-cylinder engine with an inline four-cylinder engine that is effective in reducing pumping loss and friction losses. However, the engine vibration increases in the range between low and middle frequencies, because the per-cylinder torque increases when an engine with fewer cylinders generates the same engine torque as that of an existing engine (Fig. 1).

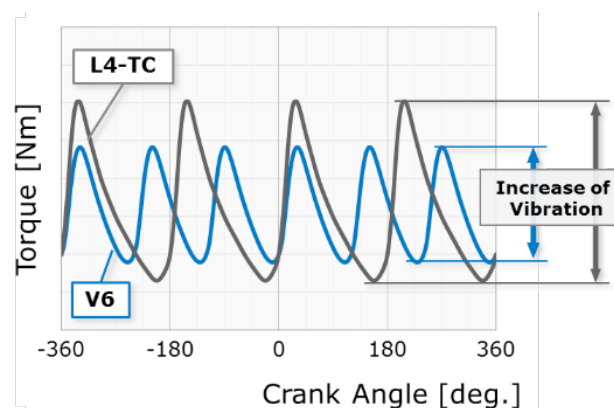


Fig. 1 Increase in torque fluctuations due to downsizing

Moreover, if the compression ratio is increased or rapid combustion such as homogeneous charge compression ignition is applied to improve the combustion efficiency, the engine vibration increases owing to the high-frequency component generated by the combustion pressure. An example of the effect of increasing the compression ratio is depicted in Fig. 2. As described above, the technology for fuel economy improvement results in a trade-off between noise and vibration, and these phenomena may increase in the range between low and high frequencies in downsizing-type engines with improved combustion efficiencies, such as variable compression ratio (VCR) engines. To address this issue, an engine mount with a high vibration cutoff performance must be developed.

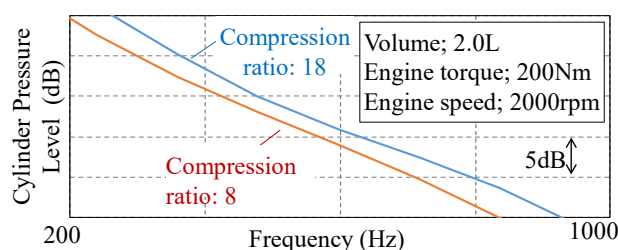


Fig. 2 Increase in combustion exciting force with increasing compression ratio

\*Powertrain and EV Performance Engineering Department

\*\*Chassis Engineering Department

\*\*\*Vehicle Performance Engineering Department

### 1.3 Newly developed mount system

A large vibration-isolating subframe was developed as a conventional measure for preventing the excitation force of the engine from being transmitted to the body (Fig. 3). For low frequencies of 100 Hz or less, an active control mount (ACM) was employed to eliminate the effect of the rigid-body resonance of the subframe. The ACM increases the force using the resonance of the liquid inside the hydraulic mount because it requires a high control force. Consequently, the ACM increases in size, which raises concerns regarding weight gain.

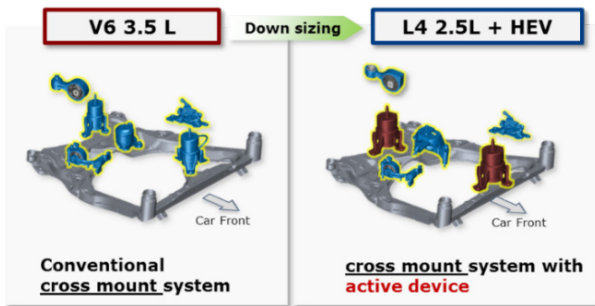


Fig. 3 Conventional vibration-isolating subframe and active mount

By contrast, a simple solenoid actuator is commonly used for reducing the cost. A controlled force is required to nullify the excitation force of the engine, in order to suppress the booming noise caused by the basic order of the engine. Because the harmonics resulting from the driving principle of the solenoid are suppressed by the fluid orifice, the actuator control force corresponding to frequencies of approximately 100 Hz or higher is significantly small, and the control ability on the high-frequency side is limited.

#### 1.3.1 Invention of a new mount system

A VCR engine that realizes ideal combustion under all driving conditions was developed, with the aim of realizing a high torque (390 Nm) exceeding that of a V6, which will help improve driving comfort and fuel economy (to approximately 30% or more than that of a V6) simultaneously (Figs. 4 and 5). This ideal engine fulfills the dreams of engineers. However, it raises more concerns regarding noise and vibration than the conventional DST, as described above.

Typically, engines with good fuel economies cannot provide high torque outputs owing to their high compression ratios. Nevertheless, when the torque demand is high, the VCR engine, which features good fuel economy and in which a high-frequency exciting force acts as an input under partial loads, is operated at a low compression ratio, thereby enabling full-throttle turbocharging. Accordingly, its mount must support the engine in a more rigid and secure manner than conventional engines. Thus, a greater high-frequency engine exciting force is transmitted to the body (Fig. 2).

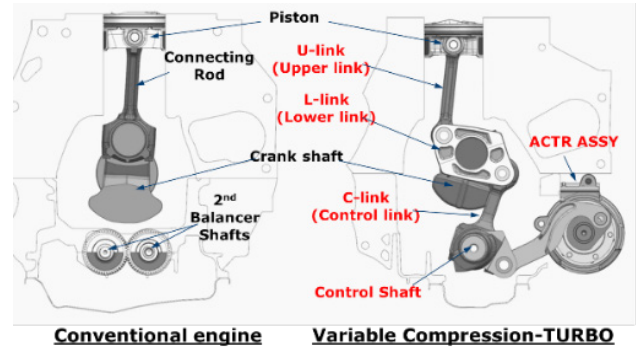


Fig. 4 Mechanism of the VCR engine

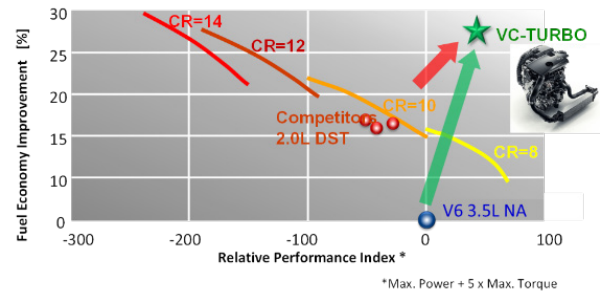


Fig. 5 Satisfactory VCR performance and fuel economy

Consequently, a completely new mount concept was invented. An outline of the concept is presented in Fig. 6. As the conventional torque rod was required to support a high engine torque, the insulator was considerably stiff, and the resonance frequency of the torque rod was approximately 700 Hz. By designing the insulator as detailed later in this paper, the exciting force transmitted to the body was significantly reduced by lowering the natural frequency of the rod and setting the acceleration noise region as a vibration-isolating region, while also supporting the high torque.

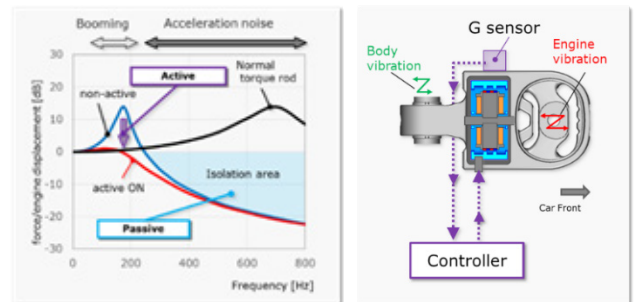


Fig. 6 Concept of the new active mount

However, if the resonance lowered to the booming noise region is addressed by increasing the damping of the insulator itself, the improved vibration-isolation region will disappear. To prevent this issue, active control measures were implemented to dampen the resonance.

First, the vibration input from the engine was reduced using an engine-side insulator, as shown in Fig. 6. Thereafter, the resonance was absorbed by increasing the damping of the torque rod electrically, rather than physically, by providing a controlled force proportional to the vibration velocity of the torque rod.

### 1.3.2 Axiomatic design

Axiomatic design is useful for this development. The following three functions are required for the torque rod:

1. Secure support of the torque generated by the engine;
2. Improved prevention of the transmission of the high-frequency exciting forces generated by rapid combustion to the body;
3. Prevention of the excitation of rod resonance due to engine torque fluctuations.

However, the design solutions (variables) for realizing these benefits are mutually related, and the functions conflict with each other. Therefore, an equation that meets the requirements was developed using independent design solutions (variables), where the functions and design variables have a one-to-one correspondence. Furthermore, to realize a single functional requirement using several design variables, the design variables were integrated to the extent possible in order to satisfy the functional requirement automatically (utilization of the independence axiom and information axiom).

Examples of the abovementioned equations are presented in Figs. 7 and 8. To support the high torque generated by the engine, an engine-side insulator was utilized, and a body-side insulator was used to lower the rod resonance. In this manner, Equations (1) and (2) were satisfied. A careful observation of Fig. 8 indicates that the contours in Fig. 8 (a) are horizontal with respect to  $k_2$  (body-side stiffness), whereas those in Fig. 8 (b) are vertical to  $k_2$ , which indicates that they are orthogonal and independent of each other. By developing Equations (1) and (2) to define this relationship, these characteristics could be identified.

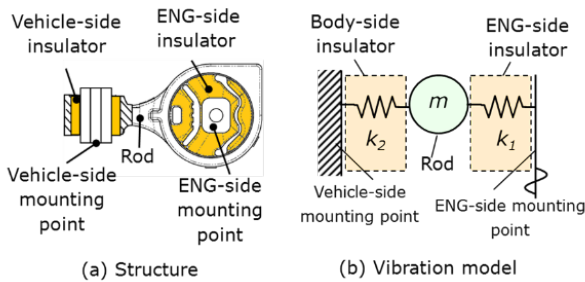


Fig. 7 Vibration model of the torque rod

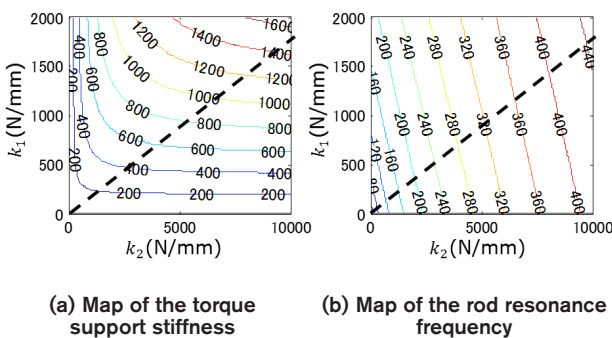


Fig. 8 Satisfying the torque supporting function (high stiffness) and vibration-isolation function (low stiffness)

In addition, the rod resonance was damped with an inertial mass actuator based on Equations (1)–(3), without using the damping characteristics of the insulator. This approach also makes the design independent (Fig. 9). In other words, the control force only affects the resonance amplitude and does not deteriorate the vibration-isolation performance at high frequencies.

The following describes the method of reducing the resonance amplitude of the torque rod using equations. The structure of the velocity feedback control that suppresses resonance was studied by generating the control force  $F_{cont}$  as a damping force that is proportional to the measured vibration velocity of the torque rod, which is indicated in Equation (5), due to the inertial mass actuator built in the torque rod.

By applying this control force to Equation (3), Equation (6) can be obtained. Furthermore, organizing Equation (6) yields Equation (7). The numerator, which affects the vibration-isolation region, does not include the feedback gain  $G$ , and the feedback gain  $G$  proportional to the velocity can be applied to the damping term in the denominator on the right side and the resonance can be suppressed.

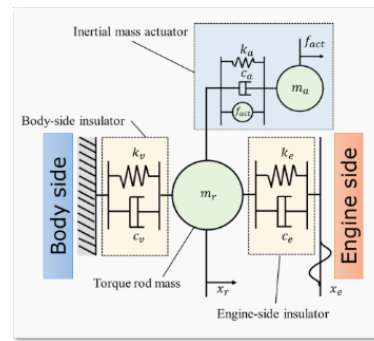


Fig. 9 Diagram of the active torque rod model

$$k_t = 1/(1/k_1 + 1/k_2) \tag{1}$$

$$f_t = \frac{1}{2\pi} \sqrt{(k_1 + k_2)/m} \tag{2}$$

$$m\ddot{x}(t) + (c_1 + c_2)\dot{x}(t) + (k_1 + k_2)x(t) = k_1 x_{eng}(t) + c_1 \dot{x}_{eng}(t) \tag{3}$$

$$\frac{F_{trod}}{X_{eng}} = \frac{(c_2 S + k_2)X}{X_{eng}} = k_t(S) \tag{4}$$

$$= \frac{c_1 c_2 S + k_1 k_2}{mS^2 + (c_1 + c_2)S + (k_1 + k_2)} \tag{4}$$

$$F_{cont} = -G\dot{x}(t) \tag{5}$$

$G$  : Feedback gain

$$m\ddot{x}(t) + (c_1 + c_2)\dot{x}(t) + (k_1 + k_2)x(t) = k_1 x_{eng}(t) + c_1 \dot{x}_{eng}(t) + F_{cont} \tag{6}$$

$$\frac{F_{trod}}{X_{eng}} = \frac{c_1 c_2 S + k_1 k_2}{mS^2 + (c_1 + c_2 + G)S + (k_1 + k_2)} \tag{7}$$

## 2. Usability of technology

The adoption of DST and a high compression ratio to improve the fuel economy increases the engine exciting force and deteriorates the booming and acceleration noise. This concept was verified based on the active damping mechanism, where an actuator was built in a single torque rod, as shown in Fig. 10.

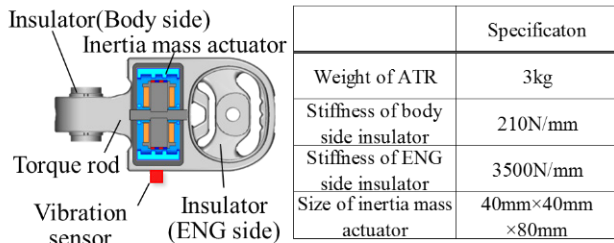


Fig. 10 Structure of the active torque rod (specifications)

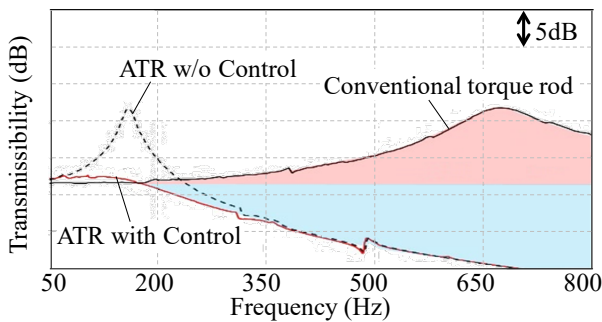


Fig. 11 Concept verification with a single torque rod

The test was conducted by inputting specific exciting forces into the engine-side insulator of a single torque rod to compare the displacement of the torque rod caused by each exciting force with or without control. By lowering the natural frequency of the torque rod to 200 Hz or less, the frequency range in which transmissibility was increased by the higher resonance in the conventional torque rod formed a vibration-isolation region, which considerably improved the transmissibility.

Furthermore, although damping was increased at the resonance frequency, the transmission characteristic at 300 Hz or higher was the same as that without control (denoted by the red solid line in Fig. 11). Accordingly, this was confirmed using an actual engine, and the resonance peak could be lowered without sacrificing the vibration-isolation performance. This technology is epochal because it enables a single system to cover the range from low to high frequencies.

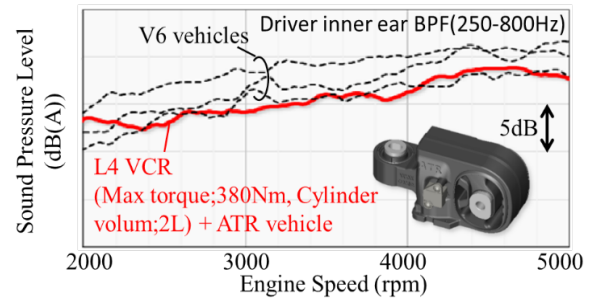


Fig. 12 Effect of the active torque rod on interior noise during acceleration

Next, the sound pressure at the ear position of the driver was measured by setting an active torque rod (ATR) on a vehicle equipped with an L4-VCR engine, which outputs a V6-equivalent torque. The interior noise under full-throttle acceleration is depicted in Fig. 12. The vibration cutoff effect of the ATR achieves the same noise level as that in a V6-equipped vehicle. The weight of the engine mount system was also reduced by 40% (8 kg), as compared to that of the conventional ACM technology.

Because the exciting force transmitted to the body was significantly reduced, the zone for the pendulum mount system was considerably enlarged, as compared to that under the previous setting (Fig. 13).

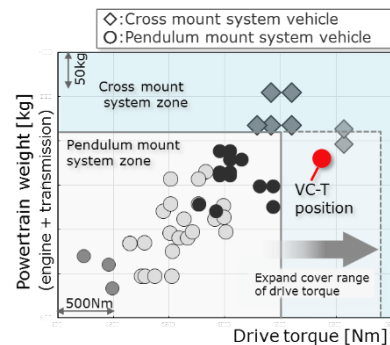


Fig. 13 Enlargement of the engine mount system range

This technology utilizes a control force proportional to the rod velocity for damping; however, by assuming that the control force generated by the actuator is proportional to the displacement, the stiffness of the insulator can be varied. Furthermore, because the control force proportional to the acceleration allows for mass variations, the natural frequency of the rod can be flexibly varied in the future (Fig. 14).

Consequently, the potential for improving quietness will be enhanced under any scenario in which the high-frequency exciting force is increased through the ultimate pursuit of thermal efficiency. The former constraints associated with the natural frequency layout design, such as the efforts required to avoid overlap between the resonance frequencies of individual components at the time of platform change, will be overcome. Thus, it will be feasible to focus on and share target controls, and quietness will eventually be improved.

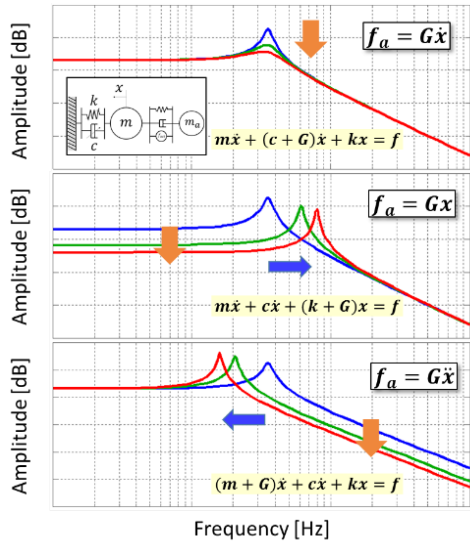


Fig. 14 Increase of control flexibility

### 3. Novelty, originality, and innovativeness of technology

#### 3.1 Realization of the first compact inertial mass actuator in the world built in a torque rod

The solenoid actuator for conventional ACM suffers from issues pertaining to its high-frequency output characteristics. First, solenoids can only generate attractive magnetic forces; moreover, owing to their nonlinearity, the output force waveform is distorted. As they also generate higher-order forces at frequencies other than the target frequency, they must be designed such that these forces are not transmitted to the target structure. To realize a superior actuator, a new reciprocal actuator was developed as an inertial mass actuator that showed excellent linearity even at high frequencies. The frequency characteristics of the control force are depicted in Fig. 15. The control force of the solenoid decreases considerably at high frequencies. By contrast, the reciprocal actuator developed in this study exhibits high output and linearity.

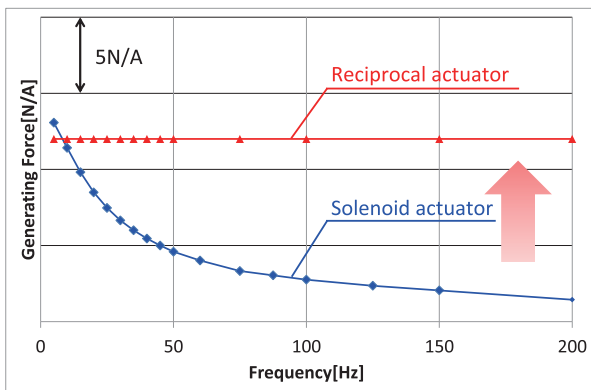


Fig. 15 Improvement in the linearity of the reciprocal actuator, as compared to the solenoid

To achieve the control target force with a limited input energy of 12 V up to 200 Hz, it is significantly important to optimize the magnetic circuits and reduce the coil inductance for realizing sufficient currents at high frequencies. To maximize the electromagnetic force of the permanent magnet based on the condition of reducing the number of coil turns, the actuator was downsized by optimizing the gap and the gap shape between the moving element and the magnet. Furthermore, to improve the quality of the generated thrust, magnetic steel sheets (i.e., laminated steel sheets) were used for all the magnetic circuits of the reciprocal motor. This approach helped solve the major concerns associated with the solenoid, which were the deterioration of current-generated thrust due to iron loss in the high-frequency region and the phase lag of the generated thrust for the thrust command. Thus, an ideal actuator with improved linearity was realized.

The finalized structure is shown in Fig. 16. The moving element was fixed to the stator with a leaf spring, and the actions of both the magnetic field generated by the stator coil and the magnet were applied. The electromagnetic forces and control forces generated in the moving element are depicted in Figs. 17 and 18, respectively. The function of the inertial mass actuator can be fulfilled by alternating the orientations of the current applied to the coil in order to alternate the uneven distribution of the magnetomotive forces of the magnetic fluxes of the magnet.

Regarding the supporting method, the moving element was changed to a leaf spring from a general bearing or a slide bearing. This change facilitated downsizing, improved durability, and reduced the additional power required for positioning the moving element.

However, although downsizing was achieved, an inertial mass of approximately 400 g was necessary for the required control force. Therefore, it was found that it was impractical to build this mass into the torque rod. This issue was solved by reversing the positioning of the moving element and the stator (Fig. 19).

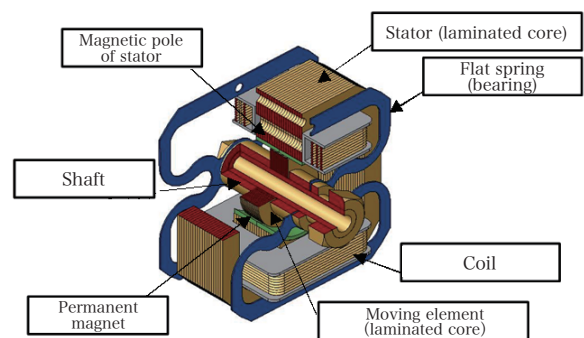


Fig. 16 Operating principle of the actuator (inner type)

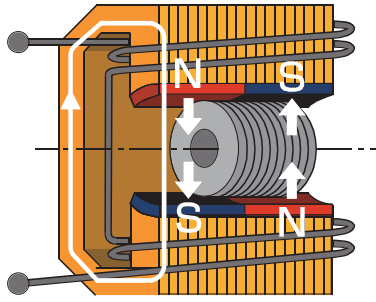


Fig. 17 Magnetic fluxes of the magnet

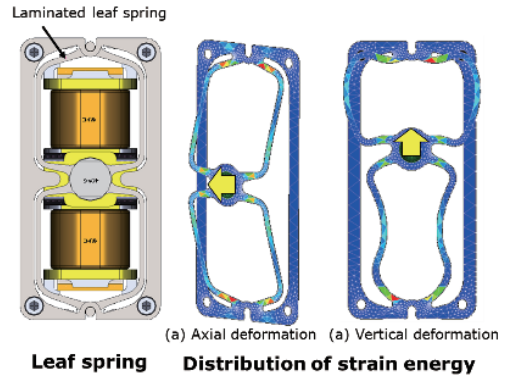


Fig. 20 Structure of the leaf spring for supporting the moving element

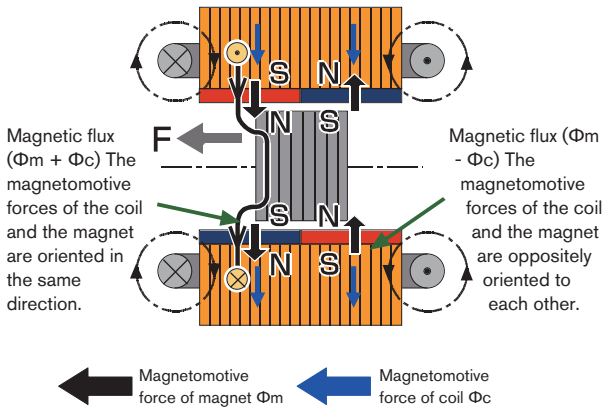


Fig. 18 Principle of control force generation by the magnetic fluxes of the magnet and the coil

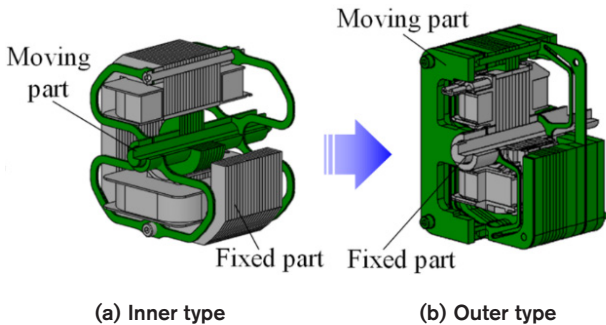


Fig. 19 Inner and outer types of moving elements

An optimally shaped leaf spring was devised after thoroughly analyzing the structure and mechanism in order to set a lower axial natural frequency for the moving element; this strongly affects the control and sets the natural frequency of pitching beyond the control frequency. Using this approach, the intended layout for important modes was realized by utilizing the anisotropic stiffness, although the yaw mode that does not affect the control was within the control frequency range (Figs. 20 and 21). As shown in Fig. 21, the stiffness in the vertical direction was increased to bring the pitching resonance of the moving element to the high-frequency side, while also lowering the stiffness in the depth direction.

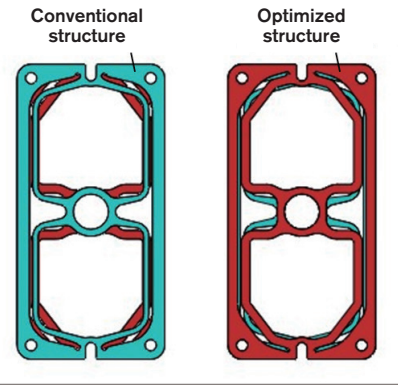


Fig. 21 Optimization of the leaf spring structure (realization of anisotropic stiffness)

### 3.2 Damping control of the rod

The resonance amplitude of the torque rod can be reduced by applying a control force that is proportional to the vibration velocity of the torque rod by using the actuator.

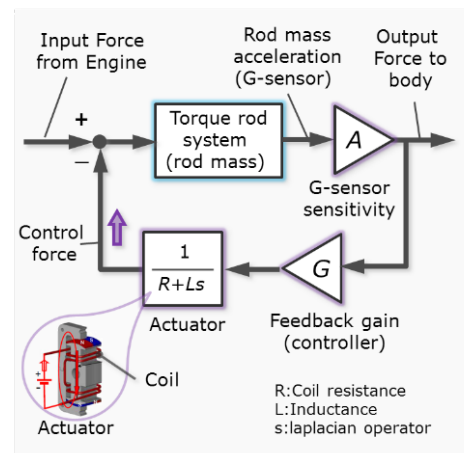


Fig. 22 Incorporation of the integrating function into the actuator

Typically, velocity is obtained using a speed sensor or by integrating the acceleration with a controller. However, the former approach leads to upsizing and increases the cost, whereas the latter method decreases controllability owing to the calculation delay or constrains the control frequency. In this work, the coil for the actuator was emphasized. The current output characteristics of the coil with respect to the voltage input exhibit a simple integrating function at or above a certain frequency. By sensing the acceleration of the torque rod and inputting it as a voltage to the coil, a control that automatically becomes proportional to the velocity was realized without using a controller.

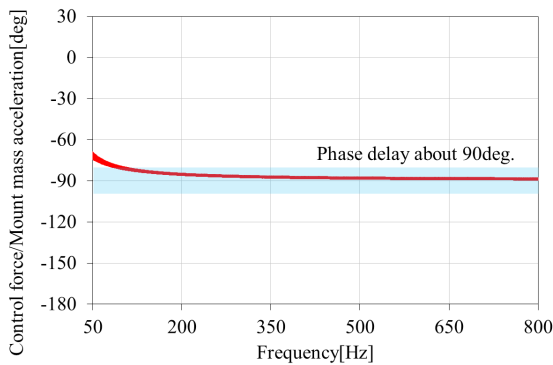


Fig. 23 Frequency range for 90° phase lag in the acceleration sensor output

#### 4. Reliability of the technology

As described above, the support stiffness of the torque rod was realized by utilizing the stiffness of the engine-side insulator, and the rigid-body natural frequency of the torque rod was reduced by utilizing the stiffness of the vehicle-side insulator. Ideally, only the axial natural frequency of the torque rod should be decreased. However, as the stiffness in other directions decreased, the pitching mode of the torque rod decreased as well (Figs. 24 and 25). As the actuator can only control the axial direction, the vibration characteristics of the torque rod must be designed such that they do not create practical issues.

The vertical excitation force of the vehicle caused by the reciprocal inertial force of the engine significantly excites the pitching mode of the torque rod. The VCR engine with the optimized link geometry can nullify the vertical force to a greater extent than balance-shaft-equipped engines. However, as it was difficult to perfectly match the vector of the exciting force caused by the rolling vibration of the engine in the axial direction of the torque rod, measures were implemented to prevent the pitching mode of the torque rod from being excited. First, a moderate damping force was added to the vehicle-side insulator to suppress the pitching resonance. Furthermore, a sensor installation position that would prevent the sensor from incorrectly identifying the generated pitching vibrations as the vibrations at the front and rear of the torque rod was determined (Fig. 24).

Next, the important factors were identified by developing an equation for the pitching mode using the major dimensions of the rod. As the center distance of the torque rod varies according to the preload of the engine, the most complicated aspect of the equation that expresses the pitching amplitude is that it is a nonlinear equation of the preload function. Subsequently, optimization analysis was conducted by performing numerical analyses of the developed equation; this involved employing the moment of inertia ( $I$ ) and mass ( $m$ ) of the torque rod and the distance from the center of gravity of the torque rod to the installation points of the engine and the body ( $a$  and  $b$ ) as variables. By satisfying the relationship  $l = m \cdot a \cdot b$  under any load condition as a basic concept, an insulator shape that achieved the target dynamic spring constant was identified (Figs. 26 and 27).

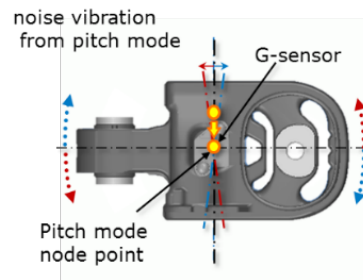


Fig. 24 Installation position of the acceleration sensor

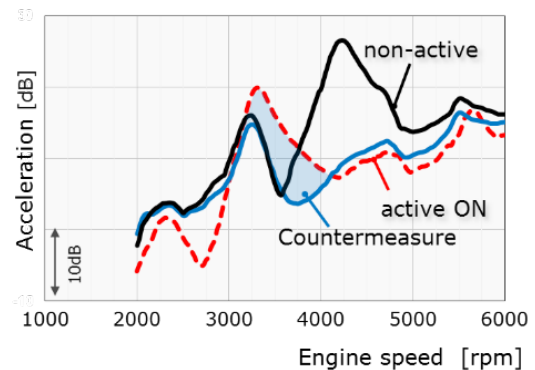


Fig. 25 Reduction of rod vibration via appropriate installation of the acceleration sensor

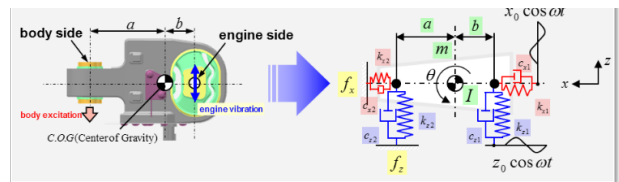


Fig. 26 Torque rod vibration model for pitching vibration calculation

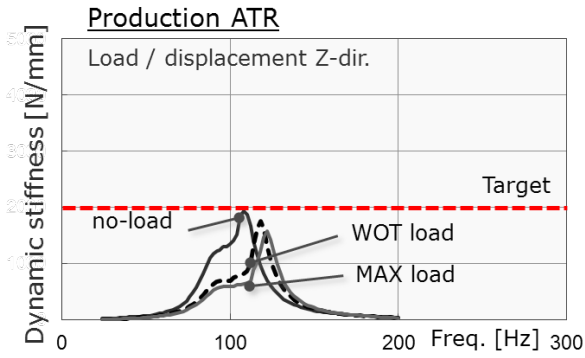


Fig. 27 Load-specific frequency characteristics of pitching dynamic stiffness

As the control detects the vibration velocity of the rod to provide a damping force, the damping force can be flexibly applied even if the resonance frequency of the rod varies owing to the engine load, thus confirming that this control system is robust.

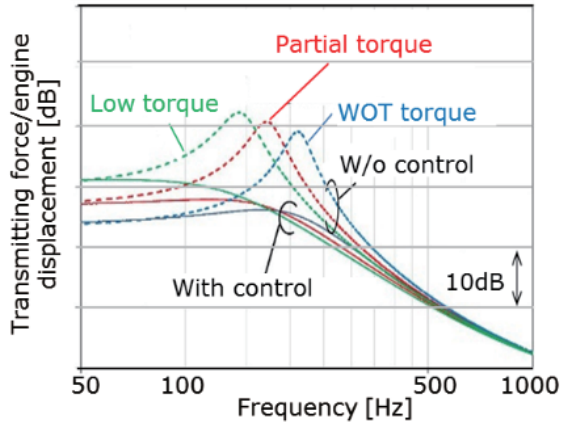


Fig. 28 Robustness of the control with respect to engine load

## Recipients



Masahiko Kondo



Koji Tanimura



Ryosuke Yamauchi



Yuta Oana

## Awards

### 2020 JSAE Award The Technological Development Award

Masahiko Kondo    Koji Tanimura    Yuta Oana

### 2019 JSME Medal for New Thecnology

Masahiko Kondo    Koji Tanimura    Ryosuke Yamauchi



# Development of New-generation e-POWER Hybrid Powertrain

Naoki Nakada\* Tomoyuki Hanyu\* Makoto Kimura\*

**Abstract** We developed a new powertrain, called e-POWER, for the new Nissan NOTE to provide the pleasure of a motor-drive experience for larger numbers of customers. The drive motor (e-Motor) and control system were originally developed for the Nissan LEAF electric car. The newly developed e-POWER Drive mode provides a new driving experience for customers. In this mode, the driver can easily control the vehicle speed just by operating the accelerator pedal alone.

## 1. Introduction

e-POWER is a new electric power train that was developed in Nissan’s electrification program, which forms one axis of the company’s technology strategy. It was developed for application to compact cars and is mounted on the latest generation of the NOTE. This article explains the development aims set for e-POWER, presents an overview of the system, and describes its design and the newly developed e-POWER Drive mode.

## 2. Development Aims

The Nissan LEAF pure electric vehicle that was released in 2010 has continued to evolve through extension of its driving range and improvement of driveability, among other attributes. Cumulative global sales have reached more than 200,000 units. The Nissan LEAF is highly acclaimed for its excellent driving performance achieved with a motor-drive system. It takes advantage of the drive motor (e-Motor)’s ability to generate maximum torque from a vehicle speed of 0 km/h and to generate driving force directly at a fixed gear ratio over a wide range of vehicle speeds. The e-POWER powertrain was developed with the aim of providing this outstanding driving experience to larger numbers of customers. To accomplish that, it was developed for application to the compact car class in terms of both cost and packaging.

## 3. Overview of e-POWER

### 3.1 System configuration and principal specifications

Classified as a series hybrid, one of e-POWER’s most significant features is that the drivetrain system and power generation system are mechanically separated. The system configuration is shown in Fig.1. The e-POWER system is controlled by the vehicle control module (VCM), which is linked to the motor controller (MC), generator controller (GC), battery management system (BMS) and the engine control module (ECM). VCM performs energy management and driving force control at all times through optimal power generation.

The distinct feature that the drivetrain system and power generation system are mechanically separated provides the following significant advantages. (1) EV technologies can be shared for the basic components and control of the drivetrain system, and all driving force can be generated by the e-Motor. (2) The speed and torque of the engine used for power generation can be set flexibly regardless of the operating state of the vehicle. The first advantage enables the provision of excellent driving

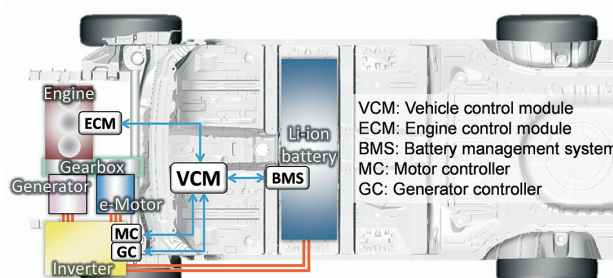


Fig.1 Configuration of e-POWER system

\*Powertrain and EV Project Management Department

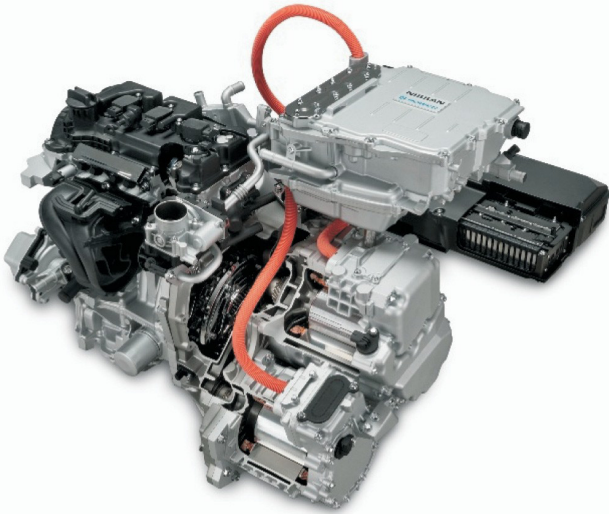


Fig.2 Appearance of e-POWER

Table 1 Specifications of e-POWER components

Drive system	Motor power	80 kW
	Motor torque	254 Nm
Generating system	Generator power	55 kW
	Engine type	Gasoline L3
	Engine displacement	1.2 L
Battery	Type	Li-ion
	Capacity	1.47 kWh

performance obtained with the same motor drive as that of an EV. The second advantage enables fuel economy to be improved by operating the engine at the point for the best fuel economy, and it also allows engine operation advantageous for noise, vibration and harshness (NVH) performance. The appearance of e-POWER is shown in Fig.2, and the major specifications of the constituent units are listed in Table 1.

The maximum motor power and torque specifications are the same as those of the current Nissan LEAF. Figure 3 compares the acceleration characteristics of the NOTE e-POWER system and two other types of hybrid vehicles A and B. It is seen in the figure that the NOTE e-POWER system provides better acceleration response than the other types of hybrid vehicles A and B. Acceleration G rises quickly to provide smooth acceleration, like the performance of the Nissan LEAF.

The power generation system consists of an internal combustion engine (ICE) modified specifically for power generation use combined with a generator. The engine was developed based on the HR12DE engine mounted on ICE-powered NOTE models. The battery is of the lithium-ion type. A high-output type was adopted to provide quick acceleration response. The e-Motor, generator and inverter have an independent water cooling system separate from that of the engine. The Li-ion battery has a dedicated air cooling system provided inside the battery pack.

### 3.2 Packaging

Figure 4 shows the in-vehicle layout of the e-POWER system including the battery pack. The gearbox houses two gear trains within one package; one serving as the motor-drive reducer and the other as the multiplier for engine-based power generation. The drivetrain system and the power generation system including the engine are integrally assembled via the gearbox. The inverter is attached to the vehicle body as a separate unit from the powertrain. It is connected to both the e-Motor and the generator via a three-phase wiring harness.

The battery pack features a compact design, enabling it to be positioned below the front seats. This position does not affect the occupant space and allows virtually the same cabin space and luggage area as the ICE-powered NOTE models. In addition, positioning the battery inside the frame shared with the ICE-powered models achieves both protection for the high-voltage components and occupant safety without adding any new frame parts. This made it possible to mount e-POWER on the compact B-segment platform of the NOTE.

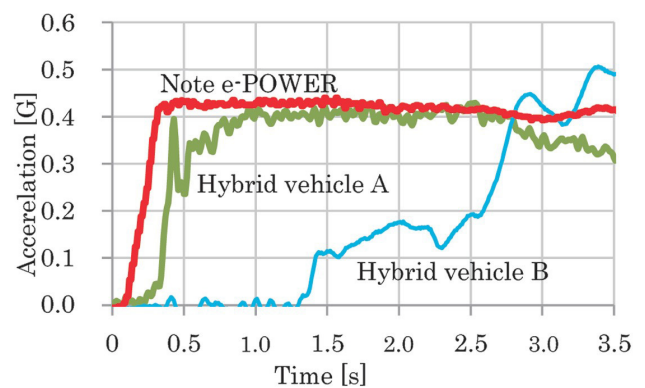


Fig.3 Acceleration G at standing start (wide open throttle, WOT)

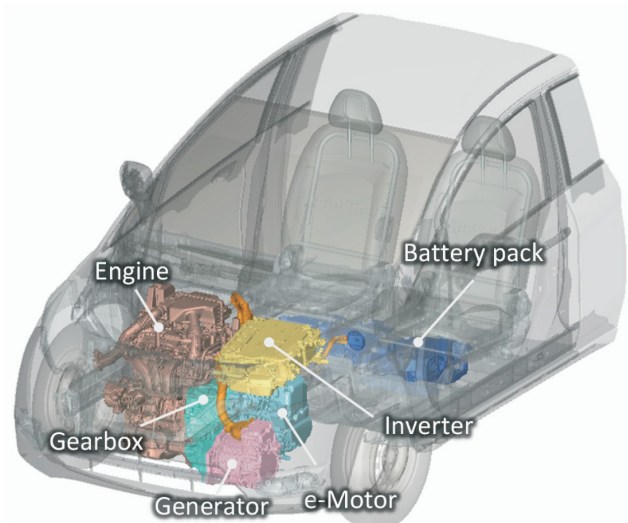


Fig.4 In-vehicle layout of e-POWER system

### 3.3 Configuration of e-POWER control system

The basic concept for the e-POWER system configuration was to add an engine as the energy source for power generation and a generator, thereby enabling the battery capacity to be reduced and the battery charger to be discontinued. This is in contrast to an EV that is configured with an e-Motor, an inverter, a Li-ion battery and a charger. The structure of the control system designed on the basis of this concept is shown in Fig.5 in comparison with that of the Nissan LEAF.

In this comparison of control system structures, in order to replace the Nissan LEAF's charging system with a power generation system, the on-board charger (OBC) was discontinued and replaced with the ECM and GC. The drivetrain system has the same control configuration as that of the Nissan LEAF. The structure of this control system shares the motor-drive technology and components honed with the Nissan LEAF.

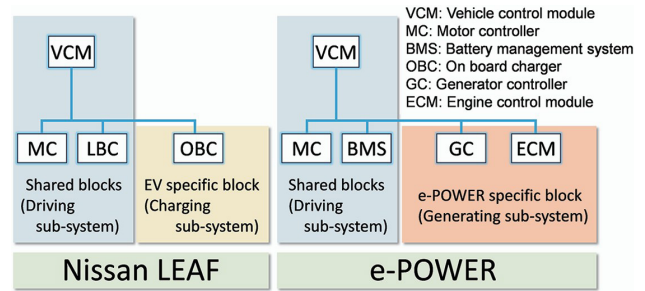


Fig.5 Comparison of control systems

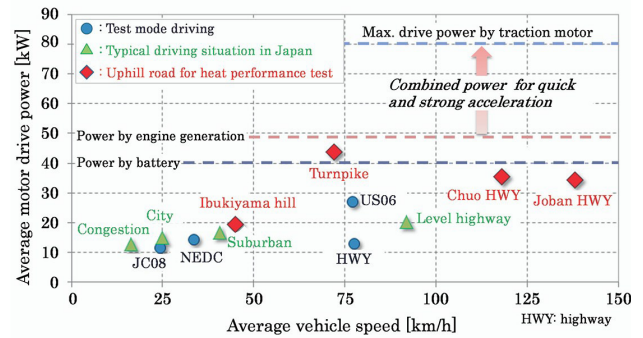


Fig.6 Energy consumption and power generation balance

## 4. System Design

### 4.1 Basic system design concept

The e-POWER system has the ability to propel the vehicle on the power provided only by the Li-ion battery in typical driving situations (blue and green points in Fig.6). The system is designed such that power for propelling the vehicle is also supplied by the generator under continuous high-load operation such as when traveling on mountain roads, among other situations (red points in Fig.6). Combining the power supplied by the Li-ion battery and that of the generator delivers powerful acceleration like that of the Nissan LEAF.

### 4.2 Top-level fuel economy

Figure 7 shows the fuel consumption rate of the HR12DE engine used in the e-POWER system and the frequency of engine operation in the practical fuel economy mode (representative of customers' driving style in real-world driving). The fact that the drivetrain system and the engine are completely separated is used effectively to select the operating point for the best fuel economy within the allowable range for various requirements. These include power performance, driveability, NVH, emissions, heat, cabin heating, brake negative pressure, parts protection and diagnosis, among others. For that purpose, the VCM calculates the target performance for each component. As a result, e-POWER operates at the point of the best fuel economy (near 2400 rpm and 70 Nm) with an overwhelmingly high frequency compared with other vehicles in this class.

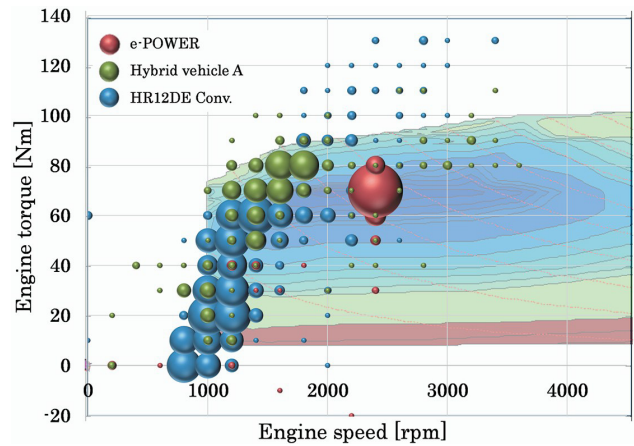


Fig.7 Operating point for real-world fuel economy (Nissan's definition)

### 4.3 EV-like quietness

To ensure EV-like quietness, the EV-mode driving region, i.e., operation on power supplied by the Li-ion battery alone, has been defined to encompass the low- to medium-speed range where vehicles are frequently driven in the Japanese market. In addition, it has also been defined wider than that of other hybrid vehicles (Fig.8). Moreover, in the high-speed region as well, EV-mode driving is continued as long as possible when the battery state of charge (SOC) is high. When the SOC falls, power is generated to charge the Li-ion battery to the extent that engine noise does not become overly conspicuous, which is a measure taken against noise.

Figure 9 shows the share of EV-mode driving in each vehicle speed range for typical driving modes used by customers in the real world, including driving on city, mountain, congested and high-speed roads, among other

situations. EV-mode driving accounts for a high percentage of the driving time, for approximately 90% at speeds below 25 km/h and for approximately 50% in the medium- to high-speed range.

#### 4.4 Engine speed suitably designed for various driving situations

Figure 10 shows the target engine speed designed to match the vehicle speed and acceleration G. In all vehiclespeed ranges, the engine speed is designed to remain near 2400 rpm as much as possible for excellent fuel economy. When the driver presses the accelerator pedal hard, the engine speed is designed to rise to a high level to match the increase in vehicle acceleration. In addition, in the high-speed range where large power is needed for acceleration, the engine speed is held high in preparation for the next acceleration event.

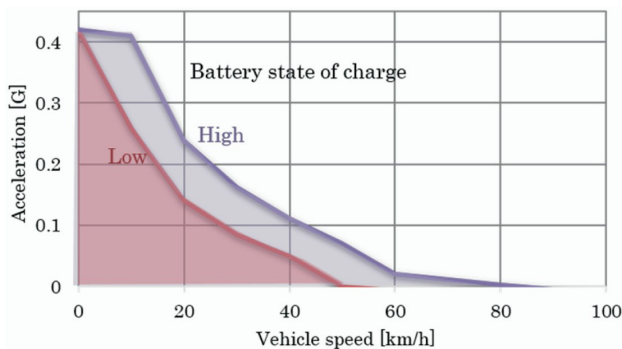


Fig.8 Scope of EV driving depending on vehicle speed and battery state of charge

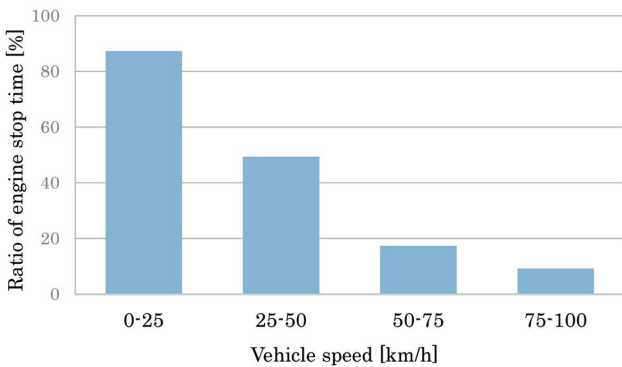


Fig.9 Ratio of engine stop time (EV time) in each vehicle speed range

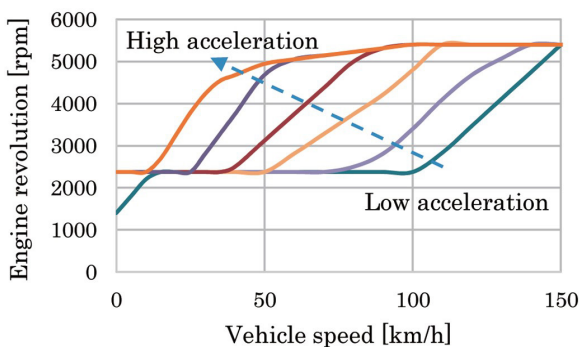


Fig.10 Target engine speed

## 5. e-POWER Drive Providing a New Driving Feel

A new drive mode has been defined that takes advantage of the e-Motor used as e-POWER's only source of motive power. Called e-POWER Drive, this mode combines a new strong power regeneration system, slope assist, slip-suppression control on low- $\mu$  surfaces and other advanced features intended to appeal to customers. The following sections explain the control procedures and their effects in this drive mode.

### 5.1 New driving style provided by e-POWER Drive

Approximately 90% of real-world driving can be done in the e-POWER Drive mode by just operating the accelerator pedal alone, thus providing a new driving style. This requires the provision of the following two elements. (1) Coasting torque generated by the driver's operation of the accelerator pedal must be designed for decelerating the vehicle. (2) It must be easy to control deceleration until the vehicle stops.

With regard to the first element of designing coasting torque, effective use is made of the design flexibility that is one strength of e-Motor propulsion. As shown in Fig.11, that makes it possible to cover more than 90% of the deceleration events that occur in real-world driving. As a result, operation of the accelerator pedal alone provides sufficient deceleration, thereby reducing the need to switch the foot to the brake pedal to depress it when decelerating the vehicle.

As for the second element of easy control of deceleration, an analysis was made of drivers' operations when decelerating by operating the accelerator pedal. The results revealed three patterns that were focused on. One is operation by ankle motion to produce slight acceleration

when following a preceding vehicle. Another is accelerator pedal operation by using knee action to produce deceleration for stopping at intersections, for example. The third one is to lift the foot off the accelerator pedal to decelerate when the distance to a preceding vehicle is too close. As shown in Fig.12, these operating patterns are combined with the driver's demanded deceleration to achieve easy control of deceleration with e-POWER Drive through operation of the accelerator pedal alone, similar to deceleration of an ICE-powered vehicle by depressing the brake pedal.

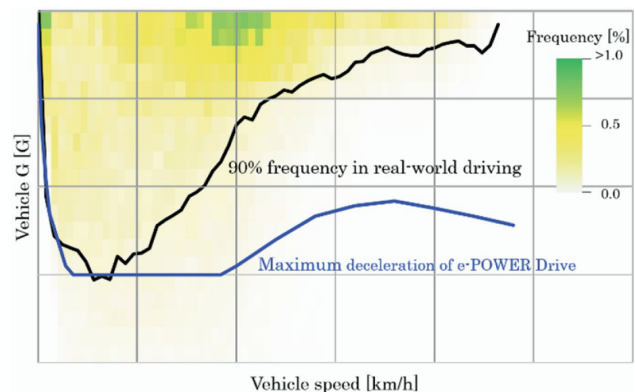


Fig.11 Real-world deceleration frequency and deceleration G characteristic of e-POWER Drive

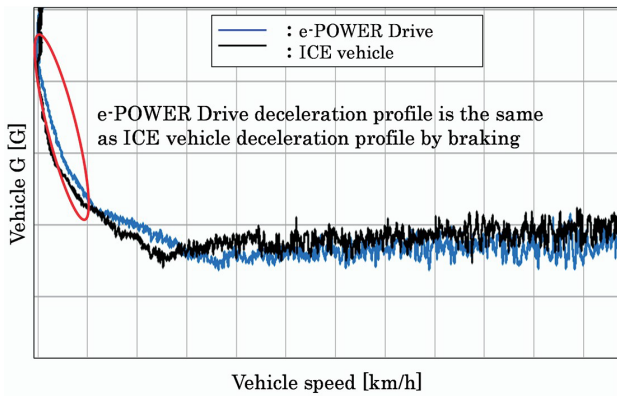


Fig.12 Deceleration profiles

The neutral position of the accelerator pedal with acceleration of 0 km/h was designed on the basis of the concepts noted below. This achieves the three points of easy control of acceleration/deceleration, ease of steady-speed driving, and little feeling of fatigue when continuing to depress the accelerator pedal.

- Acceleration pedal ef for t allowing a stable driving posture when accelerating.
- A sufficient accelerator pedal angle for controlling deceleration.
- Attaining a natural acceleration pedal angle when depressing the accelerator pedal.

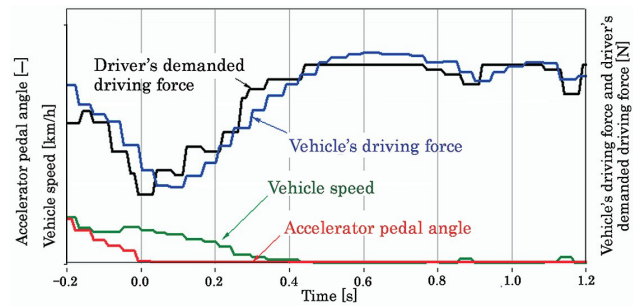
To further enhance its attractiveness, slope assist control, slip-suppression control on low- $\mu$  surfaces, and gliding control were also incorporated in e-POWER Drive.

## 5.2 Various control features supporting e-POWER Drive

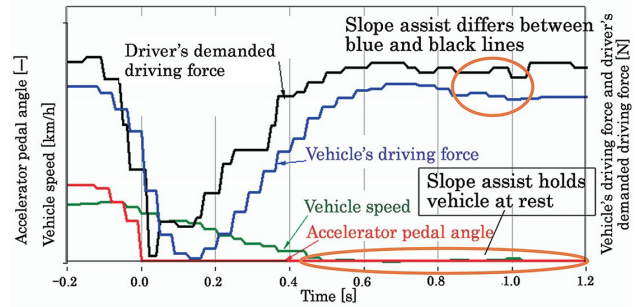
### 5.2.1 Slope assist control

The driving force control system detects constantly changing road surface information, estimates the slope on that basis, and provides torque compensation. This feature is called slope assist control. This control enables the vehicle to be launched and stopped on uphill/downhill slopes with the same operation of the accelerator pedal as on flat road. On downhill slopes in particular, deceleration may be insufficient if torque compensation control is not performed, thus requiring operation of the brake pedal for controlling the vehicle speed. However, with this control feature, the vehicle speed can be controlled by operating the accelerator pedal alone up to a downhill slope of -3%.

Figure 13 shows the effect of this slope assist control. The results in (a) show that the driver's demanded driving force and the vehicle's driving force coincided, resulting in zero vehicle velocity and the vehicle stopped. These results are for complete release of the accelerator pedal on a flat road. In contrast, the results in (b) are for complete release of the accelerator pedal on a -2% downhill slope. Owing to slope assist control, the vehicle's driving force was smaller than the driver's demanded driving force (due to torque matching with the slope), resulting in zero vehicle velocity.



(a) On flat road



(b) -2% downhill slope

Fig.13 Experimental results for effect of slope assist

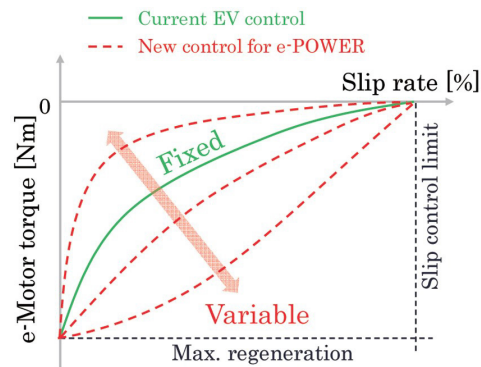


Fig.14 Slip rate-coasting torque characteristic

### 5.2.2 Slip-suppression control low- $\mu$ road surfaces

The e-POWER Drive mode provides larger coasting torque than the Nissan LEAF, so the control system was improved to maintain stability on low- $\mu$  road surfaces. Specifically, as shown in Fig.14, the previous system limited coasting torque according to the slip rate. The e-POWER Drive mode uses a reference model to vary the coasting torque even at the same slip rate so that it matches the change in the slip rate. As shown in Fig.15, this improved control procedure provides stable deceleration even in cases involving larger deceleration than that of the Nissan LEAF.

### 5.2.3 Gliding control

Repeated acceleration/deceleration by slight operation of the accelerator pedal causes charging/ discharging of battery power. Attention was focused on improving fuel economy by eliminating these tiny conversions of energy. Specifically, the system detects the desire for slight deceleration in steady-speed driving, such as when following a preceding vehicle, based on the driver's operational inputs and vehicle data and makes the motor torque 0 Nm. This control suppresses wasteful charging/ discharging of battery power and also suppresses unnecessary deceleration, which leads to improved fuel economy. It has the effect of improving fuel economy by approximately 3-4% in real-world city driving compared with that without the control. Figure 16 shows the difference in the frequency of a 0-Nm increase in e-Motor torque with/without gliding control.

As described here, the e-POWER Drive mode was achieved through the coasting torque design, which takes advantage of the design flexibility that is one strong point of motor drive, and the addition of various control features. This drive mode delivers a new driving feel and improved fuel economy in the new-generation NOTE.

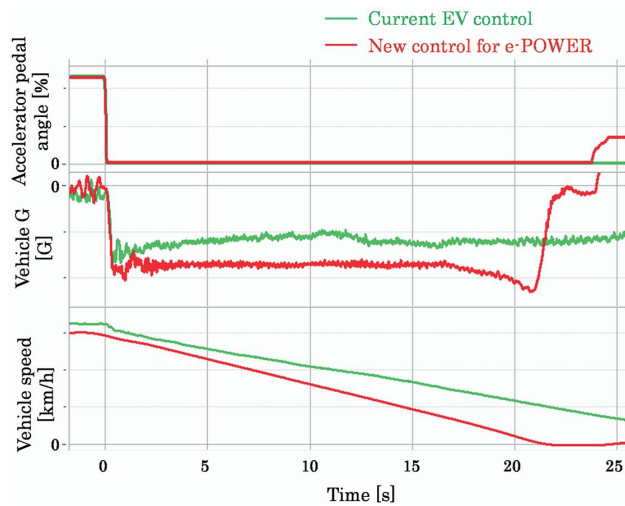


Fig.15 Deceleration G profile on low- $\mu$  surface

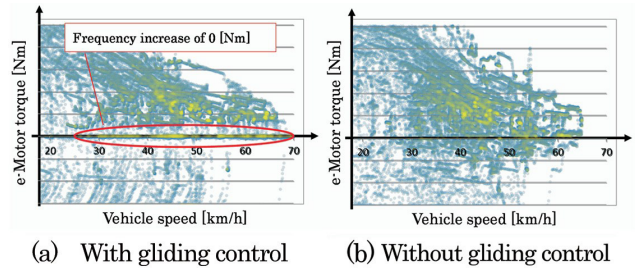


Fig.16 Operating point for e-Motor torque

## 6. Conclusion

The e-POWER system was developed and implemented on the new NOTE with the aim of enabling larger numbers of customers to enjoy an excellent driving experience based on the features of motor drive. Toward that end, the drive system shares the same control system structure and motor drive control technology and parts with the Nissan LEAF. In addition, the e-POWER Drive mode that facilitates driving just by operating the accelerator pedal alone provides a new driving feel, thanks to its easy control of vehicle acceleration/deceleration.

Finally, the authors would like to thank everyone involved within and outside Nissan for their invaluable cooperation with the development of the new e-POWER electric powertrain.

### References

- 1) S. Nakazawa et al.: The Nissan LEAF electric powertrain, 32nd International Vienna Motor Symposium (2011).
- 2) H. Shimizu et al.: Development of an integrated electrified powertrain for a newly developed electric vehicle, SAE Paper No. 2013-01-1759 (2013).
- 3) T. Nakada et al.: The New Electric Powertrain on the 2013 MY Nissan LEAF, 34th International Vienna Motor Symposium (2013).
- 4) Y. Fukunaga et al.: Development of a Highly-Responsive Acceleration Control for Nissan LEAF, Nissan Technical Review, No. 69/70, pp. 16-20 (2012).

## Recipients



Naoki Nakada



Tomoyuki Hanyu



Makoto Kimura

## Awards

2020 The Ichimura Prize in Industry for Distinguished Achievement

2019 World New Energy Vehicles Congress Global NEV Innovative Technology Award"

# Development of World First Mass Production Variable Compression Ratio Engine

Shuji Kojima\* Shinichi Kiga\* Katsuya Moteki\*  
Kazuya Matsuoka\* Yoshiaki Tanaka\*

## 1. Introduction

The variable compression ratio (VCR) refers to the compression ratio of an engine changed according to driving scenarios to meet the universal needs of engines, combining good thermal efficiency and high power. However, the practical use of this idea has not been realized due to the complexity of the mechanism and its control. The variable compression turbo (hereinafter referred to VC-Turbo) engine (model: KR20DDET) introduced here is the first mass production VCR engine. It achieves both fuel economy and output performance at high levels with its unique VCR system and supercharged downsizing technology.

## 2. Purpose of development and effect in performance

Fuel economy- and power-oriented engines have higher and lower compression ratios, respectively (left side of Fig.1).

This technology variably controls the compression ratio according to the driving conditions of the vehicle. Therefore, a higher compression ratio is achieved for higher thermal efficiency when driving in city roads, where better fuel economy is required; lower compression ratio is temporarily achieved by avoiding a high pressure of combustion chambers, due to supercharging for safe vehicle acceleration, when deeply pressing the accelerator pedal for explosive high power, such as an entry to an expressway or during overtaking (right side of Fig.1). The VC-Turbo engine has only 2.0 L of displacement, but realizes high torque, exceeding a V6 3.5-L engine, as shown in Fig.2, with high supercharging at a compression ratio of 8. Furthermore, as a result of downsizing (from 3.5 to 2.0 L of displacement; from six to four of cylinder count) and improvement of the thermal efficiency due to a compression ratio of 14, the fuel economy in actual traffic is improved by 27% in comparison with a V6 3.5-L engine (Fig.3). In addition, as the covered operation range is extended from low to high output compared with existing engines with fixed compression ratios, the flow-rate ranges of fluids (air, fuel, lubricant, and coolant) passing/circulating through an engine are also extended.

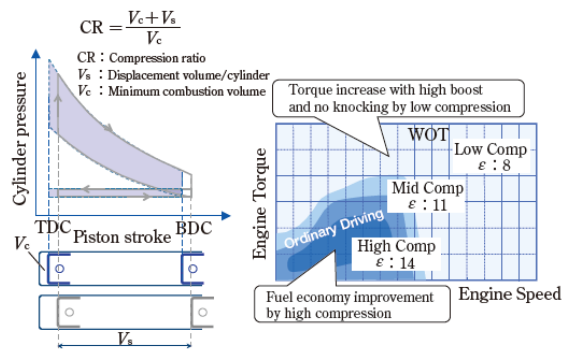


Fig.1 Concept of performance improvement with VCR

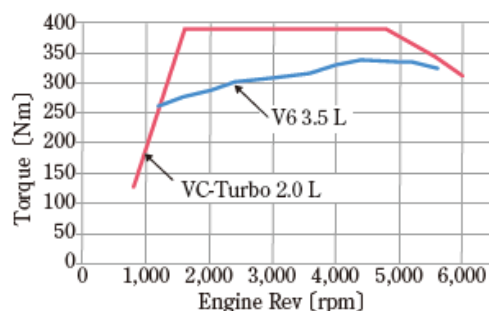


Fig.2 Torque curve of VC-Turbo engine

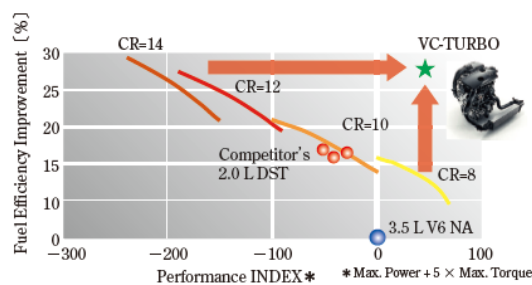


Fig.3 Performance advantages of VCR

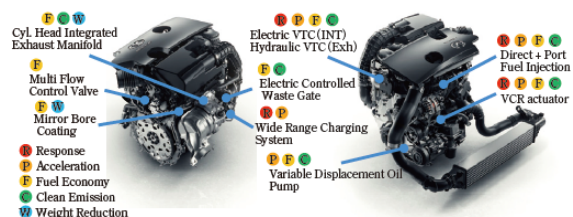


Fig.4 Primary technological items installed to VC-Turbo engine

\*Powertrain and EV Project Management Department

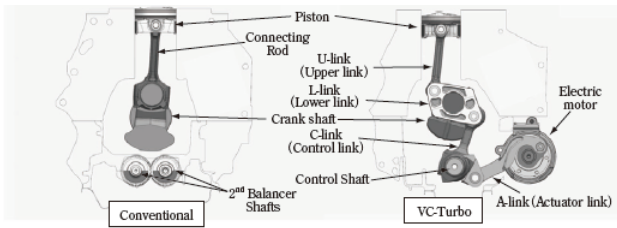


Fig.5 Arrangement of multilink mechanism

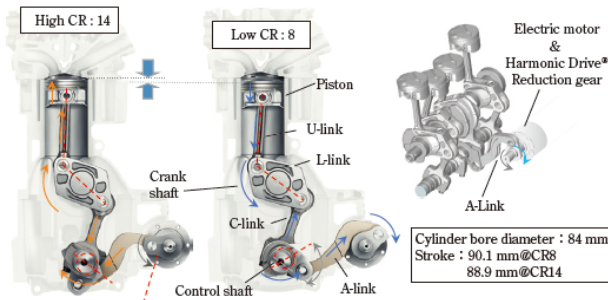


Fig.6 Compression ratio changing method

Accordingly, to synergistically enhance the performance using VCR, it is equipped with technological aspects such as electric valve timing control (VTC), a wide-range turbocharger with an electronically-controlled waste gate, a fuel injection system using both direct and port injections, a variable displacement oil pump, and a coolant passage changeover valve (Fig.4).

### 3. System configuration and features

#### 3.1 Multilink mechanism and compression ratio changing method

In the VC-Turbo engine, a conventional crank mechanism (hereinafter referred to “conventional mechanism”) is replaced with a unique multilink mechanism (Fig.5). Its compression ratio is simultaneously adjusted in all cylinders by changing/maintaining the rotational attitude of a control shaft with an eccentric shaft (Fig.6). The rotational attitude of the relevant shaft is controlled by a compression-ratio controlling actuator composed of an electronically-controlled electric motor and a small-sized, highly-reduced, and silent strain wave reduction gear set by Harmonic Drive® Systems Inc., according to engine operation conditions.

#### 3.2 Characteristic piston stroke

The piston movement of the conventional mechanism becomes fast at the top dead center and slow at the bottom dead center due to the oscillation of the connecting rod. The imbalance causes inertial second-order oscillation.

In this mechanism, inertial second-order oscillation due to the oscillation of the U-link corresponding to the

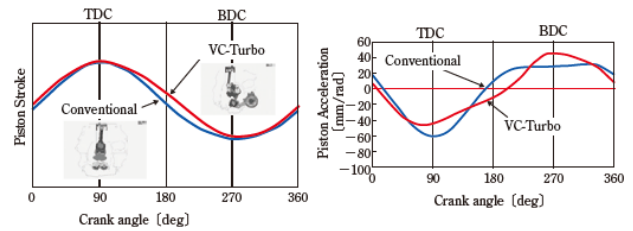


Fig.7 Piston movement of VC-Turbo and existing engines

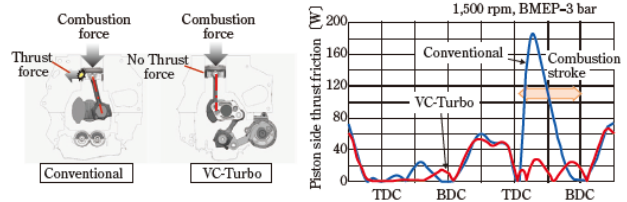


Fig.8 Piston-side thrust friction of VC-Turbo and existing engines

connecting rod of the conventional mechanism is almost canceled by antiphase inertial second-order oscillation due to another inverted oscillating link (C-link) to reduce the imbalance described above (Fig.7). This eliminates the need for a second-order balancer, which has been used in an inline four-cylinder engine with the conventional mechanism as a measure to avoid booming noise.

#### 3.3 Friction control effect

In this mechanism, the U-link just below the piston maintains an almost upright attitude during the descent of the piston. In this process, the combustion pressure acts on the piston so that a load in its lateral direction decreases, and the friction generated in that area also drastically reduces (Fig.8). This cancels an increase in friction caused by more bearing points due to multilink mechanism application, resulting in the achievement of a friction level less than or equal to that of the conventional mechanism.

### 4. Summary

The VC-Turbo engine accelerated the evolution of the automotive-engine crank mechanism, unchanged since the nineteenth century, into a unique multilink mechanism and established the first mass production VCR engine in the world. It provides the maximum potential of supercharging output performance while significantly improving fuel economy performance. The mass production of this engine should accelerate the pursuit of thermal efficiency, which has been restricted due to contradictions with output performance, and diversify applied fuel types, which has been restricted by compression ratios. This engine is expected to extend the potential of internal combustion engines in the future.

#### Source

公益社団法人自動車技術会  
自動車技術  
Vol.73NO.6 文献番号:20194478



## Recipients



Shuji Kojima



Shinichi Kiga



Katsuya Moteki



Kazuya Matsuoka



Yoshiaki Tanaka



Eiji Takahashi

## Awards

### 2019 JSPMI Prize

Shinichi Kiga   Shuji Kojima   Katsuya Moteki   Kazuya Matsuoka   Yoshiaki Tanaka

### 2019 JSAE Award The Technological Development Award

Katsuya Moteki   Shinichi Kiga   Shuji Kojima   Kazuya Matsuoka   Yoshiaki Tanaka

### 2018 The Combustion Society of Japan Award

Shuji Kojima   Shinichi Kiga   Katsuya Moteki   Kazuya Matsuoka   Eiji Takahashi

### 2018 JSME Medal for New Thecnology(Japan Society of Mechanical Engineers)

Shinichi Kiga   Shuji Kojima   Katsuya Moteki   Kazuya Matsuoka   Eiji Takahashi



# Analysis of relationship between self-excited oscillation and coulomb friction in spool of electro- magnetic proportional valve and design method for stabilization

Katsuhiko Sando\*

**Abstract** This paper describes self-excited oscillation caused by coulomb friction of electromagnetic proportional valve. Especially, this research focuses on a hydraulic system in which electromagnetic proportional and pressure proportional valves are located tandem. In the system, the coulomb frictional force effects on the displacement direction of the spool of the former valve and the piston is established in the downstream region of the latter valve. Each valve is stable, but, the connection of them causes instability. This paper analyzes the mechanism of this unstable vibration and then investigates an anti-vibration design method. In analysis, this paper clarifies that vibration is caused by an elastic deformation delay of the oil in the piston. This delay increases the phase delay of the spool due to the coulomb frictional force. After replacing the coulomb frictional force with hysteresis, the proposed method uses the describing function method to express phase delay phenomenon due to the coulomb frictional force. The describing function is the complex function which expresses an amplitude ratio and phase difference with the input and output of nonlinear element. The delay of a vibration factor is linearized by converting coulomb friction into hysteresis. The effectiveness of the proposed method is demonstrated via practical experiment and non-linear simulation results.

## 1. Introduction

Control using a pressure valve and a cylinder is applied to various sections in construction machinery, automobiles, and other applications, because it provides a smaller size and larger force generation. Typical examples include engine valve-timing control (Toyoda, Tanaka in 2006) and CVT shifting control (Wakahara and others in 2005). The associated instability of this pressure valve has motivated several studies (Kumagai and others in 2014), and its design method is also used widely.

In recent years, to downsize hydraulic systems and reduce their losses, another pressure valve has been placed in the downstream section of the pressure valve to amplify the control pressure to a cylinder. This combination of two pressure valves and one cylinder is also a factor to cause instability to the system, and the occurrence of unstable vibrations has been reported. However, there are few examples covering the design method of combined pressure valves, and the mechanism of such vibration phenomenon is not yet clear. This study focuses on a problem in which a stable pressure valve as a single part becomes unstable after incorporated into a hydraulic system. This problem is a vibration phenomenon due to combination, and it is empirically well-known that there is a Coulomb frictional force acting on the spool of a pressure valve. The practical issue is that a minimum Coulomb frictional force to prevent such vibration cannot be theoretically predicted. Accordingly, this study will elucidate the principle of unstable vibration due to Coulomb frictional force and report the results of the evaluation of a design method for stabilization.

An issue to be addressed for elucidating the mechanism is to clarify how the Coulomb frictional force, which

should lead to a damping factor in general, leads to a destabilizing factor in a combined state. Thus, an issue for a design method is to manage the strong nonlinear characteristics of the Coulomb frictional force. In a linear model analysis based on the existing knowledge, the Coulomb frictional force is expressed as a constant by which a speed term is multiplied. Therefore, the analysis of the destabilization only using a linear model is difficult because the characteristics caused by the Coulomb frictional force cannot be completely represented.

In this study, three methods of experiment, nonlinear simulation, and stability analysis were applied to manage and check for any problems and verify the conformity of vibration frequencies and the conditions of unstable vibration occurrence among the methods. Details are described below.

## 2. Hydraulic circuit and experimental results

Figure 1 illustrates the structure of a hydraulic circuit. The function of this hydraulic system is to regulate the internal pressure of the hydraulic cylinder to control the piston. The hydraulic circuit has a structure commonly applied, in which an inflow-throttling pressure proportional valve is placed in the downstream of an electromagnetic proportional valve, and a piston is placed in the downstream of this valve. As a larger thrust is necessary for controlling the spool of the pressure proportional valve, by utilizing supplied oil pressure and providing the electromagnetic proportional valve in the upstream section instead of adding a solenoid to the pressure proportional valve, a smaller thrust can be used to control the larger pressure. To adjust the internal pressure of the hydraulic cylinder, an electric current is applied to the solenoid to generate a thrust and control

\*Powertrain and EV Advanced Technology Department

the spool of the electromagnetic proportional valve to adjust the discharge pressure. Then, the discharge pressure of the electromagnetic proportional valve controls the spool of the pressure control valve placed at the tip.

In this structure, unstable vibration can be measured experimentally with a section into which an/ a stable electromagnetic proportional valve is incorporated as a single part. The results are shown in Fig.2. An input applied in this case is an external force from the piston side. flow is opposite, from the downstream to the upstream side, and the flow rate is small compared to the piston volume. The pressure sensor is placed between the piston and the pressure proportional valve. The results show that the pressure in the downstream section of the pressure proportional valve vibrates at a frequency of 8 to 10 Hz.

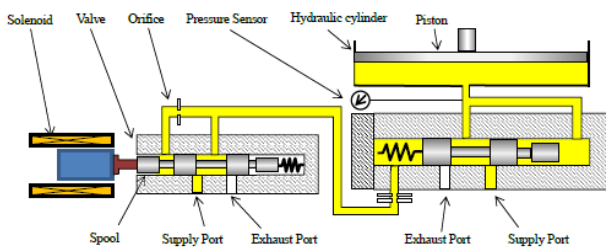


Fig.1 Analysis model of the self-excited vibration valve system. An electromagnetic proportional valve and pressure proportional valve are arranged in series.

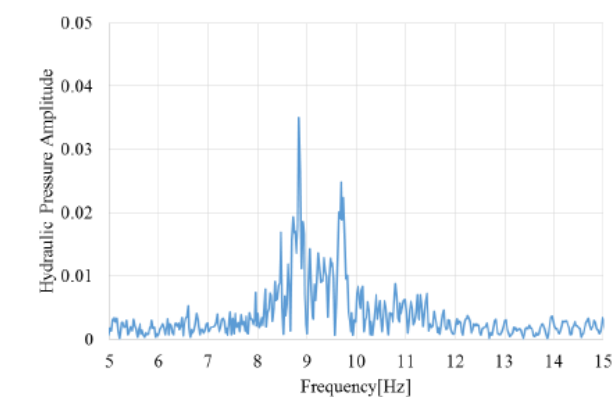
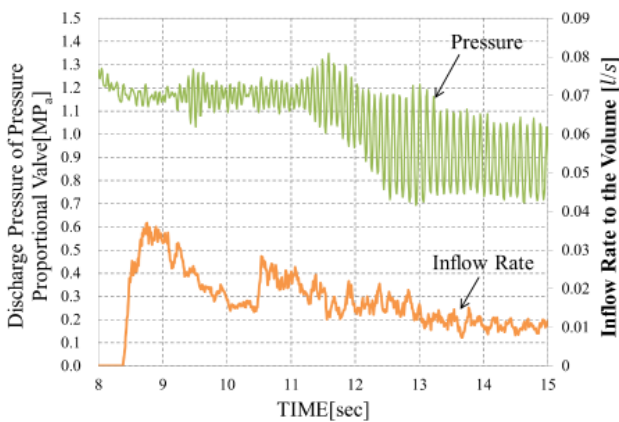


Fig.2 A result of experiment that has coulomb frictional forces more than the rated value. The data on the downstream pressure shows unstable vibration. As the FFT analysis result, the frequency of Self-excited oscillation is from 8 to 10 Hz.

To clarify the conditions of unstable vibration occurrence, a unit test of the electromagnetic proportional valve was performed. The results are shown in Fig.3. In this test, ramp inputs were applied as currents to the solenoid to compare between the occurrence and the nonoccurrence of unstable vibration. The test confirmed that the single part does not cause unstable vibration and also revealed that a part causing unstable vibration has larger Coulomb frictional force and is hard to move.

The experiment results in Figs. 2 and 3 show that the Coulomb frictional force of the electromagnetic proportional valve causes unstable vibration in the combined structure.

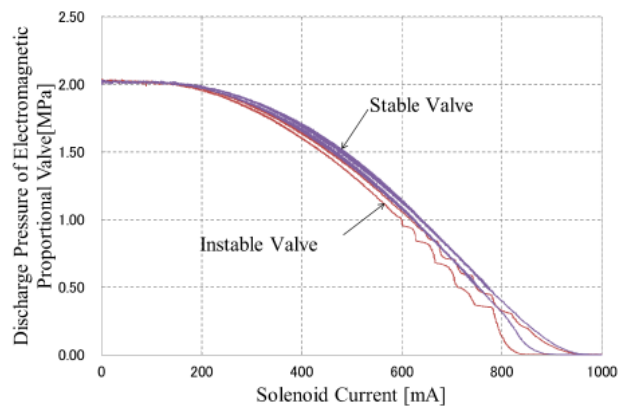


Fig.3 A result of electromagnetic proportional valve experiment. The vibration does not happens in a unit test result. Furthermore, the coulomb frictional force of the instable valve is big.

### 3. Nonlinear analysis

#### 3.1 Effects of Coulomb frictional force

To investigate the effect of the Coulomb frictional force on the transient response, nonlinear simulation was performed focusing only on the spool of the electromagnetic proportional valve without a hydraulic circuit. The calculation method considers that sine-curve thrust is forcibly input to the spool to obtain the displacement of the spool as an output. Equation (1) is used for calculation.

$$m_s \cdot \ddot{x} + R_s \cdot \dot{x} + R \cdot \text{sign}(\dot{x}) + k_s \cdot x = F \sin(2\pi ft) \quad (1)$$

$$R_s = \frac{\pi \cdot \mu \cdot L_s \cdot D_s}{\delta_s} \quad (2)$$

Here,  $m_s$  indicates the spool's mass [kg];  $R_s$  indicates viscosity [N s/m];  $k_s$  indicates spring constant [N/m];  $x$  indicates the moving displacement of the spool valve [m];  $L_s$  indicates the length of the spool sliding section [m];  $D_s$  and  $\delta_s$  indicate the spool valve's diameter radial clearance, respectively [m]; and  $\mu$  indicates the viscosity coefficient of the hydraulic oil [Pa s]. The results are shown in Fig.4. Displacement becomes moderate as the difference between the external force and the Coulomb frictional force decreases, and sticking occurs in the

range where the external force has the same value as the Coulomb frictional force or less. This demonstrates that the effect of the Coulomb frictional force causes a phase delay and a reduction in amplitude.

Then, the entire hydraulic system shown in Fig.1 is focused. The hydraulic circuit on the discharge side of the valve has a structure in which a feedback is provided for the spool, such that a closed-loop circuit is established. From the viewpoint of control engineering, which manages the stability of a closed-loop system, it is supposed that the unstable oil-pressure vibration in Fig.2 is caused by the phase delay (insufficient phase margin) of the closed loop system. It seems that the phase delay due to the Coulomb frictional force causes a phase difference of  $180^\circ$  between the spools of the electromagnetic proportional valve and the pressure proportional valve, resulting in a limit cycle. However, a general phase delay due to the Coulomb frictional force does not exceed  $90^\circ$ . That is to say, there seems to be any factor causing a phase delay other than the Coulomb frictional force.

Accordingly, consideration is given to the elastic deformation of oil in the oil pressure chamber placed in the downstream section of the pressure proportional valve. It is well-known that as hydraulic systems for transport equipment also provide a function as lubricants for rotational machinery, gears' stirring causes the oil to contain approximately 10 to 20% of air. Oil in a high-capacity oil pressure chamber containing considerable air content is softer and its deformation is longer, resulting in delays. Accordingly, it is hypothesized that the Coulomb frictional force causes the electromagnetic proportional valve to have a phase delay of  $90^\circ$ , the air causes the pressure proportional valve to have a phase delay of  $90^\circ$ , and these phase delays are combined in the control chamber of the pressure proportional valve, resulting in  $180^\circ$  of phase difference between the spools of the electromagnetic and pressure proportional valves. This hypothesis will be verified with nonlinear simulation.

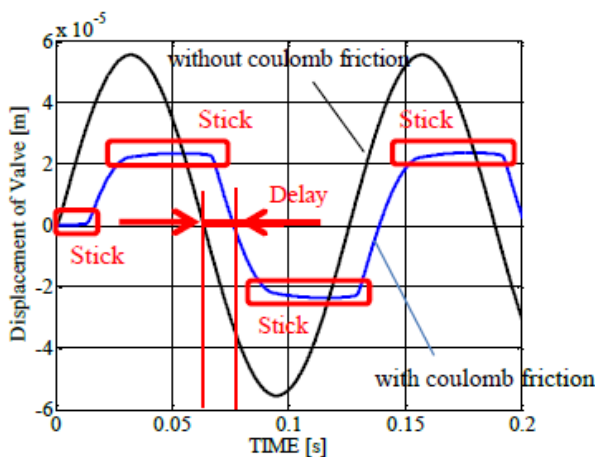


Fig.4 Phase lag due to the fixing strength of the coulomb frictional force.

### 3.2 Derivation of nonlinear-model equation

The motion equation of the hydraulic system for nonlinear simulation (Tanaka in 1987) (Tanaka in 1974)

will be derived. First, the calculation formula of the electromagnetic proportional valve is derived. The motion equation of the spool can be represented as Equation (3). As the phenomenon in this case has a vibration frequency of 8 to 10 Hz, which is lower than a fluid-caused vibration frequency, unsteady fluid force is neglected. Discharged oil pressure acts through the feedback circuit on the thrust of the spool.

$$(m_s + \rho V_s) \cdot \ddot{x} + R_s \cdot \dot{x} + R \cdot \text{sign}(\dot{x}) + k_s \cdot x = P_{sr} \cdot A_{sr} + F_{sj} + F_m \quad (3)$$

$$F_{sj} = -\rho \cdot Q_{so} \cdot v_{so} \cdot \cos\theta \quad (4)$$

$$Q_{sr} = C_{sr} \cdot A_{sr0} \sqrt{\frac{2(P_{so} - P_{sr})}{\rho}} \quad (5)$$

Here,  $\rho V_s$  indicates the mass of fluid in the valve [kg];  $F_m$  indicates cyclic external force [N];  $P_{sr}$  indicates feedback pressure [Pa];  $A_{sr}$  indicates the area of return pressure section of the electromagnetic proportional valve spool [m<sup>2</sup>];  $F_{sj}$  indicates the axial force component caused by jet force [N];  $P_{so}$  indicates spool valve discharge pressure [Pa];  $v_{so}$  indicates jet ejecting speed [m/s];  $\theta$  indicates the ejecting angle [rad];  $\rho$  indicates the density [kg/m<sup>3</sup>];  $Q_{so}$  indicates the valve discharge flow rate [L/s];  $Q_{sr}$  indicates the flow rate to the feedback section [L/s];  $C_{sr}$  indicates the flow coefficient of the orifice section; and  $A_{sr0}$  indicates the orifice area on the downstream side of the electromagnetic proportional valve [m<sup>2</sup>]. The relation of the flow on the discharge side of the electromagnetic proportional valve can be represented in Equation (6).

$$Q_{sv} = Q_{so} - Q_{sr} \quad (6)$$

Here,  $Q_{sv}$  indicates the flow rate into the control chamber of the pressure proportional valve, and  $Q_{so}$  indicates the discharge flow rate from the valve.

Then, the motion equation of the oil flowing in the valve is derived. The flow in the valve is regarded as a network orifice, as shown in Fig.6.

$$Q_{so} = Q_{si} - Q_{exh} \quad (7)$$

$$Q_{so} = C_{so} \cdot A_{so} \sqrt{\frac{2(P_{si} - P_{so})}{\rho}}, \quad Q_{exh} = C_{exh} \cdot A_{exh} \sqrt{\frac{2(P_{si} - P_{exh})}{\rho}}, \quad Q_{si} = C_{si} \cdot A_{si} \sqrt{\frac{2(P_{ss} - P_{si})}{\rho}} \quad (8)$$

Here,  $C_{so}$  indicates the flow coefficient on the valve discharge side;  $A_{so}$  indicates the opening area of the spool-valve discharge side [m<sup>2</sup>];  $P_{si}$  indicates the pressure in the valve [Pa];  $Q_{si}$  indicates the supplied flow rate [L/s];  $Q_{exh}$  indicates the leak flow rate [L/s];  $C_{exh}$  indicates the flow coefficient in the leak section;  $A_{exh}$  indicates the opening area of spool valve in the leak section [m<sup>2</sup>];  $P_{exh}$  indicates the atmospheric pressure [Pa];  $C_{si}$  indicates the flow coefficient on the supply side;  $A_{si}$  indicates the opening area on the supply side of the spool valve [m<sup>2</sup>]; and  $P_{ss}$  indicates the supply oil pressure [Pa].

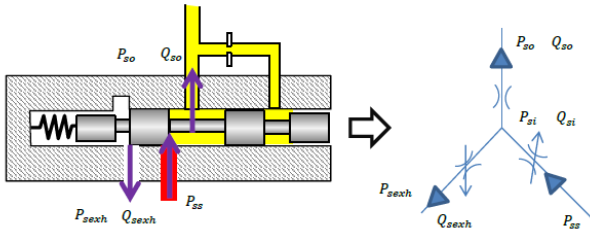


Fig.5 The oil flow rate in the valve is expressed as network orifice.

The control order pressure from the electromagnetic to the pressure proportional valve is represented as Equation (9).

$$\frac{d}{dt}P_{sc} = \frac{B}{V_{so}}(Q_{sv} - Q_{sc}) \quad (9)$$

Here,  $P_{sc}$  indicates the control order pressure to the pressure proportional valve [Pa];  $Q_{sc}$  indicates the amount of change in volume of the control chamber [L/s];  $V_{so}$  indicates the volume of piping on the discharge side of the electromagnetic proportional valve [m<sup>3</sup>]; and  $B$  indicates the bulk modulus of the oil [Pa].

The calculation formula of the pressure proportional valve is shown below. Unsteady fluid force is also neglected on the side of the pressure proportional valve.

$$(m_c + \rho V_c) \cdot \ddot{y} + R_c \cdot \dot{y} + K_c \cdot y = P_{sc} \cdot A_c - P_{cr} \cdot A_{cr} + F_{cj} \quad (10)$$

$$R_c = \frac{\pi \mu L_c D_c}{\delta_c} \quad (11)$$

$$F_{cj} = -\rho \cdot Q_{co} \cdot v_{co} \cdot \cos\theta \quad (12)$$

$$Q_{cr} = C_{cr} \cdot A_{cro} \sqrt{\frac{2(P_{cr} - P_{co})}{\rho}} \quad (13)$$

$$Q_{ss} = C_{cc} \cdot A_{cco} \sqrt{\frac{2(P_{so} - P_{co})}{\rho}} \quad (14)$$

Here,  $m_c$  indicates the spool mass [kg];  $\rho V_c$  indicates the mass of fluid in the valve [kg];  $R_c$  indicates the viscosity [N·s/m];  $K_c$  indicates the spring constant [N/m];  $y$  indicates the moving displacement of the spool valve [m];  $P_{sc}$  indicates the control pressure from the electromagnetic proportional valve [Pa];  $P_{cr}$  indicates the feedback pressure [Pa];  $A_{cr}$  indicates the area of return pressure section of the spool valve [m<sup>2</sup>];  $F_{cj}$  indicates the axial force component by jet force [N];  $L_c$  indicates the length of spool sliding section [m];  $D_c$  indicates the spool valve diameter [m];  $\delta_c$  indicates the radial clearance of the spool valve [m];  $P_{co}$  indicates the spool valve discharge pressure [Pa];  $v_{co}$  indicates the jet ejecting speed [m/s];  $Q_{co}$  indicates the valve discharge flow rate [L/s];  $Q_{cr}$

indicates the flow rate in the feedback section [L/s];  $C_{cr}$  indicates the flow coefficient of the return orifice;  $A_{cro}$

indicates the return orifice area [m<sup>2</sup>];  $Q_{ss}$  indicates the flow rate into the control chamber [L/s];  $C_{cc}$  indicates the flow coefficient of the orifice on the side of the

electromagnetic proportional valve; and  $A_{cco}$  indicates the orifice area on the side of the electromagnetic proportional valve [m<sup>2</sup>].

The influence of the flow on the discharge side of the pressure proportional valve can be represented as Equation (15).

$$Q_{cv} = Q_{co} + Q_{cr} \quad (15)$$

Here,  $Q_{cv}$  indicates the flow rate into the piston [L/s], and  $Q_{co}$  indicates the flow rate discharged from the valve [L/s].

Then, the motion equation of the oil flowing in the valve is derived. The flow in the valve is regarded as a network orifice similarly to the electromagnetic proportional valve.

$$Q_{co} = Q_{ci} - Q_{cexh} \quad (16)$$

$$Q_{co} = C_{co} \cdot A_{co} \sqrt{\frac{2(P_{ci} - P_{co})}{\rho}}, \quad Q_{cexh} = C_{cexh} \cdot A_{cexh} \sqrt{\frac{2(P_{ci} - P_{cexh})}{\rho}}, \quad Q_{ci} = C_{ci} \cdot A_{ci} \sqrt{\frac{2(P_{cs} - P_{ci})}{\rho}} \quad (17)$$

Here,  $C_{co}$  indicates the flow coefficient on the valve discharge side;  $A_{co}$  indicates the opening area of the spool-valve discharge side [m<sup>2</sup>];  $P_{ci}$  indicates the pressure in the valve [Pa];  $Q_{cexh}$  indicates the leak flow rate [L/s];  $C_{cexh}$  indicates the flow coefficient in the leak section;  $A_{cexh}$  indicates the opening area of the spool valve in the leak section [m<sup>2</sup>];  $P_{cexh}$  indicates the atmospheric pressure [Pa];  $Q_{ci}$  indicates the flow rate on the supply side [L/s];  $C_{ci}$  indicates the flow coefficient on the supply side;  $A_{ci}$  indicates the opening area on the supply side of the spool valve [m<sup>2</sup>]; and  $P_{cs}$  indicates the supply oil pressure [Pa].

Here, focusing on the results in Fig.2, where unstable vibration occurs, the amount of backflow from the cylinder is 0.01 L/s, which is a small value. If converted into a change in volume in the cylinder per amplitude of unstable vibration, it becomes  $1 \times 10^{-3}$  to  $1.25 \times 10^{-3}$  [L], which can be neglected as an extremely small value compared to a cylinder volume of 0.385 L. Accordingly, the hydraulic cylinder is treated as a large oil chamber for simplification of the calculation formula. Therefore, the control order pressure from the pressure proportional valve to the piston is represented as Equation (18).

$$\frac{d}{dt}P_{cc} = \frac{B}{V_p}(Q_{cv} - Q_{cc}) \quad (18)$$

Here,  $P_{cc}$  indicates the supply pressure to the oil pressure chamber [Pa];  $Q_{cv}$  indicates the flow rate into the oil pressure chamber [L/s];  $Q_{cc}$  indicates the amount of leak from the oil pressure chamber [L/s]; and  $V_p$  indicates the piston-chamber volume [m<sup>3</sup>].

The electromagnetic and pressure proportional valves are combined in Equation (19).

$$Q_{ss} = A_c \cdot \dot{y} \quad (19)$$

### 3.2 Nonlinear simulation

The results of performing the nonlinear simulation applying Equations (3) – (19) are shown in Fig.6. Tables 1 and 2 show the parameters related to the electromagnetic proportional valve used in the calculation and the parameters of the pressure proportional valve and the oil pressure chamber placed on the downstream side, respectively. Both the applied electromagnetic and pressure proportional valves have under-lap characteristics. Their characteristics are shown in Figs. 7 and 8, respectively. For the applied oil, the calculated values of bulk moduli by pressure (Imagine in 2007) are shown in Fig.9. Figure 6 shows that the spools of the electromagnetic and pressure proportional valves have a maximum phase delay of 180°. Additionally, vibration frequency is approximately 8 Hz, conforming to the experimental results. Furthermore, similarly to the actual unit, such results also agree regarding the occurrence of unstable vibration with larger Coulomb frictional force and no occurrence with smaller one. The relationship between air content rates and unstable vibration occurrence were also examined with the nonlinear simulation, but not with the actual unit. As a result, it was revealed that the occurrence/nonoccurrence of vibration varies with air content rates and that vibration frequency also varies. If the air content rate is 10%, vibration frequency is approximately 10 Hz. If the air content rate decreases, no vibration occurs. In contrast, if the air content rate is approximately 15% or more, no vibration occurs as well. The cause seems that a lower air content rate makes a phase delay insufficient (a larger phase margin), and a higher air content rate

makes the restoring force of the oil pressure chamber insufficient.

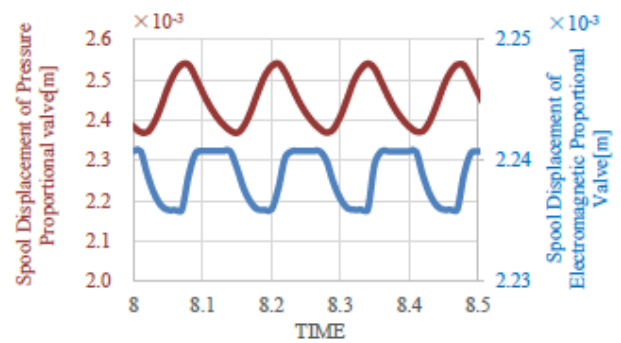


Fig.6 The nonlinear simulation result in the analysis model of Fig.1. The phase difference of the pressure proportional valve and the electromagnetic proportional valve has 180 deg.

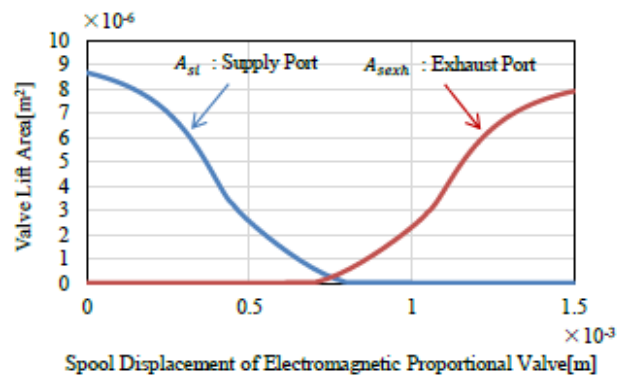


Fig.7 Relationship between spool displacement of electromagnetic proportional valve and valve lift area. The proportional valve has properties of underlap.

Table 1 Electromagnetic proportional Valve (EPV) parameter of nonlinear model.

$m_s$	0.348E-03	kg	Mass of the EPV Spool
$L_s$	2.45E-02	m	Length of the EPV Spool Sliding Portion
$D_s$	8.49E-3	m	Diameter of the EPV Spool
$\delta_s$	3.40E-5	m	Radial Clearance of the EPV Spool
$R$	0.06	N	Coulomb's Frictional Force
$k_s$	1800	N/m	Spring Stiffness
$V_s$	1.00E-06	m <sup>3</sup>	Volume in the EVP Spool
$A_{sr}$	5.34E-06	m <sup>2</sup>	Area of the EPV Return Pressure Surface
$A_{sro}$	4.15E-06	m <sup>2</sup>	Orifice Area of the EVP Return Pressure Side
$A_{so}$	8.31E-06	m <sup>2</sup>	Hydraulic Linear Leakage Coefficient in the Control Line between the EPV and the PPV
$P_{ss}$	1.5	MPa	Supply Pressure
$V_{so}$	6.77E-07	m <sup>3</sup>	Delivery Pipe Volume of the EVP

Table 2 Pressure proportional valve (PPV) parameter of nonlinear model.

$m_c$	1.85E-2	kg	Mass of the PPV Spool
$L_c$	2.49E-02	m	The Length of the PPV Spool Sliding Portion
$D_c$	9.33E-03	m	The Diameter of the PPV Spool
$\delta_c$	3.33E-05	m	Radial Clearance of the PPV Spool
$K_c$	75	N/m	Spring Stiffness
$V_c$	5.48E-06	m <sup>3</sup>	Volume in the PPV Spool
$A_c$	2.27E-04	m <sup>2</sup>	Area of the PPV Control Pressure Surface
$A_{cr}$	6.83E-05	m <sup>2</sup>	Area of the PPV Return Pressure Surface
$A_{cro}$	7.85E-07	m <sup>2</sup>	Orifice Area of the PPV Return Pressure Side
$A_{cco}$	5.03E-07	m <sup>2</sup>	Orifice Area of the PPV Control Pressure Side
$A_{co}$	1.26E-05	m <sup>2</sup>	Orifice Area of the PPV Outlet Pressure Side
$P_{cs}$	1.5	MPa	Supply Pressure
$V_p$	3.58E-04	m <sup>3</sup>	Oil Pressure Volume

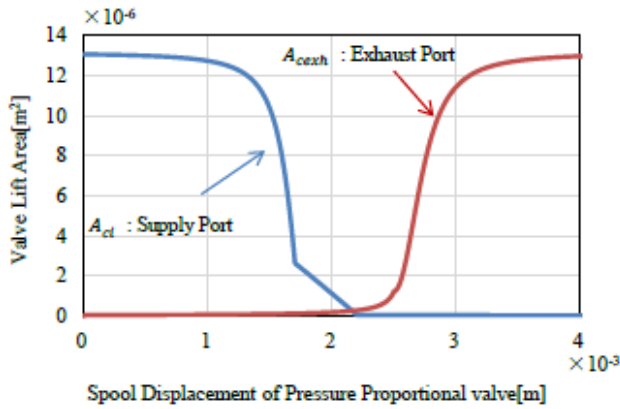


Fig.8 Relationship between spool displacement of pressure proportional valve and valve Lift area. The proportional valve has properties of underlap.

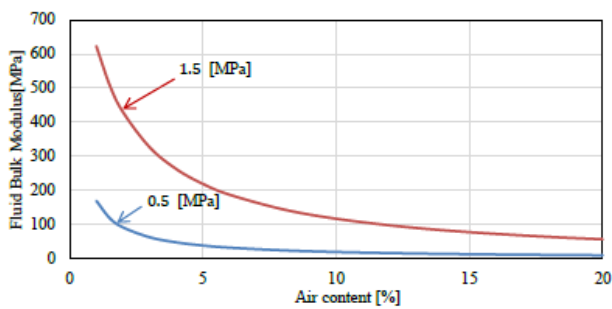


Fig.9 Relationship between air content and fluid bulk modulus  $B$  in each pressure. Air content of the oil is about 10 to 20%.

#### 4. Linearization of nonlinear hydraulic equation

The model of an electromagnetic proportional valve represented by Equations (3) – (9) was linearized (Loiget al in 2006). Omitting the Coulomb frictional force, which has strong nonlinear characteristics, it is represented as Equations (20) – (24). The linearization of the Coulomb frictional force and the linearized representative points will be explained in Chapter 5 and Section 6.2, respectively.

$$M_s \cdot \ddot{X} + R'_s \cdot \dot{X} + K_s \cdot X = F_m + P_{sol} \cdot A_{sr} \quad (20)$$

$$R'_s = R_s + \frac{A_{sr}^2}{Y_{sr}} \quad (21)$$

$$Q_c = Q_v - A_{sr} \cdot \dot{X} \quad (22)$$

$$Q_{sv} = G_{sv} \cdot X - Y_{sv} \cdot P_c \quad (23)$$

$$P'_{cc} = KHS \cdot (Q_c - Q_{sv}) \quad (24)$$

Then, the pressure proportional valve and the oil pressure chamber models represented by Equations (10) – (19) are linearized as Equations (25) – (29).

$$M_c \cdot \ddot{Y} + R'_c \cdot \dot{Y} + K_c \cdot Y = P_{sol} \cdot A_c - P_{col} \cdot A_{cr} \quad (25)$$

$$R'_c = R_c + \frac{A_c^2}{Y_{cc}} + \frac{A_{cr}^2}{Y_{cr}} \quad (26)$$

$$Q_{cv} = Q_{co} + A_{cr} \cdot \dot{Y} \quad (27)$$

$$Q_{co} = G_{cv} \cdot Y - Y_{cv} \cdot P_t \quad (28)$$

$$P'_{cc} = KHL \cdot (Q_{cv} - Q_{cc}) \quad (29)$$

Here,  $M_s$  indicates the mass of the electromagnetic proportional valve spool including fluid in the valve [kg];  $K_s$  indicates the spring constant in the linearized electromagnetic proportional valve [N/m];  $Y_{sr}$  indicates the flow coefficient of the return orifice of the linearized electromagnetic proportional valve [ $\text{m}^3/\text{s}/\text{Pa}$ ];  $G_{sv}$  indicates the flow-rate gain of the linearized electromagnetic proportional valve [ $\text{m}^3/\text{s}/\text{m}$ ];  $Y_{sv}$  indicates the flow coefficient of the linearized electromagnetic proportional valve [ $\text{m}^3/\text{s}/\text{Pa}$ ];  $KHS$  indicates the stiffness of oil on the side of the linearized electromagnetic proportional valve [ $\text{Pa}/\text{m}^3$ ];  $M_c$  indicates the mass of the pressure proportional valve spool including fluid in the valve [kg];  $K_c$  indicates the spring constant in the linearized pressure proportional valve [N/m];  $Y_{cc}$  indicates the flow coefficient of the side orifice on the linearized electromagnetic proportional valve [ $\text{m}^3/\text{s}/\text{Pa}$ ];  $Y_{cr}$  indicates the flow coefficient of the return orifice on the linearized pressure proportional valve [ $\text{m}^3/\text{s}/\text{Pa}$ ];  $G_{cv}$  indicates the flow-rate gain of the linearized pressure proportional valve [ $\text{m}^3/\text{s}/\text{m}$ ];  $Y_{cv}$  indicates the flow coefficient of the linearized pressure proportional valve [ $\text{m}^3/\text{s}/\text{Pa}$ ];  $QL$  indicates the amount of oil into the oil pressure chamber [L/s]; and  $KHL$  indicates the stiffness of oil on the side of the linearized pressure proportional valve [ $\text{Pa}/\text{m}^3$ ]. The linearized equations can be illustrated in the block diagram of Fig.10, which is a cascade-type model.

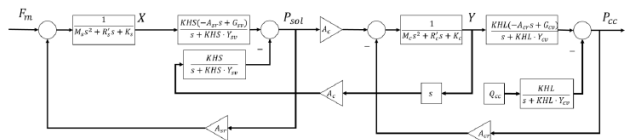


Fig.10 Linearization model of the hydraulic system has cascade structure.

### 5. Linearization of Coulomb frictional force

#### 5.1 Managing Coulomb frictional force for unstable vibration analysis

As previously described, the factors of this unstable vibration are the air content rate of oil and the Coulomb frictional force as a nonlinear element. The former is represented by the values of the oil stiffness in the



linearized model, KHS, and KHL, in Fig.13, but the latter loses its characteristics through linearization. Accordingly, this study uses the describing function method to represent this nonlinear element. A describing function is a complex function representing the amplitude ratio and the phase difference between the sine-wave input to a nonlinear element and the fundamental wave component, which is extracted from the output component and has the same frequency as the input.

In contrast, a phase delay causing vibration is not represented in the function describing the Coulomb frictional force. The cause and the management method are described below.

The equation of the Coulomb frictional force is shown in Equation (30).

$$Z(t) = -D(-\pi \leq \omega t < 0), D(0 \leq \omega t < \pi) \tag{30}$$

Here,  $D$  indicates the Coulomb frictional force. To derive the describing function (Hirai in 2010) (Mochizuki and others in 2015), output  $Z(t)$  indicates Fourier-transformed. As  $Z(t)$  is an odd function,

$$A_1 = 0 \tag{31}$$

$$B_1 = \frac{2}{\pi} \int_0^{\pi} z(t) \sin(\omega t) d(\omega t) = \frac{2D}{\pi} [-\cos \theta]_0^{\pi} = \frac{4D}{\pi} \tag{32}$$

Therefore, the describing function  $N(a)$  is represented as follows:

$$|N(a)| = \frac{z}{a} = \frac{4D}{\pi a} \tag{33}$$

$$\angle N(a) = \tan^{-1}\left(\frac{A_1}{B_1}\right) = 0 \tag{34}$$

Therefore, Equations (33) and (34) represent equivalent viscous damping, and they affect only the amplitude.

Then, the representation of the Coulomb frictional force as hysteresis is examined. In various hysteresis models, the linear approximate expression of hysteresis holds the input of the last sample as a memory to apply to the current friction force (Wakasa in 2013). At first, nonlinear simulation is applied to verify whether a hysteresis model can reproduce the response of a spool displacement in a model with Coulomb frictional force.

Equation (35) is the motion equation of a single-degree-of-freedom system imitating the spool of an electromagnetic proportional valve with Coulomb frictional force. Equation (36) is a hysteresis model.  $N(x)$  is a hysteresis element.

$$M \cdot \ddot{x} + C \cdot \dot{x} + R \cdot \text{sign}(\dot{x}) + K \cdot x = F \cdot \sin(2\pi f) \tag{35}$$

$$M \cdot \ddot{x} + C \cdot \dot{x} + K \cdot x = F \cdot \sin(2\pi f) \cdot N(x) \tag{36}$$

Here, it is assumed that  $|N(x)| \leq 1$ . The conformity of Equation (35) to Equation (36) is demonstrated in the time axis. Figure 11 illustrates the results of the nonlinear simulation of the displacement when a cyclic

external force is applied to the single-degree-of-freedom model, and to Equations (35) and (36). The results show that the spool displacement responses of both models have good agreement. This demonstrates that Coulomb frictional force causing vibration can be converted into hysteresis and also that the nonlinear model of a hydraulic system can be separated into linear and nonlinear elements of an input section.

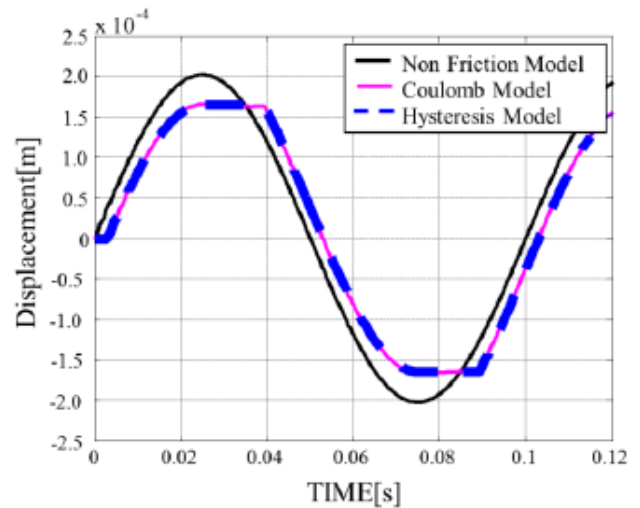


Fig.11 Comparison hysteresis model with coulomb's friction model. The both models accord well. Therefore, the coulomb model is converted into the hysteresis model.

### 5.2 Describing the function of hysteresis

Figure 12 illustrates the hysteresis model used in Equation (35), in which the horizontal and vertical axes represent the displacement of the model without hysteresis and with hysteresis, respectively. The describing function of this hysteresis element can be expressed as Equation (37). Refer to Fig.12 for the outline of  $N(a)$  and the meanings of the parameters  $a$ ,  $b$ , and  $m$ .

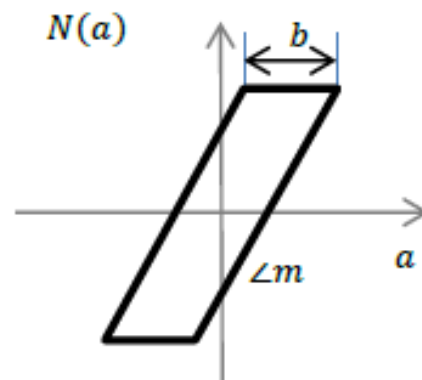


Fig.12 Hysteresis.

$$N(a) = \frac{m}{2} \left( 1 + \frac{2}{\pi} (\phi + \sin \phi \cos \phi) \right) - j \frac{2bm}{\pi a} \left( 1 - \frac{1}{2} \left( \frac{b}{a} \right) \right) \tag{37}$$

$$\phi = \frac{\pi - b}{a} \tag{38}$$

### 5.3 Error valuation of describing function

Various methods have been proposed for nonlinear vibration analyses (Okumura and others in 1987), all of which are approximate solvers. The describing function method utilizing the fundamental wave component of Fourier transform is not an exception. Accordingly, the validity of this method is examined by grasping the error characteristics of the describing function.

#### 5.3.1 Error evaluation in time response

To quantify the error given to the time response of hysteresis by approximation with the describing function, the response in the time axis is used. Equation (37) cannot be used as it is for the error evaluation in the time axis response, thus inverse Fourier transform is necessary. First, Equation (37) is converted into Equation (39).

$$\frac{m}{2} \left( 1 + \frac{2}{\pi} (\theta + \sin\theta \cos\theta) \right) - j \frac{2bm}{\pi a} \left( 1 - \frac{1}{2} \left( \frac{b}{a} \right) \right) = \sqrt{A^2 - B^2} \left( \frac{A}{\sqrt{A^2 - B^2}} - j \frac{B}{\sqrt{A^2 - B^2}} \right) \quad (39)$$

$$A = \frac{m}{2} \left( 1 + \frac{2}{\pi} (\theta + \sin\theta \cos\theta) \right) \quad (40)$$

$$B = \frac{2bm}{\pi a} \left( 1 - \frac{1}{2} \left( \frac{b}{a} \right) \right) \quad (41)$$

In addition to the above, assuming

$$\cos \theta = \frac{A}{\sqrt{A^2 - B^2}}, \quad \sin \theta = \frac{B}{\sqrt{A^2 - B^2}} \quad (42)$$

Equation (39) can be converted into Equation (43) according to Euler's formula. Here,  $\omega = 2\pi f$ , where  $f$  indicates the frequency of the input signal.

$$\sqrt{A^2 - B^2} e^{-j\frac{\theta}{\omega}} \quad (43)$$

By inverse-Fourier-transforming, Equation (44) is obtained. Here,  $u$  indicates a *sin*-wave input signal.

$$\sqrt{A^2 - B^2} \cdot u \left[ t - \frac{\theta}{\omega} \right] \quad (44)$$

This indicates that the time response of inputting a *sin* wave into the describing function of  $N(a)$  is represented by a gain and a dead time element. Equation (45) means a linear one-degree-of-freedom model, Equation (46) means a nonlinear hysteresis model, and Equation (47) means a hysteresis describing function model.

$$M \cdot \ddot{a} + C \cdot \dot{a} + K \cdot a = F \quad (45)$$

$$M \cdot \ddot{a} + C \cdot \dot{a} + K \cdot a = F \cdot N(a) \quad (46)$$

Here, it is assumed that  $|N(a)| \leq 1$ .

$$M \cdot \ddot{a} + C \cdot \dot{a} + K \cdot a = F \cdot \sqrt{A^2 - B^2} \cdot u \left[ t - \frac{\theta}{\omega} \right] \quad (47)$$

Figure 13 illustrates the results of the error evaluation of the describing function in the time axis by using these equations. An input of 5 Hz was applied as a forced-cycle

external force. The left graph in Fig.13 illustrates the comparison in Coulomb frictional force equivalent to the actual unit, in which the phase differences generally conform to each other. The right graph illustrates the results assuming Coulomb frictional force equivalent to or higher than that of the actual unit. In the right graph, errors in both amplitude and phase are larger. The results demonstrate that the describing function method is valid in this vibration analysis applying hysteresis. Additionally, as smaller hysteresis improves the accuracy, it can be regarded as appropriate for estimating the stability margin.

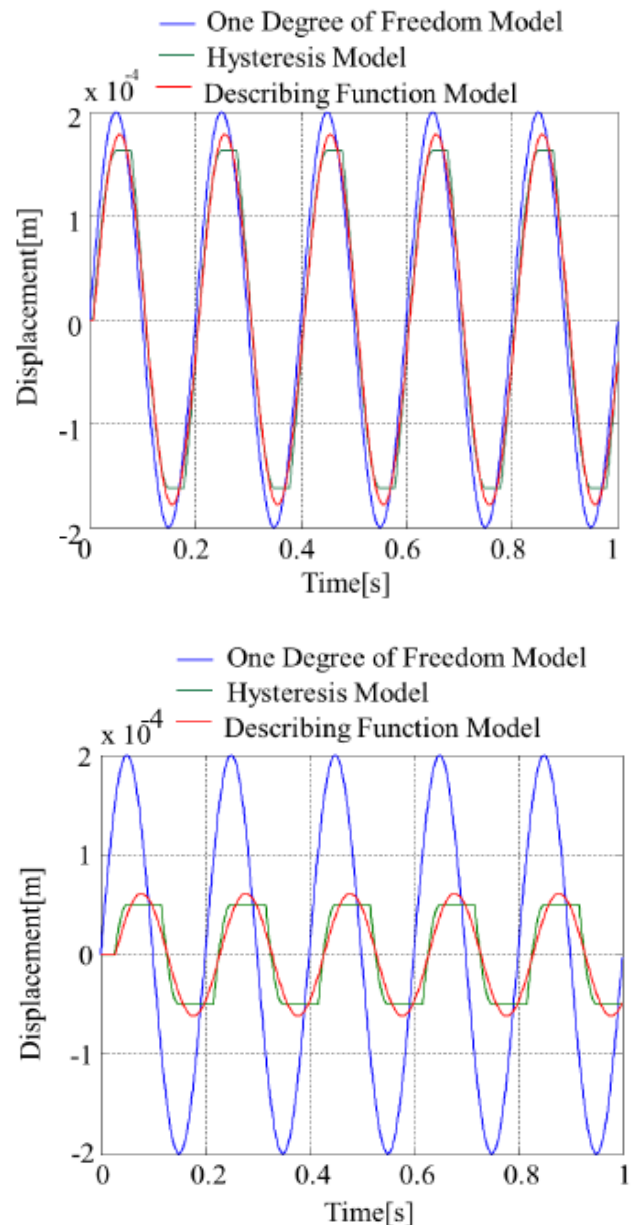


Fig.13 Error estimates in time axis. It is thought that this technique is appropriate to measure stability margin. This is because the error becomes small so that a coulomb frictional force is small.

### 5.3.2 Error evaluation in vibration frequency range

As Equation (37) shows, the describing function uses only the fundamental wave component of Fourier transform, such that it is a transfer function dependent on input amplitude and not input frequency. Therefore, to use the describing function to perform a vibration analysis applying hysteresis, it will be necessary to extract only the hysteresis characteristics at a given frequency to perform an analysis in the frequency range. To perform an analysis in the entire frequency range, it will be necessary to change the parameters of hysteresis for each input frequency. Accordingly, the amount of error for input frequency should be evaluated. The examination method is as follows: input a variable frequency of 1 to 100 Hz into the simulation model of Equation (48); perform FFT analysis of the obtained results to draw a Bode diagram; compare the Bode diagram with the Bode diagram of Equation (49); and adjust the describing function in Equation (49) to the amount of hysteresis with a cyclic external force of 5 Hz input into Equation (48).

$$M \cdot \ddot{x} + R \cdot \text{sign}(\dot{x}) + K \cdot x = F \tag{48}$$

$$M \cdot \ddot{x} + K \cdot x = F \cdot \left\{ \frac{m}{2} \left( 1 + \frac{2}{\pi} (\theta + \sin\theta \cos\theta) \right) - j \frac{2bm}{\pi a} \left( 1 - \frac{1}{2} \left( \frac{b}{a} \right) \right) \right\} \tag{49}$$

Figure 14 illustrates the results of the calculation. The red and the blue lines represent the results of Equations (48) and (49), respectively. The phase delay from the approximate expression of Equation (49) indicates a flat characteristic. For Equation (48), the lower the frequency, the larger the delay, but the error is approximately 2 to 4° in the range of 1 to 10 Hz, showing conformity in general. In addition, for amplitude, the higher the frequency, the larger the error. Therefore, the sensitivity of phase delay to an increase in frequency can be regarded as low in the unstable-vibration frequency range of 8 to 10 Hz for this case. In addition, the strictest condition requiring a stable analysis can be considered to be the low-frequency side of vibration frequency. For a vibration range of 8 to 10 Hz, the analysis at 8 Hz is valid.

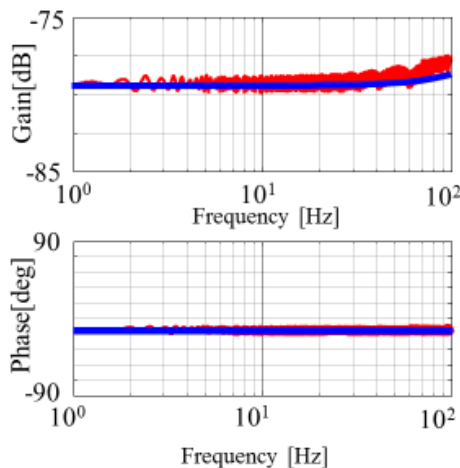


Fig.14 Error estimate in frequency response. The phase of Equation (48) almost accords with Equation (49).

## 6. Stabilization analysis with describing function method

### 6.1 Analysis of block diagram

The method of incorporating a specific hysteresis model into Fig.10 and the method of drawing a Nyquist diagram including a describing function for a stabilization analysis are illustrated with a linearized block diagram. The block diagram of this hydraulic system with hysteresis incorporated into Fig.10 is shown as Fig.15. On  $G_{SV}$  side of the electromagnetic proportional valve (the block from  $F_m$  to  $P_{sol}$ ), hysteresis  $N$  exists. Additionally, it is shown that electromagnetic proportional valve  $G_{SV}$  and control valve  $G_c$  (the block from  $A_c P_{sol}$  to  $P_{cc}$ ) are coupling-connected. Here, parameter  $A_c$  can be regarded as a gain for connecting the two systems.

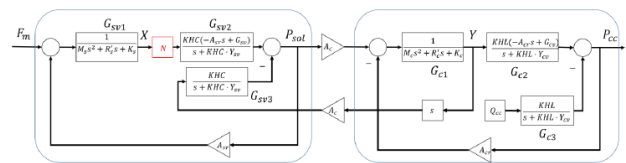


Fig.15 Linearization model including hysteresis factor. The nonlinear element is included in hydraulic pressure model. It is necessary to separate the linear element and the nonlinear element for the purpose of analysis.

Here,

$$Y = G_{c1} A_c P_{sol} - G_{c1} A_{cr} G_{c2} Y \tag{50}$$

is valid, thus the transmission characteristics from  $P_{sol}$  to  $Y$  can be expressed as follows:

$$Y = \frac{G_{c1} A_c}{1 + G_{c1} A_{cr} G_{c2}} P_{sol} \tag{51}$$

$G_{c3}$  indicates not included in Equation (51) because it is not in the feedback loop. From the above, Fig.15 can be converted into Fig.16. Here, when representing Fig.16 as a Lur'e system, the stability conditional expression is that the characteristic Equation (52) has no solution. In addition, based on Fig.16, the analysis object is a fundamental closed-loop system, thus the Nyquist's graphical solution in the general describing function method can be applied.

$$1 - N(X) G_{sv1}(s) A_{sv} \hat{G}_{sv3}(s) G_{sv2}(s) = 0 \tag{52}$$

$$\hat{G}_{sv3} = \frac{1}{1 + \frac{G_{sv2} G_{c1} A_c^2 s}{1 + G_{c1} A_{sv} G_{c2}}} \tag{53}$$

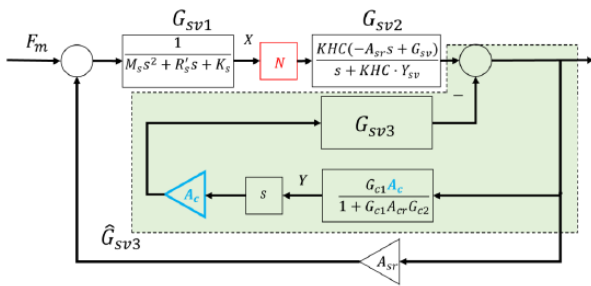


Fig.16 Deformation of Figure 12 results in a Lur'e system. The linear element and the nonlinear element are separated so that the describing function analysis is applied easily.

### 6.2 Representative point

The analysis is performed considering a point representative of the linearized hydraulic circuit model. This point is the one that provides the maximum phase difference between the spools of the electromagnetic and pressure proportional valves, where the most unstable state is established in the results of Fig.6. Various parameters for the electromagnetic and pressure proportional valves are shown in Tables 3 and 4.

Table 3 Electromagnetic proportional valve (EPV) parameter of linearization model.

$M_e$	1.18E-03	kg	Mass of the EPV spool + Mass flow in the spool valve
$R_e$	1.91	N·s/m	EPV Friction Coefficient on the Spool Including not only Friction but also Induced Damping from Hydraulic Orifices
$K_e$	7.55E+03	N/m	Spring Stiffness and Equivalent Stiffness Including Jet Forces on the EPV spool
$KHS$	1.12E+12	$P_a/m^3$	Hydraulic Stiffness of the Control Volume between the EPV and the PPV side
$Y_{sv}$	6.82E-07	$m^3/s/P_a$	Hydraulic Linear Leakage Coefficient in the Control Line between the EPV and the PPV
$Y_{sv}$	1.02E-11	$m^3/s/P_a$	Leakage Gain of the EPV
$G_{sv}$	-5.43E-01	$m^3/s/m$	Flow Gain of the EPV

Table 4 Pressure proportional valve (PPV) parameter of linearization model.

$M_e$	2.30E-2	kg	Mass of the PPV spool + Mass flow in the spool valve
$R_e$	2.18	N·s/m	PPV Friction Coefficient on the Spool Including not only Friction but also Induced Damping from Hydraulic Orifices Around
$K_e$	75.2	N/m	Spring Stiffness and Equivalent Stiffness Including Jet Forces on the PPV Spool
$KHL$	3.56E+11	$P_a/m^3$	Hydraulic Stiffness of External Volume
$Y_{ec}$	2.32E-11	$m^3/s/P_a$	Hydraulic linear Leakage Coefficient in the PPV Control Line
$Y_{sv}$	2.38E-11	$m^3/s/P_a$	Hydraulic linear Leakage Coefficient in the PPV Return Line
$Y_{sv}$	1.23E-11	$m^3/s/P_a$	Leak Gain of the PPV
$G_c$	-9.86E-2	$m^3/s/m$	Flow Gain of the PPV

## 7. Analysis of results

The left side of Fig.17 is the Nyquist diagram showing each locus of the frequency-dependent hydraulic linear element (blue line) and the amplitude-dependent hysteresis nonlinear element (red line) in the block diagram in Chapter 6.1. In the diagram, “ $\omega$ ” means frequency, and “ $a$ ” means amplitude. There are two intersection points where the characteristic Equation (52) has solutions: one is called Point-A, and the other Point-B. At Point-B, a larger amplitude results in an unstable range, leading to a further larger amplitude. On the contrary, a smaller amplitude results in a stable range, leading to a further smaller amplitude, and consequently an unstable state. In contrast, at Point-A, a larger amplitude results in a stable range, leading to a

smaller amplitude. A smaller amplitude results in an unstable range, leading to a larger amplitude. Therefore, a limit cycle is established at Point-A. In this examination, all the actual units, the nonlinear simulation, and the stability analysis Point-A have the same integral part in the frequencies.

Additionally, considering an item with small Coulomb frictional force, this analysis method was applied to the electromagnetic proportional valve that causes no vibration in the experiment and the nonlinear simulation. The results are shown in the right diagram of Fig.17. As a dither of 305 [Hz] is provided for the electromagnetic proportional valve, vibration amplitude caused by the dither is minimum, such that the amplitude locus may break halfway. That is, it is shown that the system is stable as no intersection point exists between the frequency locus and the amplitude locus.

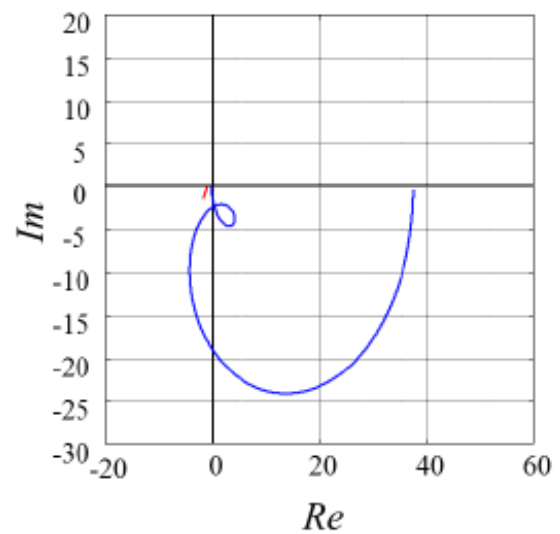
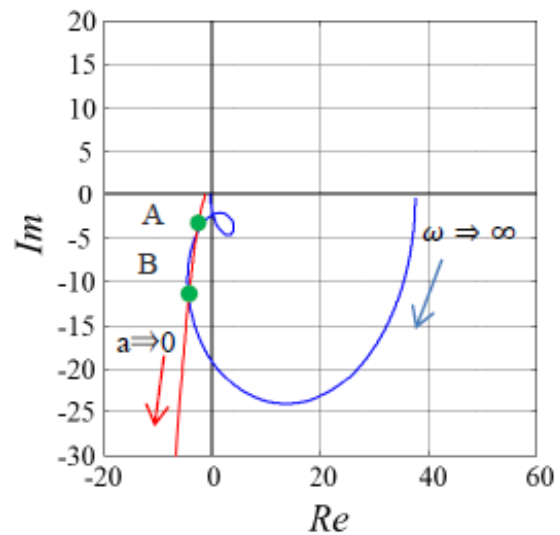


Fig.17 Pictorial solution by the describing function technique. The left-hand figure is the analysis result using the unstable vibration valve. Frequency of the intersection point is 8 Hz that corresponds with the experiment and the nonlinear simulation results. The right-hand figure result is for the stable vibration valve.

## 8. Conclusion

This study has clarified the mechanism of instability caused by the Coulomb friction force acting on the spool of the solenoid proportional valve in a hydraulic structure consisting of a solenoid proportional valve, a pressure proportional valve that amplifies the command pressure of the solenoid proportional valve, and a hydraulic cylinder. Additionally, we have presented a design method that can stabilize the Coulomb friction force, which is the cause of the vibration, by using a descriptive function method in which the amplitude ratio and phase difference from the input waveform are expressed by complex functions. The stabilization was achieved with a describing function method representing the amplitude ratio and the phase difference to the input waveform as a complex function. The findings of this study are summarized below.

### Instability mechanism

- (1) The Coulomb frictional force acts on the hydraulic system as a phase delay through the closed-loop hydraulic circuit placed in the downstream section of the electromagnetic proportional valve. Additionally, as the oil practically contains the air, the oil in a large oil chamber, such as a hydraulic cylinder in the hydraulic system, exhibits a delay in deformation. Such phase delays are combined, making the hydraulic system unstable.

### Design method for stabilization

- (2) Converting the Coulomb frictional force into hysteresis enables the linear analysis, which represents a phase delay causing vibration. For stabilization, this linearized model must be separated into a frequency locus and an amplitude locus, and it must not generate any intersection point in the Nyquist diagram;
- (3) As a measure for no generation of any intersection point, a reduction in the Coulomb frictional force is effective practically as well as theoretically.
- (4) This method can calculate the threshold of the Coulomb friction force, which is the stability limit.

## References

Hirai, K., Nonlinear control systems, Corona Publishing (2010), pp. 66–90 (in Japanese).  
 Imagine, S.A., Hyd advanced fluid properties, Technical bulletin, No. 117, Rev. 7 (2007).

Kumagai, K., Ryu, S., Ota, M., Maeno, K. and Zou, J., Vibration phenomenon of poppet valve in hydraulic system (Relationship between poppet valve vibration and cavitation phenomenon), Transactions of the Japan Fluid Power System Society, Vol. 45, No. 6 (2014), pp. 10–16 (in Japanese).

Loig, A., Stephane, N. and Antoine, V., Linear analysis approach for modelica models, Proceedings 7th Modelica Conference (2009), pp. 646–656.

Mochizuki, K., Awaya, I., Tani, H. and Shinohara, S., High-speed and high-precision control to overcome

response limit- control method of suppressing limit-cycle caused by backlash, Mitsubishi Heavy Industries Technical Review, Vol. 52, No.1 (2015), pp. 112–119 (in Japanese).

Okumura, K., Matsuo, T. and Kishima, A., Analysis of self-Exciting oscillations in nonlinear system with hysteretic characteristics, Vol. J70–A, No.6 (1987), pp. 882–888 (in Japanese).

Tanaka, H., Digital control and application of hydro-pneumatic, Kindaitosho (1987), pp.43–47 (in Japanese).

Tanaka, H., Ishihara, T. and Kojima, E., A study of dynamics of hydraulic pressure control valve, Transaction of the Japanese Society of Mechanical Engineers, Vol. 40, No. 340 (1974), pp. 3410–3417 (in Japanese).

Toyoda, N. and Tanaka, H., Acceleration of the electro-hydraulic variable valve actuator for a cam-less engine by using a 3– port switching valve, Transactions of the Japan Fluid Power System Society, Vo. 137, No. 4 (2006), pp.8–12 (in Japanese).

Wakahara, T., Izumi, T., Iida, T. and Tanaka, H., Research on hydro–mechanical shift system of belt–cvt to improve both efficiency and performance, Transactions of the Japan Fluid Power System Society, Vol. 36, No.6 (2005), pp.10–15 (in Japanese).

Wakasa, Y., Data–driven control for systems with nonlinearities, the Society of Instrument and Control Engineers, Vol. 52, No. 10, (2013), pp. 872–877 (in Japanese).

## Source

一般社団法人日本機械学会  
 日本機械学会論文集  
 Vol.83, No.852, 2017年

## Recipient



Katsuhiko Sando

## Awards

**2019 FA Foundation Award**

**2018 JSME Medal for Outstanding Paper**

**2018 Fluid Power Technology Promotion Foundation Award**

## Editorial Postscript

Thank you for your continued interest in our Nissan technical review. This edition, No. 87, is focused on two aspects.

First, the newest topics ProPILOT 2.0 and e-POWER were covered, which are based on the two areas to which Nissan is committed, i.e., vehicle intelligence and electrification, respectively. ProPILOT 2.0 offers secure, comfortable, and stress-free driving, serving as a partner of the driver. This system is the result of the research and development conducted for over 20 years in the field of vehicle control. This feature comprehensively covers the technical background. Meanwhile, e-POWER provides customers with a pleasant experience when driving electric motor-driven vehicles. This system could not have been achieved without the research and development conducted since the 1990s. This feature introduces the latest e-POWER adopted in the new Nissan NOTE and discusses the efforts devoted toward achieving the EV-ness unique to motor drives in the first AWD vehicle with e-POWER.

Second, to help more people access the review, it was decided to distribute the literature electronically online rather than distributing printed literature. It is hoped that this electronic format will facilitate tasks such as archiving and searching articles of interest to readers.

Finally, we would like to express our gratitude to those who wrote and edited the review online under the unusual circumstances due to the COVID-19 pandemic. We will be delighted if all our readers recognize the sophisticated technological capabilities of Nissan, of which we are proud.

Research Division  
Research Planning Department  
Osamu Niikura

### NISSAN TECHNICAL REVIEW 2021 No.87

Published	July, 2021
Publishing office	NISSAN MOTOR CO., LTD. Research Division Research Planning Department 1-1, Morinosatoaoyama, Atsugi-shi, Kanagawa 243-0123 Research Division Research Planning Department General Manager OSAMU NIIKURA
Editorial office	NISSAN CREATIVE SERVICES CO., LTD. Product Planning/R&D Business Services Department 560-2 Okatsu.Koku Atsugi Kanagawa 243-0192 C/O NISSAN Nissan Technical Center

